

Galaxy tilting in the era of *Gaia*

Samuel W. F. Earp

A thesis submitted in partial fulfilment for the requirements for the degree
of *Doctor of Philosophy* at the University of Central Lancashire.

March 2018

Declaration

Type of Award: Doctor of Philosophy

School: Physical Sciences and Computing

I declare that while registered as a candidate for the research degree, I have not been a registered candidate or enrolled student for another award of the University or other academic or professional institution.

I declare that no material contained in the thesis has been used in any other submission for an academic award and is solely my own work.

No proof-reading service was used in the compilation of this thesis.

Samuel W. F. Earp

March 2018

To my loving family, whom I owe everything.

Abstract

Determining the orientation of galaxies with respect to their dark matter halo is vital in understanding effects such as gravitational lensing. Disc galaxies, like the Milky Way, can be orientated simply by using the angular momentum of the stellar disc. However, this angular momentum is not constant. The change in direction of the angular momentum vector, with respect to time, can be considered as a tilting rate. The tilting direction provides an indication of the angular momentum reaching the disc. Both gas and satellite accretion can deliver misaligned angular momentum directly to the disc. It has also been argued that torques imposed by the dark matter halo can also change the angular momentum of the disc.

This thesis presents the tilting rates for galaxies evolving in two Λ cold dark matter cosmological hydrodynamic simulations. All of the galaxies comparable with the Milky Way have tilting rates higher than *Gaia's* detection limit of $0.28^\circ \text{ Gyr}^{-1}$ (Perryman et al., 2014).

Debattista et al. (2015) found that red galaxies tend to be aligned with the minor axis of their dark matter halo, whereas, blue galaxies tend to have random orientations. Observationally, similar trends are found, for example between the alignment distribution of the brightest satellite galaxies and the major axes of their host groups (Li et al., 2013). This thesis finds a very strong correlation between the specific star formation rate and the tilting rate, using the state-of-the-art Numerical Investigation of One Hundred Astrophysical Objects (NIHAO) suite of cosmological zoom-in simulations. Galaxies with higher star formation rates tilt faster and therefore are likely to be perturbed from any stable orientation,

between the disc and the host halo. Moreover, for the predominantly blue galaxies within the NIHAO suite, there is no preferential orientation, with respect to the dark matter halo.

The local environment provides a reservoir of angular momentum available to the disc. For both of the cosmological simulations presented, the normalized local overdensity was compared to the tilting rate of the disc, finding a strong correlation at $R = 6$ Mpc. On the other hand, no correlations are found between the shape of the dark matter halo, and the tilting direction of the stellar disc, contrary to previous claims that the torques imposed by the halo will drive the tilting of the stellar disc (e.g. Yurin and Springel, 2015).

Five of the NIHAO galaxies are looked at in greater detail, comparing tilting direction of the stellar disc to the angular momentum of various features and interactions. For two of the galaxies, the tilting direction is dominated by interactions/mergers with satellites. The remaining three are all driven by the infall of cool gas with misaligned angular momentum compared to that of the hot gas corona and the stellar disc. By the time the cool gas reaches the disc its angular momentum has been torqued by the hydrodynamical forces imposed by the hot gas and has angular momentum aligned with the hot gas. The same process has been proposed for forming warps in cosmological simulations (Roškar et al., 2010), and this thesis also finds that in this case the cool gas disc is misaligned in the direction of tilting.

Contents

Contents	vi
List of Figures	x
List of Tables	xiv
1 Introduction	1
1.1 Galaxies and their components	1
1.1.1 Gas	17
1.1.2 Dark matter	23
1.2 Simulations	30
1.2.1 N-Body	30
1.2.2 Smoothed Particle Hydrodynamics	32
1.3 Orientations of galaxies	38
1.3.1 Briggs figures	38
1.3.2 Scale Varying Alignments	39
1.3.3 Theory	41
1.4 Galaxy tilting	43
1.4.1 Interactions	44
1.4.2 Dark matter torques	44

1.4.3	Gas accretion	45
1.5	Predicted observational limit of Gaia	47
2	The tilting rate of the Milky Way’s disc	49
2.1	Introduction	50
2.2	Numerical Simulation (VICTOR)	53
2.3	The Samples	55
2.4	Analysis	59
2.5	Results	60
2.5.1	Tilting rates	60
2.5.2	Environmental dependence	60
2.5.3	Dependence on gas	62
2.6	Discussion and Conclusions	68
3	NIHAO: Tilting discs in cosmological zoom-in simulations	70
3.1	NIHAO: a Numerical Investigation of a Hundred Astrophysical Objects . .	70
3.1.1	Brief Introduction	70
3.2	Sample Selection	74
3.3	Abundance Matching	79
3.4	Sample Comparison	81
3.5	samples NIHAO:A and NIHAO:B	84
3.5.1	Dark Matter Halo	86
3.5.2	Local density	88
3.5.3	Gas	88
3.5.4	Star formation rate	89
3.5.5	Mass fractions	90
3.5.6	Angular Momentum	91

3.6	Chapter summary	105
4	NIHAO: Sample B	106
4.1	Brief introduction	106
4.2	Analysis	109
4.3	Substructure driven tilting	110
4.3.1	Galaxy: g7.66e11	111
4.3.2	Galaxy: g8.26e11	124
4.4	Gas driven tilting	137
4.4.1	Galaxy: g2.79e12	138
4.4.2	Galaxy: g7.55e11	149
4.4.3	Galaxy: g1.92e12	161
4.5	Chapter summary	173
4.5.1	Hierarchical processes	173
4.5.2	Accretion of misaligned gas	174
5	Conclusions and Future Work	175
5.1	Conclusions	175
5.1.1	Tilting rate and Gaia limit	175
5.1.2	Environmental factors	176
5.1.3	Secular processes	177
5.2	Predictions for the Milky Way	180
5.2.1	Using the warp	180
5.3	Future work	181
5.3.1	Sample improvements	181
5.3.2	More details about the corona	182
	References	183

Appendix A Chapter 4 Figures Continued	204
A.1 g7.55e11	204
A.2 g7.66e11	213
A.3 g8.26e11	223
A.4 g1.92e12	231
A.5 g2.79e12	239
Appendix B Earp et. al 2017	251

List of Figures

1.1	Hubble-de Vaucouleurs classification system.	3
1.2	NGC 5866.	4
1.3	M81.	6
1.4	ESO 510-G13.	8
1.5	NGC 5907.	9
1.6	M104.	10
1.7	Galaxy colour-magnitude diagram.	13
1.8	Boxy/peanut bulge.	14
1.9	NGC 1300.	16
1.10	Two-degree-Field Galaxy Redshift Survey.	19
1.11	Circumgalactic medium.	22
1.12	Galactic rotation curve.	28
2.1	Abundance matching at $z = 0$	56
2.2	Distribution of stellar mass change.	58
2.3	Tilting rate of the stellar disc versus satellite mass fraction.	61
2.4	Tilting rate of the stellar disc versus local density.	63
2.5	Tilting rate of the stellar disc versus the distance to the nearest high mass neighbour.	64
2.6	Tilting rate of the stellar disc versus the tilting rate of the hot gas corona.	65

List of Figures

2.7	Tilting rate of the the stellar disc versus the orientation of the hot gas corona.	67
3.1	Maximum stellar mass change versus specific star formation rate.	77
3.2	Maximum stellar mass change versus specific star formation rate, with sam- ples NIHAO:A and NIHAO:B defined.	78
3.3	Abundance matching for NIHAO galaxies.	80
3.4	Tilting rate of the stellar disc versus stellar mass.	82
3.5	Tilting rate versus maximum change in stellar and baryonic mass.	83
3.6	Tilting rate versus stellar mass for sample NIHAO:A and B.	85
3.7	Tilting rate versus halo axis ratios and triaxiality.	93
3.8	Tilting rate versus halo alignment.	94
3.9	Distribution of halo alignments.	95
3.10	Tilting rate versus local density.	96
3.11	Tilting rate of the stellar disc versus alignment and tilting rate of the hot gas corona.	97
3.12	Tilting rate versus gas misalignment.	98
3.13	Tilting rate versus specific star formation rate.	99
3.14	Tilting rate versus stellar mass ratios.	100
3.15	Tilting rate versus gas mass ratios.	101
3.16	Tilting rate versus stellar angular momentum.	102
3.17	Tilting rate versus cool gas angular momentum.	103
3.18	Tilting rate of the stellar disc versus angular momentum of the cold gas. . .	104
4.1	g7.66e11: Stellar surface density.	111
4.2	g7.66e11: stellar disc angular momentum.	113
4.3	g7.66e11: total stellar angular momentum.	114
4.4	g7.66e11: HI column density.	115

4.5	g7.66e11: hot gas corona shape and alignment with cool gas.	116
4.6	g7.66e11: warp angular momentum.	117
4.7	g7.66e11: hot gas angular momentum.	119
4.8	g7.66e11: dark matter angular momentum.	120
4.9	g7.66e11: gas flow.	121
4.10	g7.66e11: stellar flow.	123
4.11	g8.26e11: Stellar surface density.	124
4.12	g8.26e11: stellar disc angular momentum.	126
4.13	g8.26e11: total stellar angular momentum.	127
4.14	g8.26e11: HI column density.	128
4.15	g8.26e11: hot gas corona shape and alignment with cool gas.	128
4.16	g8.26e11: warp angular momentum.	130
4.17	g8.26e11: hot gas angular momentum.	131
4.18	g8.26e11: dark matter angular momentum.	133
4.19	g8.26e11: gas flow.	134
4.20	g8.26e11: dark matter flow.	136
4.21	g2.79e12: Stellar surface density.	138
4.22	g2.79e12: stellar disc angular momentum.	140
4.23	g2.79e12: total stellar angular momentum.	141
4.24	g2.79e12: HI column density.	142
4.25	g2.79e12: hot gas corona shape and alignment with cool gas.	142
4.26	g2.79e12: warp angular momentum.	144
4.27	g2.79e12: hot gas angular momentum.	145
4.28	g2.79e12: dark matter angular momentum.	146
4.29	g2.79e12: gas flow.	148
4.30	g7.55e11: Stellar surface density.	149

List of Figures

4.31	g7.55e11: stellar disc angular momentum.	151
4.32	g7.55e11: total stellar angular momentum.	152
4.33	g7.55e11: HI column density.	153
4.34	g7.55e11: hot gas corona shape and alignment with cool gas.	153
4.35	g7.55e11: warp angular momentum.	155
4.36	g7.55e11: hot gas angular momentum.	156
4.37	g7.55e11: dark matter angular momentum.	158
4.38	g7.55e11: gas flow.	160
4.39	g1.92e12: Stellar surface density.	161
4.40	g1.92e12: stellar disc angular momentum.	163
4.41	g1.92e12: total stellar angular momentum.	164
4.42	g1.92e12: HI column density.	165
4.43	g1.92e12: hot gas corona shape and alignment with cool gas.	165
4.44	g1.92e12: warp angular momentum.	167
4.45	g1.92e12: hot gas angular momentum.	168
4.46	g1.92e12: dark matter angular momentum.	170
4.47	g1.92e12: gas flow.	171
4.48	g1.92e12: realignment of cool gas.	172

List of Tables

3.1	All error-weighted Pearson’s correlation coefficients reported in this chapter, between the x -axis listed and the tilting rate of the stellar disc ($\Delta\theta/\Delta t$). .	71
3.2	Recent values for different components of the Milky Way which will be used in this chapter.	72
4.1	Galaxies in sample B, all values are calculated at $z \sim 0.3$. Total stellar mass is calculated within R_{200} , $\max(v_{\text{circ}})$ is for star particles inside $R < 30$ kpc. The mass and angular momentum of the hot gas corona M_{corona} & L_{corona} were determined using all hot gas ($T > 50,000\text{K}$) within R_{200}	107
4.2	Galaxies in sample B, all values are calculated at $z = 0$. Total stellar mass is calculated within R_{200} , $\max(v_{\text{circ}})$ is for star particles inside $R < 30$ kpc. The mass and angular momentum of the hot gas corona M_{corona} & L_{corona} were determined using all hot gas ($T > 50,000\text{K}$) within R_{200}	108

Acknowledgements

I would like to thank my supervisor Professor Victor P. Debattista for his patience and generosity throughout my time at the University of Central Lancashire. As well as Professors Andrea Macciò and Derek Ward-Thompson for their support and guidance during my doctoral studies. I am also grateful to Doctors Mark Norris, Tim Cawthorne, John Magorrian and David Cole for their feedback and advice.

I would like to thank former research students Dr. Dominic Bowman, Dr. Adam Clarke and Dr. Min Du for their feedback, advice and most importantly friendship, and all current research students within the Jeremiah Horrocks Institute, especially Tigran Khachatryan for his useful comments regarding this thesis.

I would also like to thank the Max Planck Institute for Astronomy in Heidelberg for their hospitality.

Chapter 1

Introduction

1.1 Galaxies and their components

Galaxies are a diverse family of gravitationally bound stellar structures. The first classification system was proposed by Hubble (1926), by dividing galaxies into two groups based on their ellipticity E_i ($i = (a - b)/a$), with the decimal place omitted. Galaxies with ellipticities ranging from E0 to E7 were called ellipticals, galaxies with an ellipticity greater than E7 are generally spirals and given the symbol S. Elliptical galaxies resemble unremarkable diffuse blobs with differing luminosity and shape. Spiral galaxies, such as the Milky Way (MW), appear visually much more diverse.

Hubble further divided spiral galaxies into two more distinct families, barred (SB) and unbarred spirals (S). Both S and SB galaxies can be classified by the tightness of the spiral arms, tightly wrapped spirals are classified Sa or SBa galaxies, loosely wrapped spirals are classified Sc or SBc. Surprisingly, in the local universe barred galaxies are more common than unbarred galaxies; about two in three spiral galaxies are barred (Buta et al., 2015). Galaxies with an ellipticity greater than an E7, without spiral arms, were classified as a lenticular galaxy and denoted as S0. Anything that did not fall into these categories was given the name irregular. With these four families Ellipticals (E), Regular Spirals (S), Barred

Spirals (SB), and Irregulars (I) one can form the Hubble tuning fork.

This classification system was extended by de Vaucouleurs, as shown in Figure 1.1. Elliptical galaxies remain unchanged from the Hubble classification system. Spirals were split into three families, non-barred (SA), weakly barred (SAB) and strongly barred (SB). A galaxy in any of these families can be classified further by the tightness of their spiral arms, Sa being tightly wound and Sc being loosely wound, with a further class d for diffuse spiral arms, and m for irregulars. Intermediate classifications are allowed, for example, SAab would be a galaxy with spiral arms bound looser than an SAa galaxy, but tighter than a SAB galaxy. Lenticular galaxies were split into two families SOA (non-barred) and SOB (barred). Purely irregular galaxies were given the symbol Im. As this form of classification is done visually it poses problems for galaxies at high redshift where the angular resolution of the telescope is comparable to the size of the galaxy.

Stellar Disc

The shapes of late-type galaxies are very different from typical elliptical galaxies. Figure 1.2 shows the edge-on lenticular galaxy NGC 5866. During the formation of the galaxy, the collapsing gas has angular momentum; early work assumed that this angular momentum was conserved in detail during the formation of a thin rotating disc (Fall and Efstathiou, 1980a). Only a fraction of the total gas within the halo forms the gas disc, however, the resulting disc contains most of the available angular momentum (van den Bosch et al., 2001). Modern simulations are able to reproduce this phenomenon (e.g. Brook et al., 2012), where stellar feedback drives galactic fountaining, redistributing the angular momentum. Gas with the lowest angular momentum will be denser and reside on orbits with smaller radii. This gas will be able to cool faster and will take less time to form a disc. The thin gas disc can then form stars, according to the Kennicutt-Schmidt law $\Sigma_{\text{SFR}} \propto (\Sigma_{\text{gas}})^n$ (Kennicutt, 1998; Schmidt, 1959a), where n is the power index with values ranging from 0 to 2, creating the

1.1 Galaxies and their components

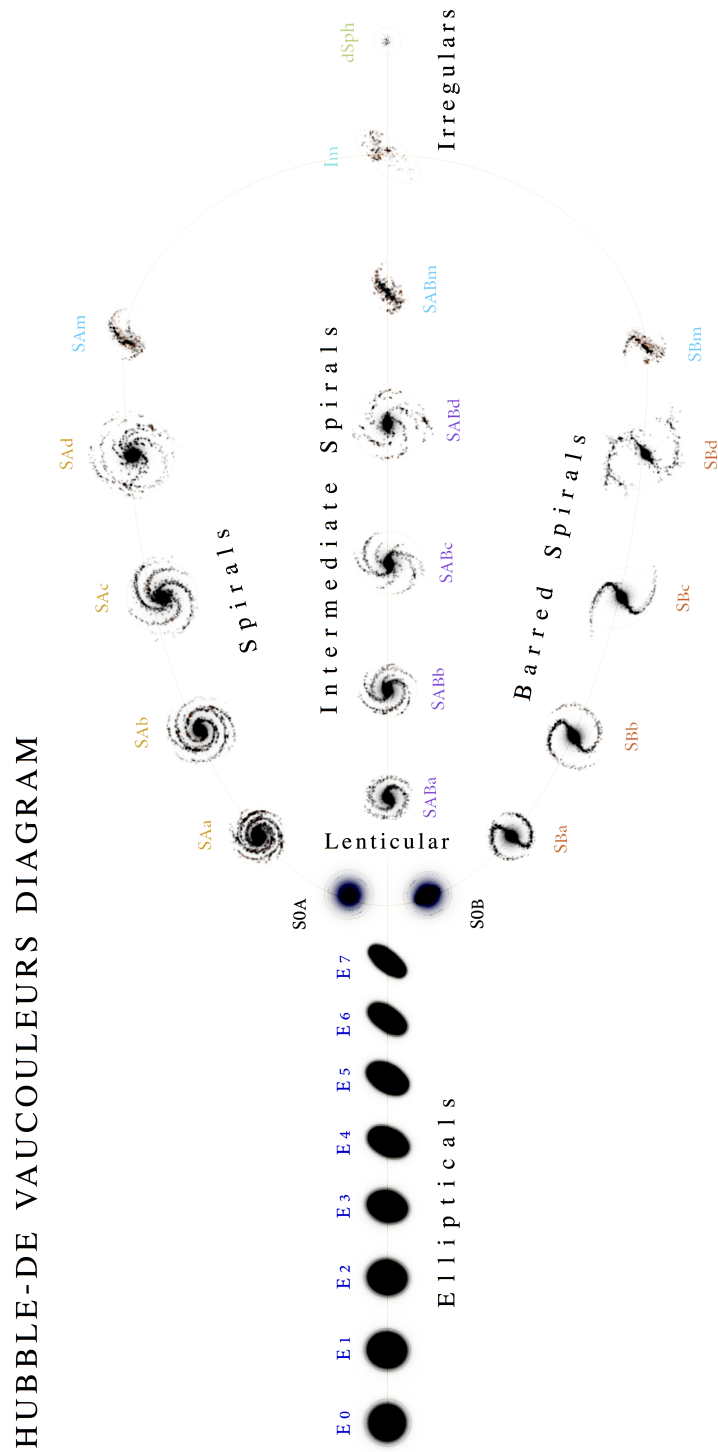


Fig. 1.1 Hubble-de Vaucouleurs classification system. Image credit: A. Ciccolella & M. De Leo



Fig. 1.2 NGC 5866: a lenticular S0 galaxy. Credit: NASA, ESA, and The Hubble Heritage Team (STScI/AURA); Acknowledgment: W. Keel (University of Alabama, Tuscaloosa).

stellar disc. Lower angular momentum material forms stars first, followed by higher angular momentum material, resulting in a larger disc at later times—this is referred to as inside-out growth. One prediction of this is that stars nearer the centre of a galaxy should be older than stars further out. When looking at the age profile of stars, one does indeed find that there is an average decrease in stellar age with radius (Bell and de Jong, 2000; Dale et al., 2016; de Jong, 1996; Gogarten et al., 2010; MacArthur et al., 2004; Williams et al., 2009).

To determine where the cool gas resides in the galaxy's disc one can look at the neutral hydrogen (HI) using the 21cm emission line. This emission is given out when an electron within a hydrogen atom changes its spin, transitioning between hyperfine energy levels. Having such a long wavelength this emission can easily pass through the earth's atmosphere and is unhindered by extinction. A dense enough ($\sim 4 M_{\odot} \text{pc}^{-2}$) region of HI will be able to shield the inner region from UV radiation allowing molecular hydrogen to form and eventually star formation to occur. The HI can extend beyond the disc of the galaxy, meaning that at some radius it stops forming stars. At larger radii, the gas might not be dense enough to collapse and the differential rotation starts to prevent the formation of clouds. Studying

1.1 Galaxies and their components

this region is difficult observationally due to its low surface brightness, and this difficulty is not alleviated when studying simulations, where the low resolution in this region hampers progress. However, this region of our Galaxy has led to major discoveries, as discussed later in this thesis.

In late-type galaxies, the disc normally has the largest fraction of stellar mass. For our own galaxy the mass can be dynamically measured to be $M_*^D = 4.6 \pm 0.3 \times 10^{10} M_\odot$ (Bovy and Rix, 2013). In order to determine the mass of the stellar disc, one can describe its density using an exponential profile that declines with radius,

$$\rho(R) = \rho_0 e^{-R/R_D} \quad (1.1.1)$$

where R_D is the *scale length* of the disc (the radius at which the density falls by a factor of e) and ρ_0 is the central density. A recent value for the scale length of the MW's disc is 2.5 ± 0.4 kpc (Bland-Hawthorn and Gerhard, 2016). The stellar disc is often broken into two separate components; the thin stellar disc and the thick stellar disc. The thin stellar disc consists of stars that are on average younger and more metal-rich than stars in the thick stellar disc. The density of stars in the disc falls off exponentially in the z -direction, given by

$$\rho(R, z) = \rho(R, 0) e^{-|z|/z_D(R)} \quad (1.1.2)$$

where z is the height from the plane of the disc, $\rho(R, 0)$ is the density in the plane of the disc and $z_D(R)$ is the scale height of the disc at radius R . A typical value for the scale height of the MW's thick and thin discs are $z_D \simeq 900$ pc and $z_D \simeq 300$ pc, respectively (Bland-Hawthorn and Gerhard, 2016; Jurić et al., 2008). However, even within the thin disc, the scale height depends on the age of the stellar population: very young O and B stars have a smaller scale height than older G, K or M stars (Binney and Tremaine, 2008).

The ordered rotation of disc galaxies turns out to be extremely useful. Tully and Fisher

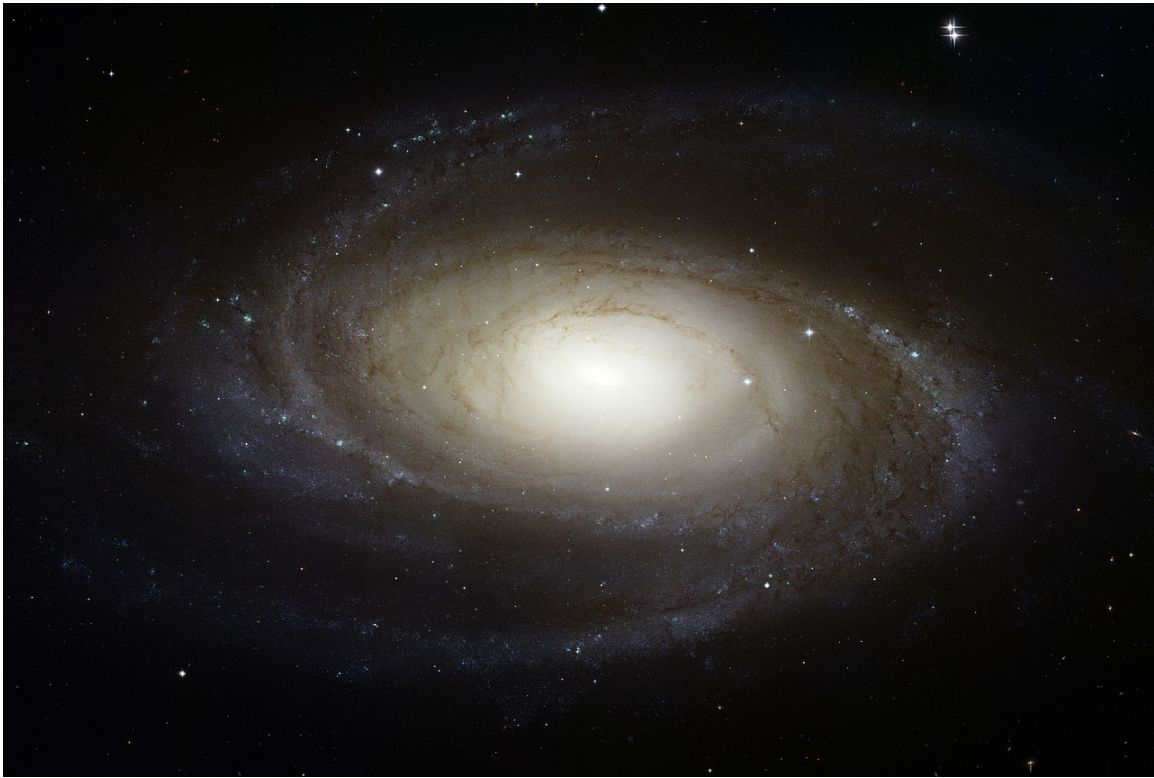


Fig. 1.3 M81: a SA(s)ab grand design spiral galaxy. Credit: HST.Credit: NASA, ESA, and The Hubble Heritage Team (STScI/AURA).

(1977) found that the rotational velocity of disc galaxies are tightly correlated with their luminosity. This has been verified since by numerous authors and helps us determine the distance using the galaxy's apparent magnitude.

Spirals

In the local Universe, observers find that the majority of galaxies contain spiral structure, Figure 1.3 shows M81, a grand design spiral, which shows prominent and well-defined spiral structure. Nair and Abraham (2010) looked at 14,034 galaxies from the Sloan Digital Sky Survey (SDSS), finding 61 per cent of their sample were classical spirals. Willett et al. (2013) compared the classifications of 304,122 galaxies from the Galaxy Zoo 2 project (also observed using SDSS), and found, that out to redshift $z = 0.2$, the fraction of spirals is as

high as ~ 80 per cent. Such observations indicate that spiral galaxies are dominant throughout the low redshift Universe, however, spiral galaxies become rarer at higher redshifts. At redshift $z \gtrsim 2$ only two spiral galaxies have been kinematically confirmed, the first by Law et al. (2012) at $z = 2.18$, and possibly an even more ancient one at $z = 2.54$ (Yuan et al., 2017). This apparent under-abundance of spiral galaxies could be a symptom of the requirements for a very thin, cold and rotationally stable disc to be present to form the spiral structure (Sellwood, 2014; Toomre, 1977). In addition, the high merger rates (Hammer et al., 2009), gas accretion rates, and cold flows (Cen, 2014) at higher redshift may make it hard for the conditions for spiral formation to arise. Moreover, such studies are magnitude limited imposing a bias towards detecting more early-types, also, the low resolution at high redshifts makes it difficult to identify spiral features (Bouwens et al., 2004; Ribeiro et al., 2016). However, some cosmological simulations have argued for the formation of spiral structure as early as $z \sim 3$ (Fiacconi et al., 2015). The spiral arms can be separated into two kinds, leading and trailing. Leading spiral arms are where the end of the spiral is pointing in the same direction as the rotation, whereas trailing is the opposite. Trailing spiral arms are by far the most common, one example of a leading spiral galaxy is NGC 4622: which has both leading and trailing arms (Buta et al., 2003).

Warps

As previously mentioned, the HI gas disc extends beyond the stellar disc. Sancisi (1976, 1983) investigated the distribution of this extended HI disc in the edge-on disc galaxy NGC 5907, finding that the column density contours did not align with the plane of the disc, as shown in Figure 1.5. This *warp* in the extended HI disc can be found even in more face on galaxies by looking at the kinematics of the HI disc (Bosma, 1978; Shostak and van der Kruit, 1984). The velocity fields of warps are well behaved, and have been modelled well by sets of concentric rings (e.g. Rogstad et al., 1974, 1976). An edge-on warped galaxy shows

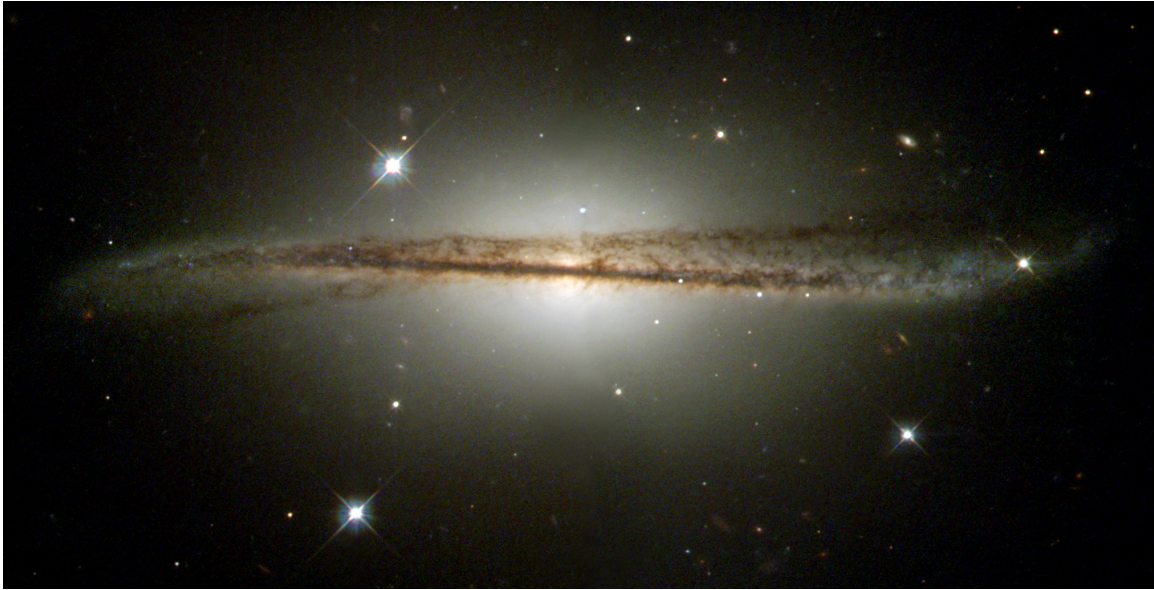


Fig. 1.4 ESO 510-G13: a highly warped spiral galaxy. Credit: NASA and The Hubble Heritage Team (STScI/AURA); Acknowledgment: C. Conselice (U. Wisconsin/STScI).

an HI disc twisting upwards on one side and downwards on the opposite side, appearing similar to an *integral sign*. This can be seen in Figure 1.4. Various formation mechanisms have been proposed to form warps, ranging from misaligned cosmic infall (Jiang and Binney, 1999; Ostriker and Binney, 1989; Quinn and Binney, 1992; Shen and Sellwood, 2006), misalignment between the plane of the disc and the angular momentum of the dark matter halo (Debattista and Sellwood, 1999), and from perturbations caused by nearby satellites (Weinberg and Blitz, 2006a). An extreme example of warps can be seen in polar ring galaxies, where the plane of the HI disc is almost orthogonal to the plane of the stellar disc (e.g. Whitmore et al., 1990). Polar rings are more exotic and are thought to require interactions (e.g. Bekki, 1998) or cold gas accretion from the surrounding filamentary structure to form (Brook et al., 2008; Macciò et al., 2006). The strength of a warp can be given by the warp angle ϕ , given by the angle between the plane of the inner (non-warped) isophotes, and the plane of the outer (warped) isophotes. Warps appear to be a common phenomenon, with studies finding that $\gtrsim 50$ per cent of galaxies in the local universe have a warp with warp

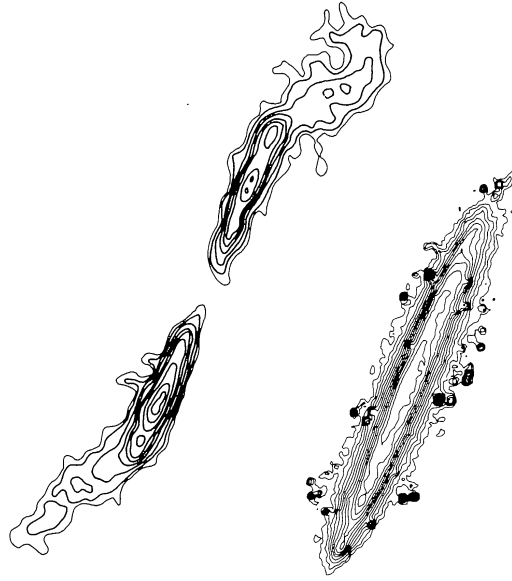


Fig. 1.5 HII (left) and optical (right) images of NGC 5907 Sancisi (1983) showing the warp in the outer HII disc.

angle $\phi > 2 - 2.5^\circ$ (García-Ruiz et al., 2002; Reshetnikov and Combes, 1998; Sanchez-Saavedra et al., 1990). As a further example of this ubiquity, all the spiral galaxies in the Local Group (the MW, M31 and M33) appear to be warped (Binney and Tremaine, 2008; Burton, 1988). Warps can also harbour a small stellar component; Verdes-Montenegro et al. (2002) found that the warp of the spiral galaxy NGC 3642 has ongoing star formation. Similar discoveries have been found using the UV emission of ionized HII regions in the warped region of other galaxies, implying recent star formation has taken place (Thilker et al., 2005, 2007).

Bulge

The bulges of late-type galaxies are among the densest stellar systems. They appear visually very similar to elliptical galaxies but contain both young and old stars with metallicities higher than the thick disc. One of the most visually impressive examples is the Sombrero Galaxy (Figure 1.6), where the bulge extends to almost the edge of the disc. This visual



Fig. 1.6 M104: the Sombrero Galaxy M104. Credit: NASA/ESA and The Hubble Heritage Team (STScI/AURA).

similarity with elliptical galaxies has been studied by looking at photometric scaling relations (e.g. central surface brightness versus core radius), finding that the classical bulges of disc galaxies are indeed closely related to ellipticals (Kormendy, 1985). However, it was already found they vary kinematically, bulges of late-type galaxies rotate much faster than ellipticals (Davies et al., 1983).

The total stellar mass of the bulge in late-type galaxies is less than that of the disc; for the MW Bland-Hawthorn and Gerhard (2016) give an estimate for the stellar mass of $(1.4 - 1.7) \times 10^{10}$, roughly four times less than the mass of the stellar disc.

Classical bulges are the most similar to elliptical galaxies. The surface brightness of a classical bulge generally follows a *Sersic profile*,

$$I(R) = I_0 \exp(-kR^{1/n}), \quad (1.1.3)$$

1.1 Galaxies and their components

where I_0 is the central intensity, n is a constant called the Ser sic index, and k is a constant. Astronomers have used the best fitting value of $n = 4$ for elliptical galaxies, which is called the *de Vaucouleurs profile* (de Vaucouleurs, 1948),

$$I(R) = I_0 \exp(-kR^{1/4}). \quad (1.1.4)$$

As elliptical galaxies are formed mainly due to the hierarchical merging of galaxies, one might expect the formation process for classical bulges to be the same. Some evidence for this can be found by comparing galaxies in the field to galaxies in clusters. Kormendy et al. (2010) found that less than half of their sample of high mass field galaxies contained classical bulges or were ellipticals, whereas 2/3 of all the stellar mass in the Virgo cluster is found in merger remnants (e.g. classical bulges or elliptical galaxies). Classical bulges are now considered exclusively as the class of bulge that have formed due to violent processes, such as hierarchical clustering via minor mergers. As a result of their formation process, they generally have low angular momentum compared to the disc, which I will come back to later in this thesis.

When plotting a galaxy’s colour against the mass (magnitude) for a large number of galaxies, one finds a bimodal distribution with two components the *red sequence* and the *blue cloud* (Bell et al., 2004; Schawinski et al., 2014; Strateva et al., 2001), see Figure 1.7. The red sequence is comprised of ‘red and dead’ (non-star-forming) early-type galaxies, whereas the blue cloud is populated by blue star-forming late-type galaxies. The same strategy can be implemented for the bulges of late-type galaxies, where classical bulges fall in the red sequence (as expected if they are similar to ellipticals) and *pseudobulges* fall in the blue cloud (Drory and Fisher, 2007). Pseudobulges are a separate class of bulges that are dynamically cold, and more flattened than classical bulges. Where classical bulges form via violent processes, pseudobulges are thought to form through slow rearrangement of disk material (see Kormendy and Kennicutt, 2004, for review). Due to this apparent

dichotomy, the type of bulge residing within a galaxy can give us some information about the global history of the galaxy. Gadotti (2009) found that pseudobulges follow a mass-size relation similar to that of bars (see Section 1.1), and when plotted on the *fundamental plane* (see Djorgovski and Davis, 1987) they occupy the same locus as discs. Therefore, pseudo and classical bulges are very different structures. Fisher and Drory (2011) found that for galaxies more massive than $M_* > 10^9 M_\odot$, only $17\% \pm 10\%$ host classical bulges (including elliptical galaxies), $45\% \pm 12\%$ are galaxies with pseudobulges, and $35\% \pm 12\%$ are purely disc galaxies.

A further type of bulge is the boxy (or peanut) bulge, first observed in the galaxy NGC 128 (Burbidge and Burbidge, 1959) which were shown to be shaped like a peanut. Similarly, de Vaucouleurs (1974) presented more galaxies with this peculiar ‘boxy’ shape. After their discovery, two competing theories were suggested to explain these strange objects. Combes and Sanders (1981) used three-dimensional N-body simulations of galaxies, and showed that bars could be formed over a wide range of stellar masses and in the process, they showed that when viewing such barred galaxies edge-on resulted in the bulge appearing to be boxy, similar to observed galaxies. A few years later a competing theory was suggested by Binney and Petrou (1985). The authors argued that a boxy/peanut bulge could be formed instead by the merging of satellite galaxies. It is now generally accepted that boxy/peanut bulges are the result of a bar. Erwin and Debattista (2017) found that for a sample of 84 local barred galaxies, 79 per cent of galaxies with mass $\log(M_*/M_\odot) \gtrsim 10.4$ have a boxy/peanut bulge. However, this fraction decreases to 12 per cent for lower mass galaxies. As all of these galaxies are barred one would expect all to exhibit boxy/peanut shapes. However, if the bar is seen end-on (with the long axis of the bar orientated towards the observer) the bulge would look more like a classical bulge, accounting for the missing boxy/peanut bulges (see Figure 1.8 Athanassoula, 2005).

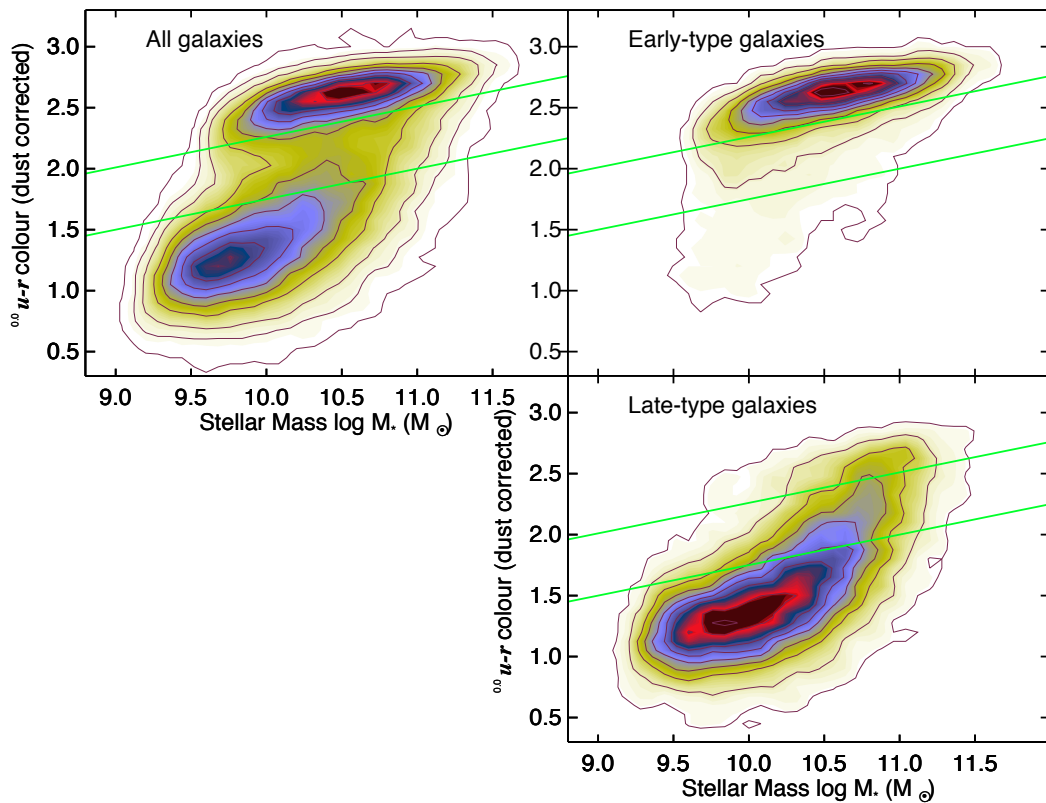


Fig. 1.7 Reddening-corrected colour ($u-r$) versus stellar mass for 8978 early- and 16707 late-type galaxies using spectra from SDSS (Schawinski et al., 2014). The morphological type was determined visually as part of the Galaxy Zoo citizen science project (Lintott et al., 2011, 2008). This plot illustrates the bimodality present in the distribution, with the red sequence at the top and the blue cloud at the bottom of the left plot. The green lines denote the *green valley*, lying between the two components which has been argued as a transition region between the two regimes (Schawinski et al., 2014).

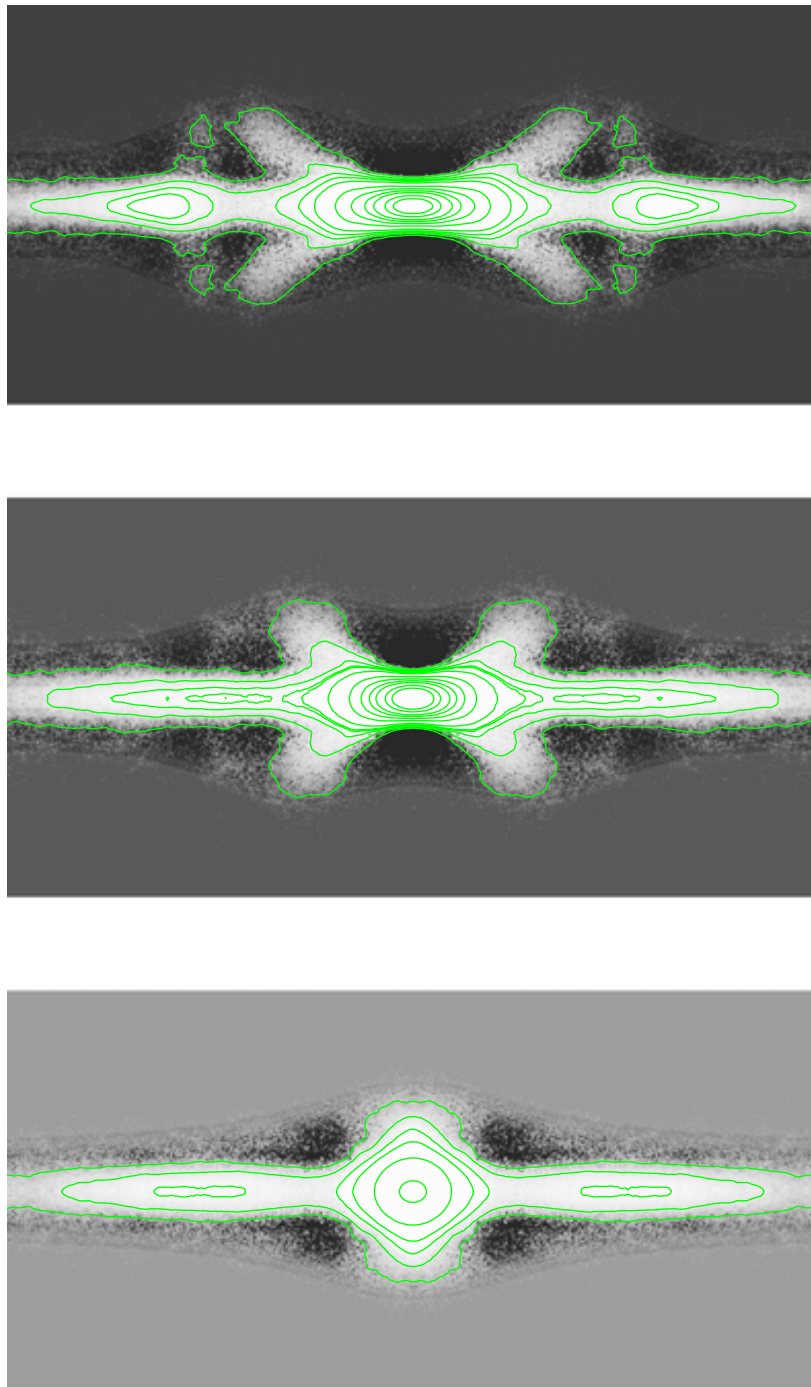


Fig. 1.8 A boxy/peanut bulge of a simulated barred galaxy, viewed along the intermediate axis (top), 45° from the major axis (middle) and along the major axis (bottom) from Athanassoula (2005). This image shows that the boxy/peanut shape can be created by a barred galaxy, and when viewed along the major axis, the bulge seems to be classical.

Bars

Bars can be detected photometrically, or and kinematically using the streaming velocities of stars on bar orbits. Bars vary in size and *strength*; from the density expansion of the instantaneous distribution of disc particles in logarithmic spirals (Debattista and Sellwood, 2000), given as

$$A(m, \gamma, t) = \frac{1}{N_d} \sum_{j=1}^{N_d} \exp[im(\phi_j + \tan \gamma \ln R_j)]. \quad (1.1.5)$$

The bar strength is then given by

$$A(2, 0, t) = \mathcal{A} e^{2i\phi}, \quad (1.1.6)$$

where \mathcal{A} is the bar strength. Some bars are barely visible as a minor non-axisymmetric perturbation in the light distribution. As mentioned previously the majority of spiral galaxies in the local universe are barred (Buta et al., 2015). However, for higher redshifts, there does not appear to be a clear consensus. Surveys using SDSS photometric data have found a wide range of barred fractions ranging from 50 per cent (Aguerri et al., 2009; Barazza et al., 2008; Yoshino and Yamauchi, 2015) to ~ 25 per cent using Galaxy Zoo classifications Cheung et al. (2013); Lintott et al. (2011, 2008); Masters et al. (2011); Skibba et al. (2012). Higher redshifts studies (e.g. Simmons et al., 2014, and references therein) found that the fraction drops even further. It has been argued that SDSS might miss bars in, lower-mass, bluer galaxies, and that as bars grow in length over cosmic time the bar fraction is systematically underdetermined (see Erwin, 2017).

Figure 1.9 shows NGC 1300, a galaxy with an extremely pronounced bar at the centre. As mentioned in Section 1.1, barred galaxies can be found in all types of disc galaxies. Some elliptical galaxies have also been found to have bars (see de Zeeuw and Franx, 1991, for review on elliptical galaxies). The bar is not stationary, it rotates with a pattern speed which can be measured observationally (Tremaine and Weinberg, 1984). Bars are mostly



Fig. 1.9 NGC 1300: A SB(s)bc galaxy with a bar with short- to long-axis ratio of 1 : 5.
Credit: NASA, ESA, and The Hubble Heritage Team (STScI/AURA); Acknowledgment: P. Knezek (WIYN).

comprised of stars on elongated orbits that travel the length of the bar; they are not transient density waves like spiral arms (Chemin et al., 2006; Gnedin et al., 1995; Goldreich and Lynden-Bell, 1965; Grosbøl et al., 2004; Lin and Shu, 1964; Schweizer, 1976; Shetty et al., 2007; Visser, 1978; Zibetti et al., 2009). Numerical simulations have shown that instabilities in rotationally supported discs can begin to form a bar (e.g. Hohl, 1971), this bar then grows by trapping more orbits (Lynden-Bell, 1979) and can eventually disperse the spiral structure. After a bar has had time to settle it begins to experience a second instability, because of a vertical resonance. This *buckling* of the bar thickens the bar out of the plane and is thought to be the cause of the boxy/peanut shaped bulges mentioned previously (Martinez-Valpuesta et al., 2006, and references therein). The buckling instability weakens the bar (Debattista et al., 2004, 2006), as energy is transferred from horizontal motion to vertical.

It is well established from a variety of simulations that the potential from a rigidly-rotating bar drives gas within the bar towards the centre and drives gas outside the corotation radius outwards (Athanassoula, 1992; Kim and Stone, 2012; Matsuda and Isaka, 1980; Sanders and Huntley, 1976; Sanders and Tubbs, 1980; Schwarz, 1981; van Albada and Roberts, 1981). This behaviour could explain the large amounts of gas that has been detected in the centres of barred galaxies (Sheth et al., 2005).

1.1.1 Gas

At the largest scales, gas resides in the intergalactic medium, which is dominated by the large filamentary structures of the cosmic web that funnel slowly cooling gas into dark matter haloes. Surrounding a galaxy, the circumgalactic medium, hosts hot gas that slowly cools and replenishes the gas in the disc. Through the disc, the interstellar medium condenses in the disc eventually forming stars.

Galaxy formation

When discussing gas in the universe, it would be remiss if we did not take this opportunity to give an overview of the history of the universe. The currently accepted paradigm is the Λ -CDM (dark energy-cold dark matter) model, also known as the standard model. The very early universe ($z = 1100$) was not completely homogenous but contained tiny fluctuations in the form of a Gaussian random field (Bardeen et al., 1986). As the universe expanded, the small overdensities were able to grow through self-gravity forming larger overdensities. Such clumps were generally not isolated, and they began to form the *cosmic web*, a collection of sheets, filaments and voids. Cosmological simulations have been able to reproduce this structure with ever-increasing resolution. One of the largest was the Millennium simulation (Springel et al., 2005). The large over densities were able to begin merging with each other at a high rate forming large peaks in the density (dark matter haloes). With the onset of reacceleration due to dark energy (Λ), the density peaks became more isolated and the rapid merging subsided. Figure 1.10 shows the results from the Two-degree-Field Galaxy Redshift Survey (2dFGRS), which measured the redshift of 232,155 galaxies back to a redshift of ~ 0.3 (Colless et al., 2001). The distribution of galaxies in 2dFGRS agrees with the standard model and gives us a good view of the cosmic web.

Intergalactic Medium

In the standard cosmological model, roughly half of all the dark matter in the universe resides in the large virialised dark matter haloes that harbour galaxies, the other half lies between galaxies. As previously mentioned this matter forms the cosmic web, a large collection of filaments and voids throughout the universe. However, the cosmic web is not solely comprised of dark matter, it also contains a large amount of gas. This intergalactic medium (IGM) plays a vital role in galaxy formation and evolution, funnelling gas along its filaments and delivering it to galaxies. Kereš et al. (2005) found that half of the gas that falls

1.1 Galaxies and their components

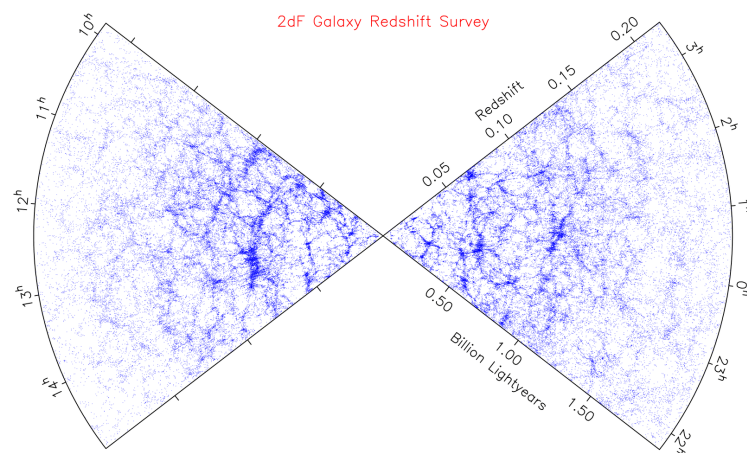


Fig. 1.10 Final results from the Two-degree-Field (2dF) Galaxy Redshift Survey (Colless et al., 2001), showing the location of galaxies out to a redshift of $z = 0.3$ with a 1° field of view. This shows the cosmic web, one of the fundamental predictions of the Λ -CDM cosmogony.

into the halo is shock heated joining the hot gas corona, referred to as ‘hot mode’ accretion, and the other half is able to radiate its gravitational energy at lower temperatures and reach smaller radii, called ‘cold mode’ accretion. High mass galaxies are generally dominated by hot mode accretion, and lower mass systems are dominated by cold mode accretion, with a transition at $M_{\text{halo}} \sim 10^{11.4} M_{\odot}$. Kereš et al. (2005) also found there is a redshift dependence, with cold mode accretion dominating at high redshifts and hot mode accretion dominating at low redshift.

Circumgalactic Medium

Gas surrounding galaxies within the virial radius of the dark matter halo, that does not reside in the disc or interstellar medium (ISM), is known as the *circumgalactic medium* (CGM). Using NaI and CaII absorption in stellar spectra at high Galactic latitudes, Spitzer (1956) was able to show the existence of a diffuse hot gas ($T \sim 10^6$ K) component of the MW. This component is now called the hot gas corona, and has been observationally detected in both late- and early-type galaxies using X-ray emission (e.g. Anderson and Bregman, 2011; Anderson et al., 2016; Bogdán et al., 2013; Dai et al., 2012; Savage and de Boer, 1979; Walker et al., 2015; Wang et al., 2001). Moreover, satellites passing through the hot gas corona are being ram-pressure stripped and can be a probe (Gatto et al., 2013). This section will not be limited to just the hot gas that comprises the hot gas corona, but gas at all temperatures that is within the virial radius, but not in the ISM. The amount of cold gas ($T < 10^4$ K) in the CGM is small, Putman et al. (2012) measured the amount of gas in high velocity clouds (excluding the Magellanic Stream) and found just $M = 2.6 \times 10^7 M_{\odot}$, whereas Tumlinson et al. (2017a) found a value of just $M = 2 \times 10^8 M_{\odot}$. Increasing in temperature slightly, the total mass of cool gas ($\sim 10^{4-5}$ K) is significantly higher, with recent work finding values of $9.2 \pm 4.3 \times 10^{10} M_{\odot}$ out to 160 kpc (Prochaska et al., 2017). Estimates for the amount of warm gas ($\sim 10^{5-6}$ K) are hard to achieve, because this temperature range poses several

observational problems (see Tumlinson et al., 2017a). Tumlinson et al. (2011) gives a lower estimate of $M = 2 \times 10^9 M_\odot$, with very conservative assumptions. The temperature of the hot gas should be the virial temperature of the halo (Rees and Ostriker, 1977; Silk, 1977), given by

$$T_{vir} = \frac{GM_{halo}m_p}{kR_{vir}} \quad (1.1.7)$$

where m_p is the proton mass. A halo of mass $M_{halo} > 10^{12} M_\odot$ gives a temperature above 10^6 K. For the MW, Anderson and Bregman (2010) gave an estimate for the total mass of the hot gas corona of up to $M_{hot} \sim 1.5 \times 10^{10} M_\odot$.

As the hot gas corona is ionized, the gas is able to cool via Bremsstrahlung radiation (braking radiation). As the corona is hot, the ions are moving fast and the resulting Bremsstrahlung radiation is emitted at short wavelengths, typically in the X-ray. The gas cools from the hot gas corona and is eventually able to reach lower and lower radii. Eventually, it reaches the disc, where its angular momentum will be changed by the disc's potential and its orbit will align with the galactic plane. However, the amount of gas reaching the disc by this process alone is quite small (Binney et al., 2009; Hobbs et al., 2013; Joung et al., 2012), an alternative mechanism is galactic fountaining (Fraternali, 2017; Hobbs et al., 2015) where SN ejecta mixes with the hot gas corona and can quickly cool back onto the disc.

Gas is also driven out of the ISM and into the CGM (and even into the IGM) by various processes. These *galactic winds* were first observed in the 1960s (Lynds and Sandage, 1963). Stellar winds given off by OB stars and more evolved Wolf-Rayet stars drive gas from the ISM and are able to heat it sufficiently for it to rejoin the CGM. Supernovae, type II first followed by type Ia, dump even more energy into the surrounding gas and are able to eject gas back into the CGM and also into the IGM. Active galactic nuclei (AGN) feedback, from supermassive black holes being fed by an accretion disc, can heat the gas in the inner regions and drive large jets out of the galaxy (see Veilleux et al., 2005, for a

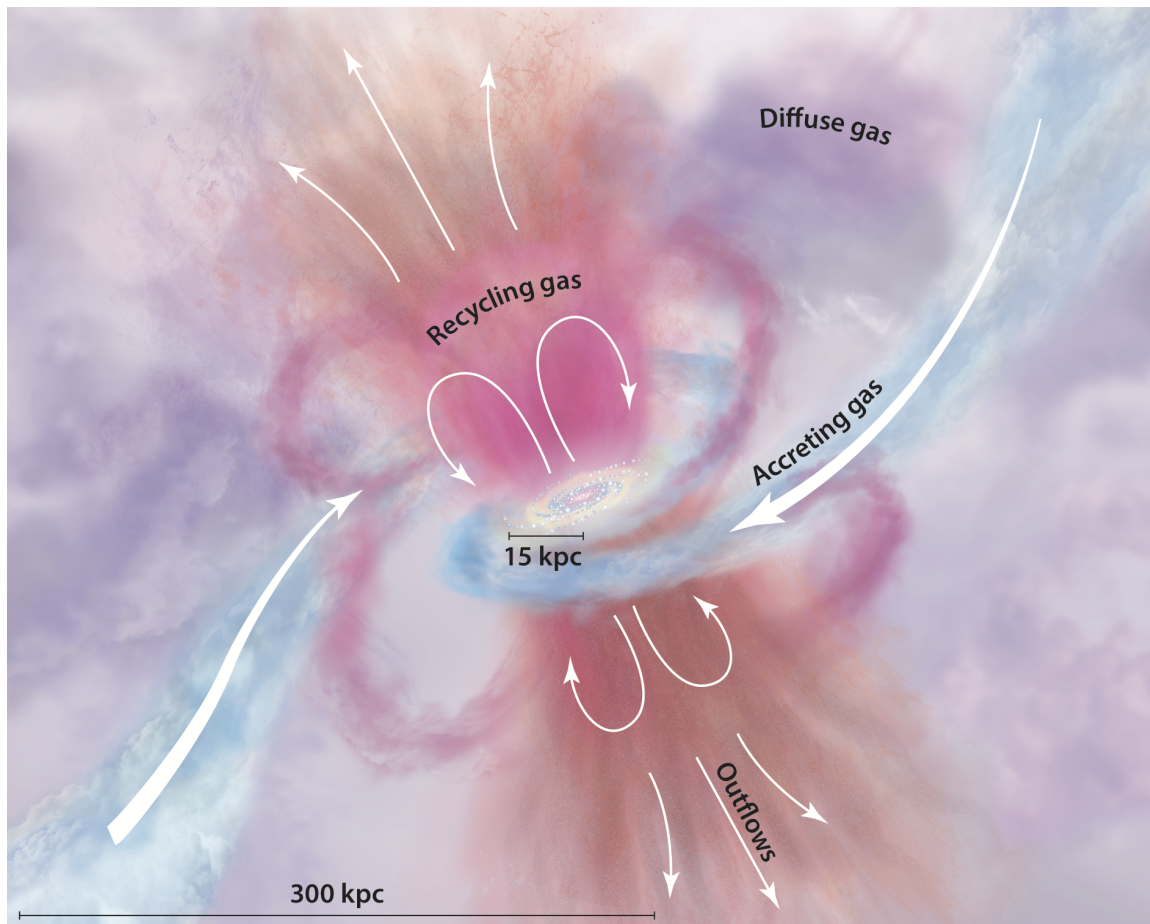


Fig. 1.11 A cartoon of the CGM from Tumlinson et al. (2017b). The galaxy at the centre of the image is being fed by the inflow (blue) of accreted gas from the IGM. Gas is constantly recycled from the galaxy to the CGM (pink) caused by supernovae and stellar winds, while some gas is ejected in outflows (brown).

detailed review of galactic winds). Figure 1.11 shows a cartoon of the different flows of gas in the CGM. Some authors (e.g. Lilly et al., 2013) have proposed models for galaxies where the star formation rate is almost self-regulated, due to the inflow and outflow rates being strongly related to the star formation rate. However, such simple treatment does not explain the various components of the CGM (Tumlinson et al., 2017a). The CGM is a dynamic environment that plays a vital role in the evolution of the galaxy.

Interstellar Medium

The interstellar medium (ISM) is the primary galactic repository for cool gas and the spawning grounds for most of the stars in a disc galaxy. Throughout the ISM there are dark clouds consisting of cold molecular hydrogen and dust. Such clouds are the stellar nurseries, able to shield molecular hydrogen from dissociating ultraviolet radiation, eventually allowing new stars to be born. Once star formation begins ionizing photons are released, creating bubbles of hot ionized plasma, called HII regions. HII regions can be observed by looking at H α emission. By mass, the ISM consists of 70 per cent hydrogen, 28 per cent helium and the remaining 2 per cent are heavier elements referred to as *metals*. It also contains dust, which makes up roughly one per cent of the total mass. For a recent review on the ISM see Klessen and Glover (2016).

1.1.2 Dark matter

Λ CDM cosmogony

Consider all the photons in the entire universe, the vast majority of them do not come from bright objects, such as stars, but from the *Cosmic Microwave Background* (CMB). The CMB is the leftover light created by the big bang, which has now been stretched so much by the expansion of the universe it is now only visible in microwave radiation. This radiation seems extremely isotropic, however, with enough sensitivity small fluctuations can be detected. These fluctuations correspond to quantum fluctuations in the very early universe. Using satellites such as Wilkinson Microwave Anisotropy Probe (WMAP) and Planck, astronomers have been able to use the CMB to constrain the cosmogony of our universe. We now have values for the critical density of the universe ρ_{crit} , curvature k and the Hubble constant H . The next thing to consider is what the early universe looked like before it expanded, cooled and started forming galaxies. If the early universe had been completely isotropic and

homogeneous, gravity would not be able to act on clumps of matter to cause them to collapse, eventually allowing galaxies to form. Anisotropy in the early universe is the seed for all structure in the universe. Looking at the CMB one can build a power spectrum to fit the different scales of structures. The choice of power spectrum can greatly affect the universe created and can be described by two quantities, σ_8 and n . The first of the two, σ_8 , is the *power spectrum normalization* or the density fluctuations on the scale of 8 Mpc. Planck gives a value of $\sigma_8 = 0.829 \pm 0.014$ (Planck Collaboration et al., 2016) A value close to unity would result in the universe being fairly homogenous at scales of 8 Mpc. The second value n is the *power spectrum slope* or the scalar spectral index, which is a measure of how the fluctuations depend on the scale. Planck gives a value of 0.9655 ± 0.0062 (Planck Collaboration et al., 2016) This is also close to unity, meaning the size of the fluctuation does not depend much on the scale. The combination of these two values would imply that the universe is quite homogenous.

In the Λ -CDM cosmogony, cold dark matter makes up roughly 85 per cent of all matter in the universe (Planck Collaboration et al., 2016). The cold dark matter is thought to be comprised of, yet undiscovered, massive weakly interacting particles (WIMPS). In this section, I will discuss some of the indirect evidence for the existence of cold dark matter, and the large dark matter haloes that are thought to envelop galaxies throughout the universe.

Indirect observations

Zwicky (1933) measured the velocity dispersion of galaxies in the Coma Cluster. Assuming that the cluster is in virial equilibrium, the average kinetic energy should be equal to half the average potential energy, also assuming that the mass is uniformly distributed, and each of the 800 galaxies has a mass $M_* = 10^9 M_\odot$, it is possible to calculate the potential energy.

1.1 Galaxies and their components

Take the mass to be

$$M_{\text{coma}} \sim N_{\text{galaxies}} \times M_{\text{galaxy}} \times M_{\odot} \sim 800 \times 10^9 \times 2 \times 10^{33} = 1.6 \times 10^{45} \text{ g} \quad (1.1.8)$$

combining this with the gravitational potential energy per unit mass

$$E_p = -\frac{3GM_{\text{coma}}}{5R_{\text{coma}}} \sim -6.4 \times 10^{13} \text{ cm}^2 \text{ s}^{-2} \quad (1.1.9)$$

yields the average velocity

$$E_k = \bar{v}^2/2 = -E_p/2 = 3.2 \times 10^{13} \text{ cm}^2 \text{ s}^{-2} \quad (1.1.10)$$

$$\bar{v} = 80 \text{ km s}^{-1}. \quad (1.1.11)$$

However, the observed velocity dispersion was far higher, $\sigma \sim 1000 \text{ km s}^{-1}$, implying the total mass is far higher than just the mass contributed from the luminosity of the galaxies—the factor of two from the assumption of being in virial equilibrium does not come close to alleviating this discrepancy. Zwicky (1933) reported that the Coma cluster has an average density 400 times greater than the density derived solely from the luminous matter. The missing mass, referred to as Dark Matter, was not only needed to reach the observed velocity dispersion of the cluster but needed to be more abundant than the luminous matter.

Using nebulae inside Andromeda Babcock (1939) found that the mean rotational velocity curve was remarkably flat. Similarly, Rubin and Ford (1970) measured the radial velocities of 67 HII region in the Andromeda galaxy. The authors found that the radial velocity profile was flat between 8 and 23 kpc. Also, a similar result was found for the rotation curve of M33 (Corbelli and Salucci, 2000; Volders, 1959). As mentioned in section 1.1, in a spiral galaxy like Andromeda most of the stellar mass is in the disc which has an exponentially declining density profile. The second most massive stellar component is the

bulge, which extends to even shorter radii than the disc. Therefore, at large radii, the mass enclosed by an orbit can be assumed to be constant. With this assumption, and considering Kepler's second law, the rotational velocity will fall with increasing radius. This is clearly not the case for Andromeda, where the rotational velocity is not falling at high radii, thus the assumption that the mass is constant must be wrong. For a particle at radius r , with tangential velocity v and a mass m , the force required to maintain a circular orbit is given by

$$F = \frac{mv^2}{r}. \quad (1.1.12)$$

If the particle is in a circular orbit, this force must be equal to the force due to gravity, therefore

$$F = \frac{mv^2}{r} = \frac{GMm}{r^2}, \quad (1.1.13)$$

and the mass enclosed by an orbiting particle can be considered as a point mass (M) at the centre of mass. Therefore, by rearranging this equation, the mass enclosed is given by

$$M = \frac{v^2 r}{G}. \quad (1.1.14)$$

From the observation of Rubin and Ford (1970), one can assume that the velocity is constant, yielding the relationship

$$M \propto r. \quad (1.1.15)$$

The density of the mass enclosed is given by

$$\rho = \frac{M}{\pi r^2}, \quad (1.1.16)$$

therefore, the density enclosed falls off at a rate

$$\rho \propto 1/r. \quad (1.1.17)$$

1.1 Galaxies and their components

But in section 1.1 it was noted that the density of the disc falls at an exponential rate, so there must be missing mass out to 22 kpc in the Andromeda galaxy.

Figure 1.12 shows the favoured model for the rotation curve of the MW proposed by Klypin et al. (2002). The non-solid lines show the velocity contributed by each component of the galaxy. At small radii ($r < 15$ kpc) the disc dominates with a small contribution from the bulge. Past 15 kpc the velocity curve is dominated by the dark matter halo which extends well beyond any of the main stellar components. The authors show comparisons to observed rotational velocities of the Galaxy, displaying indirect evidence of dark matter.

Gravitational lensing is one of the predictions of general relativity (Einstein, 1936), and it allows observers to measure the mass of an object by the bending of background light. Taylor et al. (1998) used gravitational lensing to measure the mass of the galaxy cluster Abell 1689. The authors found that the mass is in good agreement with mass derived from line-of-sight velocity dispersions, similar to the method used by Zwicky (1933). Finding that the distribution of mass is far more extended and massive than the light would suggest. This leads us to arguably the most compelling evidence for the existence of dark matter, the Bullet Cluster—a merger between two galaxy clusters. Clowe et al. (2006) compared the distribution of mass, derived from the weak-lensing observations, to the distribution of X-ray emitting plasma. The authors found that the distribution of mass did not trace the plasma, but followed the distribution of the stellar components of both clusters. Stars are very small and dense compared to the size of a galaxy, and as such rarely collide, this is an example of a *collisionless* system. Cold dark matter is also collisionless (Clowe et al., 2006; Harvey et al., 2015; Read et al., 2018), however, gas is not. As the two clusters pass through each other the gas collides, shock heating it to high temperatures at the centre of the two clusters. However, the stars and dark matter are able to pass through each other with little impediment. The observations agree with this theory, with the X-ray emitting hot gas in between the mass distribution of the two clusters.

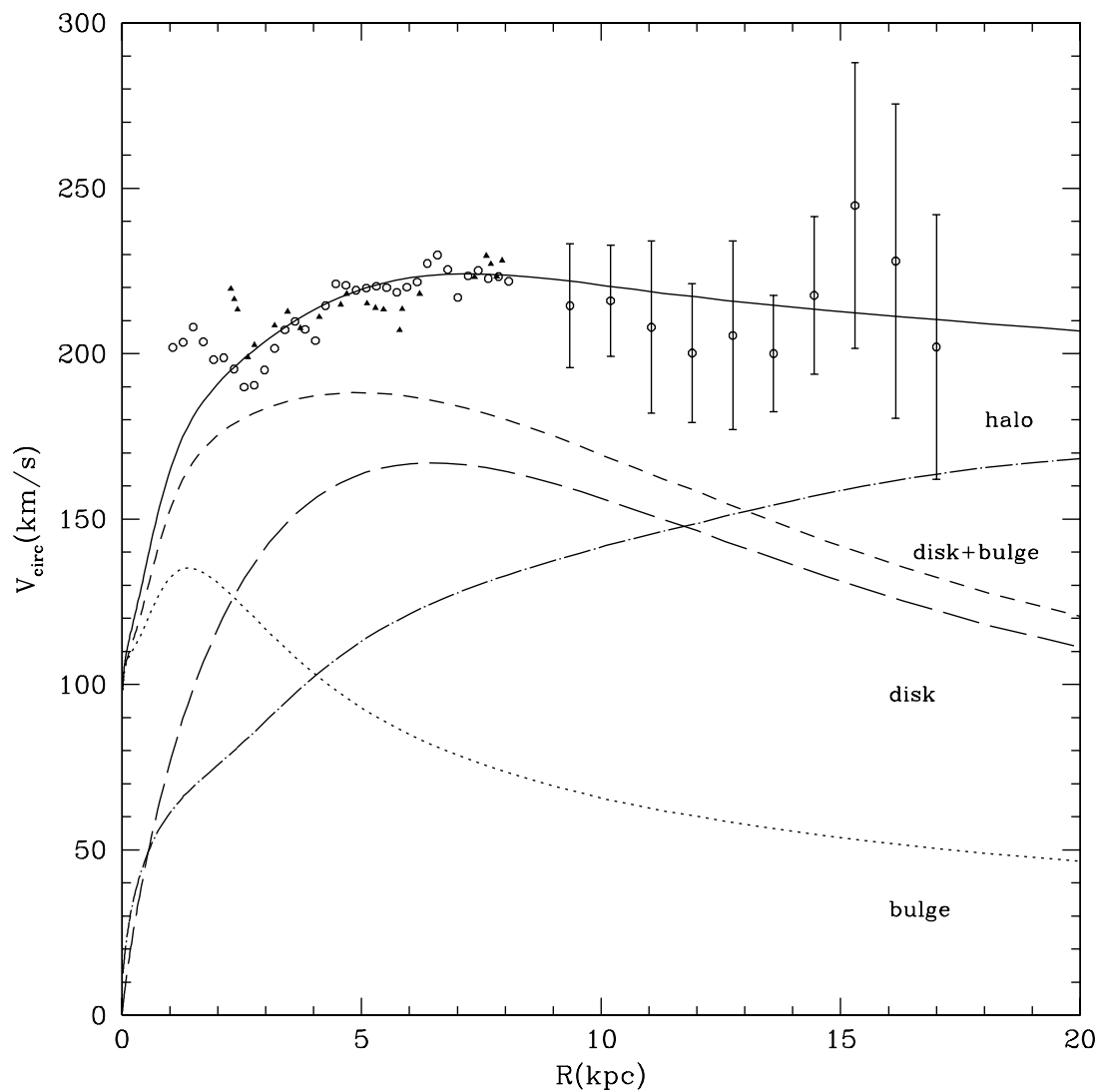


Fig. 1.12 The circular velocity profile for the favoured model from Klypin et al. (2002) (with exchange of angular momentum). Observational data from HI measurements of Knapp et al. (1985, circles) and Kerr et al. (1986, triangles). At large radii the velocity curve is dominated by the dark matter halo.

Profile and shape

I have previously discussed the formation of density peaks in the early universe (see section 1.1.1) and mentioned that these peaks are the building blocks of the dark matter haloes thought to be harbouring galaxies throughout the universe. The structure of dark matter haloes can tell us about the cosmological parameters (Hoffman, 1988; Hoffman and Shaham, 1985). With a large value for the spectral index (n) and a low value for the density parameter (Ω) haloes should have steeper density profiles. Whereas for low n and high Ω the density profiles should be shallower, which has been confirmed by N-body simulations (e.g. Frenk et al., 1988, 1985). It was initially assumed that dark matter haloes were isothermal spheres, with a density profile,

$$\rho(r) = \frac{\sigma^2}{2\pi Gr^2/r_c^2}, \quad (1.1.18)$$

where σ is the velocity dispersion, and r_c is the core radius. With such a dependence between density and velocity one might expect correlations between the velocity of satellite galaxies and the rotation velocity of the disc, and between pairs of galaxies, but such correlations are not found (Navarro et al., 1996). Dubinski and Carlberg (1991a) studied the density profiles of dark matter haloes in a variety of simulations, finding that the profiles were *cuspy*, not completely isothermal. Using N-body simulations of dark matter haloes ranging in mass from dwarf galaxies to large clusters, Navarro et al. (1996) found a universal profile. The universal profile was approximately isothermal near the virial radius but shallower near the centre. The Navarro-Frenk-White (NFW) profile,

$$\frac{\rho(r)}{\rho_{\text{crit}}} = \frac{\delta_c}{(r/r_s)(1+r/r_s)^2}, \quad (1.1.19)$$

where $r_s = r_{200}/c$ is a characteristic radius, ρ_{crit} is the critical density, and δ_c and c are dimensionless parameters. The mass of the halo is given by

$$M_{200} = 200 \times \rho_{\text{crit}} (4\pi/3) r_{200}^3 \quad (1.1.20)$$

where r_{200} is the radius at which the mean density enclosed is equal to 200 times that of the critical density. The dimensionless parameter δ_c is defined as

$$\delta_c = \frac{200}{3} \frac{c^3}{[\ln(1+c) - c/(1+c)]}. \quad (1.1.21)$$

The parameters δ_c , r_s and c are often referred to as the characteristic overdensity, scale radius and concentration, respectively. Jing and Suto (2002) extended the NFW profile to triaxial systems, using triaxial models for dark matter haloes within a large cosmological simulation.

1.2 Simulations

1.2.1 N-Body

A popular set of methods for modelling the motions of particles are *N-Body* simulations, which track the motion of large numbers of particles under their own gravitational field. The resolution of such simulations has come a long way from the earliest experiments. The first *N*-body simulation was presented by Holmberg (1941), using a novel set-up with light-bulbs. Computational Peebles (1970) presented one of the first *N*-body simulations utilizing just 300 particles, whereas, more recent *N*-body simulations have reached 374 billion particles (Kim et al., 2011). Such methods fall into two categories, *collisional* and *collisionless*. Collisional *N*-Body codes are used for simulating systems where the resolution is comparable to the system itself $N = N_*$, and where the relaxation time is less than the duration

1.2 Simulations

of the numerical integration. They accurately follow the close encounters of particles in multiple particle systems. Due to resolution limits, such codes are very useful for globular cluster scale objects, but not useful for galaxy scale systems. Collisionless codes are used for systems where the relaxation time is much longer than the integration time, and where the resolution is much lower than the system itself $N \ll N_*$. Due to the resolution being much lower the relaxation time of the simulation will be much smaller than the system, as such one must choose an integration time much shorter than the relaxation time. As the number of particles in the simulation is far less than in the real astrophysical system, the particles are massive by comparison. Therefore, close encounters between such particles are unrealistic. To alleviate this issue a *softening kernel* is used, modifying the gravitational potential of each particle using a function that reduces the force between particles when they are extremely close, but leaves the potential unchanged for large distances. An example of a form for the softening kernel can be given by the *Plummer sphere*:

$$S(r) = -\frac{1}{\sqrt{r^2 + \epsilon^2}} \quad (1.2.1)$$

where ϵ is the *smoothing length*.

The force on a particle i is the sum of contributions from all other particles in the simulation,

$$F_i = \sum_j Gm_j \frac{\mathbf{r}_j - \mathbf{r}_i}{|\mathbf{r}_j - \mathbf{r}_i|^3} \quad (1.2.2)$$

This is the direct summation approach, which works for collisional codes with small N . For a collisionless code, with smoothing, this equation requires modification. If the potential of a particle is modified by Equation 1.2.1 then the force is smoothed simply by its derivative $S_F(\mathbf{r}) = \frac{d}{d\mathbf{r}}S(\mathbf{r})$. Therefore, Equation 1.2.2 can be rewritten as

$$F_i = \sum_j Gm_j S_F(|\mathbf{r}_j - \mathbf{r}_i|) \frac{\mathbf{r}_j - \mathbf{r}_i}{|\mathbf{r}_j - \mathbf{r}_i|^3} \quad (1.2.3)$$

However, as the force of each particle requires a sum over all other particles the time taken to calculate it scales as $\frac{1}{2}N(N-1) \sim N^2$.

A more desirable approach is a tree code, which scales as $N \log N$ (Barnes and Hut, 1986). The particles are organized by putting everything into one *root* cube, then splitting this cube into eight more cubes. If any of these eight cubes contains more than one particle the cube is split into eight more, this is done iteratively until each cube has at most one particle—these are the smallest cubes called *leaves*. This results in a hierarchical structure of different size cubes called an *oct-tree*.

1.2.2 Smoothed Particle Hydrodynamics

Euler's equations for fluid dynamics can be applied to hydrodynamics which, in Lagrangian form, can be written as

$$\frac{d\rho}{dt} = -\rho \nabla \cdot \mathbf{v}, \quad (1.2.4)$$

$$\frac{d\mathbf{v}}{dt} = -\frac{\nabla P}{\rho} + \mathbf{g}, \quad (1.2.5)$$

$$\frac{du}{dt} = -\frac{P}{\rho} \nabla \cdot \mathbf{v} + \Gamma - \Lambda, \quad (1.2.6)$$

where, ρ , \mathbf{v} , u , \mathbf{g} , Γ and Λ are fluid density, velocity, internal energy, force, heating and cooling terms, respectively. The three equations express the conservation laws of mass, momentum, and energy, respectively. The equation of state $P = (\gamma - 1)\rho u$ of an ideal gas, is assumed, where γ is the adiabatic index. Smoothed Particle Hydrodynamics (SPH) is a particle-based approach to solving Euler's equations developed by Lucy (1977) and Gingold and Monaghan (1977).

For astrophysical systems, the gas is generally very low density, highly compressible, and exists at a wide range of temperatures. As such, one approximation that can be reasonably made is that the gas is a perfectly adiabatic, neglecting small-scale processes. However,

1.2 Simulations

the action of gravity causes very high-velocity flows which are often turbulent and supersonic, for example, a gas particle falling into a halo of mass comparable to the MW would reach several tens of km s^{-1} . The fluid properties are stored in moving particles, eliminating the need for advective terms found in non-particle based approaches. To find a particular value of quantity f_i of particle i at position \mathbf{r}_j in the simulation one can simply use the sum

$$f_i = \sum_j f_j S(\mathbf{r}_j - \mathbf{r}_i). \quad (1.2.7)$$

where the value of f_i is dominated by contributions from the neighbour particles. Such an approach can be married well with previous N-body methods (e.g. GASOLINE Wadsley et al., 2004).

GASOLINE

Built on the parallel N-body code PKDGRAV (Stadel, 2001), GASOLINE is a parallel SPH code used to simulate a variety of different systems, from cosmological scales to gas-giant planets. GASOLINE uses a spatial binary tree, with a similar hierarchical structure to the oct-trees mentioned previously, constructed by bisecting the initial cube and then recursively bisecting the cells longest axis until each cell has at most $n_{bucket} \sim 8 - 16$ particles. The motivation behind using buckets as opposed to single particles is to reduce the storage requirements and to make the code more efficient.

The gravitational acceleration is calculated by the tree-walking procedure from Barnes and Hut (1986), modified to calculate the interactions between buckets rather than particles. Each cell of the tree is assigned an *opening radius* with respect to its centre of mass $r_{open} = 2B_{max}/\sqrt{3}\theta_{open}$, where B_{max} is the maximum distance from a particle in the cell to the centre of mass, θ_{open} is the user specified *opening angle*. When calculating the acceleration for a bucket B_i , GASOLINE descends the tree opening all cells that are within or intersected by r_{open} . This is then repeated for all the children of the opened cells until the code reaches the

leaves (cells without children) of the tree, at which point the buckets themselves are opened. All buckets that have been opened are added to a *particle-particle interaction* list, whereas any cell that has not been opened will be added to the particle-cell interaction list.

Equation 1.2.7 shows the form for an estimate of some quantity f used throughout SPH methods, including GASOLINE. In GASOLINE the kernel function W_{ij} is rewritten, following the kernel-average from Hernquist and Katz (1989), as

$$W_{ij} = \frac{1}{2}w(|\mathbf{r}_i - \mathbf{r}_j|/h_i) + \frac{1}{2}w(|\mathbf{r}_i - \mathbf{r}_j|/h_j) \quad (1.2.8)$$

to ensure that $W_{ij} = W_{ji}$, where h is the smoothing length, thereby satisfying conservation of energy and momentum. The function $w(\mathbf{r}, h)$ is the spline function,

$$w(\mathbf{r}, h) = \frac{1}{\pi h^3} \begin{cases} 1 - \frac{3}{2}q^2 + \frac{3}{4}q^3 & \text{if } 0 \leq \frac{r}{h} \leq 1; \\ \frac{1}{4}(2 - q)^3 & \text{if } 1 \leq \frac{r}{h} \leq 2; \\ 0 & \text{otherwise} \end{cases} \quad (1.2.9)$$

where $q = \frac{r}{h}$ (Monaghan, 1992).

Density is calculated by summing over particle masses m_j

$$\rho_i = \sum_j m_j W_{ij}. \quad (1.2.10)$$

Acceleration is given by

$$\frac{d\mathbf{v}_i}{dt} = -\sum_j m_j \left(\frac{P_i}{\rho_i^2} + \frac{P_j}{\rho_j^2} + \Pi_{ij} \right) \nabla_i W_{ij} \quad (1.2.11)$$

where P_j is the pressure, \mathbf{v}_i is the velocity, and Π_{ij} is the artificial viscosity term. The

pressure is dependent on the local gas particle pressure, given as

$$\frac{du_i}{dt} = \frac{P_i}{\rho_i^2} \sum_j m_j \mathbf{v}_{ij} \cdot \nabla_i W_{ij} \quad (1.2.12)$$

where u_i is the internal energy of the particle i assumed to represent an ideal gas, with

$$u_i = \frac{P_i}{(\gamma - 1)\rho_i} \quad (1.2.13)$$

with γ the adiabatic index. The artificial viscosity term Π_{ij} is given by,

$$\Pi_{ij} = \begin{cases} \frac{-\alpha \frac{1}{2}(c_i + c_j) \mathbf{v}_{ij} + \beta v_{ij}^2}{\frac{1}{2}(\rho_i + \rho_j)} & \text{for } \mathbf{v}_{ij} \cdot \mathbf{r}_{ij} < 0, \\ 0 & \text{otherwise} \end{cases} \quad (1.2.14)$$

$$\text{where } v_{ij} = \frac{h(\mathbf{v}_{ij} \cdot \mathbf{r}_{ij})}{r_{ij}^2 + 0.01(h_i + h_j)^2} \quad (1.2.15)$$

where $\mathbf{r}_{ij} = \mathbf{r}_i - \mathbf{r}_j$, $\mathbf{v}_{ij} = \mathbf{v}_i - \mathbf{v}_j$, c_j is the sound speed, $\alpha = 1$ and $\beta = 2$ are coefficients used for shear and Von Neumann-Richtmyer viscosities, respectively. The choice of using an artificial viscosity is motivated by the widths of dissipative shocks being smaller than the resolution of the simulation, leading to instabilities in the numerical algorithms.

In galaxies, processes such as star formation and stellar feedback effect the flow of, and composition of, neighbouring gas. Star formation traps gas into stars where some of it can be slowly converted into heavier elements. Feedback transfers some of this material back into the surrounding gas, but also drastically increases its energy. Many schemes have been implemented that attempt to account for these processes. This thesis will concentrate on one, in particular, Stinson et al. (2006). Following Katz (1992), Stinson et al. (2006) imposed four criteria that must be met for a gas particle to be eligible to form a star. The particle must be

1. denser than $n_{min} = 0.1 \text{ cm}^{-3}$,
2. in an overdense region,
3. part of a converging flow,
4. Jeans unstable ($\frac{h_i}{c_i} > \sqrt{\frac{1}{4\pi G \rho_i}}$).

The overdensity required to meet criterion 2 is user specified and is motivated by the need to limit star formation in the early universe. Governato et al. (2010) compared the effects of high and low density star formation thresholds, finding that when the local density required is high (100 amu cm^{-3}) the resulting ISM is inhomogeneous, with strong outflows and gas being preferentially ejected from the galaxy centre. For a low-density threshold (0.1 amu cm^{-3}) the ISM is more homogenous, the supernova feedback more evenly distributed throughout the disc, and star formation is able to continue in the central regions. In a star-forming region the flow of gas should be converging, which can be determined from the velocity field,

$$\nabla \cdot \mathbf{v} = \frac{1}{\rho_i} \sum_j m_j (\mathbf{v}_j - \mathbf{v}_i) \cdot \nabla_i W_{ij}. \quad (1.2.16)$$

For $\nabla \cdot \mathbf{v} < 0$ the flow is converging, and criterion 3 is satisfied. The Jeans stability criterion tests if the cloud can provide sufficient pressure support so that the cloud will not collapse under its self-gravity. If the pressure support is not sufficient the gas cloud will collapse and form stars. The star formation time-scale t_{form} is a fine balance between the dynamical time t_{dyn} taken to collapse, and the time taken for the gas to cool sufficiently. Stinson et al. (2006) choose t_{form} to simply be the dynamical time, but imposed an upper limit on the temperature of the gas, so $T_{gas} < T_{max}$. The star formation rate of such a system is given as

$$\frac{d\rho_*}{dt} = c^* \frac{\rho_{gas}}{t_{form}} \quad (1.2.17)$$

where c^* is a constant corresponding to the star formation efficiency, a user prescribed

1.2 Simulations

parameter that can be used to tune the star formation rate to match observations.

A further consideration is stellar feedback. Supernova ejecta creates blastwave shocks, converting the kinetic energy of the material into thermal energy in the surrounding medium. This conversion happens on scales well below the resolution of galaxy-scale simulations, and as such the energy of the supernova is treated as purely thermal. The number of stars that go supernova depends on the IMF. Stinson et al. (2006) choose a three-piece power-law following Miller and Scalo (1979). They defined the mass range for SN type-II to be $8 \leq M/M_{\odot} \leq 40$; stars above this either collapse to black holes directly or result in SN type-Ib. However, the number of stars above this mass range is very small and contributes little to the total feedback. Combining the IMF with the stellar lifetimes of stars within this mass range (given by Raiteri et al., 1996), one can determine the rate of such supernovae. This rate multiplied by the energy ejected into the ISM from type-II supernova, $E_{SN} = 10^{50}$ erg, giving the total feedback energy. The energy is distributed, using the SPH smoothing kernel, into the gas particles surrounding the current position of the star particle, i.e. more massive gas particles will get more of the energy. However, because supernovae tend to occur in higher density regions, the thermal energy contributed to the surrounding gas will quickly be radiated away, and star formation will continue. Therefore, Stinson et al. (2006) disabled radiative cooling of nearby gas particles, to suppress the local star formation. Supernovae type-Ia, on the other hand, still distribute their energy into the surrounding gas in a similar fashion, but do not disable radiative cooling. The motivation behind this is that the average lifetime of a binary system is far longer than that of a supernova type-II candidate, and as such if one was to form in a star-forming region, it would be a long time before the supernova suppressed the local star formation rate. A further consideration is a stellar feedback for stars with $M < 8 M_{\odot}$, these stars also return a significant fraction of their mass back into the ISM (0.25 – 0.5 Kennicutt et al. (1994)) in the form of stellar winds. Again combining the IMF with the stellar lifetimes of $M < 8 M_{\odot}$ mass stars, Stinson et al. (2006) used the

same distribution technique described for supernova for stellar winds, however, returning no energy into the ISM, just metallicity.

One issue facing SPH codes is the mixing problem, where the code is unable to resolve mixing at fluid boundaries (Agertz et al., 2007; Read et al., 2010). Traditional SPH codes were unable to develop Kelvin-Helmholtz or Rayleigh-Taylor instabilities across discontinuities in thermal energy (Price, 2008). Read et al. (2010) identified two problems that lead to this unresolved mixing, a leading order error (E0) in the momentum equation and the local mixing instability. Dehnen and Aly (2012) showed that switching from traditional kernels to Wendland kernels (Wendland, 1995) can avoid the leading order error. Wadsley et al. (2008) employed turbulent diffusion to improve mixing, while Hopkins (2013) demonstrated that using modified pressure-based formulations could substantially reduce the impact of numerical surface tension which exacerbated the mixing problem. GASOLINE2 uses Wendland kernels (Wendland, 1995), turbulent diffusion based on local velocity shear to mix fluid quantities (Wadsley et al., 2008) and a new pressure force formulation to achieve similar results to Hopkins (2013) alleviating the mixing problem (Wadsley et al., 2017).

1.3 Orientations of galaxies

1.3.1 Briggs figures

Section 1.1 discussed the presence of warps in late-type galaxies. While presenting the general behaviour of galactic warps, Briggs (1990) employed a figure to illustrate how the planes of the warp and stellar disc differ. These *Briggs Figures* are polar plots containing the unit angular momentum vectors for concentric rings. Typically polar plots can be used to show 2-dimensional vectors by plotting both the radial coordinate and azimuthal coordinate, the angle ϕ from the reference axis. However, the angular momentum of a

3-dimensional system is itself 3-dimensional, and in order to visualize it in 2-dimensions requires a projection. For unit vectors the radial extent is unity, therefore, one can use the radial coordinate on the figure to show the θ value of a 3-dimensional vector. As in the spherical coordinate system (r, ϕ, θ) , ϕ shows the angle between the x -axis and the vector, and θ the angle between the z -axis and the vector. Values for ϕ and θ must lie within the ranges $0 \leq \phi \leq 180$ and $0 \leq \theta \leq 360$, respectively. Briggs (1990) chose a reference frame so that the angular momentum of the stellar disc lies along the z axis. Such Briggs Figures allow us to visualize and compare numerous 3-dimensional vectors simultaneously, without the use of 3-dimensional graphs.

1.3.2 Scale Varying Alignments

Throughout the literature, there are examples of alignments between various stellar systems over a plethora of scales. Binggeli (1982) studied 44 regular Abell galaxy clusters, finding that clusters separated by less than ~ 30 Mpc strongly tend to be aligned such that their major axes point to each other (the correlation alignment). The author also confirmed previous work that indicated that the major axes of a cluster's cD galaxy (the central massive galaxy) and the cluster itself seem to be aligned. Subsequently, Plionis (1994) looked at 637 clusters finding a comparable relationship for distances $\sim 15h^{-1}$ Mpc. Smargon et al. (2012) looked at two much larger samples containing 6625 and 8081 clusters, finding strong support for an alignment between the major axes and the line connecting the pair of clusters out to distances of $100h^{-1}$ Mpc.

On smaller scales, Pen et al. (2000) found that galaxies closer together are more likely to have similar angular momenta. This work was followed up by Lee and Pen (2007), measuring the intrinsic alignments of blue and red SDSS galaxies, finding a 3σ signal for galaxies with $a/b \leq 0.8$. Using an even larger sample of 83,773 SDSS luminous red galaxies Okumura et al. (2009) found an intrinsic ellipticity correlation function for separations up

to $30h^{-1}$ Mpc. Li et al. (2013) found that the brightest satellite galaxies (BSGs) are found in the plane of the major axis (especially in richer groups), and that red BSGs are often more aligned than blue BSGs. Hirata et al. (2007) investigated the gravitational lensing shear and intrinsic ellipticity relationship for both red and blue galaxies, finding $> 3\sigma$ detections scales up to $60 h^{-1}$ Mpc for red galaxies and no detection for blue galaxies within their samples. Paz et al. (2008) also found that redder galaxies tend to exhibit elliptical shapes that are elongated in the direction of the large-scale structure both in numerical simulations and in SDSS data. Incorporating a theoretical side, Faltenbacher et al. (2009) looked for similar alignments in both the millennium simulation and SDSS galaxies, again finding correlations for red galaxies, whereas the blue galaxies tended to exhibit more random orientations. Similarly, Tempel and Libeskind (2013) and Tempel et al. (2013) looked at the alignment of galaxy spin axes of both disc and elliptical galaxies, relative to the local filamentary structure of the cosmic web, finding that disc galaxies were only weakly aligned, whereas the more elliptical galaxies showed a strong perpendicular alignment. Zhang et al. (2013) agreed that for red galaxies the major axes of galaxies within the filamentary structure were aligned parallel to the filament, while galaxies in sheets have their major axes preferentially aligned parallel to the plane of the sheets, this relation is much weaker in spiral galaxies (Zhang et al., 2015).

Determining the alignments between satellites and host galaxies has yielded conflicting results. Early work concluded that satellites are preferentially aligned with the minor axis of the halo (Holmberg, 1969). More recent work has found that red galaxies have satellites more aligned with the halo major axis, and that blue galaxies tend to have isotropic alignments (Brainerd, 2005; Dong et al., 2014; Nierenberg et al., 2011; Wang et al., 2008, 2014; Yang et al., 2006). Lynden-Bell (1976) found a planar alignment for classical dwarfs in the stellar streams of the MW, which was later found to be rotationally coherent (Metz et al., 2008; Pawlowski et al., 2013). Similar work has been done for M31, concluding that the

satellite distribution is anisotropic with satellites preferentially populating a roughly edge-on plane with respect to the MW and almost perpendicular to the MW disk (Conn et al., 2013; Koch and Grebel, 2006; McConnachie and Irwin, 2006). However, it has been argued that such structures are not kinematically coherent (Buck et al., 2016). One important conclusion that can be drawn from these different alignments is that redder galaxies tend to follow the correlations much more tightly than bluer galaxies.

1.3.3 Theory

A prediction of tidal torque theory is that the angular momenta and shapes of dark matter haloes should be correlated over large scales (Catelan et al., 2001; Catelan and Porciani, 2001; Crittenden et al., 2001; Peebles, 1969; Porciani et al., 2002). Such a correlation would lead to the expectation of alignments between clusters of galaxies and the cosmic web. Various N-body simulations have detected the same ellipticity correlation found between clusters of galaxies in pairs of dark matter haloes (Croft and Metzler, 2000; Faltenbacher et al., 2008; Heavens et al., 2000; Jing, 2002). However, Camelio and Lombardi (2015) argue that this alignment is not dominated by the tidal field as it is too weak to account for the observed signal, but is driven by accretion and formation processes. Both galaxy clusters, dark matter haloes and ellipticals are predicted to be formed via hierarchical merging, which might explain why previous studies (e.g. Faltenbacher et al., 2008) see similar alignments with neighbours and the cosmic web. Aragón-Calvo et al. (2007) investigated the orientations of dark matter haloes in cosmological N-body simulations, with respect to the surrounding large-scale structure. The authors found that the triaxial shapes of the haloes generally had minor axes perpendicular to the wall or filament the halo was situated within. Further work expanded on this work finding similar results for the shape of dark matter haloes, however, for the spin of the halo there appears to be a high and low mass preference separated at $M \sim 5(\pm 1) \times 10^{12} M_{\odot}$ (Cuesta et al., 2008; Hahn et al., 2007a,b; Libeskind et al., 2012; Paz

et al., 2008; Trowland et al., 2013; Wang et al., 2011; Zhang et al., 2009). High mass haloes tend to have their spin axes perpendicular to the filamentary structure, while less massive haloes have spin axes parallel to their host filament (Codis et al., 2012). Such alignments between the filamentary structure and the shape of haloes are considered to be a consequence of tidal torques and via the preferential accretion of material following along the filaments (Bailin and Steinmetz, 2005; Faltenbacher et al., 2005; Jing, 2002).

In collisionless simulations, the angular momentum of dark matter haloes is typically orientated parallel to the minor axis (Bailin and Steinmetz, 2005; Dubinski, 1992; Faltenbacher et al., 2005; Porciani et al., 2002; Warren et al., 1992). It follows that the angular momentum of the baryonic components may be aligned with the dark matter halo. Hydrodynamical simulations reveal that it is not that simple, even before the galaxy has formed, the angular momenta of the hot gas that has fallen into the halo, has misaligned angular momentum relative to that of the halo (Chen et al., 2003; Sharma and Steinmetz, 2005; van den Bosch et al., 2002). Subsequently, the galaxy that forms from this misaligned gas will change the angular momentum of the inner halo, leaving the halo unchanged at large radii (Bailin et al., 2005; Butsky et al., 2016; Debattista et al., 2008; Kazantzidis et al., 2004). Within 10 per cent of the virial radius the halo and disc are well aligned, but out to the virial radius hydrodynamical simulations find on average $30^\circ - 40^\circ$ of misalignment between the disc and halo (Bett et al., 2010; Croft et al., 2009; Hahn et al., 2010). Debattista et al. (2013) showed, using numerical simulations, that redder galaxies tend to have much more stable orientations, whereas bluer galaxies tend to be randomly orientated relative to their own haloes. This discrepancy may be due to the ongoing gas accretion feeding star formation in the bluer galaxies.

1.4 Galaxy tilting

The orientation of disc galaxies can be quantified by the direction of the stellar disc's angular momentum (see Section 1.3). The angular momentum of a disc galaxy is not fixed, processes such as interactions, torques exerted on the disc by the host dark matter halo and the quiescent cooling of gas onto the disc, all influence the total angular momentum of the disc. Such processes alter the orientation of the disc, the difference in the angular momentum vectors with respect to time results in a tilting rate. The *Gaia* space astrometry mission may soon allow direct measurement of the MW's disc tilting rate, using precision measurements of stellar positions with accuracies of order $20\mu\text{as}$ with respect to distant quasars (Lindegren et al., 2008; Perryman et al., 2001).

Numerous processes drive tilting in disc galaxies. Interactions between the disc, satellites, and neighbours are the most often studied. I will exclude major mergers, which are extreme events that can destroy discs. Minor mergers and similar small-scale interactions generally leave the disc intact, resulting in a change in angular momentum. Infalling satellites cause appreciable changes to discs, such as tilting, warping and heating (Huang and Carlberg, 1997). Huang and Carlberg (1997) found that discs are mainly tilted rather than heated and that the kinetic energy associated with vertical motion is more affected than the heating in the same direction. As satellites fall into the disc, due to the transfer of angular momentum, they tilt towards alignment with the disc (Huang and Carlberg, 1997; Read et al., 2008). In the MW, two of the most massive satellites are the Large and Small Magellanic Clouds (LMC and SMC). The mass of the LMC is as high as $M_{\text{LMC}} \sim 2 \times 10^{11} M_{\odot}$ (Gómez et al., 2015; Kallivayalil et al., 2013; Peñarrubia et al., 2016), corresponding to ~ 20 per cent of the mass of the MW. This puts it above the upper mass estimate for the initial mass of the Sagittarius dwarf galaxy (Jiang and Binney, 2000), meaning it is the most important interaction in some time.

1.4.1 Interactions

Minor mergers and interactions contribute angular momentum to a galaxy's surrounding dark matter halo. Bett and Frenk (2012) examined the consequences of minor mergers and flybys on the spins of dark matter haloes from a Λ CDM simulation similar to the Millennium Simulation. They measured the angular momentum of selected haloes spanning $z = 6.2$ to $z = 0$ within a mass range of $12.0 \leq \log_{10}(M/M_{\odot})h^{-1} \leq 12.5$ at $z = 0$. The authors found that such events only caused small changes to the angular momentum of the entire halo, with only 10.5 per cent experiencing changes in their angular momentum direction by more than 45° . However, the inner halo was not so stationary, with 47 per cent of inner haloes experiencing a change in their angular momentum orientation of at least 45° during their lifetimes. Bett and Frenk (2016) expanded the study to include a broader range of halo masses ($10.5 \leq \log_{10}(M/M_{\odot})h^{-1} \leq 15.5$). They found that 35 per cent of haloes had experienced changes in angular momentum direction of at least 45° , at some point in their lifetimes, without a major merger taking place. When they considered just the inner haloes 64 per cent experienced orientation changes of a similar magnitude over just 0.5 Gyrs, during the course of their lifetime.

1.4.2 Dark matter torques

Torques imposed from the surrounding dark matter halo also influence the orientation of the disc. In the Λ -cold dark matter (Λ CDM) paradigm, haloes grow hierarchically, becoming triaxial (Allgood et al., 2006; Bailin and Steinmetz, 2005; Bardeen et al., 1986; Barnes and Efstathiou, 1987; Dubinski and Carlberg, 1991b; Frenk et al., 1988; Jing and Suto, 2002). Dubinski (1992) measured the tilting rates of dark matter haloes affected by tidal shear; he found that the major axis of each halo in the mass range $(1 - 2) \times 10^{12} M_{\odot}$ rotated uniformly with an angular momentum vector generally aligning with the minor axis, with rotation rates between $6^{\circ} - 96^{\circ} \text{Gyr}^{-1}$. Similarly, Bailin and Steinmetz (2004) detected smooth figure ro-

1.4 Galaxy tilting

tation in 288 of their 317 dark matter haloes, with angular momentum vectors aligned with the minor axis in 85 per cent of cases, and in 15 per cent of cases aligned with the major axis. They found an average tilting rate of $6.2^\circ \text{Gyr}^{-1}$, with a log-normal distribution with $\sigma = 0.58^\circ \text{Gyr}^{-1}$. Bryan and Cress (2007) found that 63 per cent of the 115 haloes they considered exhibited significant figure rotation, however, less than half of their sample showed alignment between the minor axis and the figure rotation axis with an average pattern speed of $13.8^\circ h \text{Gyr}^{-1}$. Debattista et al. (2015) showed that stellar discs, lacking gas and within a triaxial halo, align with the minor axis of the halo. After being perturbed by a satellite the disc settles back to this preferential alignment. Therefore, a disc that is misaligned with the minor axis of its halo will tilt. Thus a tilting halo will drag a disc along with it. To investigate such a coupling between the orientation of discs and dark matter haloes Yurin and Springel (2015) inserted live stellar discs into eight, MW-sized, high-resolution dark matter haloes from the AQUARIUS simulation. They found tilting rates of $5^\circ - 6^\circ \text{Gyr}^{-1}$, comparable with the halo tilting rates measured in pure N-body simulations. While no direct evidence of tilting dark matter haloes has been found, the tidal torques exerted by a rotating dark matter halo on stellar discs have been proposed as a possible cause of warps (Dubinski and Chakrabarty, 2009; Dubinski and Kuijken, 1995) and as a driving mechanism for spiral structure in the compact dwarf galaxy NGC 2915 (Bureau et al., 1999).

1.4.3 Gas accretion

Sustaining star formation in galaxies such as the MW requires there to be ongoing gas accretion onto the disc. As gas falls into a dark matter potential well it is shock heated to approximately the halo virial temperature $T_{vir} = 10^6 (v_{circ}/167 \text{km s}^{-1})^2 \text{K}$, forming a hot gas corona with a greater mass than the stellar disc itself (Dahlem, 1997; Fukugita and Peebles, 2006; Rees and Ostriker, 1977; Savage and de Boer, 1979; Silk, 1977; Spitzer, 1956; Wang et al., 2001; White and Frenk, 1991; White and Rees, 1978). This hot gas

cools slowly and eventually settles into the disc, maintaining the star formation rate (Brook et al., 2004; Brooks et al., 2009; Fall and Efstathiou, 1980b; Kereš et al., 2005; Robertson et al., 2006). Gas cooling from the corona contributes angular momentum to the disc. In hydrodynamical simulations, the angular momentum of the corona is usually misaligned with that of their embedded stellar disc (Roškar et al., 2010; van den Bosch et al., 2002). Roškar et al. (2010) showed that as the cold gas falls towards the disc it is torqued by the hot gas and by the time it reaches the disc it's angular momentum is completely aligned with that of the hot gas corona—this is true of both hot and cold mode gas accretion. This contribution of misaligned angular momentum will change the total angular momentum of the disc, causing it to tilt. Debattista et al. (2015) showed that under these circumstances, the orientation of the disc spin is determined by a balance between the torques from the triaxial dark matter halo, and the net inflow of angular momentum via cooling gas. As a result, star-forming galaxies where gas is being continually accreted onto the disc are generally misaligned with the main planes of their dark matter haloes (Agustsson and Brainerd, 2006; Azzaro et al., 2007; Brainerd, 2005; Faltenbacher et al., 2007; Li et al., 2013; Nierenberg et al., 2011; Sales and Lambas, 2004; Wang et al., 2010, 2008; Yang et al., 2006). Tidal streams such as the Sagittarius Stream may enable us to determine the orientation of the MW with respect to its dark matter halo. However, such efforts have produced best fitting models that require the angular momentum of the disc to be aligned with the intermediate axis of the halo (Deg and Widrow, 2013; Law and Majewski, 2010; Law et al., 2009). An intermediate axis alignment is extremely unstable, and hard to reproduce via simulations (Debattista et al., 2013). Debattista et al. (2013) therefore, argued that the modelling assumption of the disc residing in one of the halo's symmetry planes must be violated. Although indirect, this could support the hypothesis that gas accretion is affecting the orientation of the host galaxy.

1.5 Predicted observational limit of Gaia

Gaia was launched on December 19, 2013. Over the course of its five-year mission, *Gaia* will observe all star-like objects down to a limit of $V \sim 20$ mag (Lindegren et al., 2008; Perryman et al., 2001). This is predicted to yield over a billion objects, 500000 of which will be quasars, with redshifts between $z = 1.5-2$ (Claeskens et al., 2006). These quasars will provide an inertial reference frame of the Galaxy. The main goal of the *Gaia* mission is to provide accurate distances and proper motions for roughly one per cent of the stars in the MW. With these observations, Perryman et al. (2014) give predictions for possible detections that will be possible over the life of the mission. For example, a bulk rotation of the disk with a characteristic rate of $2 \text{ rad } H_0^{-1}$ ($30 \mu\text{as yr}^{-1}$) (like the tumbling rate presented in Bailin and Steinmetz, 2004; Bryan and Cress, 2007), will significantly exceed the inertial reference frame residual rotation ($0.2-0.5 \mu\text{as yr}^{-1}$), making it detectable. Moreover, if there is a misalignment between the disc and halo (see Section 1.3) the torques imposed should lead to a disc rotation rate that depends on the radius. Perryman et al. (2014) present simulations using realistic quasar counts demonstrating an accuracy better than $1 \mu\text{as yr}^{-1}$ ($0.27^\circ \text{ Gyr}^{-1}$) should be achieved in all inertial spin components of the Gaia reference frame. This thesis will present titling rates of simulated galaxies within cosmological simulations, and compare them to the detection limit of *Gaia*.

Thesis structure

This thesis is organised as follows. The second Chapter will present results the VICTOR simulation, a large cosmological hydrodynamical simulation. This set of simulations suffer from over-cooling, meaning that lower mass galaxies are forming too many stars for their halo mass. The third Chapter will present results from the NIHAO, suite of state-of-the-art zoom-in cosmological hydrodynamical simulations. This suite does not suffer from the

same over-cooling, as such, lower mass galaxies are able to be investigated. The fourth Chapter will present five galaxies from the suite of simulations presented in the previous Chapter in more detail. The fifth Chapter will summarize the results and present the conclusions.

Chapter 2

The tilting rate of the Milky Way's disc

This chapter was published as Earp S. W. F., Debattista V. P., Macciò A. V., Cole D. R., 2017, MNRAS, 469, 4095.

Abstract

We present tilting rates for galaxies comparable to the Milky Way (MW) in a Λ cold dark matter cosmological hydrodynamical simulation, and compare these with the predicted tilting rate detection limit of the *Gaia* satellite $0.28^\circ\text{Gyr}^{-1}$. We first identify galaxies with mass comparable to the MW ($9 \times 10^{11} \leq M_{200} \leq 1.2 \times 10^{12} M_\odot$) and consider the tilting rates between $z = 0.3$ and 0. This sample yields a tilting rate of $7.6^\circ \pm 4.5^\circ\text{Gyr}^{-1}$. We constrain our sample further to exclude any galaxies that have high stellar accretion during the same time. We still find significant tilting, with an average rate of 6.3°Gyr^{-1} . Both sub-samples tilt with rates significantly above *Gaia*'s predicted detection limit. We show that our sample of galaxies covers a wide range of environments, including some similar to the MW's. We find galaxies in denser regions tilt with higher rates than galaxies in less dense regions. We also find correlations between the angular misalignment of the hot gas corona, and the tilting rate. *Gaia* is likely to be able to directly measure tilting in the MW. Such a

detection will provide an important constraint on the environment of the MW, including the rate of gas cooling onto the disc, the shape and orientation of its dark matter halo, and the mass of the Large Magellanic Cloud. Conversely, failure to detect tilting may suggest the MW is in a very quiet configuration.

2.1 Introduction

Disc galaxies such as the Milky Way (MW) are rapidly rotating; the orientation of their spin axis represents the integral of the angular momentum accreted via gas, interactions with satellites or other galaxies, and torques exerted on the disc by the dark matter halo within which they reside. Therefore directly observing disc tilting at the present time provides clues to the nature of each of these processes. The *Gaia* space astrometry mission may soon allow direct measurement of the MW's disc tilting rate. Precision measurements will enable the construction of stellar position catalogues with accuracies of order $20\mu\text{as}$ with respect to distant quasars, which act as the measurement reference frame (Lindgren et al., 2008; Perryman et al., 2001). Perryman et al. (2014) estimate that an accuracy better than $1\mu\text{as yr}^{-1}$ should be achieved in all the inertial spin components of the *Gaia* reference frame, corresponding to $0.28^\circ\text{Gyr}^{-1}$.

Galaxies tilt for a variety of reasons. The role of interactions in disc tilting has been studied extensively. While major mergers destroy discs, smaller scale interactions are less violent, and tilt disc galaxies. Huang and Carlberg (1997) showed that infalling satellites tilt discs so that there is a preference for infalling satellites to merge in the plane of the disc. Read et al. (2008) reached a similar conclusion. Bett and Frenk (2012) investigated the effects of minor mergers and flybys on the orientation of spins of dark matter haloes of mass ($12.0 \leq \log_{10}(M/M_\odot)h^{-1} \leq 12.5$) at $z = 0$. They found that the majority of these events only caused small changes in the angular momentum of the entire halo, with only 10.5 per

cent of MW mass haloes experiencing changes in their angular momentum by more than 45° over the course of their lifetimes. However, the inner halo is not so stationary, with 47 per cent of inner haloes experiencing a large change in their angular momentum orientation of at least 45° during their lifetimes. Bett and Frenk (2016) extended this study to include a broader range of halo masses ($10.5 \leq \log_{10}(M/M_\odot)h^{-1} \leq 15.5$). They found that 35 per cent of haloes had experienced changes in orientation of at least 45° , at some point in their lifetimes, without a major merger taking place.

In the MW, the most important ongoing interaction is with the Large and Small Magellanic Clouds (LMC and SMC). The mass of the LMC is as high as $M_{\text{LMC}} \sim 2 \times 10^{11} M_\odot$ (Gómez et al., 2015; Kallivayalil et al., 2013; Peñarrubia et al., 2016), corresponding to ~ 20 per cent of the mass of the MW, making it the most important interaction in some time.

Another cause of disc tilting is torques from dark matter haloes. In the Λ -cold dark matter (Λ CDM) paradigm, haloes grow hierarchically, becoming triaxial (Allgood et al., 2006; Bailin and Steinmetz, 2005; Bardeen et al., 1986; Barnes and Efstathiou, 1987; Dubinski and Carlberg, 1991b; Frenk et al., 1988; Jing and Suto, 2002). These triaxial haloes are themselves tilting (Moore et al., 2004). Dubinski (1992) examined the effect of tidal shear on dark matter haloes; he found that in all 14 of his $(1\text{--}2) \times 10^{12} M_\odot$ haloes the major axis rotated uniformly around the minor axis with a rotation rate in the range of $6^\circ\text{--}96^\circ\text{Gyr}^{-1}$. Likewise Bailin and Steinmetz (2004) measured figure rotation in 288 of their 317 dark matter haloes, finding a tilting rate of 6.2°Gyr^{-1} with a log-normal distribution having $\sigma = 0.58^\circ\text{Gyr}^{-1}$. Bryan and Cress (2007) found that 63 per cent of the 115 haloes they considered exhibited significant figure rotation, with an average pattern speed of $13.8^\circ h \text{Gyr}^{-1}$.

The figure rotation of triaxial haloes leads to time varying torques on discs. Debattista et al. (2015) showed that a stellar disc, lacking gas, within a triaxial halo aligns its spin axis

with the minor axis of the halo. Even when perturbed by a satellite the disc settles back to this alignment. Thus a tilting halo will drag a disc along with it. Yurin and Springel (2015) inserted live stellar discs into eight, MW-sized, high-resolution dark matter haloes from the AQUARIUS simulation. They found typical tilting rates of $5^\circ\text{--}6^\circ\text{Gyr}^{-1}$, comparable with halo tilting rates. While no direct evidence of tilting haloes exists, tidal torques exerted on a stellar disc by a rotating dark matter halo have been explored as a possible cause for warps (Dubinski and Chakrabarty, 2009; Dubinski and Kuijken, 1995) and as a driving mechanism for spiral structure in dark matter-dominated galaxies (Bureau et al., 1999).

Galaxies such as the MW are generally thought to be surrounded by hot gas coronae, with masses greater than the stellar disc itself (e.g. Dahlem, 1997; Fukugita and Peebles, 2006; Savage and de Boer, 1979; Spitzer, 1956; Wang et al., 2001; White and Frenk, 1991; White and Rees, 1978). The quiescent cooling of this hot gas then sustains star formation over a long time (Brook et al., 2004; Brooks et al., 2009; Fall and Efstathiou, 1980b; Kereš et al., 2005; Robertson et al., 2006). However, the angular momentum of coronae is usually misaligned with that of their embedded stellar disc (Roškar et al., 2010; van den Bosch et al., 2002). This contributes misaligned angular momentum to the disc, causing its orientation to change. Debattista et al. (2015) showed that under these circumstances, the orientation of the disc spin is determined by a balance between the torques from the triaxial dark matter halo, and the net inflow of angular momentum via cooling gas. As a result, star forming galaxies are generally misaligned with the main planes of their dark matter haloes (Agustsson and Brainerd, 2006; Azzaro et al., 2007; Brainerd, 2005; Faltenbacher et al., 2007; Li et al., 2013; Nierenberg et al., 2011; Sales and Lambas, 2004; Wang et al., 2010, 2008; Yang et al., 2006). Debattista et al. (2013) argued for just such an orientation in the MW, by noting that the best fitting models for the Sagittarius Stream (Deg and Widrow, 2013; Law and Majewski, 2010; Law et al., 2009) require the disc spin to be along the halo's intermediate axis, an orientation they showed is extremely unstable. Debattista et al. (2013) therefore, ar-

2.2 Numerical Simulation (VICTOR)

gued that the modelling assumption of the disc residing in one of the symmetry planes must be violated. While this is indirect evidence, stacking of external galaxies has shown that the distribution of satellites around blue galaxies tends to be isotropic, contrary to what is seen around red galaxies (Brainerd, 2005; Dong et al., 2014; Nierenberg et al., 2011; Sales and Lambas, 2004; Wang et al., 2008, 2014; Yang et al., 2006). Moreover, Vera-Ciro and Helmi (2013) argue that the effect of the LMC on the shape of the halo must be taken into account.

In summary in the MW, the disc may be tilting for a variety of reasons. As a first step towards understanding the tilting of the MW, in this paper, we measure the tilting rates of MW-like galaxies in a Λ CDM cosmological simulation. We compare the tilting rates of these discs to the observational limit of *Gaia* to establish whether tilting of this nature would be detectable. In Section 2.2, we describe the cosmological simulation. Then in Section 2.3, we describe the samples of galaxies selected on the basis of virial mass, merger history and total satellite mass. In Section 2.4, we describe the methods we use to calculate the tilting rates. Section 2.5, presents the results, and provides a comparison with the observational limit of *Gaia* for a variety of different local configurations and environments. We present our conclusions in Section 2.6, showing that even galaxies in quiet systems tilt at a rate that would be detectable by *Gaia*.

2.2 Numerical Simulation (VICTOR)

The simulation we use here was performed with GASOLINE, a multi-stepping, parallel, tree code with smoothed particle hydrodynamics (SPH) (Wadsley et al., 2004). The version of GASOLINE used for this work includes radiative and Compton cooling for a primordial mixture of hydrogen and helium. The star formation algorithm is based on a Jeans instability criterion (Katz, 1992), but simplified so that gas particles satisfying constant density, and temperature thresholds in convergent flows spawn star particles at a rate proportional to the

local dynamical time (see Stinson et al., 2006). The star formation efficiency was set to 0.05 based on simulations of the MW that satisfied the Schmidt–Kennicutt Law (Kennicutt, 1998; Schmidt, 1959b), and we adopt a star formation threshold of 0.1 particles per cubic centimetre. The code also includes supernova feedback using the blast-wave formalism as described in Stinson et al. (2006), and a UV background following Haardt and Madau (1996); see Governato et al. (2007) for a more detailed description.

We used as a starting simulation one of the cosmological cubes described in Macciò et al. (2008), namely our box has a size of 180Mpc and contained 300^3 dark matter particles. This box was created using WMAP5 (Komatsu et al., 2009) initial conditions with $(h, \Omega_M, \Omega_L, \Omega_b, \sigma_8) = (0.72, 0.258, 0.742, 0.0438, 0.796)$ and was run with the code PKDGRAV as detailed in Macciò et al. (2008).

From this simulation we selected at $z = 0$ a volume of about $(25 \text{ Mpc})^3$ with the requirement of not containing any haloes with a virial mass above $5 \times 10^{12} M_\odot$. For this purpose we use the halo catalogue from Macciò et al. (2008) which was generated using a Spherical Overdensity halo finder algorithm. The choice of this particular mass threshold is motivated by our interest in studying the properties of galaxies with a total mass equal or lower than the MW.

We then traced back to the initial conditions the Lagrangian region defined by this redshift-zero volume, making sure to obtain a continuous region (i.e. no holes) at the initial redshift ($z = 99$). Finally, we used the standard zoom-in technique to enhance the resolution of the dark matter particles in the selected region by a factor of 10^3 , and adding baryons (gas particles) with the same high resolution. As a final result, this high resolution region contains more than 10^8 particles, and reaches a mass resolution of 6.6×10^6 and $1.1 \times 10^6 M_\odot$ for dark matter and gas, respectively, with a gravitational softening length of 1.24 kpc for dark matter and 0.5 kpc for gas.

We then used the GASOLINE code described above to evolve these new high resolution

initial conditions from $z = 99$ to 0 taking into account gas cooling, star formation and feedback in a self consistent way. To generate the catalogue of virially bound haloes we use the grid based code AMIGA Halo Finder (Knollmann and Knebe, 2009) on the simulation outputs.

2.3 The Samples

We identify 182 haloes spanning the mass range $9 \times 10^{10} - 4.4 \times 10^{12} M_{\odot}$. Of the 41 saved time steps during the time interval $z = 0.3$ to 0 we use a subset of ten time steps with an average separation of ~ 0.37 Gyr to determine the stellar mass fractional growth rate, and to track the merger history of each galaxy. We calculate the tilting rate once for each galaxy, by measuring the angular momentum within 5 per cent of the virial radius at $z = 0.3$ and 0.

Subsample VICTOR:A contains haloes within a specified mass range comparable to the MW. The motivation for this mass cut is two-fold. First, we are interested in galaxies with similar halo mass as the MW. Secondly, we wish to choose galaxies where the mass of the dark matter halo, and the stellar mass are in good agreement with abundance matching results. We impose an upper limit of $M_{200} \leq 1.2 \times 10^{12} M_{\odot}$ in order to constrain the sample to a mass range that is comparable with the virial mass of the MW (Klypin et al., 2002). We also find that above this limit the full sample is dominated by ellipticals that, due to their evolutionary history, generally have lower specific angular momentum. Fig. 2.1 compares the halo mass–stellar mass relation of the full sample with the relation derived by the abundance matching method of Kravtsov et al. (2014). This figure shows that galaxies residing within haloes of mass $M_{200} \geq 9 \times 10^{11} M_{\odot}$ in the simulation match this relationship well. Lower mass haloes, however, have an excess stellar mass. Therefore, we use this mass as a lower limit for subsample VICTOR:A. Implementing the mass range $1.2 \times 10^{12} \geq M_{200} \geq 9 \times 10^{11} M_{\odot}$ leaves 19 galaxies in subsample VICTOR:A.

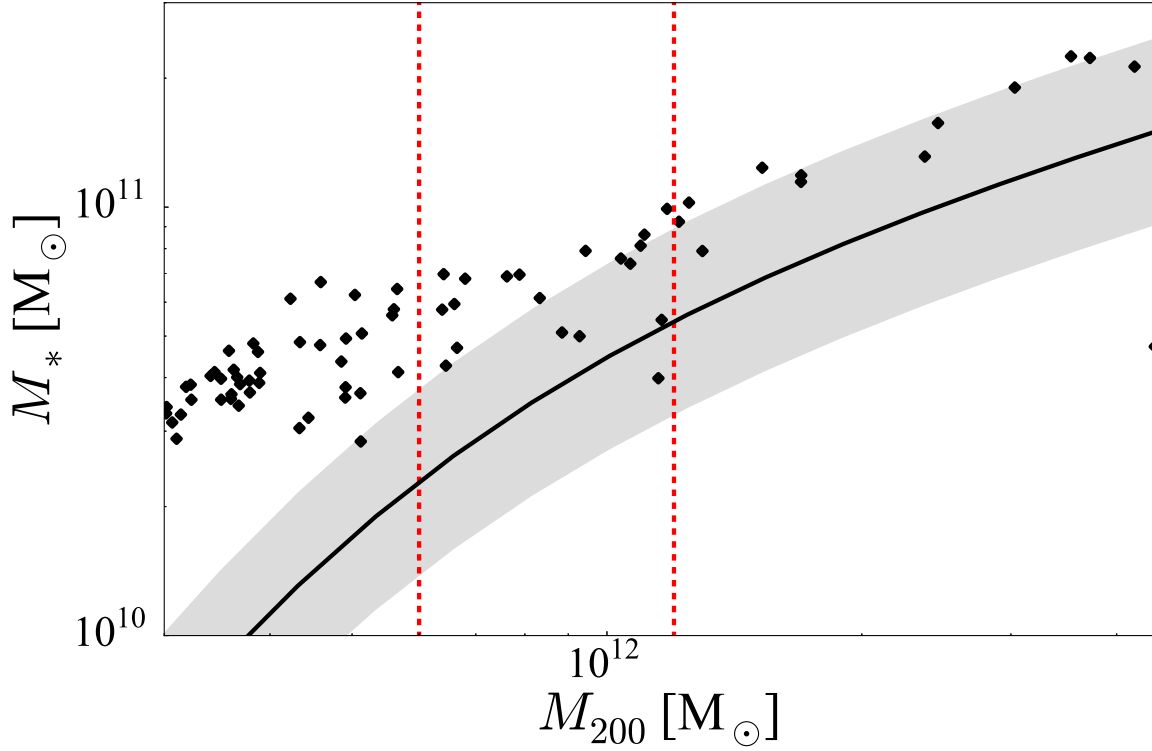


Fig. 2.1 Stellar mass versus halo mass at redshift $z = 0$ for the most massive galaxies in the initial sample (black points). We measure the stellar mass within 5 per cent of the virial radius (r_{200}), where the mean interior density is 200 times the critical density. For comparison the black line shows the M_* - M_{200} relation of Kravtsov et al. (2014) derived using halo abundance matching. The grey shaded region shows the scatter in this relation. The red dashed lines illustrate the bounds that subsample VICTOR:A lies within.

2.3 The Samples

Subsample VICTOR:B has the same mass constraint with two added limits: one on the change in stellar mass to remove galaxies that have undergone mergers above a certain mass ratio, and the second on the ratio of galaxy mass to total satellite mass. First, we observe the evolution of the galaxies by visual inspection to construct a catalogue of galaxies that have not undergone mergers between $z = 0.3$ and 0. By comparing this catalogue to the full sample we can constrain the rate of change in stellar mass such that above this limit the sample is dominated by galaxies that have undergone mergers. Fig. 2.2 shows the distribution of fractional growth rates for galaxies that do not undergo mergers and the full sample. From Fig. 2.2 we set an upper limit on the maximum stellar mass fractional growth rate of 0.16Gyr^{-1} within 5 per cent of the virial radius, under which galaxies have not undergone significant minor or major mergers. We construct subsample VICTOR:B from subsample VICTOR:A with the added constraint that $\Delta M_*/(\langle M_* \rangle \Delta t)$ must fall below this value. Two galaxies that fell below this limit were observed undergoing a minor merger, however, the maximum stellar mass accreted was roughly one per cent that of the central galaxy so they are included in subsample VICTOR:B. Lastly, we stipulate that the total satellite stellar mass must be less than 40 per cent that of the central galaxy at every time step. To measure the total satellite mass we subtract the total stellar mass within $0.1r_{200}$, where r_{200} is the virial radius, from the total stellar mass inside r_{200} . This leaves us with just seven galaxies in subsample VICTOR:B.

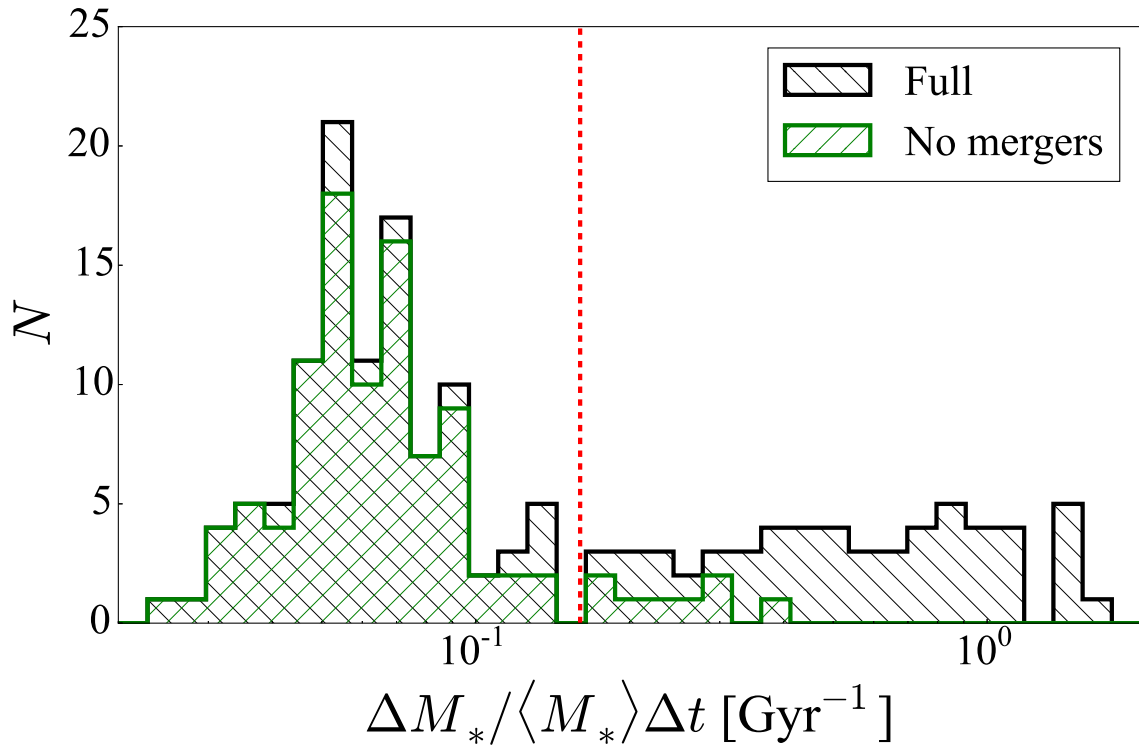


Fig. 2.2 Distribution of the maximum rate of change in stellar mass normalized by average stellar mass between t_i and t_{i+1} within 5 per cent of the virial radius. The black histogram shows the rates for the full sample of 182 haloes. The green histogram shows the distribution of rates for galaxies that did not undergo any mergers between $z = 0.3$, and 0. The red dashed line indicates the upper limit we impose on subsample VICTOR:B.

2.4 Analysis

To derive accurate tilting rates, we first find the kinematic centres of the galaxies. We adopt the position of the lowest potential dark matter particle as our kinematic centre. We verify that this method is reliable by computing the kinematic centre using an iterative shrinking sphere method. Starting with a sphere of 200 kpc, we iterate centring on the centre of mass and halving the radius each step to a final value of ~ 10 pc. Using the lowest potential dark matter particle, we are able to obtain kinematic centres for our entire sample of 182 galaxies.

We then measure the angular momentum of the galaxy by summing the angular momentum of each star particle within $R < 0.05r_{200}$. This radius is selected to include the disc of the galaxy, but exclude any warps. Briggs (1990) found that warps become detectable within the Holmberg radius (R_{Ho}). For a typical virial radius of ~ 200 kpc, we would expect a Holmberg radius of ~ 15 kpc, 5 kpc greater than the radius we would consider for $0.05r_{200} \sim 10$ kpc. We also select this radius to avoid selecting just the bulges of our galaxies, which tend to have lower specific angular momentum.

In order to determine the uncertainty in the tilting rates, we measure the difference in the direction of the angular momentum vector at different radii. We measure the angular momentum at seven linearly spaced radii spanning $0.01 < R/r_{200} < 0.04$. We then use the average angular discrepancy between the vectors as the error (σ) on the measurement of the angular momentum vector, and hence on the tilting rate. For each of these errors we assign a weight w such that $w = 1/\sigma^2$, which will be used in the calculation of the mean and standard deviation of each subsample.

2.5 Results

2.5.1 Tilting rates

First we consider subsample VICTOR:A, i.e. galaxies with virial mass comparable to the MW's, within the range $9 \times 10^{11} \leq M_{200} \leq 1.2 \times 10^{12} M_{\odot}$. We measure the tilting rate once, between the two time steps $z = 0.3$ and 0 . This subsample tilts with a mean rate of $7.6^{\circ}\text{Gyr}^{-1}$, and a standard deviation of $4.5^{\circ}\text{Gyr}^{-1}$, well above the average error for this subsample of just $0.05^{\circ}\text{Gyr}^{-1}$. All 19 of the galaxies in this subsample exhibit significant tilting above *Gaia*'s detection limit of $0.28^{\circ}\text{Gyr}^{-1}$ (Perryman et al., 2014).

Next we consider subsample VICTOR:B, i.e. the galaxies with similar mass to the MW, that have low fractional stellar mass change from $z = 0.3$ to $z = 0$, and have a maximum total satellite mass of 40 per cent that of the central galaxy. Fig. 2.3 shows tilting rates for sample VICTOR:B versus the ratio of stellar mass to satellite stellar mass. Each data point in this figure corresponds to a tilting rate of a single galaxy, with the mass ratio measured at $z = 0$. The green squares show only the five galaxies that were not observed to undergo any mergers since $z = 0.3$, while the black squares were the two galaxies that did undergo a minor merger within the same time. The tilting rates of this subsample have an average of $6.3^{\circ}\text{Gyr}^{-1}$, with a standard deviation of $6.5^{\circ}\text{Gyr}^{-1}$, well above the average uncertainty of $0.13^{\circ}\text{Gyr}^{-1}$. This subsample VICTOR:Also tilts with a rate well above *Gaia*'s detection limit.

2.5.2 Environmental dependence

To determine if there is any dependence between the tilting rates of galaxies and their local environment, we compare the tilting rates of the galaxies with their normalized local density. We calculate the density within various radii centred on each galaxy, and then normalize by the critical density at $z = 0$. Fig. 2.4 shows the distribution of densities for spheres with

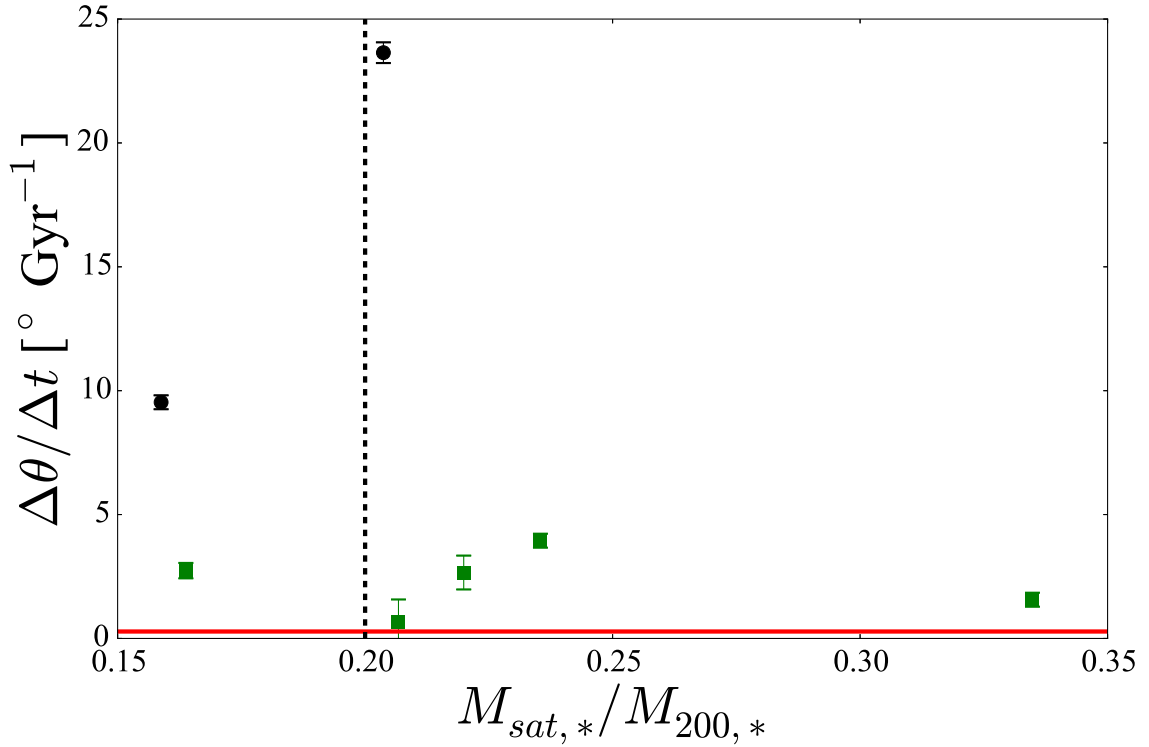


Fig. 2.3 Tilting rate versus the present day fraction of satellite to galaxy stellar mass ($M_{\text{sat},*}/M_{200,*}$) for subsample VICTOR:B, i.e. galaxies that have mass comparable to the MW, and have low fraction stellar mass change between $z = 0.3$ and 0. The (green) squares represent the galaxies that were observed to not have undergone any mergers since $z = 0.3$, the (black) circles show the galaxies that undergo a minor merger. The black dashed line shows recent estimates of the mass ratio of the LMC relative to the MW (Gómez et al., 2015; Kallivayalil et al., 2013; Peñarrubia et al., 2016). The red horizontal line is *Gaia*'s predicted detection limit (Perryman et al., 2014).

radii 3,4,5 and 6 Mpc. We find that for large radii (5 and 6 Mpc) that there is a strong correlation for subsample VICTOR:A with p values of 0.8 for both, although, for smaller radii (3 and 4 Mpc), the correlation weakens, with p values of 0.2 and 0.6 respectively. When we consider subsample VICTOR:B the correlations are enhanced, with p values of 0.7,0.95,0.97 and 0.96 for radii 3,4,5 and 6Mpc, respectively.

The MW has a close massive neighbour M31 within 1 Mpc. We compare the tilting rates with the distance D to the nearest massive ($M_* > 9 \times 10^{11} M_\odot$) galaxy in subsample VICTOR:A. Fig. 2.5 shows the tilting rate versus D ; galaxies in subsample VICTOR:A span a range of D , including some with very close neighbours and some very isolated. We see no relation between D and the tilting rate. Considering galaxies in subsample VICTOR:B we do find a weak anti-correlation. One of our galaxies does appear to be tilting extremely fast without a close neighbour.

2.5.3 Dependence on gas

The angular momenta of the hot gas corona surrounding a galaxy and of the disc are not generally aligned. As the gas corona continually feeds cool gas to the disc, this misalignment causes gas being accreted to change the angular momentum of the disc. To investigate this effect on the tilting rate, we define the hot gas corona in two different ways. In the first, we choose all gas with a temperature $T > 5 \times 10^4 \text{K}$, and in the second, we choose all gas between two spherical shells of radii $0.2r_{200}$ and r_{200} . The angular momentum calculated from each definition is in good agreement, with $p = 0.99$. We compare the tilting rates of the hot gas corona to the tilting rate of the disc for both of these methods. Fig. 2.6 shows that for both methods of defining the corona, there is no correlation between the angular momentum tilting rate of the corona and disc for MW mass galaxies. Even when we consider subsample VICTOR:B, we find no correlation for both methods.

Next we compare the tilting rates of the disc to the angular misalignment between the

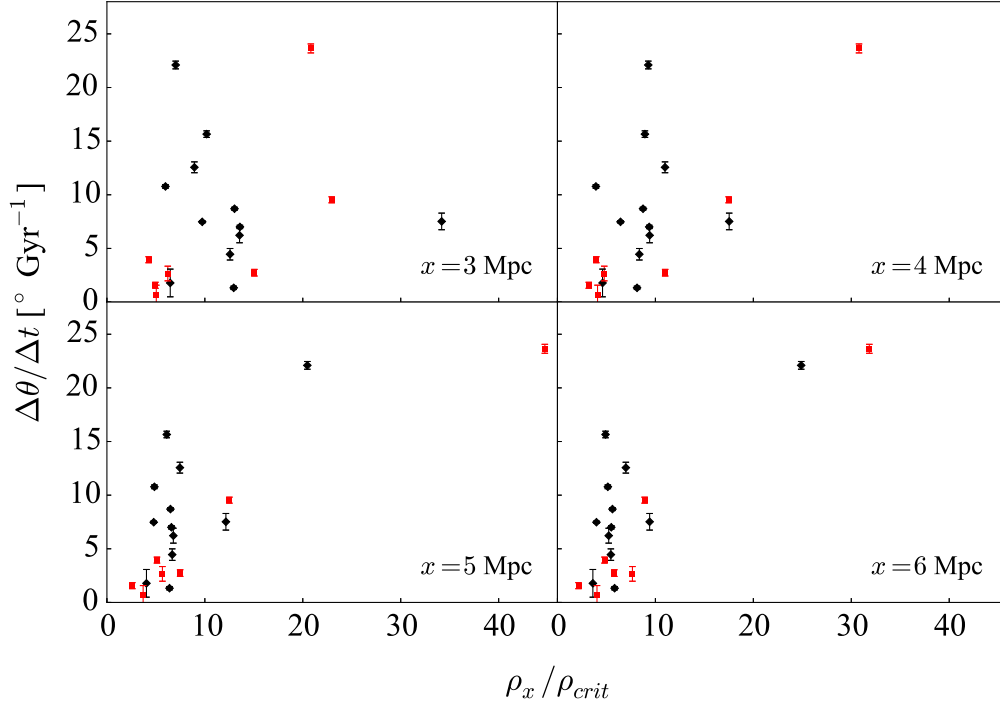


Fig. 2.4 Tilting rate versus the local density within a sphere of radius x at redshift $z = 0$. In all panels, the (black) diamonds represent galaxies in subsample VICTOR:A with masses comparable to the MW, and the (red) squares show galaxies in subsample VICTOR:B with comparable mass and undergoing no interactions since $z = 0.3$. We measure correlation coefficients for each panel $x = 3, 4, 5$ and 6 Mpc of $p = 0.2, 0.6, 0.8$ and 0.8 , respectively, for all points, while for subsample VICTOR:B, we find p values of $0.7, 0.95, 0.98$ and 0.97 , respectively.

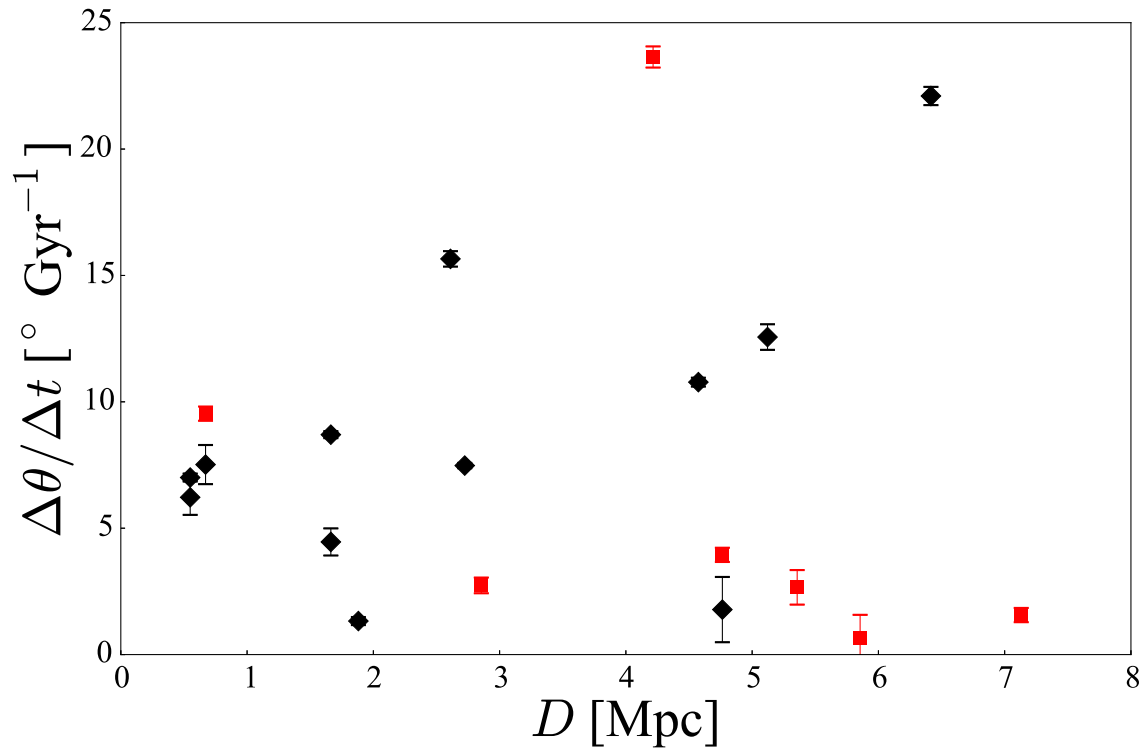


Fig. 2.5 Tilting rate versus distance D to nearest galaxy with comparable mass to the MW measured at $z = 0$. The (black) diamonds represent subsample VICTOR:A and the (red) squares show subsample VICTOR:B. We find a correlation coefficient of $p = -0.05$ for subsample VICTOR:A and $p = -0.3$ for subsample VICTOR:B.

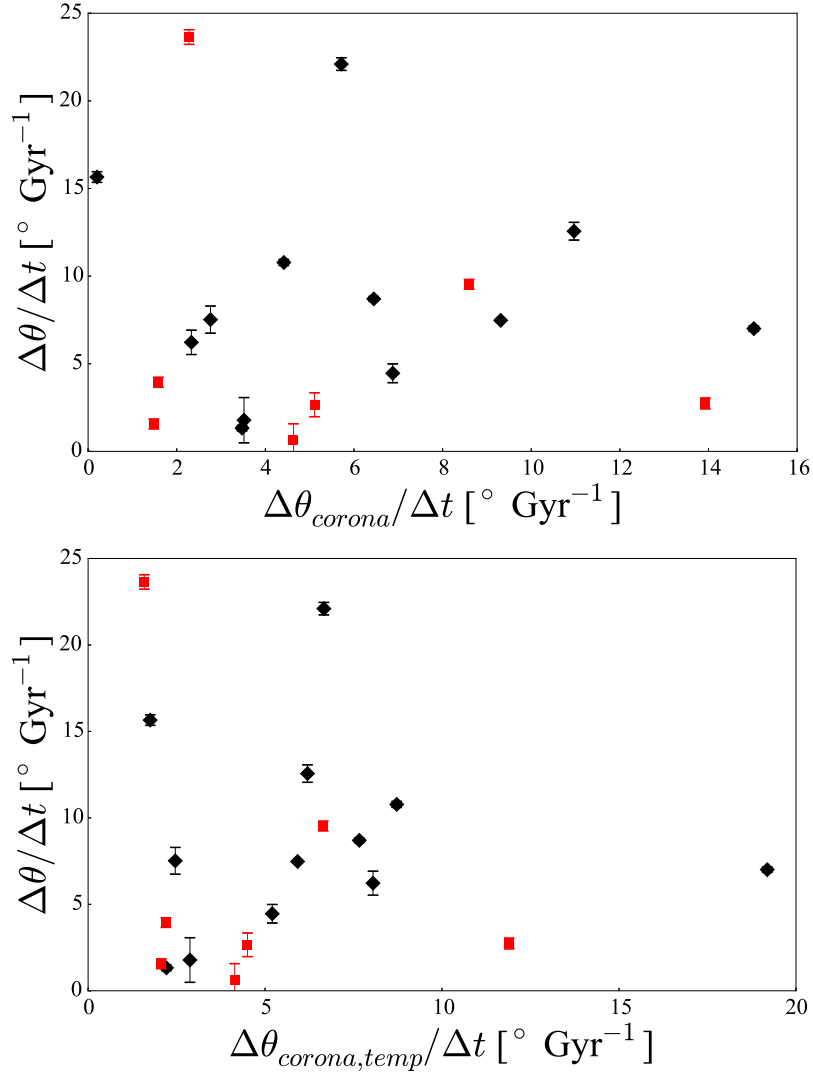


Fig. 2.6 Top panel: The tilting rate of the stellar disc versus the tilting rate of the corona, defined as all gas between radii $0.2r_{200}$ and r_{200} . We find no correlation for subsample VICTOR:A (black diamonds) with a coefficient of $p = -0.08$. For subsample VICTOR:B (red squares) we find no correlation with $p = -0.18$. Bottom panel: The tilting rate of the stellar disc versus the tilting rate of the corona, defined as all gas with a temperature $T > 5 \times 10^4$ K. We find no significant correlation for subsample VICTOR:A (black diamonds), with $p = -0.035$. Similarly for subsample VICTOR:B (red squares) we find no correlation, with $p = -0.27$.

disc and the hot gas corona for both methods of defining the hot gas corona. Figure 2.7 shows the relation between the tilting rates of discs and the angular misalignment of the hot gas corona and disc angular momentum. We find a weak correlation with p values of 0.4 and 0.5 for both methods, respectively, for subsample VICTOR:A. However, for subsample VICTOR:B, the correlation strengthens considerably for both methods with p values of 0.86 and 0.87.

The large-scale structure (LSS) may influence the flow of gas into the halo and subsequently the misalignment between the stellar and coronal angular momentum. When we compare the misalignment of the hot gas corona from the stellar disc with the normalized local density, we find similar correlations as those we found in Fig. 2.4. Therefore it is not possible to determine from this simulation if the effect of the environment directly governs the tilting of the galaxy, or if the LSS affects the tilting via its effect on the coronal angular momentum, as seems likely. Debattista et al. (2015) found that galaxies lacking gas generally aligned with the minor axis of their halo. However, when gas is allowed to cool on to the disc, the orientation can be more arbitrary. For both of our subsamples, we find that galaxies with higher star formation generally tilt with higher rates. These results favour the gas driven tilting scenario.

When we compare the angular momentum misalignment between the disc and the gas corona with the local density, we find similar correlations as those in Fig. 2.4. Thus the mechanism by which the LSS affects the disc's tilting rate is unclear. The LSS may torque the disc directly, or it may influence the flow of gas into the halo, driving the misalignment between the stellar and coronal angular momentum, which in turn drives the tilting (e.g. Debattista et al., 2015). One possible clue comes from comparing the tilting and the star formation rate. For both of our subsamples, we find that galaxies with a higher star formation rate generally tilt faster, suggesting that it is the delivery of misaligned angular momentum through gas that dominates the tilting.

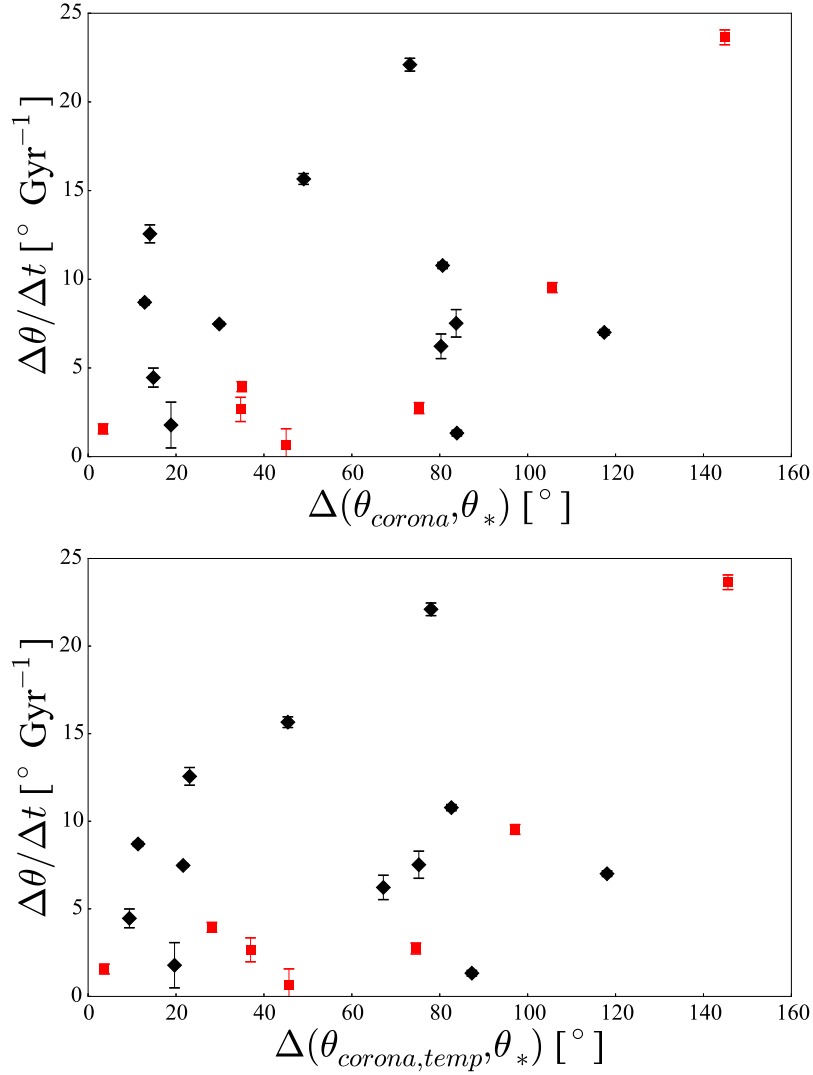


Fig. 2.7 Top panel: The tilting rate of the stellar disc versus the angular difference in angular momentum orientation between the stellar disc and the hot gas corona, defined as all gas between radii $0.2r_{200}$ and r_{200} . We find a weak correlation for subsample VICTOR:A (black diamonds), with $p = 0.4$, and a strong correlation for subsample VICTOR:B (red squares), with $p = 0.86$. Bottom panel: The tilting rate of the stellar disc versus the difference in orientation between the stellar disc and the hot gas corona, defined as all gas with temperature $T > 5 \times 10^4$ K. We find a weak correlation for subsample VICTOR:A (black diamonds) with $p = 0.5$, and a strong correlation for subsample VICTOR:B (red squares) with $p = 0.87$.

2.6 Discussion and Conclusions

When we consider galaxies with halo masses comparable to the MW (subsample VICTOR:A), we find significant tilting with an error weighted mean rate of 7.6°Gyr^{-1} and a standard deviation of 4.5°Gyr^{-1} . The entire subsample displays significant tilting with rates higher than the detection limit of *Gaia*. We further restrict to a sample with low relative stellar accretion, and a maximum stellar mass fraction in satellites of 40 per cent (subsample VICTOR:B), finding a lower mean tilting rate of 6.2°Gyr^{-1} , with a range from 0.65 to $24.6^\circ\text{Gyr}^{-1}$.

A variety of processes may drive the change in angular momentum that we have measured. Interactions with other galaxies are the most violent processes changing the angular momentum of discs drastically over a short period. However, we have found that even when we exclude strong interactions we still measure significant tilting above the detection limit of *Gaia*. Therefore, we must turn to processes such as halo torques and the accretion of misaligned cold gas on to the disc to explain the entire phenomena of disc tilting.

We investigated the effect of the local environment on the tilting rate of the disc. Comparing the local density against the tilting rate, we find that the tilting rate does not correlate with the normalized local density within 3Mpc for subsample VICTOR:A. However, for subsample VICTOR:B, we do find a correlation. When we consider larger radii, we find a correlation between the tilting rate and the local environment for both subsamples. Galaxies in denser regions generally tilt at higher rates than galaxies in lower density regions, irrespective of the galaxies stellar mass accretion.

The MW has a very close, similar mass, neighbour M31. In order to compare to the MW's configuration, we measured the distance to the nearest massive galaxy and determined the correlation with the tilting rates. We find almost no correlation for subsample VICTOR:A; however, for subsample VICTOR:B, we do find very weak anti-correlation. This suggests that the local configuration is unlikely to be a large contributing factor when the

2.6 Discussion and Conclusions

disc is accreting significant mass. Our sample contains galaxies in similar configurations to the MW with companion galaxies within a few hundred kpc; these galaxies exhibit tilting rates similar to more isolated galaxies.

To determine the effect of misaligned gas accreting from the hot gas corona, we measured both the tilting rate of the hot gas corona and the angular misalignment between the stars and the corona. We find no correlation between the tilting rates of the two different components for either subsample. We also compared the tilting rate of the disc to the angular momentum misalignment between the two components: For subsample VICTOR:A, there is a weak correlation, which becomes stronger for subsample VICTOR:B. We also find a correlation between the misalignment of the disc and coronal angular momentum and the LSS. Thus, the LSS may directly affect the tilting rate via torques, or indirectly by influencing the flow of gas into the halo. For both subsamples, galaxies with higher star formation tilt faster, perhaps indicating that the role of the LSS is in driving the misaligned gas. We conclude that the angular momentum misalignment between the corona and disc is an important, possibly dominant, driver of disc tilting.

In this chapter, we have measured the tilting rates for a wide variety of galaxies of similar mass to the MW, in various configurations, some similar to the local configuration of the MW. Every configuration yielded a tilting rate above the *Gaia* limit and should be detectable. Confirmation of a tilting disc would have important consequences for understanding the evolution of the MW. For example, the tilt of the disc will make the potential seen by the Sagittarius Stream time varying. Conversely failure to detect tilting may suggest the MW is in an unexpectedly quiet configuration.

Chapter 3

NIHAO: Tilting discs in cosmological zoom-in simulations

3.1 NIHAO: a Numerical Investigation of a Hundred Astrophysical Objects

3.1.1 Brief Introduction

The NIHAO project offers a sample of high resolution hydrodynamical simulation within a cosmological context. Wang et al. (2015) present the sample of galaxies and give a detailed description of the simulation techniques implemented in its creation, as well as comparing the sample with observations. This section gives an overview of the NIHAO project.

The sample

As the name suggests the sample contains a hundred galaxies. The halo and stellar masses span the ranges $5 \times 10^9 < M_{200}/M_{\odot} < 3 \times 10^{13}$ and $5 \times 10^4 < M_{*}/M_{\odot} < 2 \times 10^{11}$, respectively. Haloes were drawn from three cosmological simulations, two with box widths 60

x -axis	p value
M_*	-0.29
$\Delta M_{\max,*}/\langle M_* \rangle \Delta t$	0.73
$\Delta M_{\max,b}/\langle M_b \rangle \Delta t$	0.43
b/a	-0.42
c/a	-0.43
T	0.06
$\theta(*, \text{major})$	0.12
$\theta(*, \text{intermediate})$	0.3
$\theta(*, \text{minor})$	0.19
$\rho_{r=3,4,5,6\text{Mpc}}/\rho_{\text{crit}}$	0.59, 0.63, 0.65, 0.86
$\theta(*, \text{corona})$	0.21
$\Delta\theta_{\text{corona}}/\Delta t$	0.052
$\theta(*, \text{gas})$	0.45
sSFR	0.77
$\langle \text{sSFR} \rangle$	0.9
$M_*/M_{*,200}$	-0.0064
M_*/M_g	-0.45
M_g^d/M_*	0.3
M_g^d/M_g	-0.19
$ L_* (t_0)$	0.27
$\Delta L_* $	-0.22
$\Delta L_* /\langle L_* \rangle$	0.33
$ L_{\text{cool}} (t_0)$	-0.36
$\Delta L_{\text{cool}} $	-0.25
$\Delta L_{\text{cool}} /\langle L_{\text{cool}} \rangle$	-0.39
$ L_{\text{cold}} (t_0)$	-0.35
$\Delta L_{\text{cold}} $	-0.25
$\Delta L_{\text{cold}} /\langle L_{\text{cold}} \rangle$	-0.44

Table 3.1 All error-weighted Pearson's correlation coefficients reported in this chapter, between the x -axis listed and the tilting rate of the stellar disc ($\Delta\theta/\Delta t$).

Component	Bland-Hawthorn and Gerhard (2016)
Total stellar mass M_*	$5 \pm 1 \times 10^{10} M_\odot$
Hot gas corona mass M_g^c	$2.5 \pm 1 \times 10^{10} M_\odot$
Cool gas disc mass M_g^d	$0.7 \times 10^{10} M_\odot$
Total gas mass M_g	$3.2 \times 10^{10} M_\odot$
Halo mass M_{200}	$1.1 \pm 3 \times 10^{12} M_\odot$
Virial radius R_{vir}	282 ± 30 kpc

Table 3.2 Recent values for different components of the Milky Way which will be used in this chapter.

and $20 h^{-1}$ Mpc (Dutton and Macciò, 2014) and one further simulation with a box size of $15 h^{-1}$ Mpc. All of the initial N-body simulations were run in with a flat Λ CDM cosmology with parameters from Planck Collaboration et al. (2014): Hubble constant $H_0 = 67.1$ km s $^{-1}$ Mpc $^{-1}$, matter density $\Omega_m = 0.3175$, dark energy density $\Omega_\Lambda = 1 - \Omega_m - \Omega_r = 0.6824$, radiation density $\Omega_r = 0.00008$, baryon density $\Omega_b = 0.049$, power spectrum normalization $\sigma_8 = 0.8344$, and power spectrum index $n = 0.9624$. All haloes with masses $9.5 < \log_{10}(M_{200}/M_\odot) < 12.3$ were selected from each simulation. Haloes with neighbours containing more than one-fifth of the parent halo’s virial mass, within 3 virial radii, were rejected—this cut ensures the haloes are isolated. Because the mass range of the sample is so broad, Wang et al. (2015) set the dark matter resolution to be $N_{\text{dark}} \sim 10^6$ for each halo, ensuring a reliable mass profile down to 1 per cent of the virial radius, for the entire sample.

Hydrodynamics

The zoom-in simulations were run using the N-body Smooth Particle Hydrodynamics (SPH) code GASOLINE2 (Wadsley et al., 2017, 2004), with some modifications. Star formation following the Kennicutt-Schmidt law is allowed for gas particles with temperature $T < 15000$ K, and density $n_{th} > 10.3$ cm $^{-3}$. The star particles feed energy back into the ISM through the blast-wave supernova feedback formalism detailed in Stinson et al. (2006), as

well as stellar winds prior to the supernova described in Stinson et al. (2013). For NIHAO stellar winds feed 13 per cent of the total stellar energy, back into the ISM as 2×10^{50} erg of thermal energy per solar mass of the particle. This value was chosen to match the observed abundance matching relation from Behroozi et al. (2013). If a star particle has mass $8 < M_*/M_\odot < 40$ it will eject both its energy and metals into the surrounding gas particles around the formation point of the star particle. After being heated by a stellar wind the gas is able to cool via radiation, however, for the supernova itself, the cooling is delayed by ~ 30 Myr as the gas is very dense and is able to dissipate its energy too efficiently. For a full description see Wang et al. (2015).

Halo and galaxies

The haloes in the zoom-in simulations were identified using the AMIGA Halo Finder (AHF) (Gill et al., 2004; Knollmann and Knebe, 2009). AHF looks for peaks in the density field of the simulation, and tracks them over the course of the simulation. This results in merger trees that can be used to determine the building blocks of the dark matter haloes in the resulting time steps. Each halo has a mass M_{200} , which is taken to be the mass enclosed at the virial radius R_{200} , which is defined as the radius which contains a density 200 times greater than the critical density (see equation 1.1.20). This chapter will refer to the stellar mass M_* defined as the total mass of star particles enclosed by 10 per cent of the virial radius. Wang et al. (2015) compared the NIHAO sample to the observed abundance matching relationship from Behroozi et al. (2013); Kravtsov et al. (2014); Moster et al. (2013), finding that across the range of halo masses the stellar mass was in good agreement with observations. One caveat to this would be that the abundance matching results rely on the assumption of a single universal Milky Way IMF. The authors also compared the star formation rate and stellar mass of the NIHAO galaxies with observations, finding good agreement, although the observations are only able to probe higher mass galaxies. Most of the galaxies have

specific star formation rates (star formation rate divide by total stellar mass) $\gtrsim 0.1$, a value close to that estimated for the MW.

3.2 Sample Selection

At the time of this work 91 of the one hundred NIHAO simulations had reached $z = 0$. In order to measure the angular momentum of any system, it is vital that the centre of the system is correctly defined. To find the centre of each galaxy two different methods were used: a shrinking sphere, and the lowest potential particle. The shrinking sphere method followed the technique implemented by Power et al. (2003), an iterative technique to find the centre of an N-body simulation. At each step, the centre of the sphere is determined by the barycentre of the previous step, and the radius of the sphere is reduced by 2.5 per cent. This is iterated down to the smallest sphere containing at least 100 particles, at which point the centre of mass of this final sphere is returned. For the second technique, one can simply look for the dark matter particle with the lowest potential energy and use its position as the centre. Both these methods were also attempted in chapter 2, This chapter, found that the lowest potential dark matter particle obtained a reliable centre for most NIHAO galaxies. After removing galaxies where the centres were poorly determined the sample is reduced to 85 galaxies.

Measuring the angular momentum of the stellar disc was done by excluding older stars in the thick disc or halo by using only stars with ages < 1 Gyr. Then calculating the angular momentum of these young stars within a range of radii from 0.5 per cent of the virial radius out to 10 per cent of the virial radius in 0.5 per cent increments. This chapter will use the young stars within 5 per cent of the virial radius to determine the angular momentum of the stellar disc. This is motivated by that fact that radii less than 2 per cent of the virial radius sometimes resulted in a vector that was not aligned perpendicular to the plane of the disc,

3.2 Sample Selection

as one would expect. This misalignment might be due to the low angular momentum of the bulge. Further out the same problem was reproduced, however, this time of stars populating the warp were responsible. Determining the tilting rates was done by measuring the angle ($\Delta\theta$) between the angular momentum vectors of the stellar disc at t_i and t_{i+1} , and divided by the time difference $\Delta t = t_{i+1} - t_i$. The errors were obtained by measuring $\Delta\theta$ in annuli from two to five per cent of the virial radius,

$$\varepsilon = \max\{\Delta\theta(r_2, r_i), \quad r = 3, 4, 5\}. \quad (3.2.1)$$

This value was measured at $z = 0.3$ and again at $z = 0$, then summing these values in quadrature gives the final error. Any galaxy that has an error greater than 5° was removed, leaving 29 galaxies that had tilting rates with low errors.

As in chapter 2, this chapter is primarily interested in galaxies where the evolution is driven by gradual processes e.g. minor mergers and continual gas accretion. In galaxies where this evolution is dominant, the change in stellar mass should be driven by the star formation. As such one can compare the stellar mass change to the change in star formation to determine which process is dominant. However, the peak in star formation is not likely to be linked to the maximum change in the stellar mass of galaxies accreting satellites. Therefore, the comparison between the maximum change in stellar mass $\Delta M_*(t_{peak})/\langle M_* \rangle \Delta t$ to the specific star formation rate, sSFR, at the same time step t_{peak} is required. Figure 3.1 shows the resulting distribution, with the black line shows $x = y$, and the grey shaded region denoting where at least half of the stellar mass change could be attributed to the star formation rate. This plot separates the NIHAO sample (grey stars) into two subsamples, both the black and red (diamonds and squares) have well determined tilting rates, but the red (squares) are galaxies with masses greater than $M_{200} > 9 \times 10^{11} M_\odot$. In the unshaded region (galaxies where stellar accretion is dominant) only ~ 22 per cent of the galaxies have well determined tilting rates, whereas in the shaded region (galaxies where star formation

is dominant) 50 per cent of the galaxies have well determined tilting rates. Galaxies in the non-shaded region have gained a majority of stellar mass through accretion, and as such will have gained angular momentum, possibly resulting in tilting. This thesis is primarily concerned with tilting due to gradual processes, therefore, we will separate them.

Figure 3.2 shows sample NIHAO:A, all galaxies with well determine tilting rates (black diamonds) and a subsample of A, sample NIHAO:B (red squares), containing galaxies with masses $M_{200} > 9 \times 10^{11} M_{\odot}$. samples NIHAO:A and NIHAO:B contain no galaxies that have gained a majority of stellar mass through satellite accretion since $z = 0.3$. The green star indicates where the MW would lie on this figure. This estimate is calculated by subtracting the average type-II supernovae rate of 1.9 ± 1.1 per century (Diehl et al., 2006) times the integral of the Salpeter IMF (Salpeter, 1955) between the masses $M_* = 8 - 40 M_{\odot}$ from the Galaxy's sSFR rate (Licquia and Newman, 2015). For the MW this estimate predicts that ~ 30 per cent of the mass gained from star formation is lost due to supernovae, the red dashed line applies this offset to the one-to-one relationship (black line). The definitions of samples NIHAO:A and NIHAO:B used here will be continued throughout this chapter.

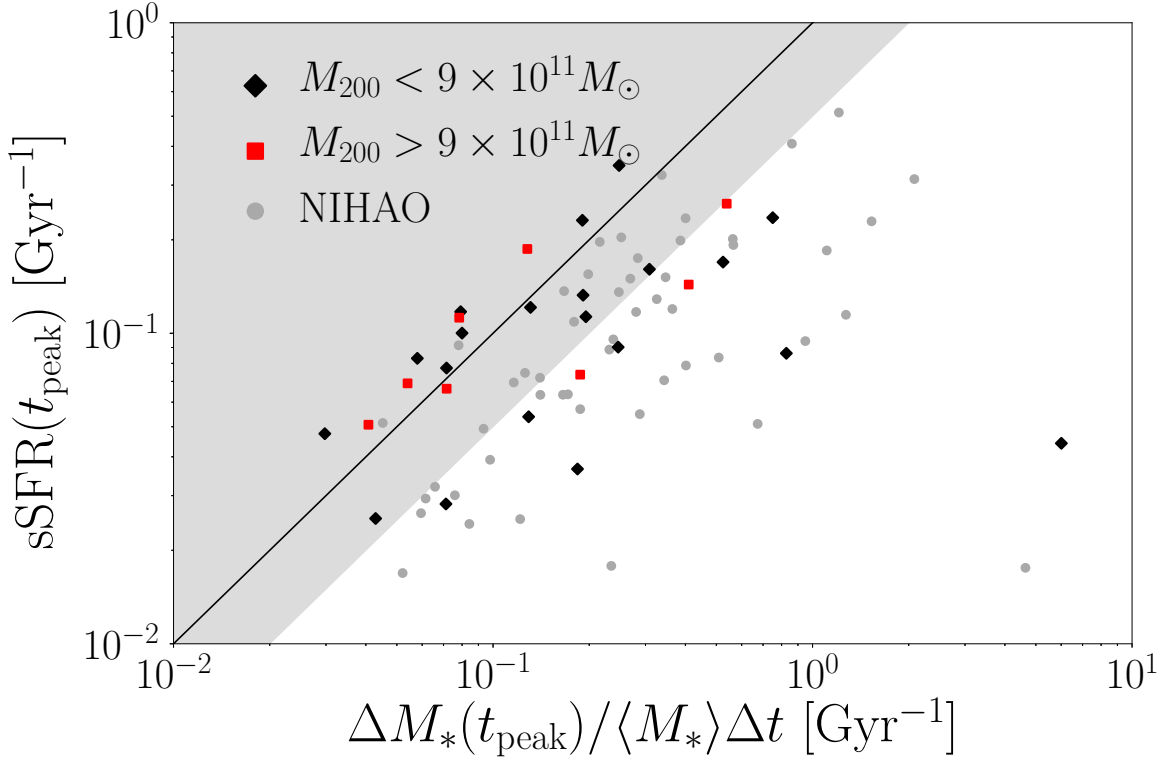


Fig. 3.1 Maximum stellar mass change versus specific star formation rate at the same epoch. The black (diamonds) show galaxies that have well determined tilting rates, red (squares) denote galaxies with well defined tilting rates as well as having a stellar mass greater than $9 \times 10^{11} M_{\odot}$, and grey (circles) denote the rest of the NIHAO galaxies. The black line shows the one-to-one relationship, and the grey shaded region highlights where star formation is the primary mode of stellar mass growth. Points lying above the line are where the star formation dominates the stellar mass change, although, stellar feedback causes the mass change to be slightly lower than expected.

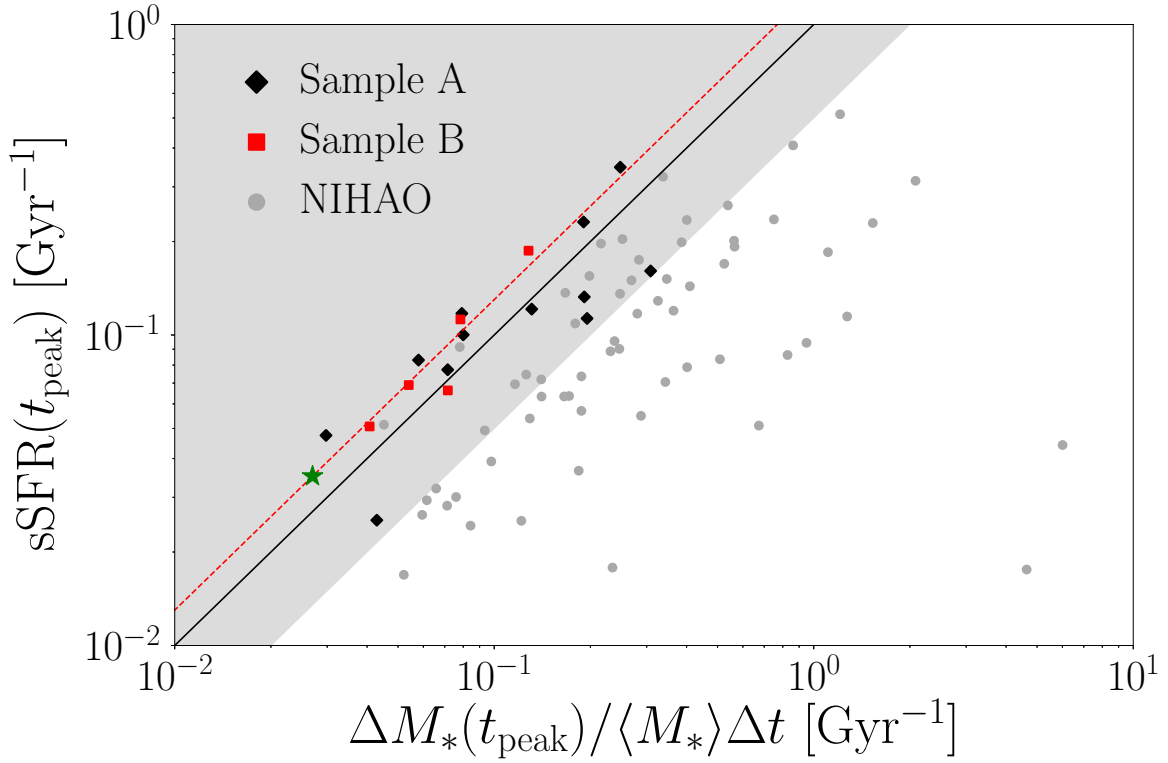


Fig. 3.2 Maximum stellar mass change versus specific star formation rate over the same time. The black diamonds show sample NIHAO:A and the red squares denote sample NIHAO:B. The green star indicates the Galaxy, calculated from values of the sSFR and supernovae rate from Licquia and Newman (2015) & Diehl et al. (2006). The red dashed line applies an offset to the one to one relation (black line) by assuming a MW supernovae rate.

3.3 Abundance Matching

Chapter 2 mentioned that the cosmological simulation suffered from over-cooling, where lower mass dark matter haloes were forming stars too efficiently (see Figure 2.1). The NIHAO galaxies do not suffer as much from over-cooling and can reproduce the observed abundance matching relationships much more closely. Figure 3.3 shows the virial mass versus the stellar mass within 10 per cent of the virial radius. The figure compares the NIHAO galaxies to the observed relationship from Kravtsov et al. (2014) derived using halo abundance matching (black line). Wang et al. (2015) present a similar figure showing that the model galaxies do not suffer from over-cooling, and extend their comparison to include the observed relationships given by Behroozi et al. (2013); Moster et al. (2013). With the stellar mass to the halo mass in good agreement with observations to much lower mass than in chapter 2, this chapter is able to consider the tilting rates of much lower mass galaxies. The green star on Figure 3.3 denotes the MW, with virial mass $M_{200} \sim 1.1 \times 10^{12} M_{\odot}$ and stellar mass $M_{*} \sim 5 \times 10^{10} M_{\odot}$ (Bland-Hawthorn and Gerhard, 2016). The low end of the NIHAO sample does still drift away from the observed relation, however, none of these galaxies fall within sample NIHAO:A and will not be studied in much detail.

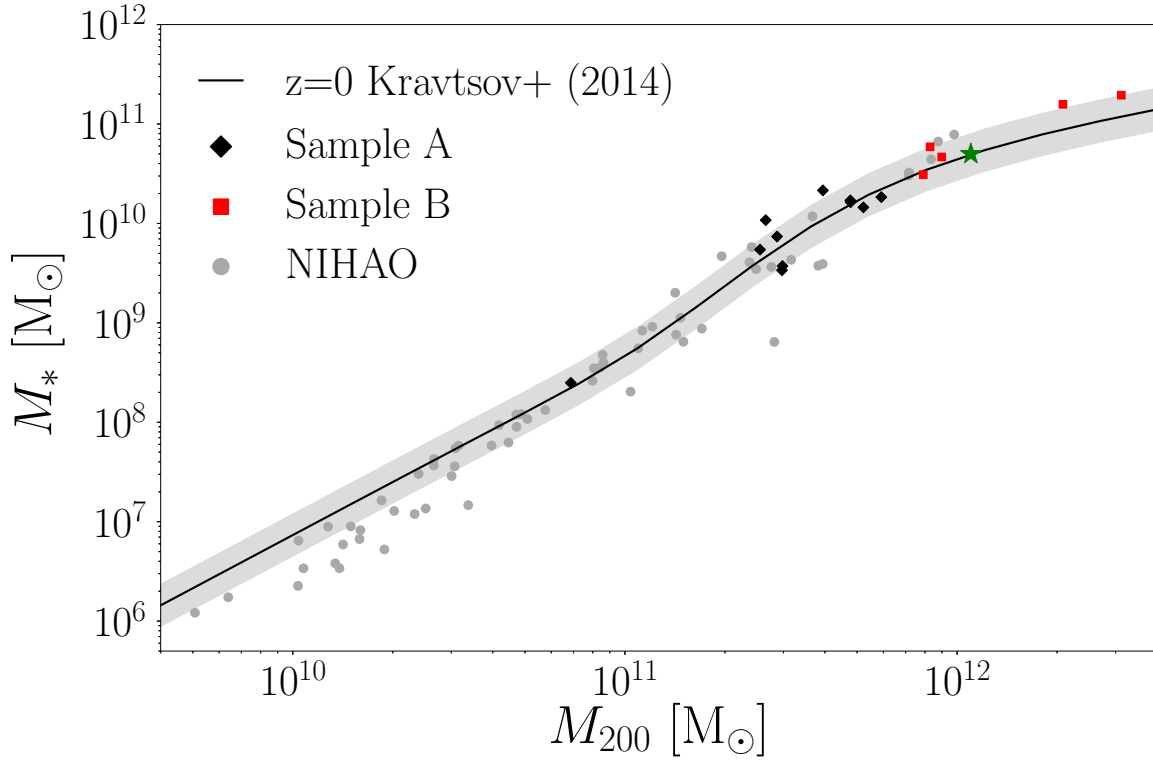


Fig. 3.3 Halo mass versus stellar mass for the NIHAO galaxies (grey), sample NIHAO:A (black diamonds) and sample NIHAO:B (red squares). All samples trace the observed abundance matching relation from Kravtsov et al. (2014) (black line and grey shaded region is the 1σ scatter). The green star denotes the position of the MW, assuming a halo mass of $M_{200} \sim 1.1 \times 10^{12} M_{\odot}$ and a stellar mass of $M_* \sim 5 \times 10^{10} M_{\odot}$ (Bland-Hawthorn and Gerhard, 2016).

3.4 Sample Comparison

This section will briefly cover the tilting rates measured for all three samples NIHAO:A, NIHAO:B and NIHAO. As a preface to this section, one must be cautious drawing conclusions from the tilting rates of the entire NIHAO sample, as they have large uncertainties.

Figure 3.4 shows the stellar mass versus the tilting rate of all the galaxies in the NIHAO sample (grey circles), sample NIHAO:A (black diamonds) and sample NIHAO:B (red squares). One can see that there is no clear relationship between stellar mass and the tilting rate of the stellar disc, however, there does appear to be a bias for galaxies with lower stellar mass to tilt at higher rates than high mass galaxies. Figure 3.5 shows the tilting rate versus the change in stellar mass (left) and baryonic mass (right). On one hand, for a galaxy accreting smaller satellites one would expect the stellar mass change to be related to the tilting rate, as the accretion of a satellite will contribute angular momentum to the disc—but not if the satellites tend to lie in the plane of the galaxy. On the other hand for an isolated galaxy evolving quiescently, there should be little relationship between change in stellar mass and the tilting rate. However, the star formation might also be considered as a proxy for gas accretion, as without ongoing gas accretion the star formation would quickly deplete the gas reservoir of the galaxy. With these considerations, one would expect the tilting rate to be correlated with the baryonic mass change, and indeed such a tendency is found for galaxies with higher accretion rates to have higher tilting rates.

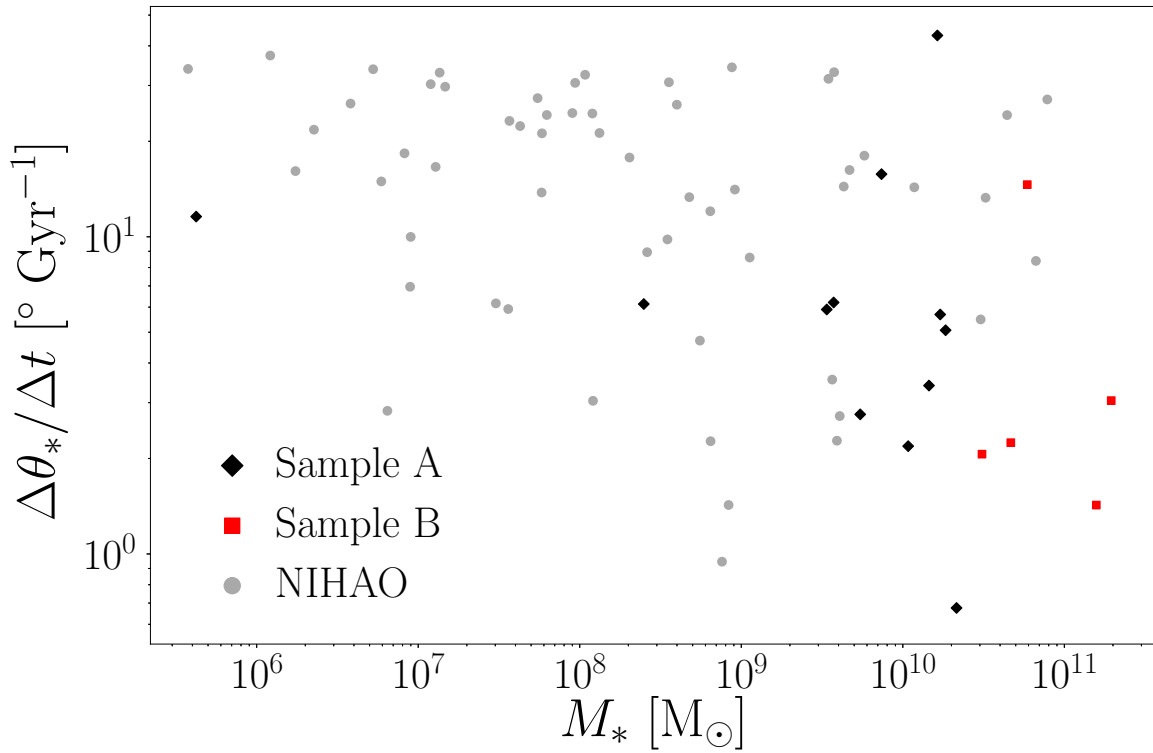


Fig. 3.4 Stellar mass versus tilting rate for NIHAO galaxies (grey), sample NIHAO:A (black diamonds) and sample NIHAO:B (red squares). The tilting rates of higher mass galaxies tend to have a wider range than lower mass galaxies, which tend to have higher tilting rates. The underrepresentation of sample NIHAO:A and sample NIHAO:B at the lower end of the mass range indicates that determining the tilting rates for lower mass galaxies is far harder than for more massive galaxies.

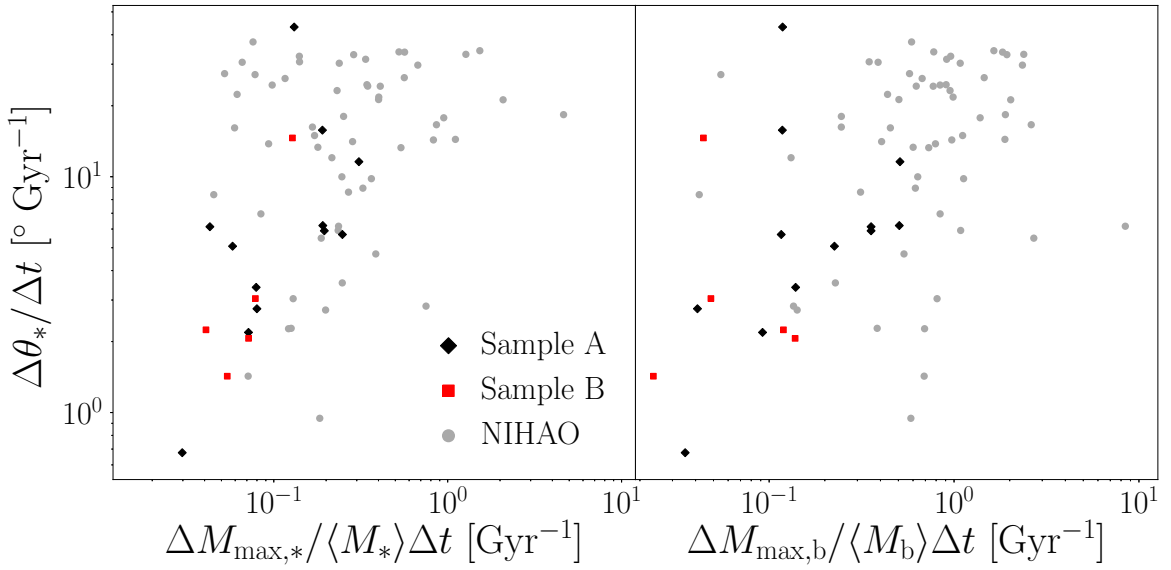


Fig. 3.5 Maximum change in stellar mass (left), and maximum change in baryonic mass (right) against the tilting rate for NIHAO (grey), sample NIHAO:A (black diamonds) and sample NIHAO:B (red squares). There is a weak correlation between the maximum stellar mass change and the tilting rate, with $p = 0.73$ for sample NIHAO:A. The correlation between baryonic mass change and tilting rate for sample NIHAO:A is weaker with $p = 0.43$.

3.5 samples NIHAO:A and NIHAO:B

This section will report the tilting rates and uncertainties for samples NIHAO:A and NIHAO:B with respect to different components of the galaxy. Throughout the error-weighted Pearson correlation coefficient, $p(x, y, \omega)$, will be reported. The weights are given by $\omega = \varepsilon^{-2}$, where ε is the error on the tilting rate. With this set of weights one can determine the error-weighted covariance, given by

$$\text{cov}_\omega(x, y, \omega) = \frac{\sum_i \omega (x - \mu_\omega(x))(y - \mu_\omega(y))}{\sum_i \omega}, \quad (3.5.1)$$

where μ_ω denotes the weighted mean. The weighed Pearson correlation coefficient is given by

$$p_\omega = \frac{\text{cov}_\omega(x, y, \omega)}{\sqrt{\text{cov}_\omega(x, x, \omega)\text{cov}_\omega(y, y, \omega)}}. \quad (3.5.2)$$

This thesis will only report p for sample NIHAO:A not for sample NIHAO:B, due to the small number of galaxies in sample NIHAO:B. A correlation coefficient of $|p| < 0.4$ will be treated as a null result and not reported here, a value between $0.4 < |p| < 0.7$ will be referred to as a weak correlation, a value between $0.7 < |p| < 0.9$ will be referred to as a strong correlation, and a value of $|p| > 0.9$ will be referred to as a very strong correlation.

Figure 3.6 shows the tilting rates for both samples A (all points) and B (red squares) versus the stellar mass within 10 per cent of the virial radius. The red dashed line denotes the observable limit of *Gaia*; as stressed in chapter 2, all the galaxies in sample NIHAO:A tilt with a rate that would be detectable. There is a weak anti-correlation between the titling rate and the stellar mass for sample NIHAO:A with $p = 0.59$.

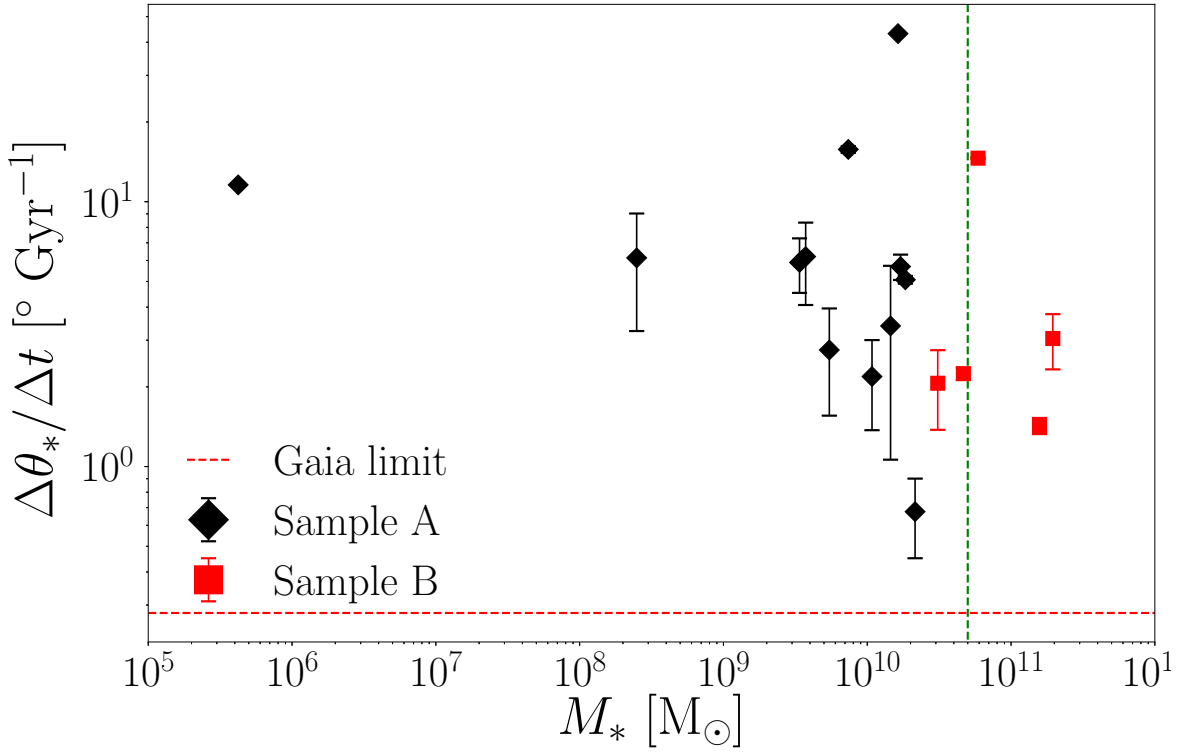


Fig. 3.6 Stellar mass versus tilting rate for sample NIHAO:A (black diamonds) and sample NIHAO:B (red squares). The green dashed line denotes the stellar mass of the MW, $M_* \sim 5 \times 10^{10} M_\odot$ (Bland-Hawthorn and Gerhard, 2016), and the red dashed line indicates the observational limit of *Gaia* (Perryman et al., 2014). As in chapter 2, all the galaxies in sample NIHAO:A tilt with a rate that would be observable by *Gaia*.

3.5.1 Dark Matter Halo

Various studies have found that the dark matter haloes in cosmological simulations tumble (Bailin and Steinmetz, 2004; Bryan and Cress, 2007; Moore et al., 2004). It has been argued that the torques imposed from such tumbling haloes would themselves cause a resident disc to tilt. Yurin and Springel (2015) inserted live stellar discs into eight, MW-sized, high-resolution dark matter haloes from the AQUARIUS simulation and found that the stellar discs tilted. This section will compare the dark matter halo to the tilting rates of the stellar discs they harbour and investigate the halo role in the tilting of the disc.

The principal axes of the dark matter halo are defined with the condition that $a > b > c$, and the principal axis ratios are given by $s = b/a$ and $q = c/a$ following Kazantzidis et al. (2004). Using an iterative process, the shape of the dark matter halo can be calculated, starting with a spherical ellipsoid with $a = b = c$. Then determining the modified inertia tensor I_{ij} , defined as:

$$I_{ij} = \sum_{\alpha} m_{\alpha} x_i^{\alpha} x_j^{\alpha} / r_{\alpha}^2$$

where x_i^{α} is the i th coordinate of the α th particle and r_{α} is the elliptical radius defined as $r_{\alpha}^2 = x_{\alpha}^2 + y_{\alpha}^2/s^2 + z_{\alpha}^2/q^2$. The eigenvalues of the modified inertia tensor are used as the new values of s and q . These iterations continue until the values of s and q converge to a fractional difference less than 10^{-2} . Following Butsky et al. (2016) the triaxiality parameter is defined as $T = \frac{1-(b/a)^2}{1-(c/a)^2}$. T can be compared to prolate, oblate and triaxial spheroids, which would have T values of 1, 0 and ~ 0.5 , respectively.

Figure 3.7 shows the tilting rate of the disc with respect to the intermediate to major axis ratios (b/a , left), minor to major axis ratios (c/a , middle) and the triaxiality parameter (T , right). The ability of a halo to cause a disc to tilt in N-body simulations (e.g. Yurin and Springel, 2015) would lead to a relationship between the halo shape and the tilting rate of the disc. There is a weak anti-correlation between both b/a and c/a and the tilting rate of

the disc with, $p = -0.42$ and -0.43 , respectively. However, there is no correlation, with the triaxiality, with $p = 0.06$. We also find that higher mass haloes have a higher average T value ~ 0.6 , meaning they are slightly more prolate than the mean of the full sample, $T \sim 0.54$. Although previous authors have claimed that they are able to cause stellar discs to tilt purely by the gravitational dynamical interactions between the disc and halo, in the case of these hydrodynamical simulations there is only a weak anti-correlation between the shape of the halo and the tilting rate of the disc.

The second possibility is that the stellar disc is tilting into alignment with the principal axis of the dark matter halo. Debattista et al. (2013) showed that red galaxies tended to be aligned such that their angular momentum was parallel to the minor axis of their parent halo, whereas blue galaxies tended to have random orientations. Figure 3.8 shows the distance between the angular momentum vector of the stellar disc and the major- (left), intermediate- (middle) and minor-axes (right). The angles were calculated at $z = 0.3$, therefore, one might assume that galaxies less aligned with a preferential axis (minor or major), would tilt with higher rates. There does not appear to be such a relationship with correlation coefficients of $p = -0.12, 0.3$ & -0.19 for the left, middle and right panels, respectively. This was also reproduced at $z = 0$, again finding no relationship between the galaxies alignment with respect to the halo and its tilting rate.

Figure 3.9 shows the distribution of alignments between stellar discs and their host haloes. Although the plot does indicate there is a slight preference to be more aligned with the minor axis of the halo, the rightmost panel shows that the majority of the galaxies are not closely aligned to any axes of the halo. All the galaxies in sample NIHAO:A are star forming blue galaxies, with sSFRs generally above the level of the MW. This confirms the previous results finding that blue galaxies generally have random alignments with respect to their dark matter halo (Debattista et al., 2013). During the investigation the alignments between the hot gas corona and dark matter were also considered, again finding no tendency

to align. Ongoing gas flow from the surrounding IGM contributes angular momentum to the corona; this angular momentum has no preference to be aligned with the angular momentum of the halo.

3.5.2 Local density

Another possible driver of the tilting rates could be the presence of high mass neighbours or the proximity of high density regions. The former is not possible in the NIHAO sample due to the strict isolation criteria imposed when constructing the sample. Chapter 2 found that galaxies in higher density areas tended to tilt with higher rates and that this correlation was stronger for larger volumes. Figure 3.10 compares the tilting rate to the local density calculated with increasing volumes, with radii between 3 and 6 Mpc. All four panels show a correlation between local density and tilting rate, the correlation tightens with increasing radius. The radii, 3, 4, 5 & 6 Mpc, have correlation coefficients of $\rho = 0.59, 0.63, 0.65$ & 0.86 , respectively. Therefore, galaxies in higher density regions of the simulation tilt with the highest rates, as reported in chapter 2. Figure 3.10 also sheds light on the galaxy with the highest tilting rate in sample NIHAO:A; this galaxy is in a high density region, within the smallest volume it has roughly twice the local density of second highest.

3.5.3 Gas

This section will compare the tilting rates to the hot gas corona and the gas disc of the galaxy. The hot gas corona is defined as all gas particles with $R < R_{200}$ and temperature $T > 50000\text{K}$. The extended gas disc is defined as all gas within 10 per cent of R_{200} . Choosing to go further out for the gas than for the stellar disc is motivated by the need to capture the angular momentum of the warp which can be extended beyond the radius of the stellar disc.

In hydrodynamical simulations, the stellar disc and hot gas corona are usually misaligned (e.g. van den Bosch et al., 2002). This misalignment allows gas to cool from the

corona onto the disc that is misaligned with the disc, possibly forming warps (Roškar et al., 2010). Gas cooling from the halo may be able to fall further inside to the disc radius contributing misaligned angular momentum to the disc, causing the disc to tilt. Figure 3.11 shows the tilting rate plotted against the angular misalignment between the hot gas corona and the stellar disc (left), and the tilting rate of the hot gas corona (right). All the galaxies in sample NIHAO:A have misaligned coronae. But there is no correlation between the misalignment of the hot gas corona or its tilting rate and the tilting rate of the stellar disc, with correlation coefficients of $p = 0.21$ and 0.052 , respectively. Chapter 2 reported a correlation between the misalignment of the corona and the tilting rate, which is not reproduced here.

The angular momentum of the warp should give a good indication of the angular momentum of the corona, as cooling gas from the corona can form warps (Roškar et al., 2010). As such the misalignment of the warp and the stellar disc should shed light on the angular momentum that is being added to the disc from the corona. Figure 3.12 compares the angle between the angular momentum vectors of the gas disc and the stellar disc against the tilting rate of the stellar disc. This figure provides some indication of the link between the tilting rate of the disc and the misaligned extended gas disc, finding a weak correlation between the misalignment and the tilting rate, with $p = 0.45$.

3.5.4 Star formation rate

Observationally detecting gas accretion or the alignment of the hot gas corona is extremely difficult. However, as the galaxy requires this ongoing accretion of gas to fuel its star formation one can assume that the star formation rate itself is a proxy for the amount of gas being accreted. Section 3.5.3 highlighted a possible connection between the accretion of misaligned gas and the tilting rate. If this misaligned gas can reach the disc it could form stars directly contributing misaligned angular momentum to the disc. This section investigates links between the star formation rate and the tilting of the stellar disc.

Star formation is calculated as the mass sum of all star particles born between $z = 0.3$ and 0, divided by the time difference. As sample NIHAO:A spans a wide range of masses it is practical to use the specific star formation rate (sSFR), by dividing the star formation rate by the average stellar mass within 10 per cent of R_{200} since $z = 0.3$. Figure 3.13 compares the sSFR at $z = 0$ and averaged over the time range to the tilting rate of the stellar disc. The green dashed line in the left panel shows a recent estimate for the sSFR of the MW (Licquia and Newman, 2015). sample NIHAO:A shows a strong correlation between sSFR at $z = 0$ and tilting rate, with an error weighted correlation coefficient of $p = 0.77$. When averaging the sSFR over the time range there is a stronger correlation, with $p = 0.9$.

3.5.5 Mass fractions

This section compares the tilting rate of the stellar disc to various mass ratios. The left panel of Figure 3.14 compares the ratio of stellar (out to $0.1R_{200}$) and total stellar mass (out to R_{200}) to the tilting rate of the stellar disc. The green line in this figure denotes an upper limit for the MW, assuming the LMC is the dominant stellar mass outside $0.1R_{200}$ and has a virial mass of $M_{\text{LMC}} \sim 2 \times 10^{11} M_{\odot}$ (Gómez et al., 2015; Kallivayalil et al., 2013; Peñarrubia et al., 2016). Determining the stellar mass from M_{200} was done by assuming the LMC follows an observed abundance matching relation (Kravtsov et al., 2014). A value of $M_* \sim 5 \times 10^{10} M_{\odot}$ was assumed for the stellar mass of the MW (Bland-Hawthorn and Gerhard, 2016). There is no correlation between the stellar mass ratio and the tilting rate of the stellar disc for sample NIHAO:A with $p = -0.064$, indicating that the presence of nearby satellites within R_{200} is not indicative of a high tilting rate. The right panel of Figure 3.14 compares the ratio of stellar (out to $0.1R_{200}$) to total gas mass (out to R_{200}) against the tilting rate of the stellar disc. The green star indicates the MW. sample NIHAO:A exhibits a weak anti-correlation, with $p = -0.45$. This mass ratio traces the total gas mass available to cool and form stars within the galaxy. It has been shown in section 3.5.4 that there is a

correlation between the sSFR and the tilting rate of the disc. Star formation is a result of the continual feeding of gas onto the disc. For galaxies with more gas available within R_{200} , relative to their stellar mass, it is therefore not surprising that they tilt faster.

The left panel of Figure 3.15 shows the ratio of gas and stellar mass (out to $0.1R_{200}$) against the tilting rate of the stellar disc. The green star shows the location of the MW. There is no correlation between this mass ratio and tilting rate of the stellar disc, with a correlation coefficient of just $p = 0.3$. The right panel of Figure 3.15 shows the ratio of gas mass in the disc (out to $0.1R_{200}$) and corona (out to R_{200}). Again there is no correlation between the mass ratio and the tilting rate with $p = -0.19$.

3.5.6 Angular Momentum

As the gas from the corona cools onto the disc, this changes the total angular momentum of the disc. This extra angular momentum is not necessarily aligned with the stellar disc, causing the direction of the angular momentum to change. This section will compare the change in total angular momentum to the change in the direction of the angular momentum (tilting rate).

Figure 3.16 shows the angular momentum of the stellar disc at $z = 0.3$ (left), the change in angular momentum from $z = 0.3$ to $z = 0$ (middle), and then the difference normalized by the mean angular momentum (right). The rough estimate for the angular momentum of the Milky Way's stellar disc $|L| = mrv = 2.6 \times 10^{13} M_{\odot} \text{ km s}^{-1} \text{ kpc}$ (green dashed line) was obtained by assuming a disc stellar mass to be 4.6×10^{10} (Bovy and Rix, 2013), putting all the mass at the scale radius $R = 2.6 \text{ kpc}$ (Bland-Hawthorn and Gerhard, 2016), and assuming a circular velocity of 218 km s^{-1} (Bovy and Rix, 2013). There are no correlations between the total angular momentum at $z = 0.3$ or the change in angular momentum when compared to the tilting rate of the stellar disc with $p = -0.27$ & -0.22 , respectively. Moreover, when comparing the absolute normalized change in angular momentum ($\Delta|L| = ||L_2| - |L_1||$) and

the tilting rate of the stellar disc there is no correlation, with a correlation coefficient of $p = 0.33$.

Figure 3.17 compares the angular momentum of the cool gas ($T < 50000\text{K}$) at $z = 0.3$ (left), the change in angular momentum since $z = 0.3$ (middle) and the change normalized by the average angular momentum over the same time (right) all versus the tilting rate of the stellar disc. All three panels show no correlation, with $p = -0.36$, -0.25 and -0.39 , for the left, middle and right panels, respectively.

Figure 3.18 shows the angular momentum of the cold gas disc ($T < 20000$) at time $z = 0.3$ (left), the change in angular momentum since $z = 0.3$ (middle), and the change normalized by the average angular momentum over the same time period (right), all versus the tilting rate of the stellar disc. All three panels show no correlation, with $p = -0.35$, -0.25 and -0.44 , for the left, middle and right panels, respectively. If the change in the angular momentum's magnitude is not related to the tilting rate of the stellar disc, one must assume that not all of the angular momentum that is added to or removed from, the disc is driving the tilting of the disc.

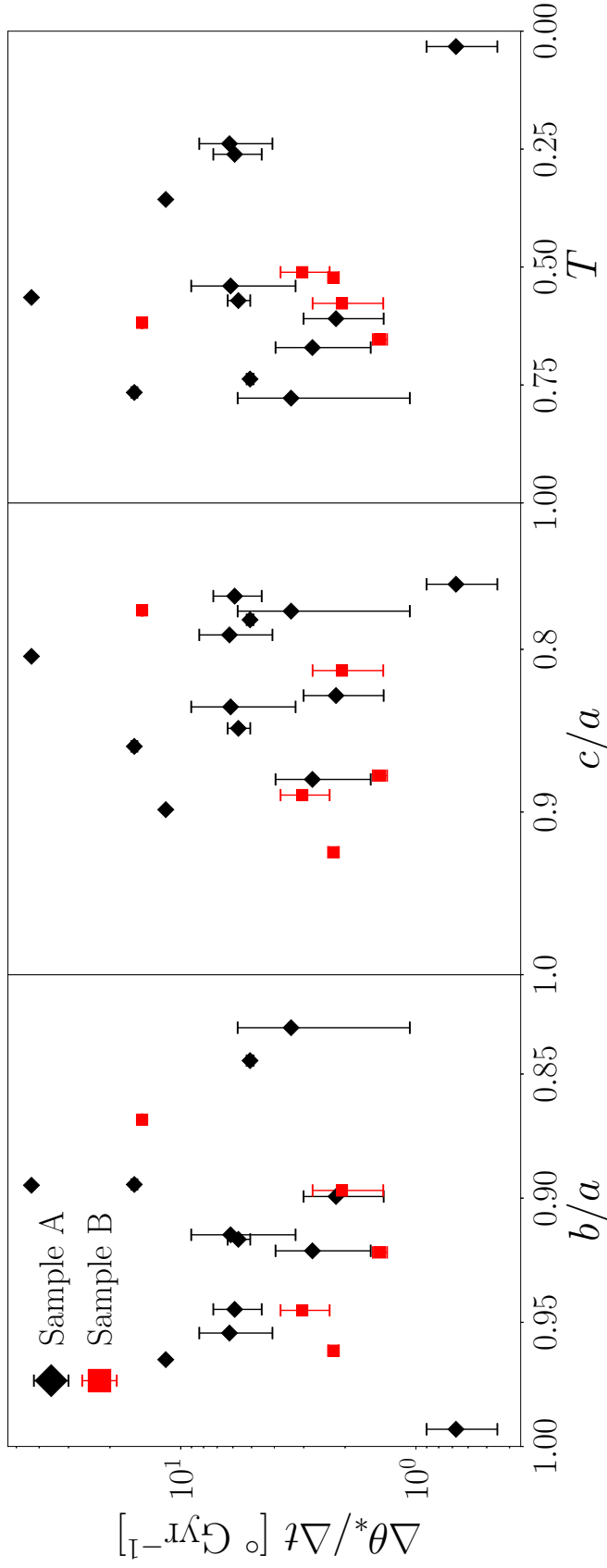


Fig. 3.7 Intermediate to major axes ratio (left), minor to major axes ratio (middle) and triaxiality (right) versus tilting rate for both sample NIHAO:A (black diamonds) and sample NIHAO:B (red squares). There is a weak anti-correlation between the axis ratios of the halos and the tilting rate of the discs, but no correlation, with the triaxiality for sample NIHAO:A with $p = -0.42$, -0.43 & 0.06 for the left, middle and right panels, respectively.

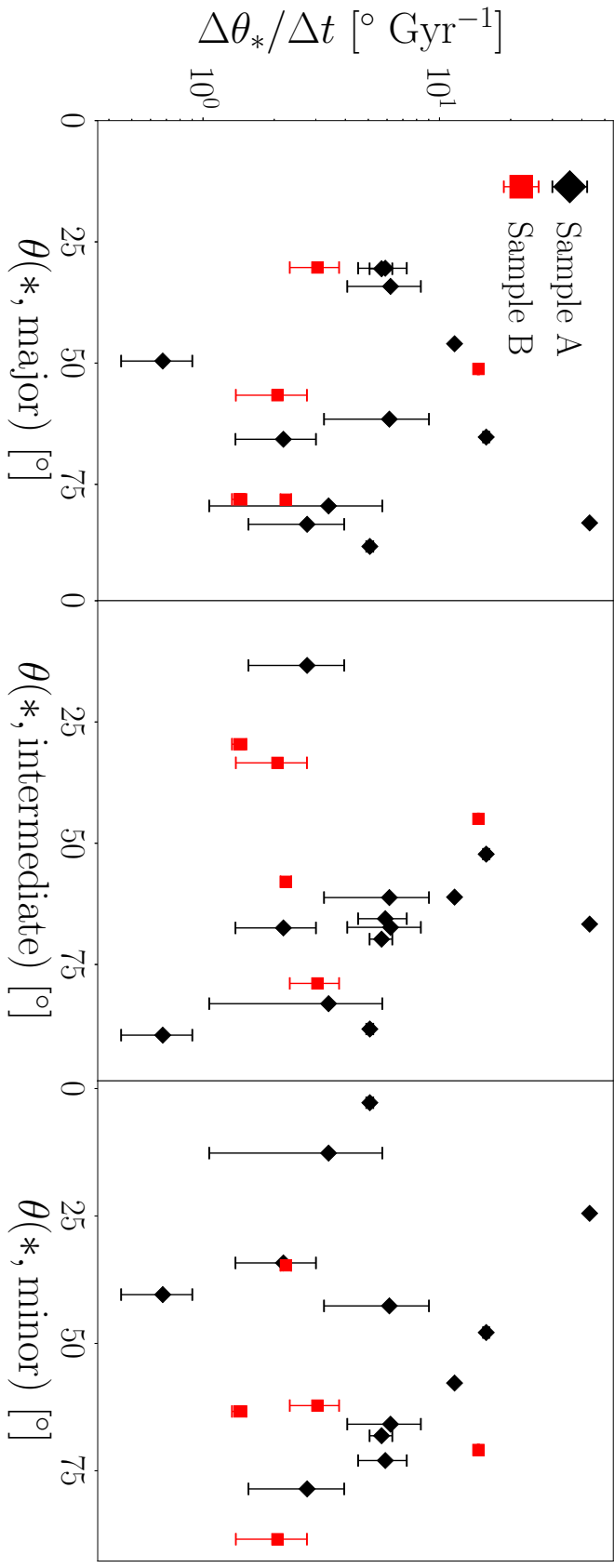


Fig. 3.8 Offset between the angular momentum of the stellar disc and the major- (left), intermediate- (middle) and minor-axis (right) versus the tilting rate of the stellar disc. Debattista et al. (2015) found that red galaxies stellar angular momenta tended to be aligned with their halos minor axis, whereas blue galaxies tended to have random orientations with respect to their dark matter halo. Such a result would suggest that galaxies not close to a preferential alignment should tilt faster than galaxies closer to alignment (at least for red galaxies). There does not appear to be such a relationship for sample NIHAO:A with $p = -0.12, 0.3$ & -0.19 for the left, middle and right panels, respectively.

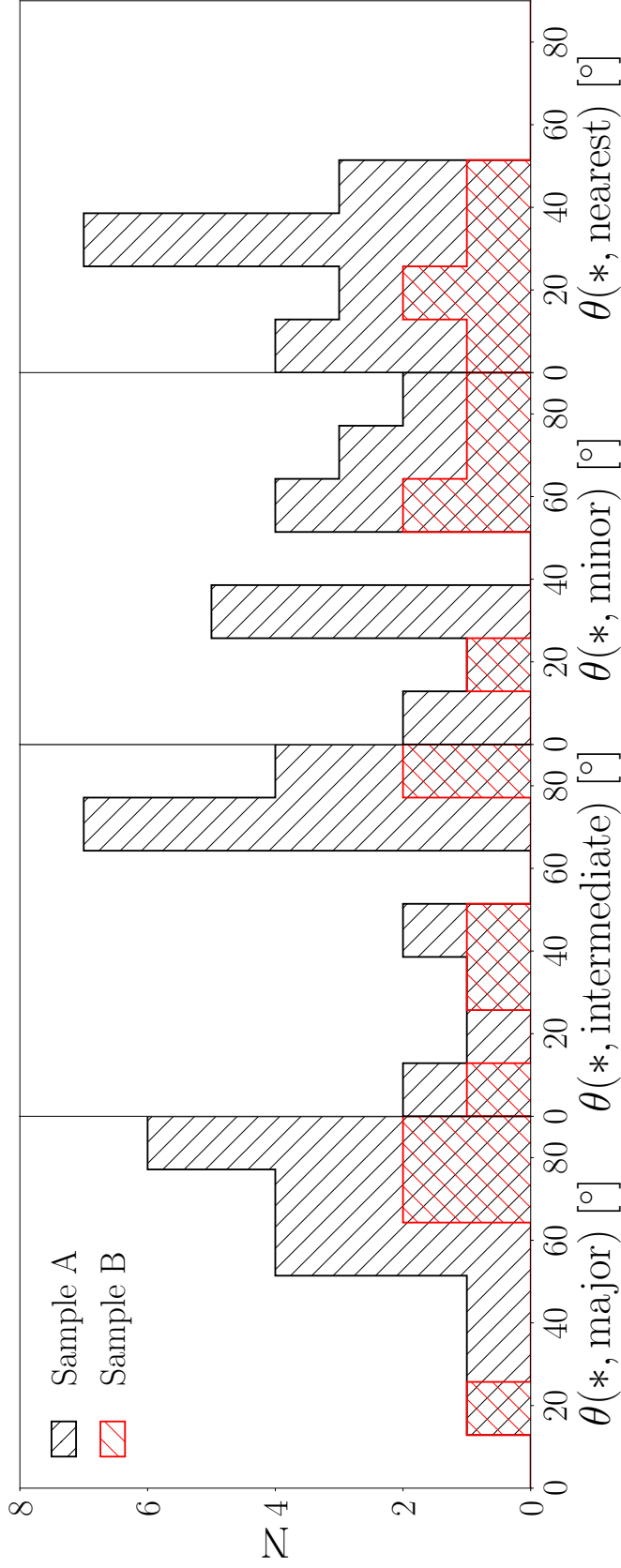


Fig. 3.9 Distribution of angular distances between the angular momentum of the stellar disc and the major- (left), intermediate- (middle left), minor- (middle right) and closest axis (right) for sample NIHAO:A. This is a small over representation of galaxies closer to the minor than any other axes, however, the right-most-panel shows that most galaxies in sample NIHAO:A have random orientations, similar to the result found by Debattista et al. (2015) for blue galaxies.

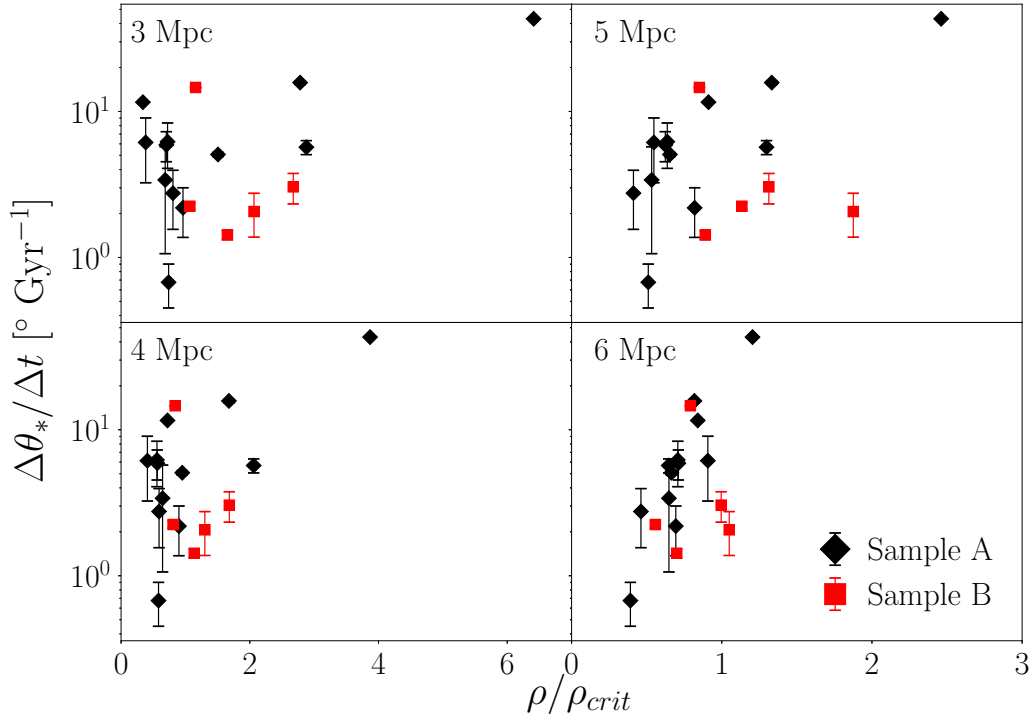


Fig. 3.10 Normalised local density out to 3 Mpc (top left), 4 Mpc (bottom left), 5 Mpc (top right) and 6 Mpc (bottom right), versus tilting rate for sample NIHAO:A (black diamonds) and sample NIHAO:B (red squares). All four plots have a correlation between local density and tilting rate, this correlation tightens with increasing volume size. For sample NIHAO:A, the radii 3, 4, 5 & 6 have correlation coefficients of $p = 0.59, 0.63, 0.65$ & 0.86 , respectively.

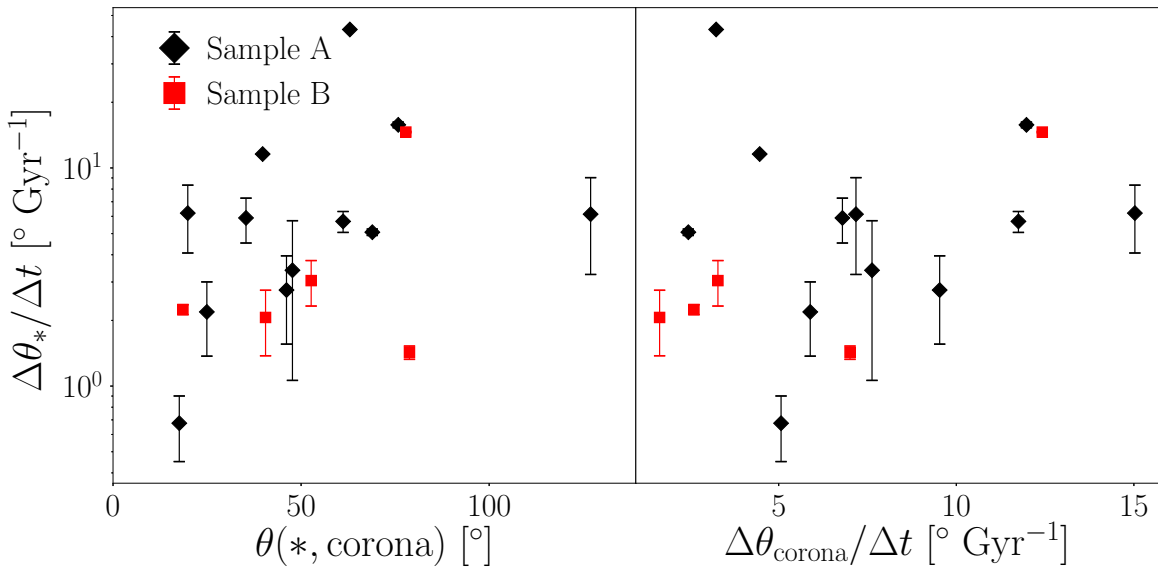


Fig. 3.11 Left: the angle between the angular momentum vectors of the stellar disc and hot gas corona versus the tilting rate of the stellar disc, right: tilting rate of the hot gas corona versus the tilting rate of the stellar disc for sample NIHAO:A (black diamonds) and sample NIHAO:B (red squares). Chapter 2 noted a correlation between the extent of misalignment between the corona and stellar disc with the tilting rate of the disc. For sample NIHAO:A there is no such correlation, with $p = 0.21$ and 0.052 for the left and right panels, respectively.

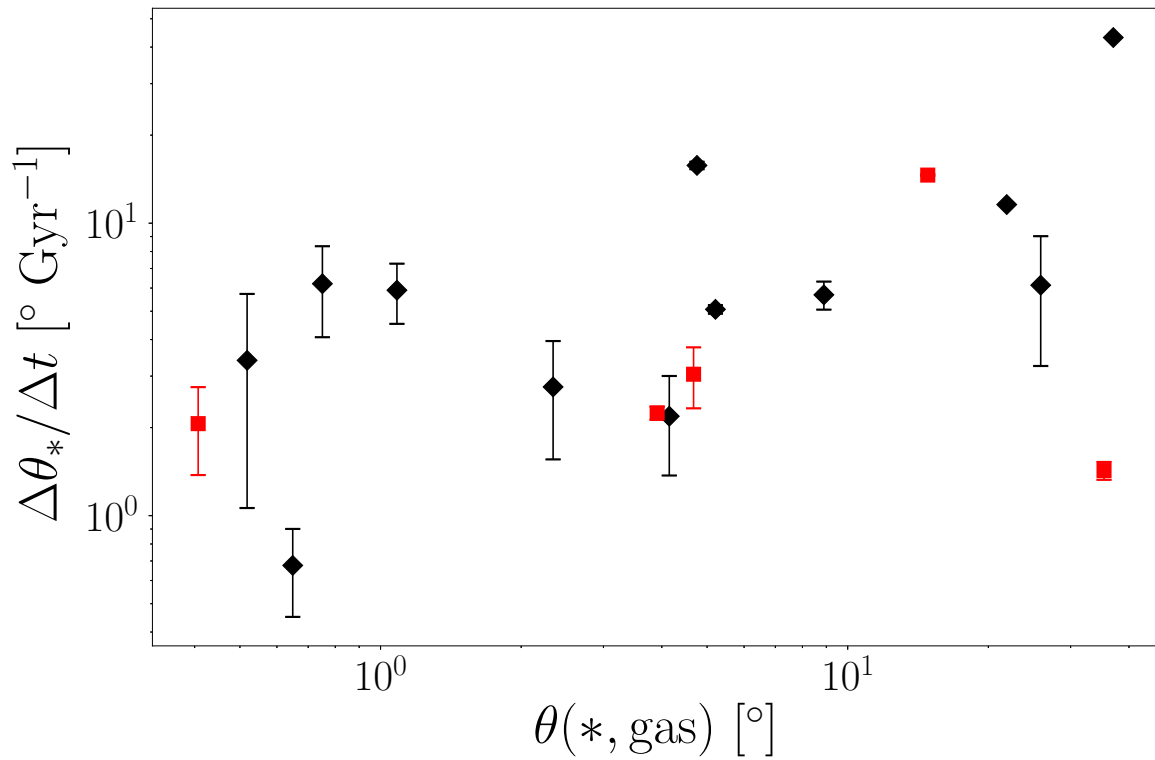


Fig. 3.12 Angular difference between the angular momentum vectors of gas within 10 per cent of the virial radius and the stellar disc versus the tilting rate for sample NIHAO:A (black diamonds) and sample NIHAO:B (red squares). There is as weak correlation between the misalignment extent and the tilting rate of the stellar disc, for sample NIHAO:A $p = 0.45$.

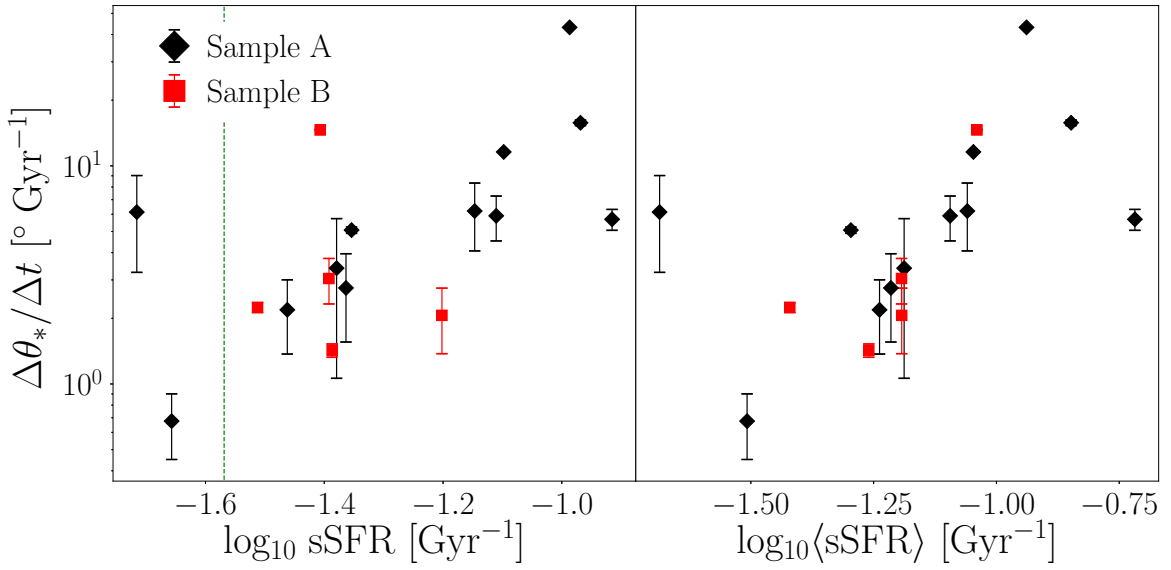


Fig. 3.13 Left: specific star formation rate, at $z = 0$, versus tilting rate of the stellar disc for sample NIHAO:A (black diamonds) and sample NIHAO:B (red squares). The green line shows the specific star formation rate of the MW (Licquia and Newman, 2015). Right: average specific star formation at each time step between $z = 0$ and 0. There are correlations for sample NIHAO:A in both the left and right plots, with correlation coefficients of $p = 0.77$ and 0.9, respectively.

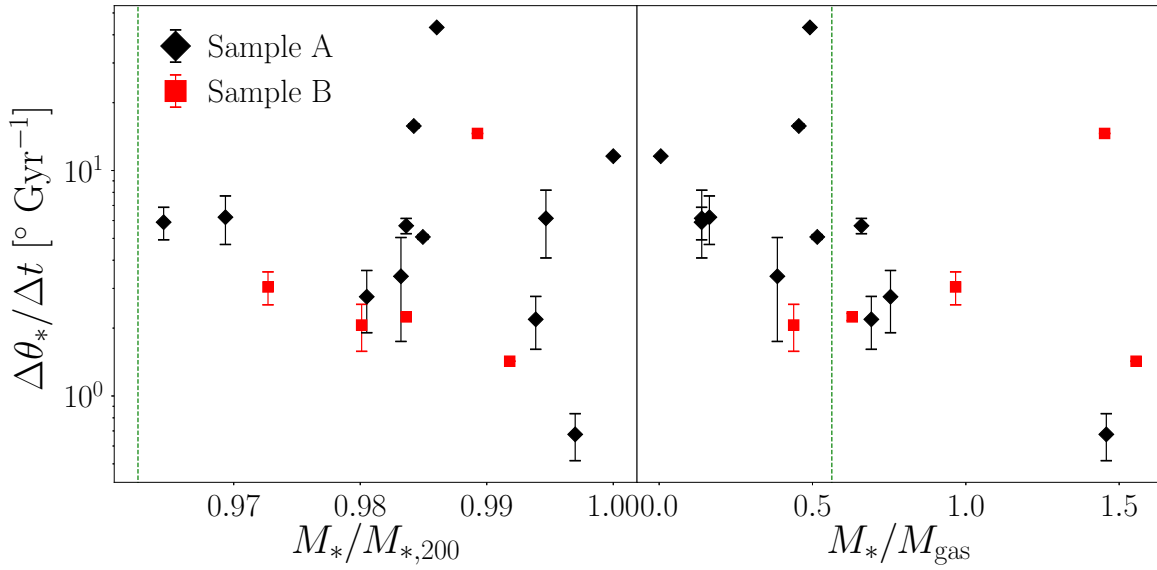


Fig. 3.14 Left: ratio of galaxy stellar mass out to 10 per cent of R_{200} to total stellar mass inside R_{200} versus tilting rate of the disc, right: ratio of stellar mass out to 10 per cent of R_{200} to total gas mass inside R_{200} versus tilting rate of the stellar disc. The green dashed line on the right panel shows the stellar to gas mass ratio of the MW (Bland-Hawthorn and Gerhard, 2016). There is no correlation for sample NIHAO:A in the left panel, with $\rho = -0.064$, and a weak anti-correlation for sample NIHAO:A (black diamonds) on the right panel, with $\rho = -0.45$.

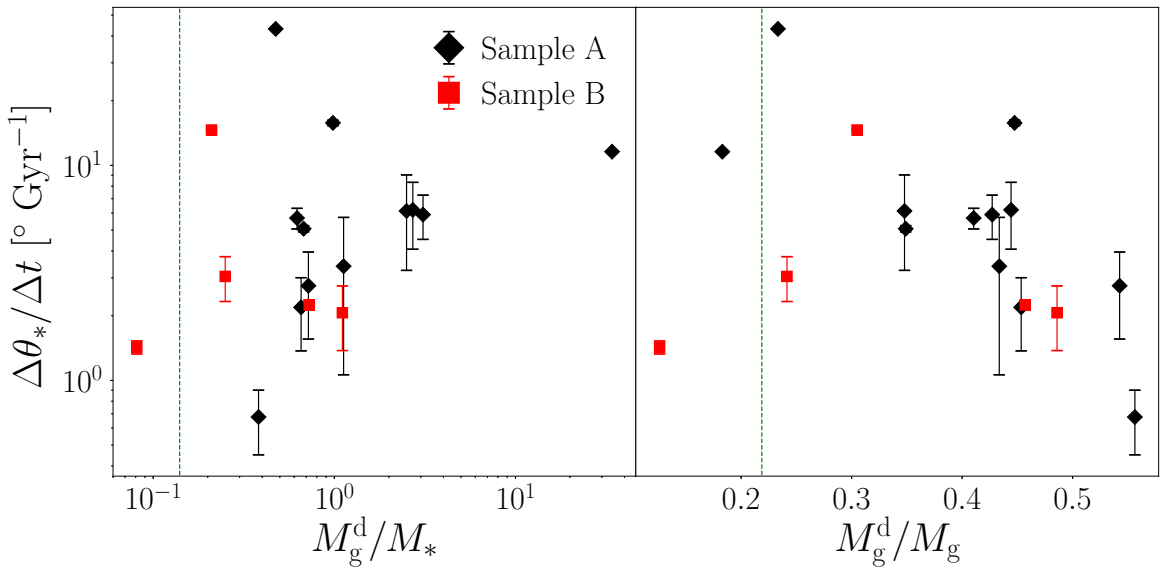


Fig. 3.15 Left: mass ratio of the gas and stellar discs versus tilting rate. Right: mass ratio of gas disc and halo. The green lines on both panels denotes the location of the MW with values for the masses taken from Bland-Hawthorn and Gerhard (2016). Both panels show no correlation for sample NIHAO:A, with $p = 0.3$ & -0.19 for left and right, respectively.

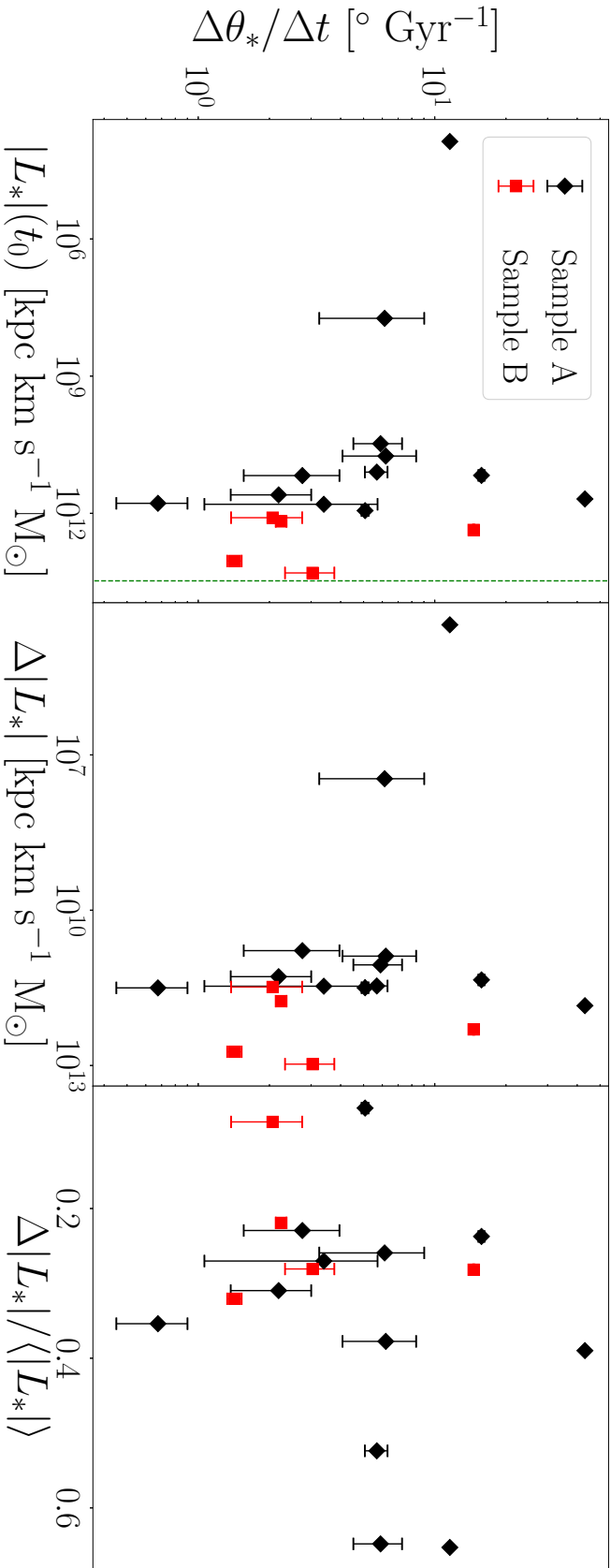


Fig. 3.16 Left: the angular momentum of the stellar disc at $z = 0.3$, middle: change in angular momentum between $z = 0.3$ and 0, right: the change in angular momentum between $z = 0.3$ and 0 divided by the mean angular momentum of the stellar disc. The green dashed line shows an estimate for the angular momentum of the MW's stellar disc. All three panels, left, middle and right, show no correlation for sample NIHAO:A, with $p = -0.27$, -0.22 and 0.33 , respectively.

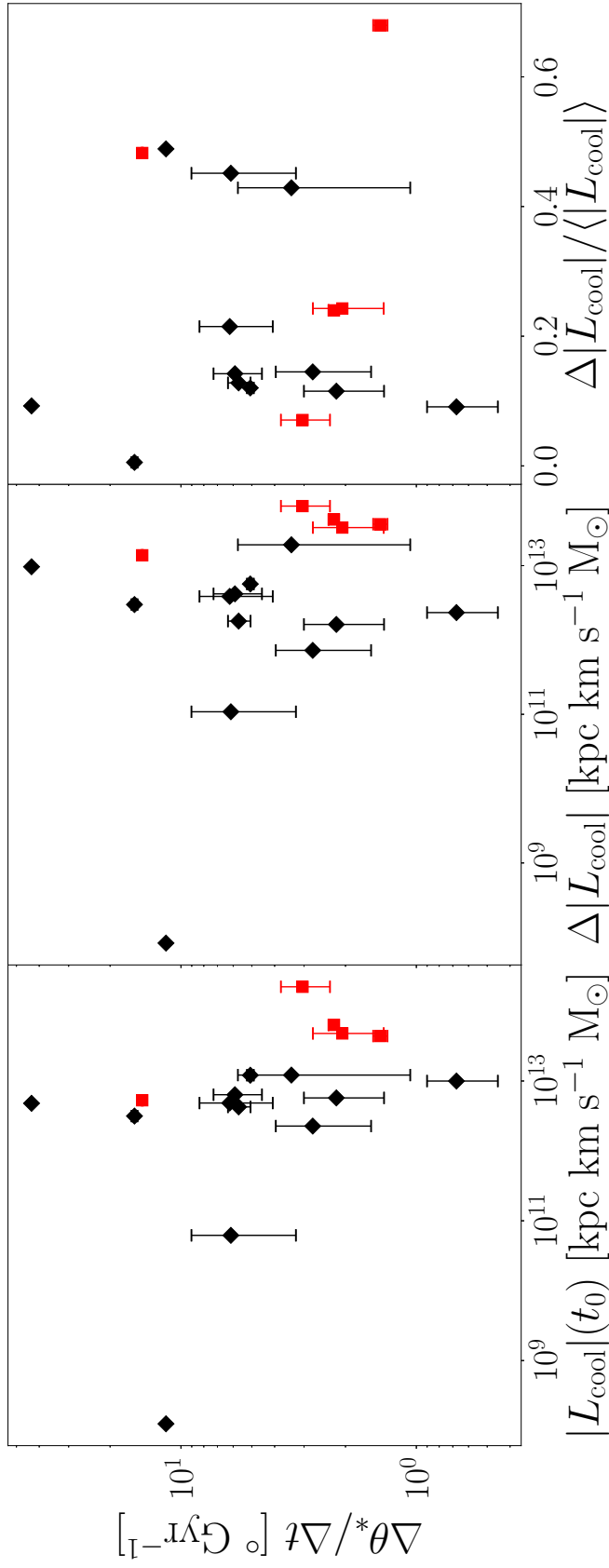


Fig. 3.17 Left: the angular momentum of the cool gas disc ($T < 50000\text{K}$) at $z = 0.3$, middle: change in angular momentum between $z = 0.3$ and 0, right: the change in angular momentum between $z = 0.3$ and 0 divided by the mean angular momentum of the cool gas disc. All three panels, left, middle and right, show no correlation for sample NIHAO:A, with $p = -0.36$, -0.25 and -0.39 , respectively.

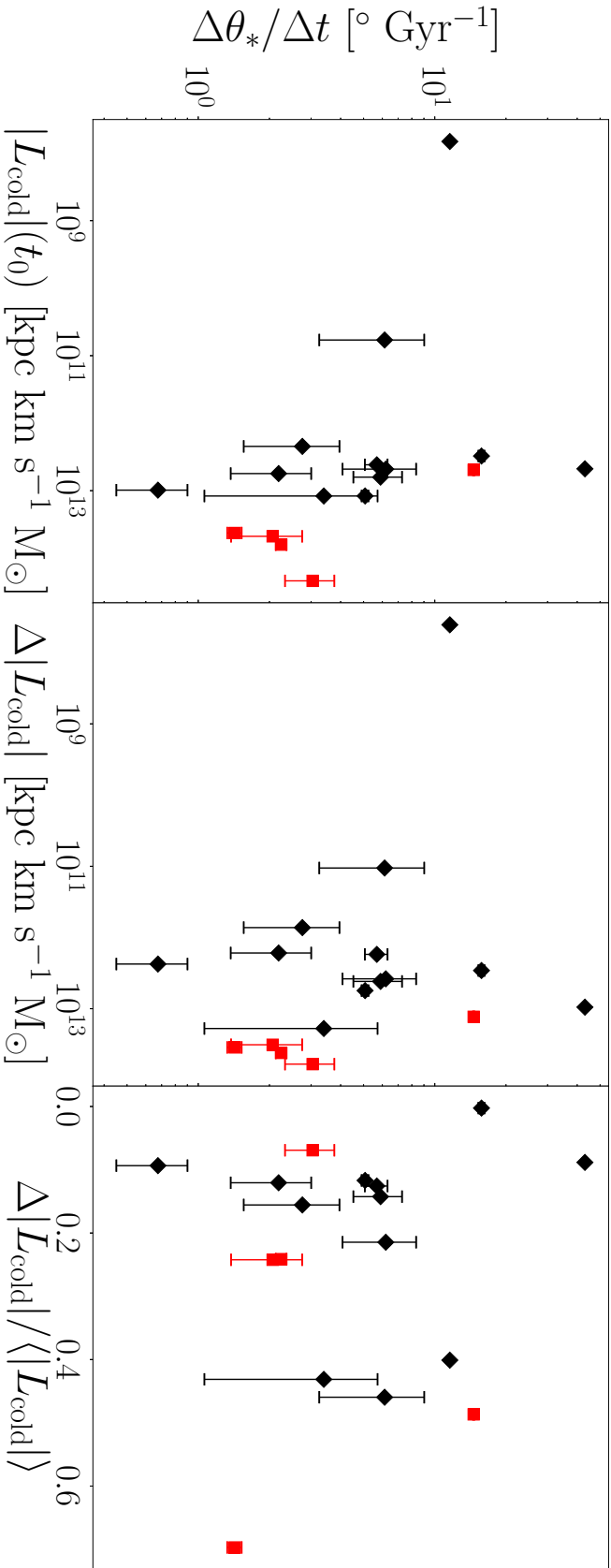


Fig. 3.18 Left: the angular momentum of the cold gas disc ($T < 20000\text{K}$) at $z = 0.3$, middle: change in angular momentum between $z = 0.3$ and 0 , right: the change in angular momentum between $z = 0.3$ and 0 divided by the mean angular momentum of the cold gas disc. All three panels, left, middle and right, show no correlation for sample NIHAO:A, with $p = -0.35$, -0.25 and -0.44 , respectively.

3.6 Chapter summary

This chapter investigated the links between the tilting rates of the stellar discs and various components of the respective galaxies. This section will provide a brief summary of the correlations found. Weak anti-correlation between the axis ratios of the halo and the tilting rate of the disc were identified. The weak correlation between the misalignment of the extended gas and stellar discs versus the tilting rate of the stellar disc were shown. When comparing the ratio of stellar (out to $0.1R_{200}$) to total gas mass (out to R_{200}) against the tilting rate of the disc, a weak anti-correlation was measured. Correlations found in chapter 2 between the local density and the tilting rate were confirmed here and again found to become tighter with increasing volume. A strong correlation was found between the maximum stellar mass change and the tilting rate. A strong correlation was found between the sSFR and the tilting rate, this correlation becomes very strong when the sSFR is averaged over the time period.

Chapter 4

NIHAO: Sample B

4.1 Brief introduction

This chapter will delve deeper into the five NIHAO galaxies with well determined tilting rates, a mass of $M_{200} > 9 \times 10^{11}$ and whose stellar mass change is dominated by star formation (sample B of Chapter 3). For each galaxy, the change in angular momentum of the stellar disc will be compared to the galaxy's cool gas disc, hot gas corona and dark matter halo. This chapter will retain the naming convention laid out in Wang et al. (2015), where the galaxy is simply referred to by the mass of the dark matter halo from the parent N-body simulation. Tables 4.1 & 4.2 shows some generic information about each galaxy at $z \sim 0.3$ and 0, respectively.

4.1 Brief introduction

Galaxy ID	g7.55e11	g7.66e11	g8.26e11	g1.92e12	g2.79e12
$M_{\text{disc},*}[10^{11} M_{\odot}]$	0.24	0.35	0.41	1.3	1.6
$M_{\text{sat},*}/M_{\text{total},*}$	0.04	0.01	0.016	0.003	0.02
$M_{\text{disc},*}/M_{\text{total},*}$	0.94	0.76	0.97	0.98	0.94
$M_{200}[10^{12} M_{\odot}]$	0.70	0.82	0.89	2.1	3.3
$M_{\text{corona}}[10^{11} M_{\odot}]$	0.23	0.21	0.23	0.79	1.5
$M_{\text{corona}}/M_{\text{disc},*}$	0.96	0.6	0.56	0.6	0.94
R_{200} [kpc]	203	214	219	291	340
$\max(v_{\text{circ}})$ [km s^{-1}]	135	229	199	399	404
λ_p	0.054	0.023	0.062	0.027	0.05
$\rho_{6\text{kpc}}/\rho_{\text{crit}}$	0.7	0.7	0.6	0.7	1
$ L_{\text{disc},*} [10^{14} M_{\odot} \text{ kpc km s}^{-1}]$	0.07	0.03	0.2	0.8	1.8
$ L_{\text{corona}} [10^{14} M_{\odot} \text{ kpc km s}^{-1}]$	1.1	4.4	1.5	2.0	11.2
$ L_{\text{corona}} / L_{\text{disc},*} $	15.5	147	7.5	2.5	6.2
R_{warp} [kpc]	25	4	21	13	28

Table 4.1 Galaxies in sample B, all values are calculated at $z \sim 0.3$. Total stellar mass is calculated within R_{200} , $\max(v_{\text{circ}})$ is for star particles inside $R < 30$ kpc. The mass and angular momentum of the hot gas corona M_{corona} & L_{corona} were determined using all hot gas ($T > 50,000\text{K}$) within R_{200} .

Galaxy ID	g7.55e11	g7.66e11	g8.26e11	g1.92e12	g2.79e12
$M_{\text{disc},*} [10^{11} M_{\odot}]$	0.3	0.47	0.46	1.5	1.9
$M_{\text{sat},*}/M_{\text{total},*}$	0.03	0.01	0.006	0.003	0.02
$M_{\text{disc},*}/M_{\text{total},*}$	0.97	0.79	0.97	0.98	0.95
$M_{200} [10^{12} M_{\odot}]$	0.90	0.93	1.02	2.3	3.5
$M_{\text{corona}} [10^{11} M_{\odot}]$	0.26	0.22	0.24	0.8	1.4
$M_{\text{corona}}/M_{\text{disc},*}$	0.87	0.47	0.52	0.53	0.74
R_{200} [kpc]	299	303	312	412	472
$\max(v_{\text{circ}})$ [km s ⁻¹]	143	260	203	402	440
λ_p	0.05	0.026	0.06	0.022	0.036
$\rho_{6\text{kpc}}/\rho_{\text{crit}}$	1	0.8	0.6	0.7	1
$ L_{\text{disc},*} [10^{14} M_{\odot} \text{ kpc km s}^{-1}]$	0.15	0.09	0.25	1.1	2.4
$ L_{\text{corona}} [10^{14} M_{\odot} \text{ kpc km s}^{-1}]$	1.3	0.71	2.0	0.85	13
$ L_{\text{corona}} / L_{\text{disc},*} $	8.7	7.9	8	0.77	5.4
R_{warp} [kpc]	25	4	21	13	28
$sSFR$ [Gyr ⁻¹]	0.063	0.039	0.0307	0.041	0.0405
$sSFR_{\text{max}}$ [Gyr ⁻¹]	0.066	0.19	0.0508	0.069	0.11

Table 4.2 Galaxies in sample B, all values are calculated at $z = 0$. Total stellar mass is calculated within R_{200} , $\max(v_{\text{circ}})$ is for star particles inside $R < 30$ kpc. The mass and angular momentum of the hot gas corona M_{corona} & L_{corona} were determined using all hot gas ($T > 50,000\text{K}$) within R_{200} .

4.2 Analysis

Throughout this chapter, the radius at which the misalignment between the cool gas and stellar disc becomes $> 5^\circ$ is used to define the start of the warp (R_{warp}) and the end of the unwarped stellar disc (R_{disc}). Here, ‘cool gas’ refers to gas with $T < 20,000\text{K}$ and ‘hot gas’ will refer to gas with $T > 50,000\text{K}$. This value is calculated using the angular momentum of cool gas in annuli from 2 kpc to 30 kpc, with widths of 2 kpc, at $z \sim 0.3$. As this value may change over the subsequent time steps, this chapter will also report the values out to 30 kpc. In order to compare the orientation of each components’ angular momentum Briggs figures will be used extensively, for a detailed explanation see section 1.3.1. In all of the Briggs figures, the colour represents the position of the unit vector in the temporal (triangles) or radial (circles) series, dark blue being the start and dark red the end. The size of each point represents the magnitude of the angular momentum vector and all magnitudes are normalised to the panel. Each Briggs figure shows the angular momentum vectors normalised and rotated with respect to the stellar disc’s angular momentum. This is done by calculating the rotation matrix needed to transform the angular momentum of the stellar disc into the z -axis, then applying this rotation matrix to all angular momentum vectors in the panel.

This chapter is interested in the impact of accreting material with misaligned angular momentum, on the tilting rate of the stellar disc. As such the inflow and outflow of angular momentum is calculated using the unique gas particle id’s. Every particle within an annulus has their id’s listed at each time step. Any particle that moves from a radius greater than R_{shell} to a radius $R < R_{\text{shell}}$ is considered *inflowing* material, any particle that moves from a radius $R < R_{\text{shell}}$ to $R > R_{\text{shell}}$ is considered *outflowing* material. To calculate the net flow, the total angular momentum was calculated for both the inflowing and outflowing material, then subtracted such that $L_{\text{netflow}} = L_{\text{inflow}} - L_{\text{outflow}}$. This results in the change in angular momentum crossing each shell. For stars and dark matter particles the net flow can be

calculated by simply comparing the particle id's at $z \sim 0.3$ and 0. However, for gas, this is done by summing $\mathbf{L}_{\text{netflow}}$ at each time step. The motivation behind this is that a gas particle can enter a bin then undergo star formation, in such a case the net flow of gas would be underestimated. It is possible that a gas particle could cross a shell and then form a star before the next snapshot, however, this should only be a small number of particles.

4.3 Substructure driven tilting

This section highlights two of the NIHAO galaxies from sample B where the tilting is primarily driven by their substructure. The accretion or interactions with satellites can contribute a large amount of misaligned angular momentum resulting in a change in the stellar disc's angular momentum. A comparison to the MW would be the interaction with the Sagittarius Dwarf Spheroidal Galaxy (Sgr Sph).

4.3 Substructure driven tilting

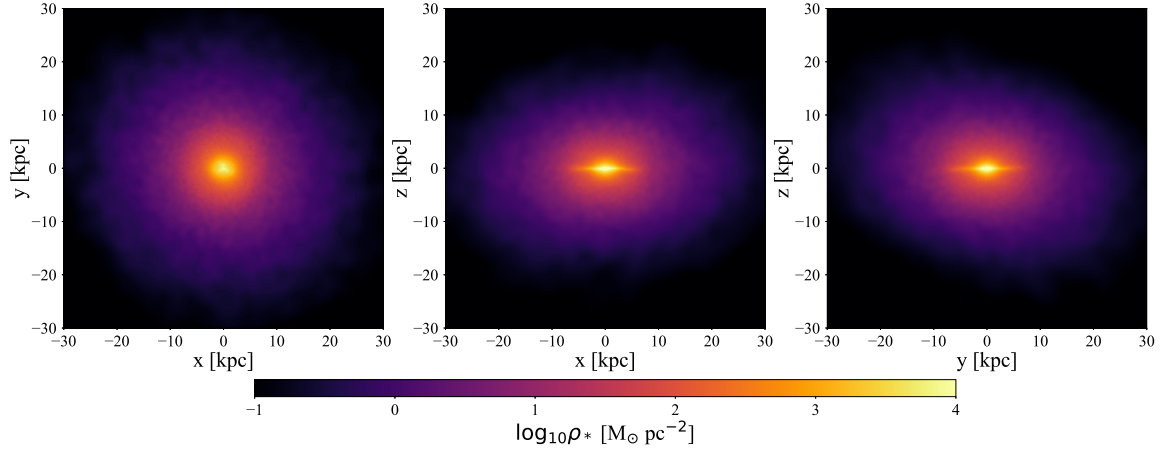


Fig. 4.1 **g7.66e11** - Stellar surface density maps at $z = 0$, projected into the x - y -, x - z - and y - z -planes.

4.3.1 Galaxy: g7.66e11

Galaxy g7.66e11 has a stellar mass of $M_{\text{disc}} = 4.7 \times 10^{10} M_{\odot}$, but a small stellar disc with a radius $\sim R_{\text{disc}} \sim 4$ kpc. The total stellar content of the galaxy extends further than the disc radius, with only ~ 79 per cent of the stellar content inside this radius, residing in a stellar warp and an extended stellar halo. It has the largest tilt rate in the sample with $\Delta\theta/\Delta t \sim 14.6^{\circ} \text{ Gyr}^{-1}$, roughly 5 times larger than the second highest tilting rate in this sample. Figure 4.1 shows the stellar surface density of g7.66e11 in three different projections.

g7.66e11: stellar disc and satellites

Figure 4.2 shows the angular momentum of the stellar disc ($\mathbf{L}_{\text{disc},*}$) (top) at each time step, with respect to $\mathbf{L}_{\text{disc},*}$ at $z \sim 0.3$. The stellar disc tilts in a very consistent direction but slows between $z \sim 0.3$ and 0. This is echoed in the angular momentum's magnitude, which grows slower at later times, starting and ending with values of $|\mathbf{L}_{\text{disc},*}| = 3.4$ and $8.9 \times 10^{12} M_{\odot} \text{ kpc km s}^{-1}$, respectively. The bottom panels show $\mathbf{L}_{\text{disc},*}$ in increasing radial bins, from 5 to 30 kpc at $z \sim 0.3$ (left) and 0 (right). Here the angular momentum is dominated by the disc for only the first annulus, after this, the angular momentum is much smaller and is widely

distributed as a result of the small stellar disc. The direction of the stellar warp's angular momentum is aligned with the tilting direction at $z = 0$. The magnitude of the angular momentum grows rapidly at low radii, with the central bin gaining roughly three times its initial angular momentum ending with $4.8 \times 10^{12} M_{\odot} \text{ kpc km s}^{-1}$, whereas the outer bin only gains twice its initial value finishing with $5.9 \times 10^{11} M_{\odot} \text{ kpc km s}^{-1}$.

Figure 4.3 shows the angular momentum of all stars (\mathbf{L}_*) within the virial radius, but with radii larger than the disc at each time step (top), with respect to $\mathbf{L}_{\text{disc},*}$ at $z \sim 0.3$. This panel shows a drastic shift at $z \sim 0.15$ and comparing this to the evolution of stellar density, at this time a satellite falls into the halo, resulting in an order of magnitude increase from $|\mathbf{L}_*| = 1.2 \times 10^{12} M_{\odot} \text{ kpc km s}^{-1}$ to $|\mathbf{L}_*| = 4.1 \times 10^{12} M_{\odot} \text{ kpc km s}^{-1}$. The bottom left panel shows the stellar angular momentum of all stars within the virial radius, here the misaligned angular momentum of this satellite is noticeable, but steadily tends towards the final position of $\mathbf{L}_{\text{disc},*}$. The bottom right plot shows \mathbf{L}_* in radial bins at $z \sim 0.3$, where one can see that before the in infall of this satellite, the angular momentum of the disc dwarfs the misaligned angular momentum of the satellites out to 160 kpc. Starting with the inner annulus of 10 kpc the angular momentum's magnitude falls three orders of magnitude from 4 to $0.004 \times 10^{12} M_{\odot} \text{ kpc km s}^{-1}$ at the outer annulus of 140 kpc at $z = 0$.

g7.66e11: gas disc, warp and hot gas corona

Figure 4.4 shows the column density of HI in g7.66e11, with three different projections. Roškar et al. (2010) used a disc galaxy forming in a high-resolution fully cosmological simulation and found that the cool gas accreting at the virial radius starts out with misaligned angular momentum with that of the hot gas corona. As the cool gas falls further towards the disc it is torqued by the hydrodynamical forces imposed by the hot gas. By the time the cool gas reaches the disc, it has angular momentum aligned with that of the hot gas. Figure 4.5 compares the axis ratios, b/a (black) and c/a (red) of the hot gas corona versus radius (left).

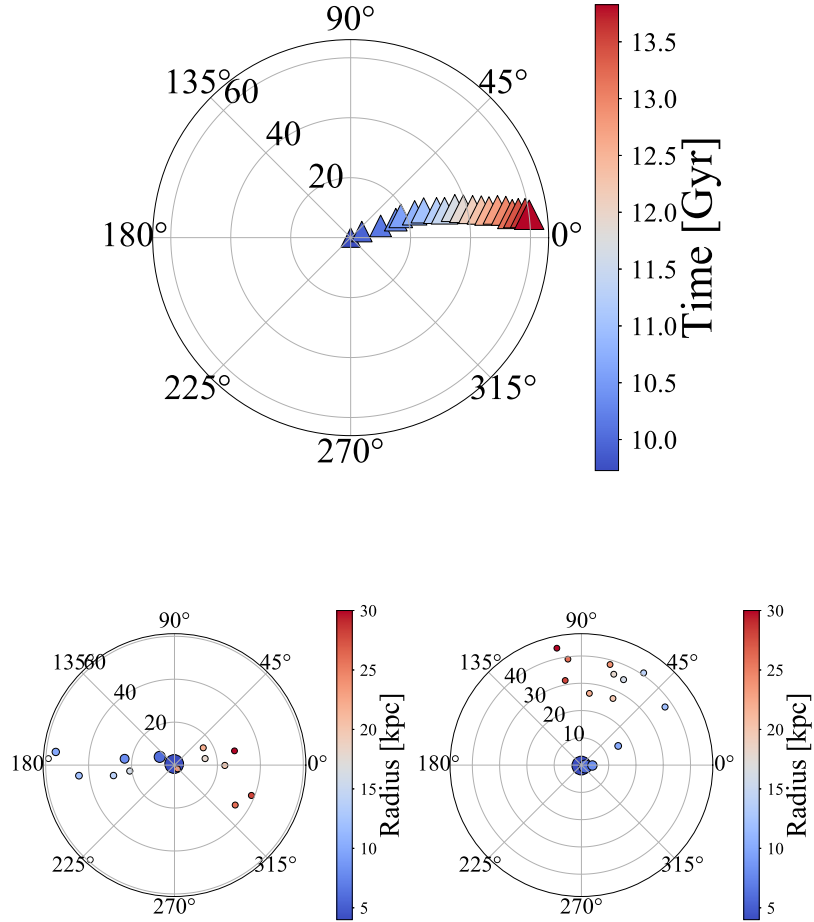


Fig. 4.2 **g7.66e11** - Top: angular momentum of the stellar disc $L_{\text{disc},*}$ at each time step (top), with respect to the angular momentum of the stellar disc at $z \sim 0.3$. Bottom left & right: $L_{\text{disc},*}$ within annuli of increasing radii from 5 to 30 kpc, with a width of 2 kpc, at $z \sim 0.3$ (left) and at $z = 0$ (right). Each bottom panel is shown with respect to the stellar angular momentum of the disc at their respective time steps. The size of each point indicates the magnitude of the angular momentum vector, the colour denotes its position in the time (top) or radial (bottom) sequence, dark blue being the start ($z \sim 0.3$ or $R = 5$ kpc) and dark red being the end ($z = 0$ or $R = 30$ kpc). The majority of the angular momentum is within $R = 15$ kpc, and the tilting direction is close to linear.

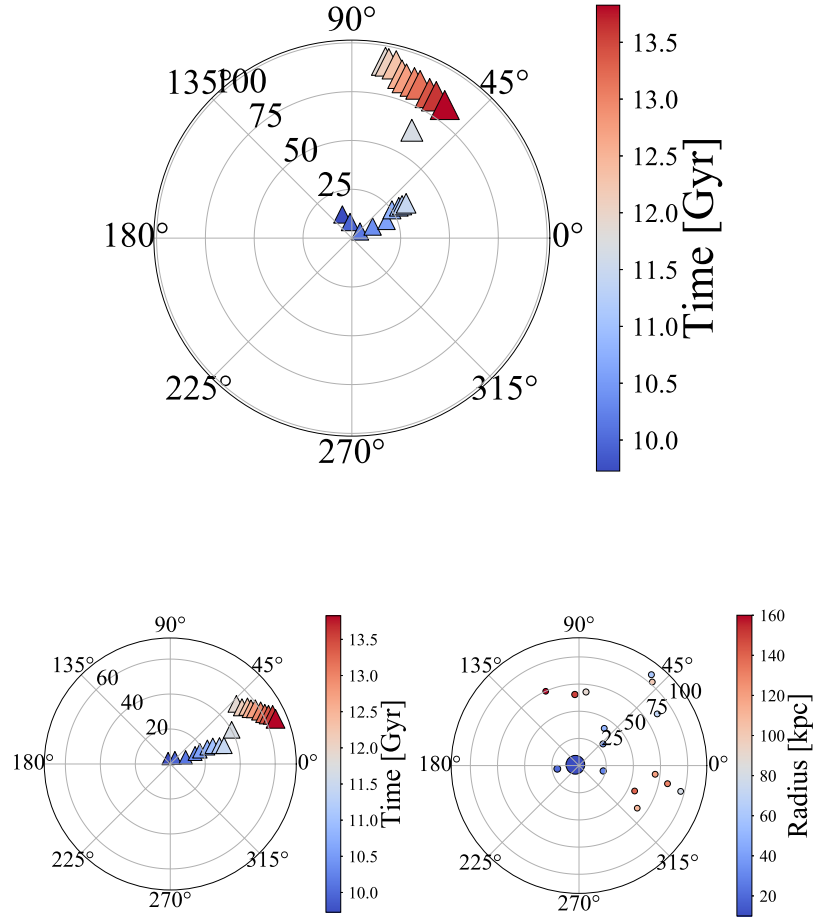


Fig. 4.3 **g7.66e11** - Top: angular momentum of all the stars L_* outside the disc and within the virial radius ($R_{\text{warp}} < R_* < R_{200}$) at each time step, with respect to the angular momentum of the stellar disc at $z \sim 0.3$. Bottom left: L_* for all stars within the virial radius R_{200} at each time step (left), with respect to the angular momentum of the stellar disc at $z \sim 0.3$. Bottom right: L_* within annuli of increasing radii from 10 to 160 kpc, with a width of 10 kpc (right) at $z = 0$, with respect to the angular momentum of the stellar disc at $z = 0$. The size of each point indicates the magnitude of the angular momentum vector, the colour denotes its position in the time (top) or radial (bottom) sequence, dark blue being the start ($z \sim 0.3$ or $R = 10$ kpc) and dark red being the end ($z = 0$ or $R = 160$ kpc). There is a drastic shift at $z \sim 0.15$ and comparing this to the evolution of stellar density, at this time a satellite falls into the halo.

4.3 Substructure driven tilting

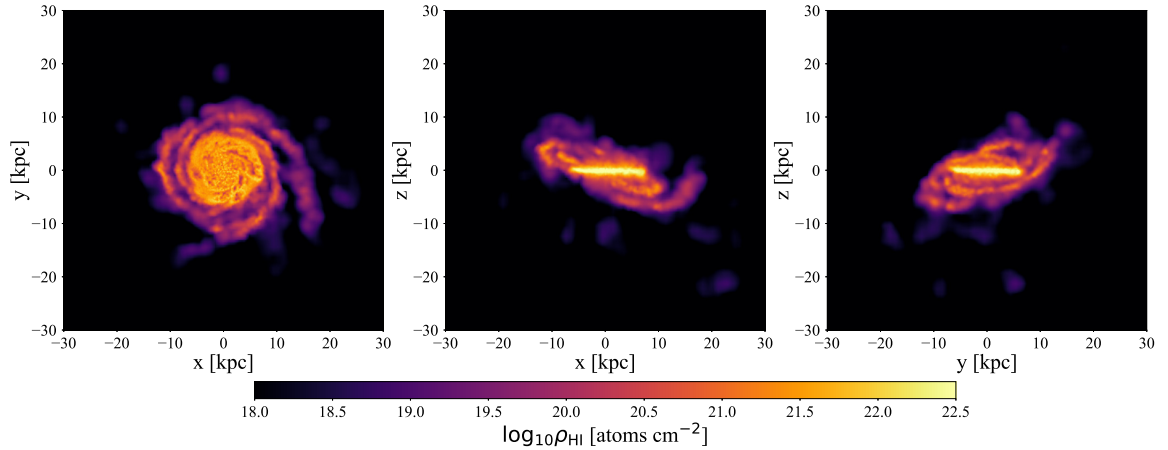


Fig. 4.4 **g7.66e11** - HI column density maps at $z = 0$, projected into the x - y -, x - z - and y - z -planes.

Here there is a transition between a more oblate shape to a more triaxial shape at 8 kpc. It is unlikely that the shape of the hot gas corona is directly responsible for the changing angular momentum direction of the infalling cool gas via gravitational torques, in agreement with Roškar et al. (2010). The right panel shows the angle between the hot gas corona's angular momentum and the angular momentum of the cool gas at $z \sim 0.3$ (black) and 0 (red). At both time steps the two components become misaligned at a radius of ~ 9 kpc, comparable to the radius at which the corona becomes more triaxial. As the cool gas falls further into the halo, it becomes more aligned with the hot gas.

Figure 4.6 shows the angular momentum of the warp \mathbf{L}_{warp} at each time step (top), with respect to $\mathbf{L}_{\text{disc},*}$ at $z \sim 0.3$. Here one can see the warp's angular momentum is oriented between $\mathbf{L}_{\text{disc},*}$ and \mathbf{L}_* outside the disc, at $z = 0$. In the first few time steps, however, \mathbf{L}_{warp} has a very different alignment and much lower total angular momentum. It is possible that before $z \sim 0.3$ there was another accretion event that might have formed this warp. The bottom left and right panels show the angular momentum of the cool gas \mathbf{L}_{gas} in annular bins from 5 to 30 kpc, with a width of 2 kpc, at $z \sim 0.3$ and 0, respectively. At the first time step \mathbf{L}_{gas} appears to be aligned very differently from the last time step where \mathbf{L}_{gas} is now

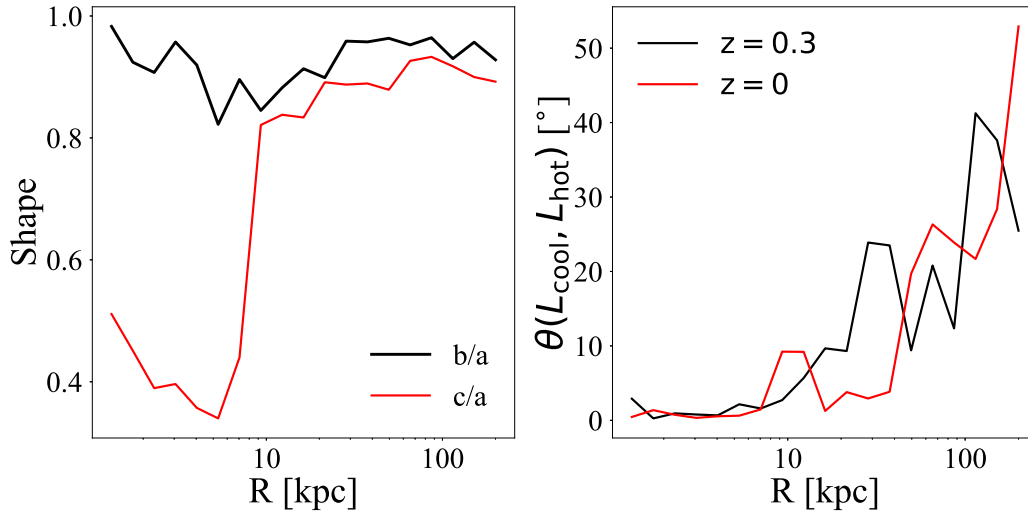


Fig. 4.5 **g7.66e11** - Left: the axis ratios b/a (black) and c/a (red) at $z \sim 0.3$, right: the angle between the cool ($T < 20,000\text{K}$) and hot ($T > 50,000\text{K}$) gas's angular momentum vectors, at $z \sim 0.3$ (black) and $z = 0$ (red). There is a transition between a more oblate shape to a more triaxial shape at 8 kpc.

aligned with the tilting direction of the stellar disc. By $z = 0$ the angular momentum of the cool gas within 10 kpc has become aligned with the tilting direction of the disc.

Figure 4.7 shows the angular momentum of the hot gas corona $\mathbf{L}_{\text{corona}}$ at each time step (top), with respect to $\mathbf{L}_{\text{disc},*}$ at $z \sim 0.3$. The angular momentum tilts in a single direction throughout all the time steps, slowing towards $z = 0$. Here again, it is possible to see that the most drastic change comes around the same time $z \sim 0.15$. The angular momentum of the corona does not seem to be indicative of the tilting direction of the stellar disc. However, it might help explain the offset between the angular momentum of the cool gas warp and the stellar disc, providing gas with angular momentum misaligned with the disc in a similar direction to the warp, with respect to the stellar disc. The bottom left and right panels show \mathbf{L}_{gas} in radial bins ranging from 40 to 200 kpc, with widths of 20 kpc, at $z \sim 0.3$ and 0, respectively. The panels show that \mathbf{L}_{gas} varies with radius and the angular momentum's magnitude increases within every bin, with an average of 2.8 and $3.2 \times 10^{13} M_{\odot} \text{ kpc km s}^{-1}$

4.3 Substructure driven tilting

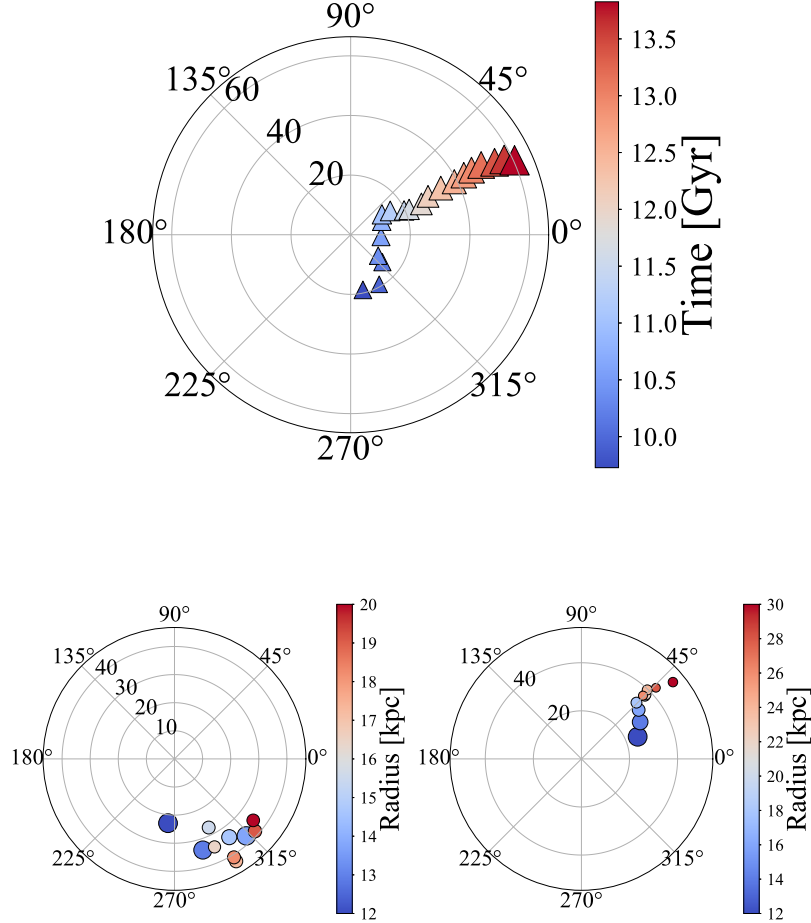


Fig. 4.6 **g7.66e11** - Top: angular momentum of the cool gas ($T < 20,000\text{K}$) beyond the stellar disc L_{warp} within 30 kpc ($R_{\text{warp}} < R_{\text{gas}} < 30$ kpc) at each time step, with respect to the angular momentum of the stellar disc at $z \sim 0.3$. Bottom left & right: L_{gas} for cool gas within annuli of increasing radii from 10 to 30 kpc, with a width of 2 kpc, at $z \sim 0.3$ (left) and at $z = 0$ (right). Both bottom panels are shown with respect to the angular momentum of the stellar disc at their respective time steps. The size of each point indicates the magnitude of the angular momentum vector, the colour denotes its position in the time (top) or radial (bottom) sequence, dark blue being the start ($z \sim 0.3$ or $R = 5$ kpc) and dark red being the end ($z = 0$ or $R = 30$ kpc). The warp does not seem to have angular momentum that aligns with the tilting direction.

for $z \sim 0.3$ and 0, respectively. The hot gas corona's angular momentum is not aligned with the tilting direction of the disc.

g7.66e11: dark matter halo

Figure 4.8 shows the angular momentum of the dark matter halo \mathbf{L}_{dark} at each time step (top), with respect to $\mathbf{L}_{\text{disc},*}$ at $z \sim 0.3$. The same drastic change at $z \sim 0.15$ is found here. The bottom panels show \mathbf{L}_{dark} in radial bins of increasing radii from 0 to 200 kpc with a width of 10 kpc. The angular momentum of the dark matter does not seem to be aligned with the disc at any time step or radial bin. However, at $z = 0$ the innermost annuli do seem more aligned with the total stellar angular momentum than that $z \sim 0.3$.

g7.66e11: integrated net gas flow

Figure 4.9 shows net flow of angular momentum in gas $\mathbf{L}_{\text{flow,gas}}$ crossing shells of increasing radius from 5 to 30 kpc, with 5 kpc spacing (top), with respect to $\mathbf{L}_{\text{disc},*}$ at $z \sim 0.3$. The panel shows that $\mathbf{L}_{\text{flow,gas}}$ becomes more aligned with \mathbf{L}_{warp} and $\mathbf{L}_{\text{corona}}$ at higher radii and more aligned with $\mathbf{L}_{\text{disc},*}$ at lower radii. This is likely a symptom of cool gas within the disc falling to smaller radii. The bottom left panel shows $\mathbf{L}_{\text{flow,gas}}$ with shells of radius 40 to 140 kpc with 20 kpc separation. Following a similar trend to the top panel, $\mathbf{L}_{\text{flow,gas}}$ becomes more aligned with $\mathbf{L}_{\text{corona}}$ at higher radii. The bottom right plot shows the magnitude of angular momentum passing through each shell, illustrating that at higher radii the amount of angular momentum crossing each shell is higher. Although these plots do not help identify the driving mechanism behind the tilting in this galaxy, they do show the gas becoming aligned with the disc as it cools from the corona.

4.3 Substructure driven tilting

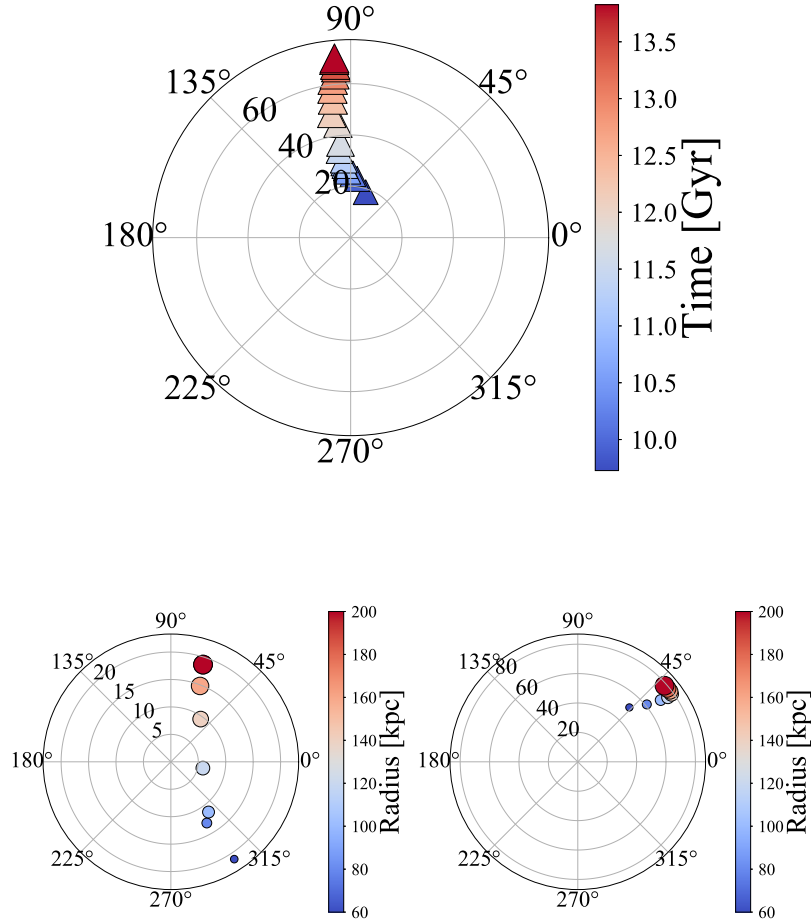


Fig. 4.7 **g7.66e11** - Top: angular momentum of the hot gas ($T > 50,000\text{K}$) beyond 40 kpc L_{corona} within the virial radius ($40\text{kpc} < R_{\text{gas}} < R_{200}$) at each time step, with respect to the angular momentum of the stellar disc at $z \sim 0.3$. Bottom left & right: L_{gas} for hot gas within annuli of increasing radii from 40 to 200 kpc, with a width of 20 kpc, at $z \sim 0.3$ (left) and at $z = 0$ (right). Both bottom panels are shown with respect to the angular momentum of the stellar disc at their respective time steps. The size of each point indicates the magnitude of the angular momentum vector, the colour denotes its position in the time (top) or radial (bottom) sequence, dark blue being the start ($z \sim 0.3$ or $R = 40$ kpc) and dark red being the end ($z = 0$ or $R = 200$ kpc).

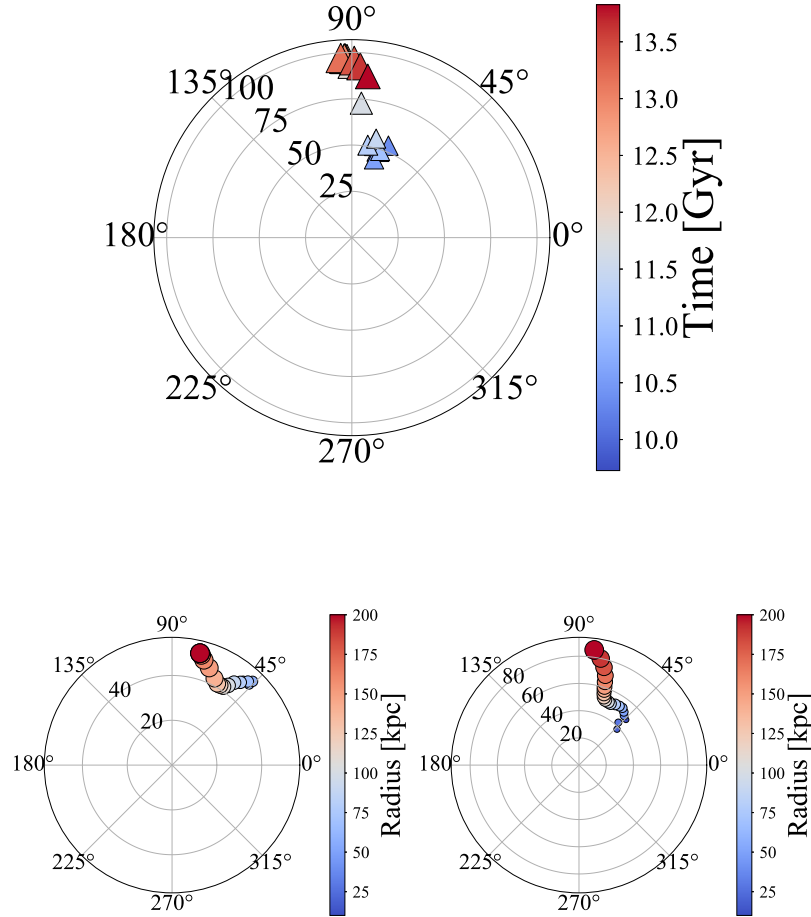


Fig. 4.8 **g7.66e11** - Top: angular momentum of the halo L_{dark} within the virial radius ($R_{\text{dark}} < R_{200}$) at each time step, with respect to the angular momentum of the stellar disc at $z \sim 0.3$. Bottom left & right: L_{dark} within annuli of increasing radii from 10 to 200 kpc, with a width of 10 kpc, at $z \sim 0.3$ (left) and at $z = 0$ (right). Both bottom panels are shown with respect to the angular momentum of the stellar disc at their respective time steps. The size of each point indicates the magnitude of the angular momentum vector, the colour denotes its position in the time (top) or radial (bottom) sequence, dark blue being the start ($z \sim 0.3$ or $R = 10$ kpc) and dark red being the end ($z = 0$ or $R = 200$ kpc). The angular momentum of the dark matter halo is not aligned with the tilting direction of the disc.

4.3 Substructure driven tilting

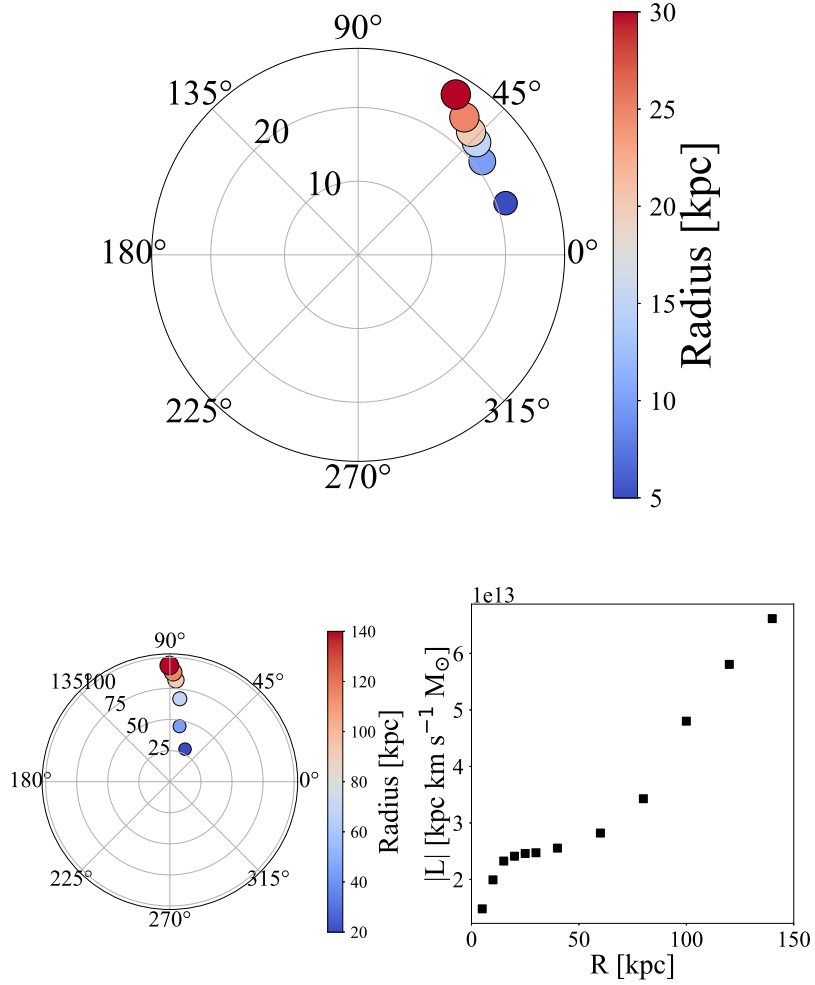


Fig. 4.9 **g7.66e11** - Top: integrated net flow of angular momentum in gas $L_{\text{flow,gas}}$ crossing shells of increasing radius from 5 to 30 kpc, with a separation of 5 kpc at each time step, with respect to the angular momentum of the stellar disc at $z \sim 0.3$. Bottom left & right: $L_{\text{flow,gas}}$ crossing shells of increasing radius from 40 to 140 kpc, with a separation of 20 kpc at each time step (left), with respect to the angular momentum of the stellar disc at $z \sim 0.3$ and the magnitude of the angular momentum vectors $|L_{\text{flow,gas}}|$ versus the shell radius (right). The size of each point indicates the magnitude of the angular momentum vector, the colour denotes its position in the radial sequence, dark blue being the smallest radius and dark red being the largest radius. The inflow of angular momentum within ~ 10 kpc is aligned with the tilting direction of the disc.

g7.66e11: integrated net stellar flow

Figure 4.10 shows the net angular momentum of stars $\mathbf{L}_{\text{flow,star}}$ crossing shells of increasing radii from 5 to 30 kpc, with a separation of 5 kpc. The bottom left and right panels show $\mathbf{L}_{\text{flow,star}}$ crossing shells with radii ranging from 40 to 140 kpc, with 20 kpc separation and $|\mathbf{L}_{\text{flow,star}}|$, respectively. The combination of these plots shows there is a large amount of angular momentum crossing the shells of $R \sim 50$ kpc, this angular momentum is aligned with the tilting direction of the stellar disc. Furthermore, the angular momentum of all stars that are beyond 50 kpc at $z \sim 0.3$ but cross this radius over the period, have angular momentum that is aligned with the tilting direction of the stellar disc.

g7.66e11: summary

The stellar disc of this galaxy gains a large amount of angular momentum between $z \sim 0.3$ and 0 and tilts with a rate far higher than any other galaxy in this sample. The angular momentum of gas reaching the disc does not appear to be the driving the tilting of the stellar disc. A more likely scenario is that the interaction with a satellite, which has angular momentum aligned with the tilting direction, is the main contributor of misaligned angular to the disc. Between $z \sim 0.3$ and 0, both the stellar and cool gas warps become aligned with the tilting direction of the disc. In the MW a comparable interaction would be with the Sagittarius Dwarf Spheroidal Galaxy (Sgr dSph). Bailin (2003) argued that the stellar warp of the MW was formed from the interaction with the Sgr dSph, finding that their angular momenta were aligned, in a similar fashion to this galaxy. In this case, the direction of the MW's tilt would be predictable using the angular momentum of the stellar warp.

4.3 Substructure driven tilting

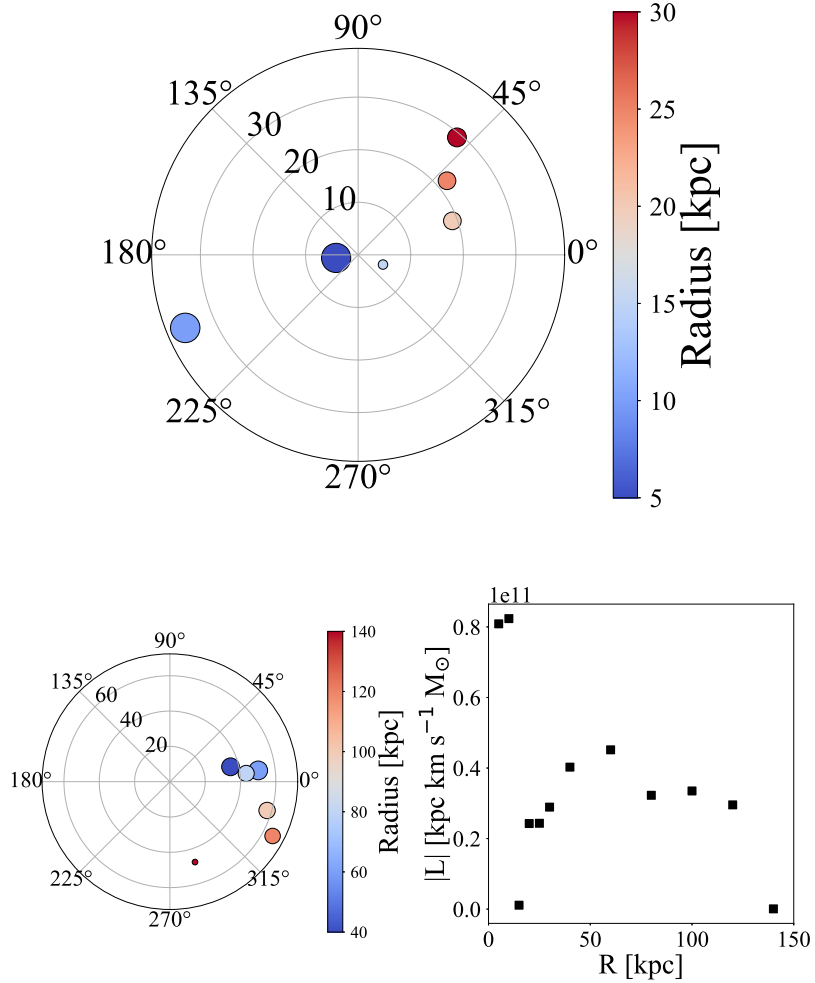


Fig. 4.10 **g7.66e11** - Top: integrated net flow of angular momentum in star particles $\mathbf{L}_{\text{flow},*}$ crossing shells of increasing radius from 5 to 30 kpc, with a separation of 5 kpc at each time step, with respect to the angular momentum of the stellar disc at $z \sim 0.3$. Bottom left & right: $\mathbf{L}_{\text{flow},*}$ crossing shells of increasing radius from 40 to 140 kpc, with a separation of 20 kpc at each time step (left), with respect to the angular momentum of the stellar disc at $z \sim 0.3$ and the magnitude of the angular momentum vectors $|\mathbf{L}_{\text{flow},*}|$ versus the shell radius (right). The size of each point indicates the magnitude of the angular momentum vector, the colour denotes its position in the radial sequence, dark blue being the smallest radius and dark red being the largest radius. The angular momentum of infalling stars is not aligned with the tilting direction of the disc.

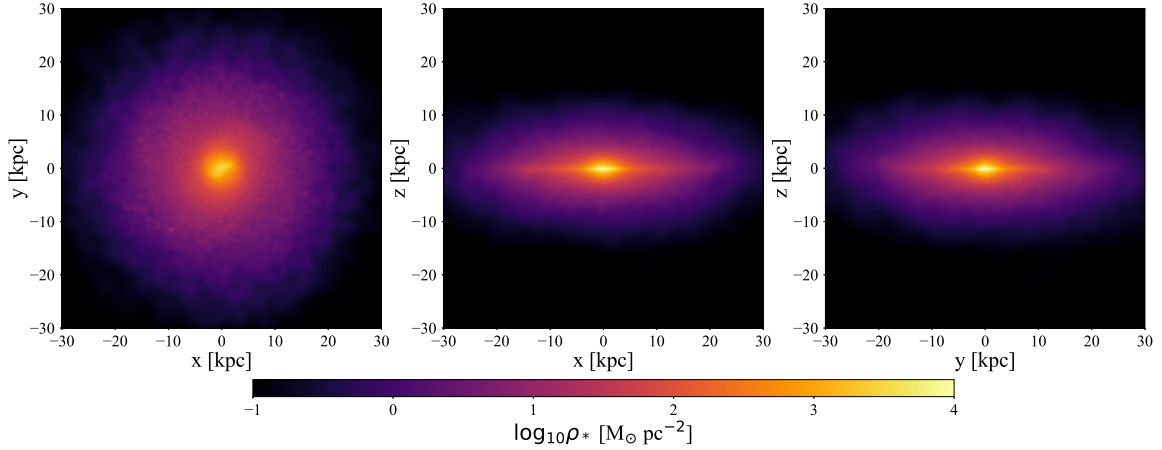


Fig. 4.11 **g8.26e11** - Stellar surface density maps at $z = 0$, projected into the x - y -, x - z - and y - z -planes.

4.3.2 Galaxy: g8.26e11

Galaxy g8.26e11 is a late-type with comparable mass and circular velocity to the MW. It sits in the middle of the sample with the median stellar and halo masses with $M_{\text{disc},*} = 4.6 \times 10^{10} M_\odot$ and $M_{200} = 1.02 \times 10^{12} M_\odot$. This galaxy has a much lower tilting rate than the other hierarchically driven galaxy, with $\Delta\theta/\Delta t \sim 2.2^\circ \text{Gyr}^{-1}$. Figure 4.11 shows the stellar surface density of g8.26e11.

g8.26e11: stellar disc and satellites

Figure 4.12 shows the angular momentum of the stellar disc $\mathbf{L}_{\text{disc},*}$ at each time step (top), with respect to $\mathbf{L}_{\text{disc},*}$ at $z \sim 0.3$. This panel shows that the tilting direction and rate are fairly consistent, ending at roughly 9° away from its starting location. The magnitude of the disc's angular momentum $|\mathbf{L}_{\text{disc},*}|$ increases from 2 to $2.5 \times 10^{13} M_\odot \text{kpc km s}^{-1}$, between $z \sim 0.3$ and 0; a much smaller increase than g7.66e11. The bottom left and right panels show $\mathbf{L}_{\text{disc},*}$ within annular bins of increasing radius from 5 to 30 kpc with 2 kpc widths, at $z \sim 0.3$ and 0, respectively. These two panels show a clear difference, at the first time step $\mathbf{L}_{\text{disc},*}$ is much more aligned out to 30 kpc where the maximum misalignment is $\sim 1.5^\circ$, whereas at later

4.3 Substructure driven tilting

times $\mathbf{L}_{\text{disc},*}$ becomes more warped with the misalignment at 30 kpc reaching ~ 6 kpc. The majority of the stellar angular momentum is within the first few radial bins and increases over the two time steps. For the central bin $|\mathbf{L}_{\text{disc},*}|$ increases from 5.1 to $5.5 \times 10^{12} M_{\odot} \text{ kpc km s}^{-1}$ and the outermost bin increases from 1.7 to $2.4 \times 10^{11} M_{\odot} \text{ kpc km s}^{-1}$.

Figure 4.13 shows the angular momentum of all stars outside the disc radius \mathbf{L}_* , but within the virial radius at each time step (top), with respect to $\mathbf{L}_{\text{disc},*}$ at $z \sim 0.3$. Here one can see that there is a noticeable jump between two fairly stable orientations, indicative of some interaction or accretion event. The magnitude of the angular momentum in all stars outside the disc radius increases from 5.4 to $6 \times 10^{12} M_{\odot} \text{ kpc km s}^{-1}$, much lower than $|\mathbf{L}_{\text{disc},*}|$. This is reflected in the bottom left plot, which shows the change in angular momentum of all stars inside the virial radius. For this panel, the change in total angular momentum is dominated by the disc and one can see that \mathbf{L}_* has become much more aligned with $\mathbf{L}_{\text{disc},*}$ at $z = 0$, hinting that an exchange of angular momentum has taken place. Again the bottom right panel highlights the dominance of the stellar disc, showing the angular momentum in radial bins from 10 to 160 kpc, with a width of 10 kpc. The angular momentum's magnitude within each bin is much greater for the inner bins reaching $1.5 \times 10^{13} M_{\odot} \text{ kpc km s}^{-1}$ and falling quickly to $3.9 \times 10^{10} M_{\odot} \text{ kpc km s}^{-1}$ for the outermost bin.

g8.26e11: gas disc, warp and hot corona

Figure 4.14 shows the column density of HI in g8.26e11 and Figure 4.15 compares the axis ratios, b/a (black) and c/a (red) of the hot gas corona versus radius (left). The transition between oblate and spheroidal is hard to determine due to the substructure, it occurs between 8 and 20 kpc. The right panel shows the angle between the hot gas corona's angular momentum and the angular momentum of the cool gas at $z \sim 0.3$ (black) and 0 (red). Here the hot and cool gas seem to be well aligned out to ~ 30 kpc.

Figure 4.16 shows the angular momentum of the warp \mathbf{L}_{warp} at each time step (top), with

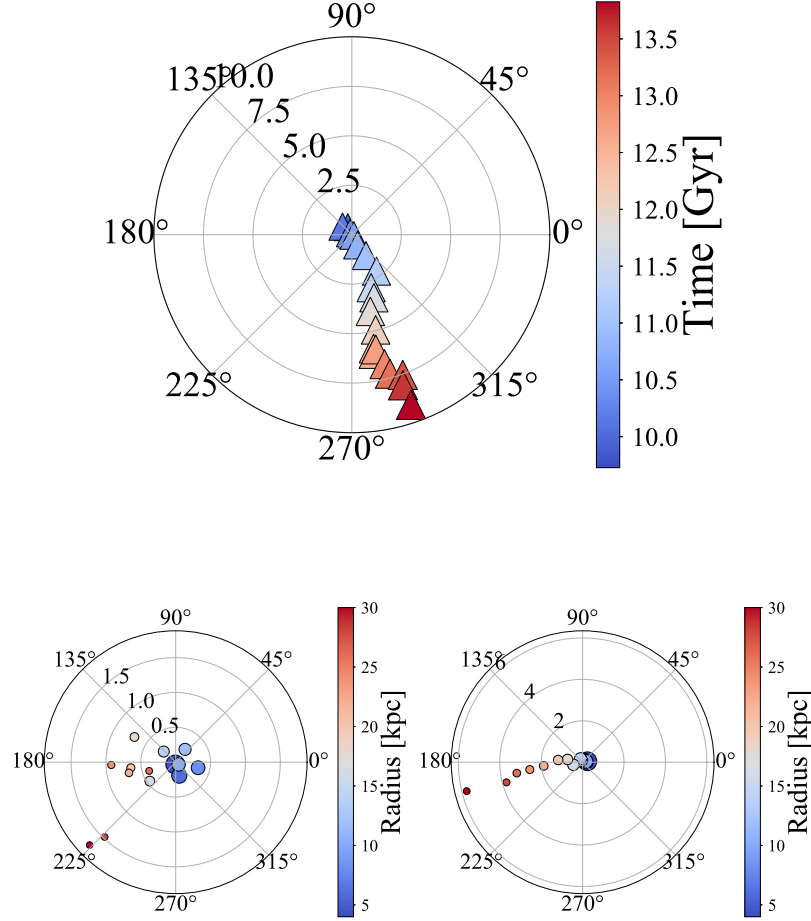


Fig. 4.12 **g8.26e11** - Top: angular momentum of the stellar disc $L_{\text{disc},*}$ at each time step (top), with respect to the angular momentum of the stellar disc at $z \sim 0.3$. Bottom left & right: $L_{\text{disc},*}$ within annuli of increasing radii from 5 to 30 kpc, with a width of 2 kpc, at $z \sim 0.3$ (left) and at $z = 0$ (right). Each bottom panel is shown with respect to the stellar angular momentum of the disc at their respective time steps. The size of each point indicates the magnitude of the angular momentum vector, the colour denotes its position in the time (top) or radial (bottom) sequence, dark blue being the start ($z \sim 0.3$ or $R = 5$ kpc) and dark red being the end ($z = 0$ or $R = 30$ kpc). The disc is aligned within 30 kpc for $z = 0.3$ but by $z = 0$ a slight warp has developed towards 190° . The tilting direction is uniform and is not aligned with the stellar warp.

4.3 Substructure driven tilting

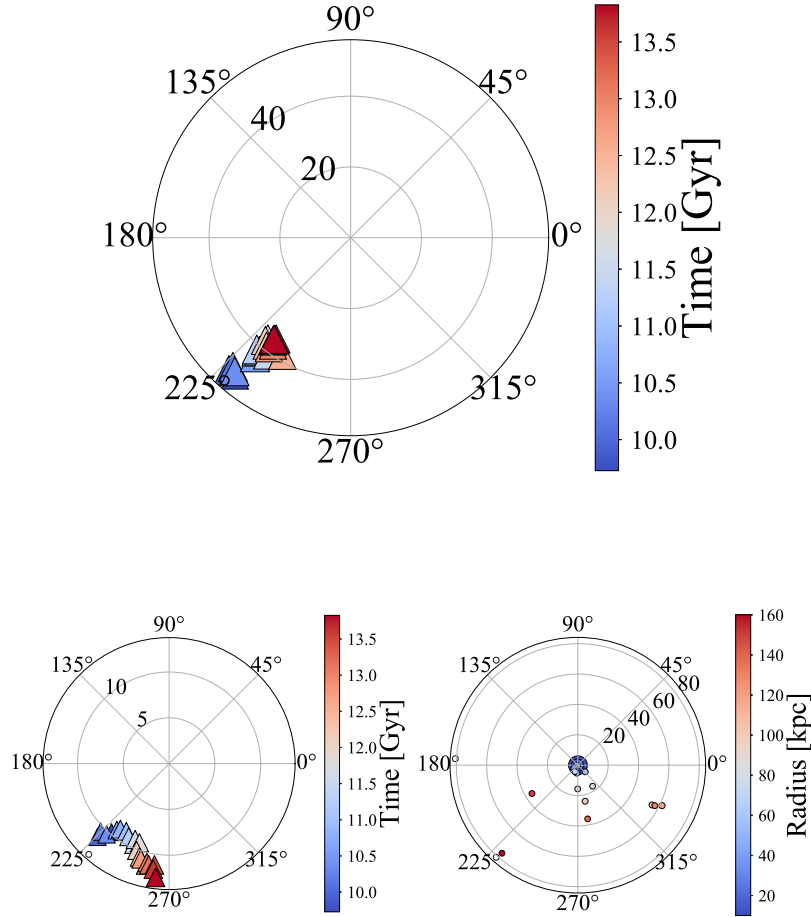


Fig. 4.13 **g8.26e11** - Top: angular momentum of all the stars L_* outside the disc and within the virial radius ($R_{\text{warp}} < R_* < R_{200}$) at each time step, with respect to the angular momentum of the stellar disc at $z \sim 0.3$. Bottom left: L_* for all stars within the virial radius R_{200} at each time step (left), with respect to the angular momentum of the stellar disc at $z \sim 0.3$. Bottom right: L_* within annuli of increasing radii from 10 to 160 kpc, with a width of 10 kpc (right) at $z = 0$, with respect to the angular momentum of the stellar disc at $z = 0$. The size of each point indicates the magnitude of the angular momentum vector, the colour denotes its position in the time (top) or radial (bottom) sequence, dark blue being the start ($z \sim 0.3$ or $R = 10$ kpc) and dark red being the end ($z = 0$ or $R = 160$ kpc). The angular momentum of all stars inside the halo is not aligned with the tilting direction of the disc.

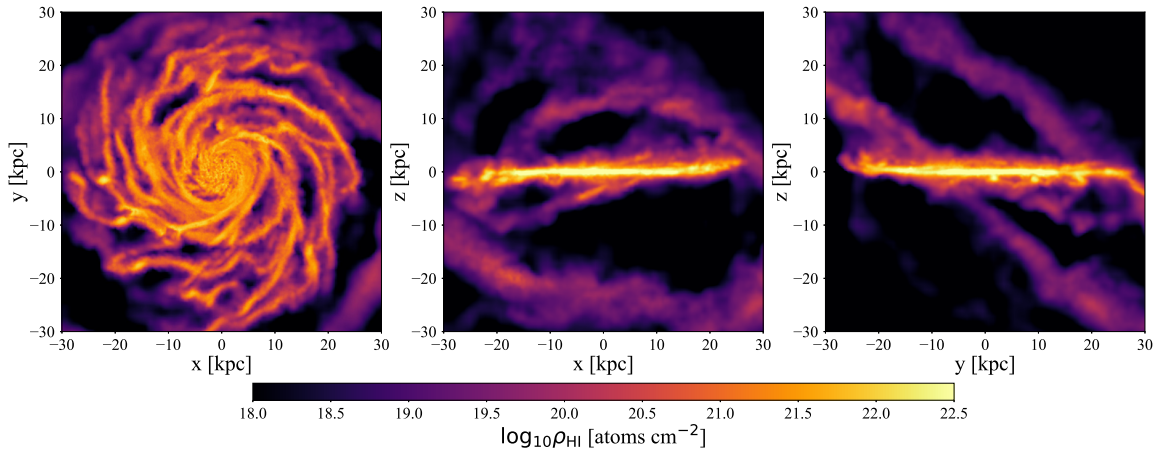


Fig. 4.14 **g8.26e11** - HI column density maps at $z = 0$, projected into the x - y -, x - z - and y - z -planes.

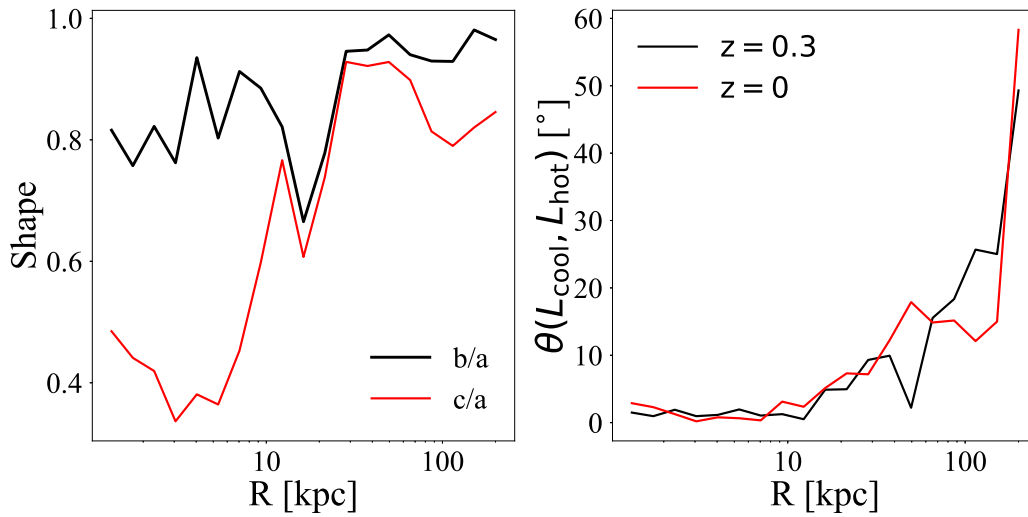


Fig. 4.15 **g8.26e11** - Left: the axis ratios b/a (black) and c/a (red) at $z \sim 0.3$, right: the angle between the cool ($T < 20,000\text{K}$) and hot ($T > 50,000\text{K}$) gas's angular momentum vectors, at $z \sim 0.3$ (black) and $z = 0$ (red). The transition between oblate and spheroidal occurs between 8 and 20 kpc.

4.3 Substructure driven tilting

respect to $\mathbf{L}_{\text{disc},*}$ at $z \sim 0.3$. The warp's angular momentum is misaligned with $\mathbf{L}_{\text{disc},*}$ in the direction of the total stellar angular momentum and the stellar warp at $z = 0$. The magnitude of \mathbf{L}_{warp} increases by a large amount, starting at 2.2 and finishing at $3.9 \times 10^{13} M_{\odot} \text{ kpc km s}^{-1}$. The bottom left and right panels show the angular momentum of the cool gas in annuli of increasing radius from 10 to 30 kpc with widths of 2 kpc, at $z \sim 0.3$ and 0, respectively. These panels show that the extent of the misalignment of \mathbf{L}_{warp} increases with time. The magnitude of \mathbf{L}_{warp} in the centre decreases from 7.5 to $5.5 \times 10^{12} M_{\odot} \text{ kpc km s}^{-1}$, whereas at $28 < r < 30$ it increases from 2.7 to $4.7 \times 10^{12} M_{\odot} \text{ kpc km s}^{-1}$. Such an increase in the warp is not likely to be caused by the gradual cooling of gas from the corona, which would not be expected to increase the angular momentum of the warp by such a large fraction. A more plausible scenario is the accretion of gas from a satellite.

Figure 4.17 shows the angular momentum of the hot gas corona $\mathbf{L}_{\text{corona}}$ at each time step (top), with respect to $\mathbf{L}_{\text{disc},*}$ at $z \sim 0.3$. This panel shows the steady evolution of $\mathbf{L}_{\text{corona}}$, which does not seem to be aligned with the warp but does seem to end aligned in a similar direction to the tilting direction of the stellar disc. The bottom left and right panels show $\mathbf{L}_{\text{corona}}$ in annuli starting with a radius of 40 kpc and ending at 200 kpc, with widths of 20 kpc, at $z \sim 0.3$ and 0, respectively. This panel shows that the majority of angular momentum in the corona is within the highest radial bins. Only the magnitude of the angular momentum at high radii increases, with the largest bin increasing from 1.5 to $1.8 \times 10^{14} M_{\odot} \text{ kpc km s}^{-1}$. For the smallest bins, the angular momentum decreases, from 7 to $4 \times 10^{12} M_{\odot} \text{ km s}^{-1}$ and on average there is a decrease from 8.3 to $7.9 \times 10^{13} M_{\odot}$.

g8.26e11: dark matter halo

Figure 4.18 shows the angular momentum of the dark matter halo (\mathbf{L}_{dark}) at each time step (top), with respect to $\mathbf{L}_{\text{disc},*}$ at $z \sim 0.3$. Similar to the jump seen in figure 4.13, again, there is a jump between two seemingly stable orientations. The angular momentum of

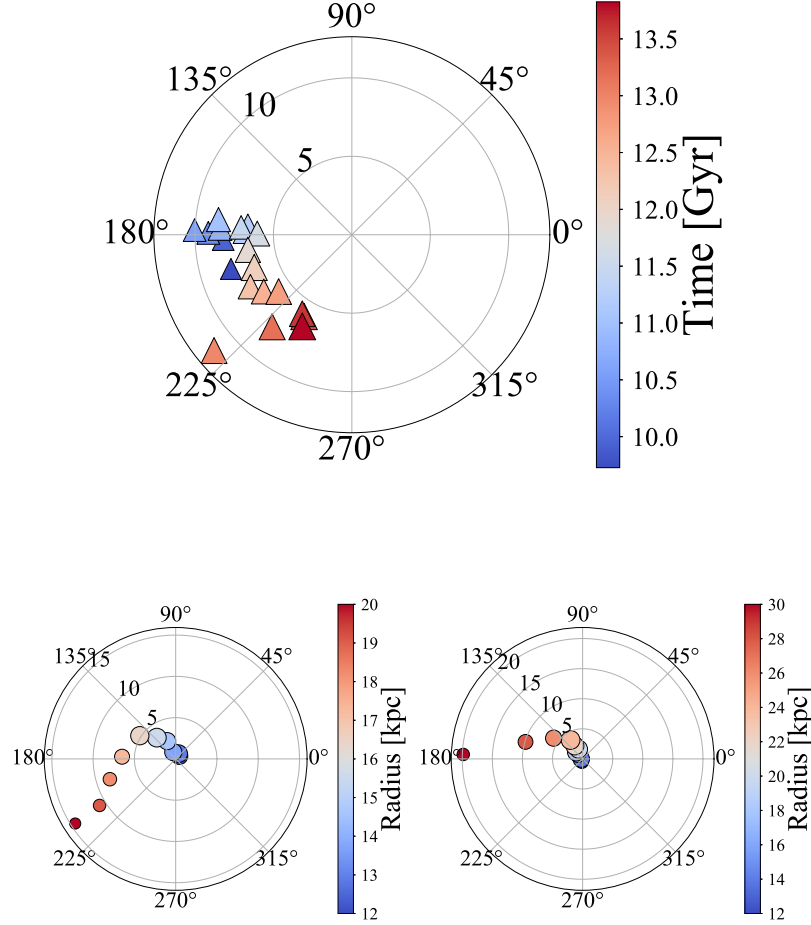


Fig. 4.16 **g8.26e11** - Top: angular momentum of the cool gas ($T < 20,000\text{K}$) beyond the stellar disc \mathbf{L}_{warp} within 30 kpc ($R_{\text{warp}} < R_{\text{gas}} < 30$ kpc) at each time step, with respect to the angular momentum of the stellar disc at $z \sim 0.3$. Bottom left & right: \mathbf{L}_{gas} for cool gas within annuli of increasing radii from 10 to 30 kpc, with a width of 2 kpc, at $z \sim 0.3$ (left) and at $z = 0$ (right). Both bottom panels are shown with respect to the angular momentum of the stellar disc at their respective time steps. The size of each point indicates the magnitude of the angular momentum vector, the colour denotes its position in the time (top) or radial (bottom) sequence, dark blue being the start ($z \sim 0.3$ or $R = 5$ kpc) and dark red being the end ($z = 0$ or $R = 30$ kpc). The cool gas warp is aligned with the stellar warp, but not the tilting direction of the disc.

4.3 Substructure driven tilting

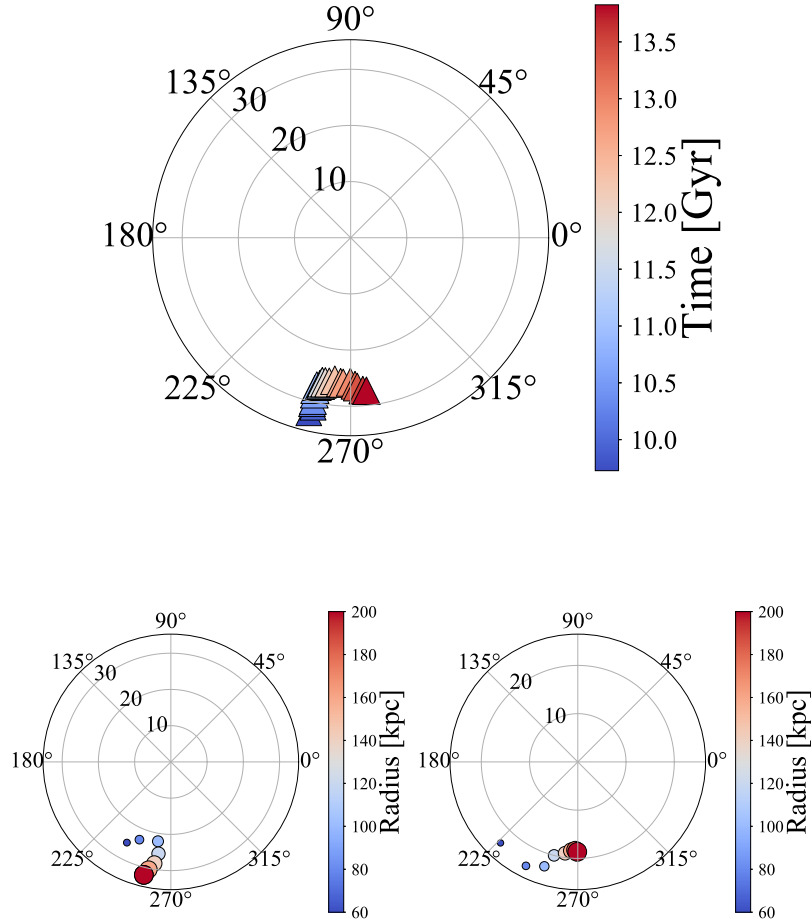


Fig. 4.17 **g8.26e11** - Top: angular momentum of the hot gas ($T > 50,000\text{K}$) beyond 40 kpc L_{corona} within the virial radius ($40\text{ kpc} < R_{\text{gas}} < R_{200}$) at each time step, with respect to the angular momentum of the stellar disc at $z \sim 0.3$. Bottom left & right: L_{gas} for hot gas within annuli of increasing radii from 40 to 200 kpc , with a width of 20 kpc , at $z \sim 0.3$ (left) and at $z = 0$ (right). Both bottom panels are shown with respect to the angular momentum of the stellar disc at their respective time steps. The size of each point indicates the magnitude of the angular momentum vector, the colour denotes its position in the time (top) or radial (bottom) sequence, dark blue being the start ($z \sim 0.3$ or $R = 40\text{ kpc}$) and dark red being the end ($z = 0$ or $R = 200\text{ kpc}$). The angular momentum of the hot gas corona is not aligned with the tilting direction of the disc.

the dark matter halo ends very similar to L_{corona} and increases in magnitude from 1.7 to $2.2 \times 10^{15} M_{\odot} \text{ kpc km s}^{-1}$. The bottom left and right panels show L_{dark} in radial bins starting at 10 kpc and ending at 200 kpc, with widths of 10 kpc, at $z \sim 0.3$ and 0, respectively. For both figures the direction of the halo's angular momentum is orientated in a similar direction to $L_{\text{disc},*}$, however, the misalignment increases slightly from ~ 23 to $\sim 33^{\circ}$. The angular momentum of all the subhaloes is not aligned with the overall angular momentum of the halo, the main halo contributes the dominant amount of angular momentum to the dark matter within the virial radius at $z \sim 0.3$.

g8.26e11: integrated net gas flow

Figure 4.19 shows the net flow of angular momentum in gas ($L_{\text{flow,gas}}$) crossing shells of increasing radius from 5 to 30 kpc with 5 kpc separation (top), with respect to $L_{\text{disc},*}$ at $z \sim 0.3$. Here one can see that $L_{\text{flow,gas}}$ does not seem to be related to the tilting direction of the stellar disc. However, it does appear to be aligned with L_{warp} . The bottom left panel extends the top to larger radii (40 to 140 kpc), again we see a possible alignment with L_{warp} , but not with the direction of stellar disc tilting. The bottom right panel shows the magnitude of angular momentum in gas crossing each shell, the outer shells have a far greater flow of the angular momentum than the inner regions.

g8.26e11: integrated net dark matter flow

Figure 4.20 shows the net flow of angular momentum in dark matter ($L_{\text{flow,DM}}$) crossing shells of increasing radius from 20 to 200 kpc with 20 kpc separation (top), with respect to $L_{\text{disc},*}$ at $z \sim 0.3$. Here there appears to be a connection between the tilting direction of the stellar disc and the flow of angular momentum in dark matter within 20 and 40 kpc. The bottom left panel shows the angular momentum of dark matter crossing half the virial radius. All the points are clustered at the bottom half of the panel, in a similar direction to

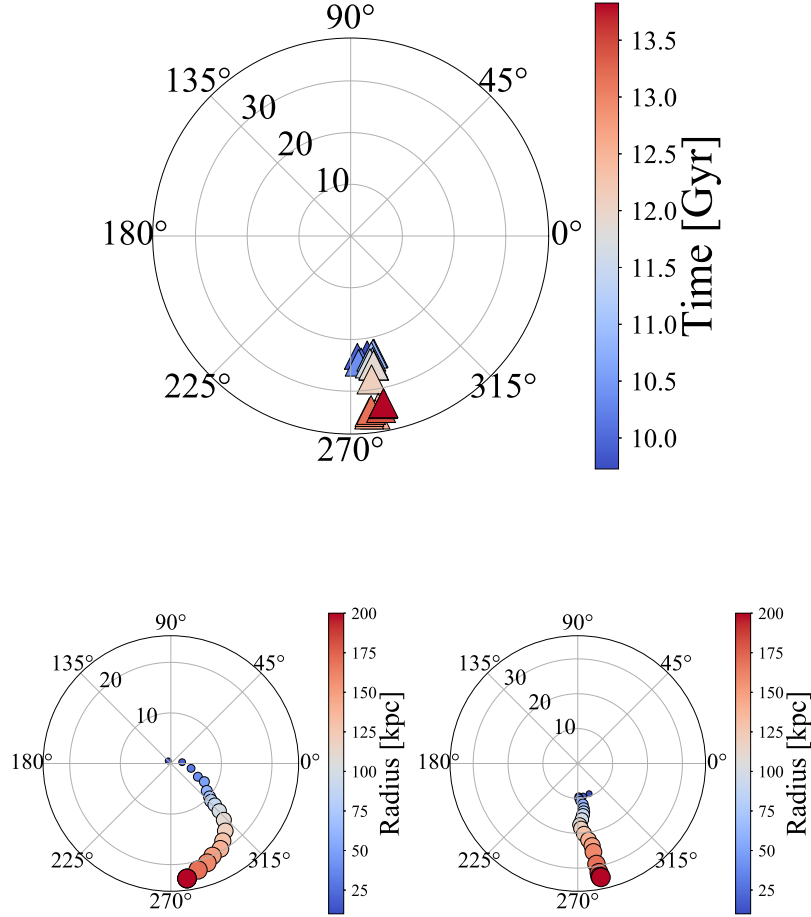


Fig. 4.18 **g8.26e11** - Top: angular momentum of the halo L_{dark} within the virial radius ($R_{\text{dark}} < R_{200}$) at each time step, with respect to the angular momentum of the stellar disc at $z \sim 0.3$. Bottom left & right: L_{dark} within annuli of increasing radii from 10 to 200 kpc, with a width of 10 kpc, at $z \sim 0.3$ (left) and at $z = 0$ (right). Both bottom panels are shown with respect to the angular momentum of the stellar disc at their respective time steps. The size of each point indicates the magnitude of the angular momentum vector, the colour denotes its position in the time (top) or radial (bottom) sequence, dark blue being the start ($z \sim 0.3$ or $R = 10$ kpc) and dark red being the end ($z = 0$ or $R = 200$ kpc). The angular momentum of the dark matter halo and its tilting direction are aligned with the tilting direction of the disc.

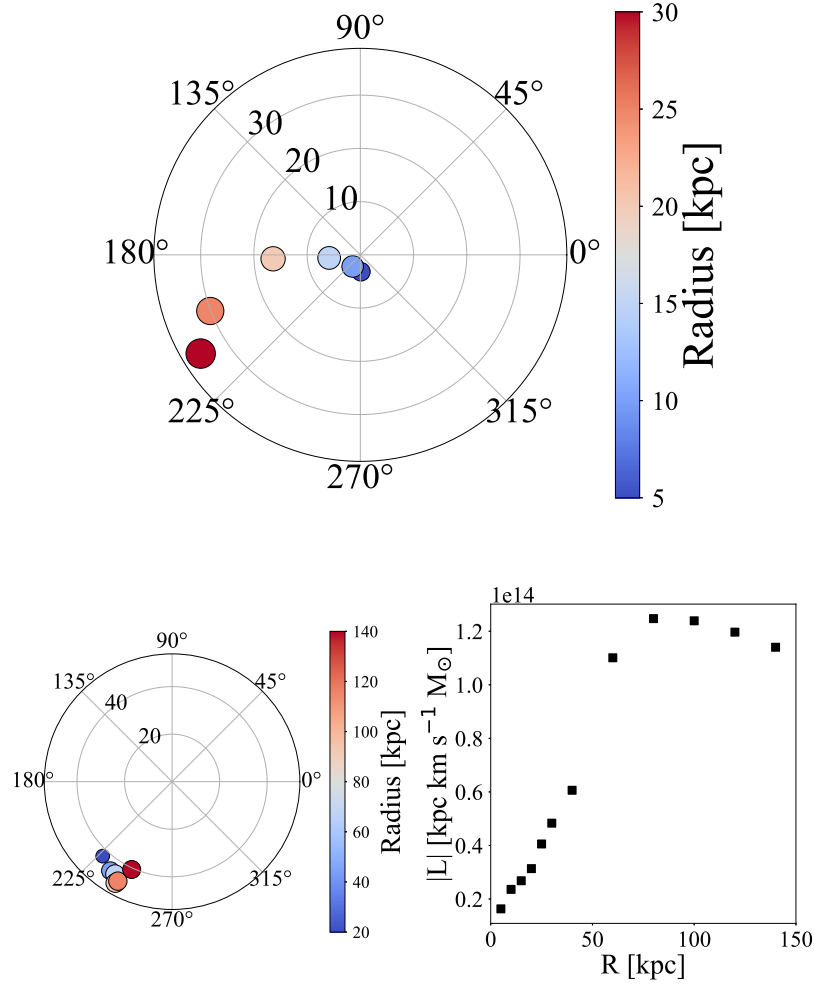


Fig. 4.19 **g8.26e11** - Top: integrated net flow of angular momentum in gas $\mathbf{L}_{\text{flow,gas}}$ crossing shells of increasing radius from 5 to 30 kpc, with a separation of 5 kpc at each time step, with respect to the angular momentum of the stellar disc at $z \sim 0.3$. Bottom left & right: $\mathbf{L}_{\text{flow,gas}}$ crossing shells of increasing radius from 40 to 140 kpc, with a separation of 20 kpc at each time step (left), with respect to the angular momentum of the stellar disc at $z \sim 0.3$ and the magnitude of the angular momentum vectors $|\mathbf{L}_{\text{flow,gas}}|$ versus the shell radius (right). The size of each point indicates the magnitude of the angular momentum vector, the colour denotes its position in the radial sequence, dark blue being the smallest radius and dark red being the largest radius. The angular momentum of inflowing gas is not aligned with the tilting direction of the disc.

4.3 Substructure driven tilting

the tilting direction of the stellar disc. The bottom right panel shows the magnitude of the angular momentum crossing each radial bin, there is a large amount of angular momentum crossing all radii. Such a large amount of angular momentum moving within the halo might explain the tilting of this disc.

Summary: g8.26e11

For this galaxy, only the angular momentum of the dark matter halo and hot gas corona seem to be aligned with tilting direction of the stellar disc. However, the misalignment between L_{dark} and $L_{\text{disc,*}}$ actually increases by $\sim 10^\circ$, whereas the misalignment between the stellar disc and L_{corona} reduces by $\sim 10^\circ$. The change in angular momentum of the dark matter halo seemed to be dominated by a single event where the angular momentum changed its alignment between two time steps. The warp of this galaxy is dominated by material stripped from of a satellite. When viewing the simulation this is indeed visible and helps to justify the misalignment between the corona, warp and tilting direction of the stellar disc. By following the angular momentum of the satellite, at $z \sim 0.3$ it was aligned with the angular momentum of the warp. The inflow of stars was also considered for g7.66e11, however, it was found to align with the warp, even when considering stars as old as 7 Gyr. Clearly the warp is contributing misaligned gas and stars to the disc, however, the magnitude of the angular momentum is not large enough to counter the amount of angular momentum in dark matter reaching the disc. This galaxy has the lowest sSFR in the sample, indicating that the amount of cool gas that reaches the disc is low. The dark matter plays a role in the tilting direction of the disc, however, it is not driven by the same processes associated with the dark matter halo (i.e. dynamical fraction or torquing). In this case, the tilting is driven by the accretion of dark matter, which contributes misaligned angular momentum to the stellar disc.

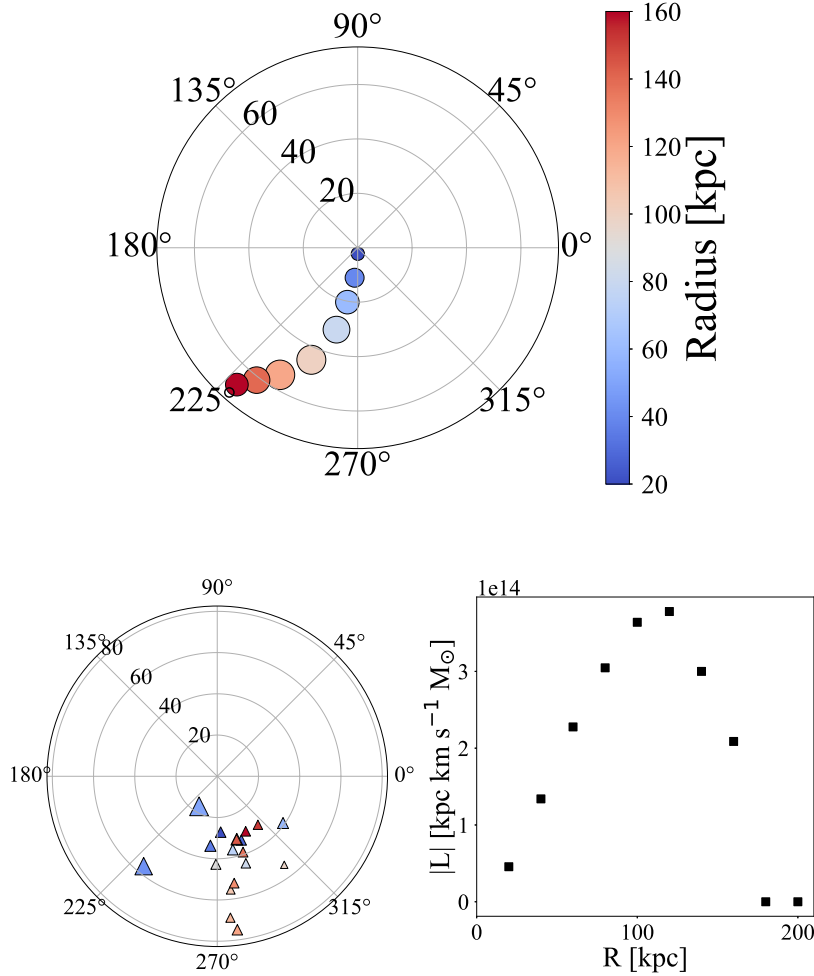


Fig. 4.20 **g8.26e11** - Top: integrated net flow of angular momentum in dark matter $L_{\text{flow,DM}}$ crossing shells of increasing radius from 20 to 200 kpc, with a separation of 20 kpc at each time step, with respect to the angular momentum of the stellar disc at $z \sim 0.3$. Bottom left and right: $L_{\text{flow,DM}}$ crossing $0.5R_{200}$ at each time step (left), with respect to the angular momentum of the stellar disc at $z \sim 0.3$ and the magnitude of the angular momentum vectors $|L_{\text{flow,gas}}|$ versus the shell radius (right). The size of each point indicates the magnitude of the angular momentum vector, the colour denotes its position in the radial sequence, dark blue being the smallest radius and dark red being the largest radius. The angular momentum of the inflowing dark matter is almost aligned with the tilting direction of the disc.

4.4 Gas driven tilting

This section presents the remaining three galaxies in the sample, which all have tilting driven by the misaligned cool gas contributing angular momentum to the stellar disc.

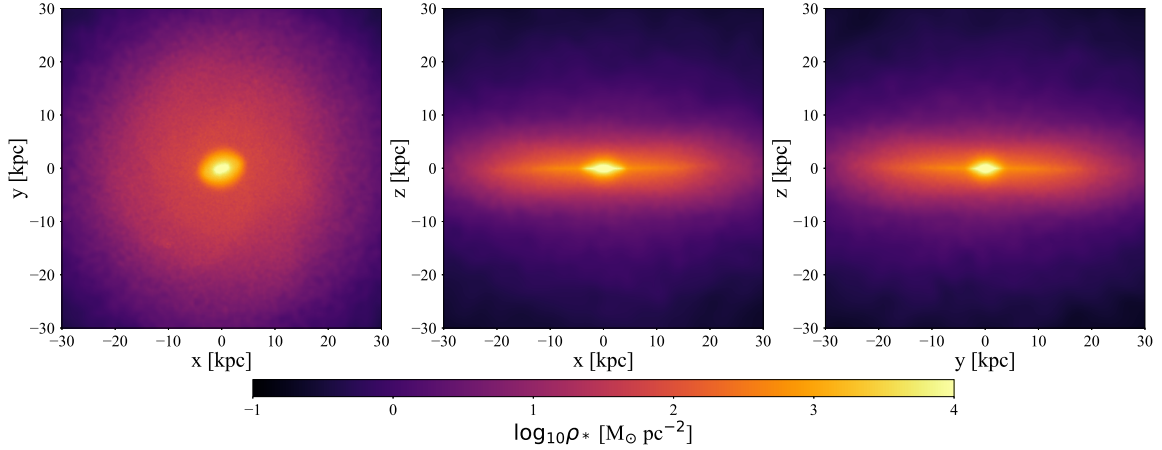


Fig. 4.21 **g2.79e12** - Stellar surface density maps at $z = 0$, projected into the x - y -, x - z - and y - z -planes.

4.4.1 Galaxy: g2.79e12

Galaxy g2.79e12 is the most massive in the sample, with $M_{\text{disc}} = 1.6 \times 10^{11} M_{\odot}$. Although this galaxy is far more massive than the MW, it has a similar morphology, being a barred spiral galaxy. This galaxy has the fastest gas driven tilting rate, with $\Delta\theta/\Delta t \sim 3^{\circ} \text{Gyr}^{-1}$. Figure 4.21 shows the stellar surface density of g2.79e12.

g2.79e12: stellar disc and satellites

Figure 4.22 shows the angular momentum of the stellar disc ($\mathbf{L}_{\text{disc},*}$) at each time step (top), with respect to $\mathbf{L}_{\text{disc},*}$ at $z \sim 0.3$. Here one can see that the tilting direction of the disc is fairly consistent, with a few very minor diversions and the tilting rate slows towards $z = 0$. The magnitude of $\mathbf{L}_{\text{disc},*}$ is very large starting at 1.8 and ending at $2.4 \times 10^{14} M_{\odot} \text{ kpc km s}^{-1}$, far greater than any other galaxy in our sample. The bottom left and right figures show $\mathbf{L}_{\text{disc},*}$ within annuli of increasing radius, from 5 to 30 kpc with a width of 2 kpc, at $z \sim 0.3$ and 0, respectively. The variation in angular momentum is small $\sim 1.2^{\circ}$ at $z \sim 0.3$ and falls slightly to $\sim 0.8^{\circ}$ for $z = 0$. The magnitude of angular momentum in each annulus also increases with time, for $R < 5$ kpc the total angular momentum increases from 2.8 to

4.4 Gas driven tilting

$3.2 \times 10^{13} M_{\odot} \text{ kpc km s}^{-1}$. Also the outer most radius $28 < r < 30 \text{ kpc}$ increases from 2.1 to $4.8 \times 10^{12} M_{\odot} \text{ kpc km s}^{-1}$. The combination of these two plots demonstrates there is no significant stellar warp inside 30 kpc .

Figure 4.23 shows the angular momentum of all stars (\mathbf{L}_*) outside the disc radius, within R_{200} (top), with respect to $\mathbf{L}_{\text{disc},*}$ at $z \sim 0.3$. The plot shows an interesting feature, where for a number of time steps the angular momentum deviates from its evolution, then returns back to its prior orientation. The total angular momentum of stars outside the disc radius is far lower than that of the disc, starting and ending at 3.4 and $3.9 \times 10^{13} M_{\odot} \text{ kpc km s}^{-1}$, respectively. The bottom left plot shows \mathbf{L}_* for all stars inside the virial radius, again, the jump is seen. However, this jump in angular momentum does not seem to have an impact on the final orientation of total angular momentum. The tilting direction of stars outside the disc is aligned in a similar direction to that of the tilting disc. The bottom right plot shows the angular momentum of stars in annuli of increasing radius, from 10 to 160 kpc with a width of 10 kpc at $z = 0$. Here one can see that outside $\sim 40 \text{ kpc}$ the stars start to become less aligned, but also have far less angular momentum.

g2.79e12: gas disc, warp and hot corona

Figure 4.24 shows the column density of HI in g2.79e12 and Figure 4.25 shows the axis ratios, b/a (black) and c/a (red) at $z \sim 0.3$ (left). There is a transition between an oblate and more spheroidal shape in the hot gas, at $\sim 20 \text{ kpc}$. The right panel shows the angle between the angular momentum of the cool and hot gas, at $z = 0.3$ (black) and 0 (red). Here there is a transition between the hot and cool gas components, again, at $\sim 20 \text{ kpc}$, from well to poorly aligned.

Figure 4.26 shows the angular momentum of the gas warp (\mathbf{L}_{warp}) at each time step (top), with respect to $\mathbf{L}_{\text{disc},*}$ at $z \sim 0.3$. Here the panel shows that at all but the first time step \mathbf{L}_{warp} falls in the upper half of the plot and ends in a similar direction to the tilting of the stellar

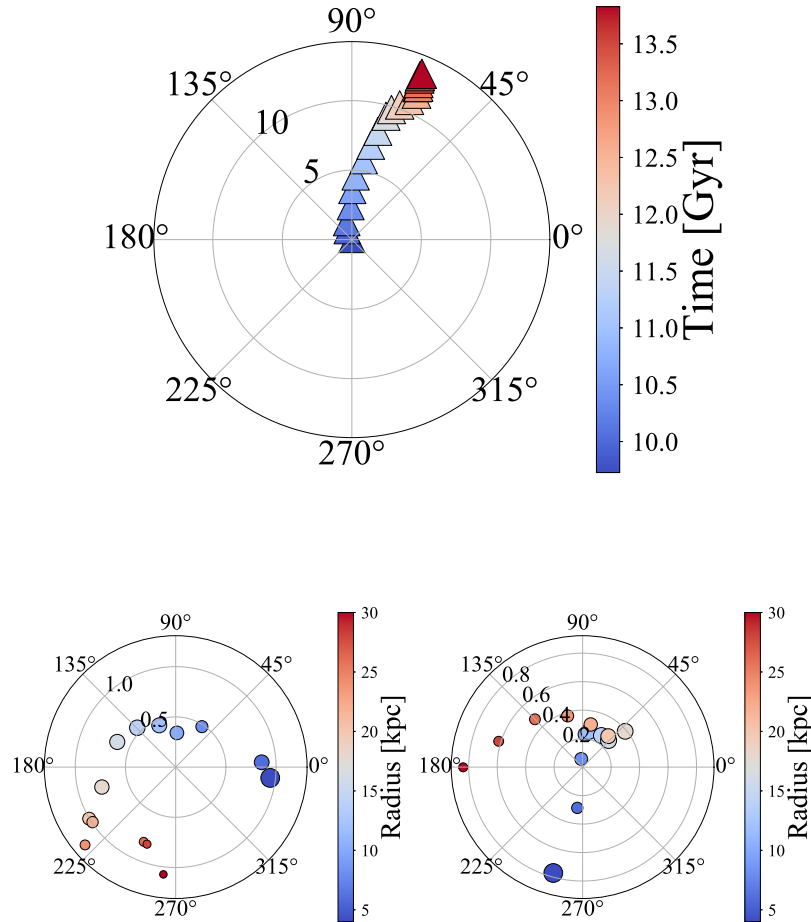


Fig. 4.22 **g2.79e12** - Top: angular momentum of the stellar disc $L_{\text{disc},*}$ at each time step (top), with respect to the angular momentum of the stellar disc at $z \sim 0.3$. Bottom left & right: $L_{\text{disc},*}$ within annuli of increasing radii from 5 to 30 kpc, with a width of 2 kpc, at $z \sim 0.3$ (left) and at $z = 0$ (right). Each bottom panel is shown with respect to the stellar angular momentum of the disc at their respective time steps. The size of each point indicates the magnitude of the angular momentum vector, the colour denotes its position in the time (top) or radial (bottom) sequence, dark blue being the start ($z \sim 0.3$ or $R = 5$ kpc) and dark red being the end ($z = 0$ or $R = 30$ kpc). The tilting direction of the disc is uniform and the disc has no warp within 30 kpc.

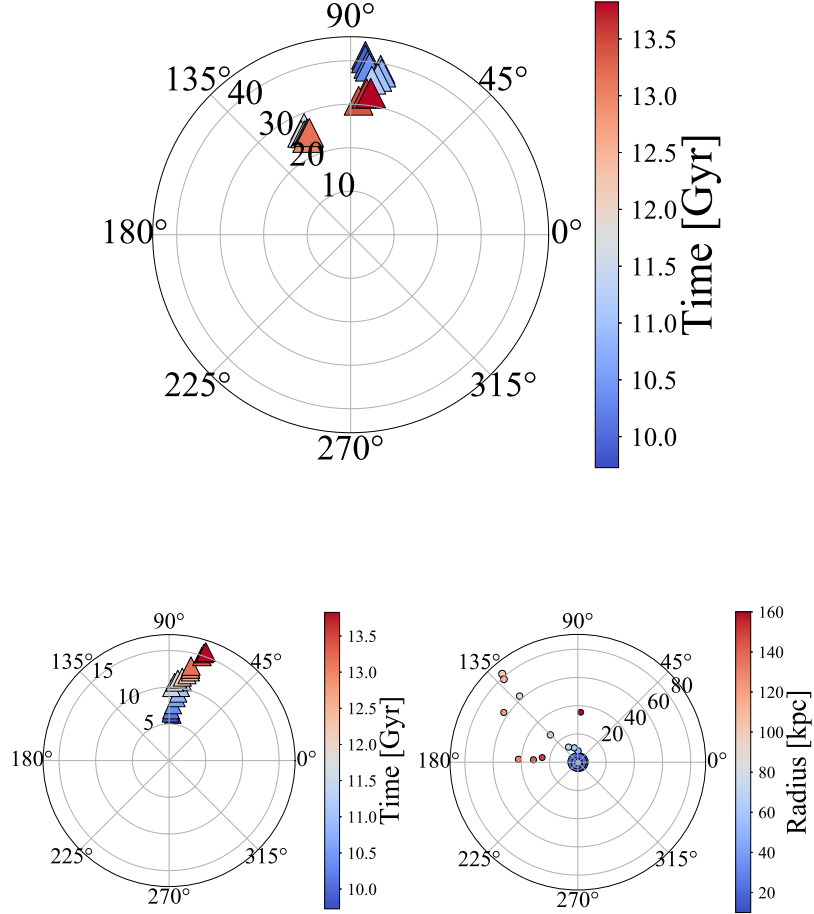


Fig. 4.23 **g2.79e12** - Top: angular momentum of all the stars L_* outside the disc and within the virial radius ($R_{\text{warp}} < R_* < R_{200}$) at each time step, with respect to the angular momentum of the stellar disc at $z \sim 0.3$. Bottom left: L_* for all stars within the virial radius R_{200} at each time step (left), with respect to the angular momentum of the stellar disc at $z \sim 0.3$. Bottom right: L_* within annuli of increasing radii from 10 to 160 kpc, with a width of 10 kpc (right) at $z = 0$, with respect to the angular momentum of the stellar disc at $z = 0$. The size of each point indicates the magnitude of the angular momentum vector, the colour denotes its position in the time (top) or radial (bottom) sequence, dark blue being the start ($z \sim 0.3$ or $R = 10$ kpc) and dark red being the end ($z = 0$ or $R = 160$ kpc). The angular momentum of all stars inside the virial radius is somewhat aligned with the tilting direction of the disc.

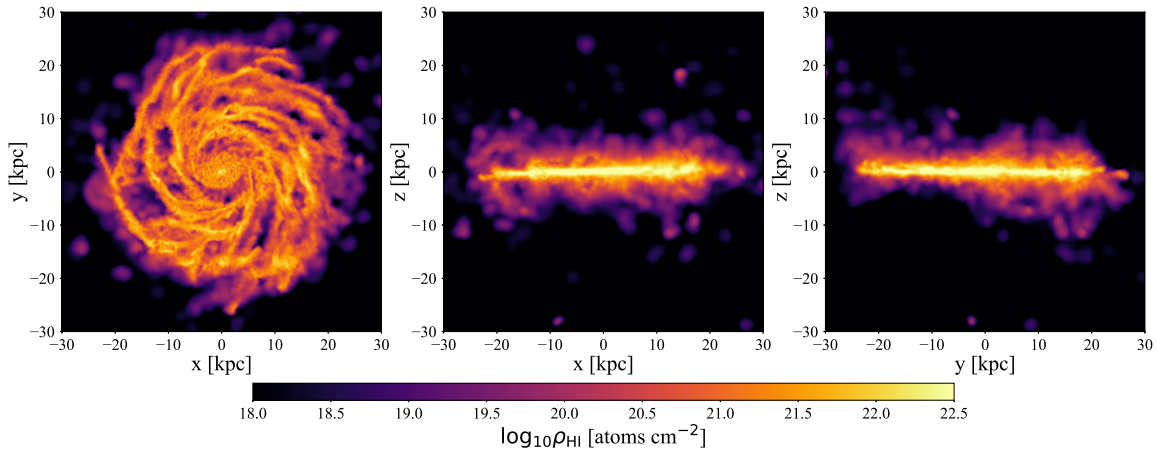


Fig. 4.24 **g2.79e12** - HI column density maps at $z = 0$, projected into the x - y -, x - z - and y - z -planes.

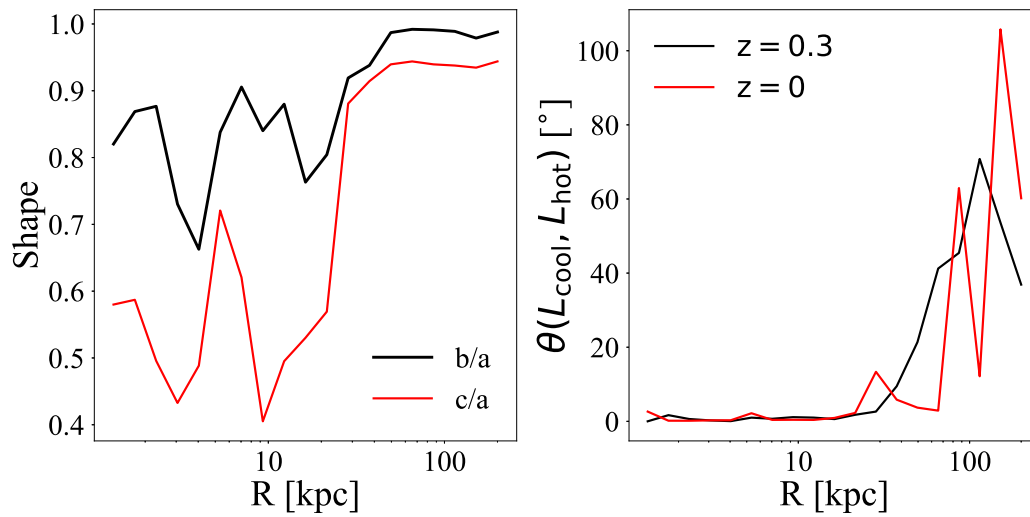


Fig. 4.25 **g2.79e12** - Left: the axis ratios b/a (black) and c/a (red) at $z \sim 0.3$, right: the angle between the cool ($T < 20,000\text{K}$) and hot ($T > 50,000\text{K}$) gas's angular momentum vectors, at $z \sim 0.3$ (black) and $z = 0$ (red). The transition between oblate and spheroidal happens at ~ 20 kpc.

4.4 Gas driven tilting

disc. The magnitude of \mathbf{L}_{warp} falls from 2.7 to $1.5 \times 10^{12} M_{\odot} \text{ kpc km s}^{-1}$ between $z \sim 0.3$ and 0. The bottom left and right plots show the angular momentum of cool gas in annuli of increasing radius, from 10 to 30 kpc with a width of 2 kpc, at $z \sim 0.3$ and 0, respectively. Here the left panel shows that for the smallest radii the direction is similar to the tilting direction of the disc, even at $z \sim 0.3$. The bottom right highlights that at $z = 0$ the cool gas begins to appear more coherently warped and is aligned with the tilting direction.

Figure 4.27 shows the angular momentum of the hot gas corona ($\mathbf{L}_{\text{corona}}$) at each time step (top), with respect to $\mathbf{L}_{\text{disc},*}$ at $z \sim 0.3$. The hot gas corona's angular momentum is aligned with both the tilting direction of the stellar disc and \mathbf{L}_{warp} , just more misaligned. The magnitude of $\mathbf{L}_{\text{corona}}$ is large, changing slightly over the period from 5.7 to $5.4 \times 10^{14} M_{\odot} \text{ kpc km s}^{-1}$. The bottom left and right panels show the $\mathbf{L}_{\text{corona}}$ in annuli of increasing radius, from 40 to 200 kpc with widths of 20 kpc, respectively. By comparing these panels, one can see that the hot gas becomes more aligned with the global angular momentum of the corona over time. The magnitude of $\mathbf{L}_{\text{corona}}$ within all these annuli also decreases over this time.

g2.79e12: dark matter halo

Figure 4.28 shows the angular momentum of the dark matter halo (\mathbf{L}_{dark}) at each time step (top), with respect to $\mathbf{L}_{\text{disc},*}$ at $z \sim 0.3$. This shows that \mathbf{L}_{dark} is similar to the $\mathbf{L}_{\text{corona}}$, but not completely aligned and is not heading towards alignment. The bottom left and right plots show \mathbf{L}_{dark} within annuli of increasing radius, from 10 to 200 kpc with a width of 10 kpc, at $z \sim 0.3$ and 0, respectively. Here one can see that \mathbf{L}_{dark} at different radii changes and at smaller radii is misaligned with the disc, preferentially towards the angular momentum of the halo as a whole.

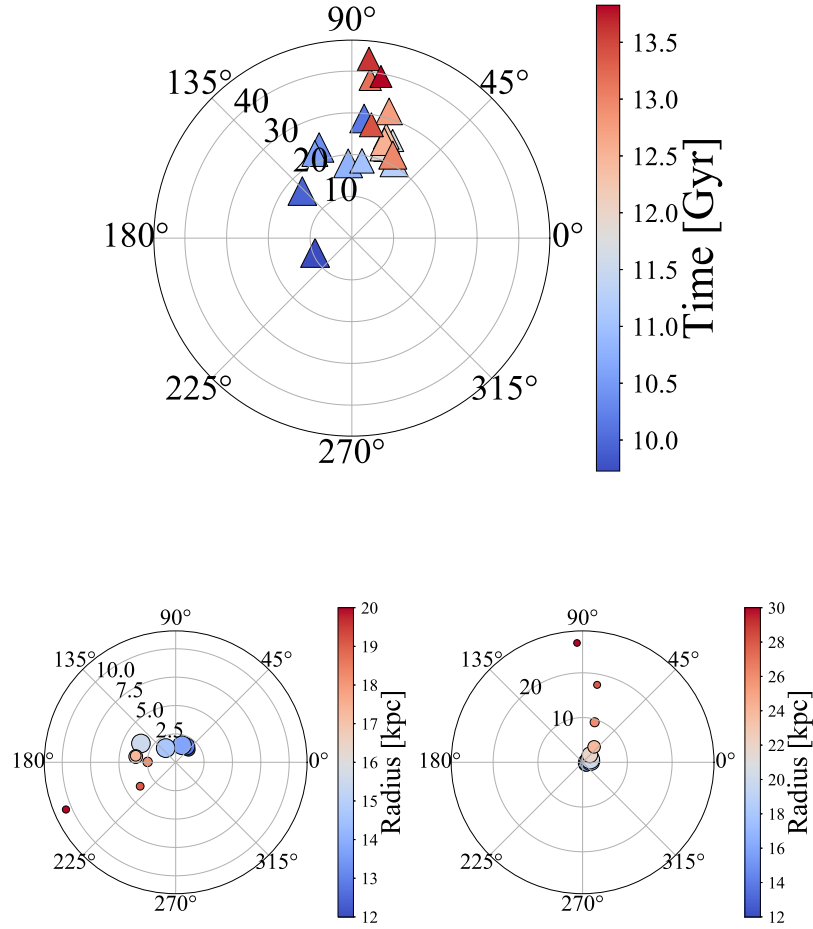


Fig. 4.26 **g2.79e12** - Top: angular momentum of the cool gas ($T < 20,000\text{K}$) beyond the stellar disc L_{warp} within 30 kpc ($R_{\text{warp}} < R_{\text{gas}} < 30$ kpc) at each time step, with respect to the angular momentum of the stellar disc at $z \sim 0.3$. Bottom left & right: L_{gas} for cool gas within annuli of increasing radii from 10 to 30 kpc, with a width of 2 kpc, at $z \sim 0.3$ (left) and at $z = 0$ (right). Both bottom panels are shown with respect to the angular momentum of the stellar disc at their respective time steps. The size of each point indicates the magnitude of the angular momentum vector, the colour denotes its position in the time (top) or radial (bottom) sequence, dark blue being the start ($z \sim 0.3$ or $R = 5$ kpc) and dark red being the end ($z = 0$ or $R = 30$ kpc). The angular momentum of the cool is not warped at $z = 0.3$, however, a warp has developed by $z = 0$. This warp is aligned with the tilting direction of the disc.

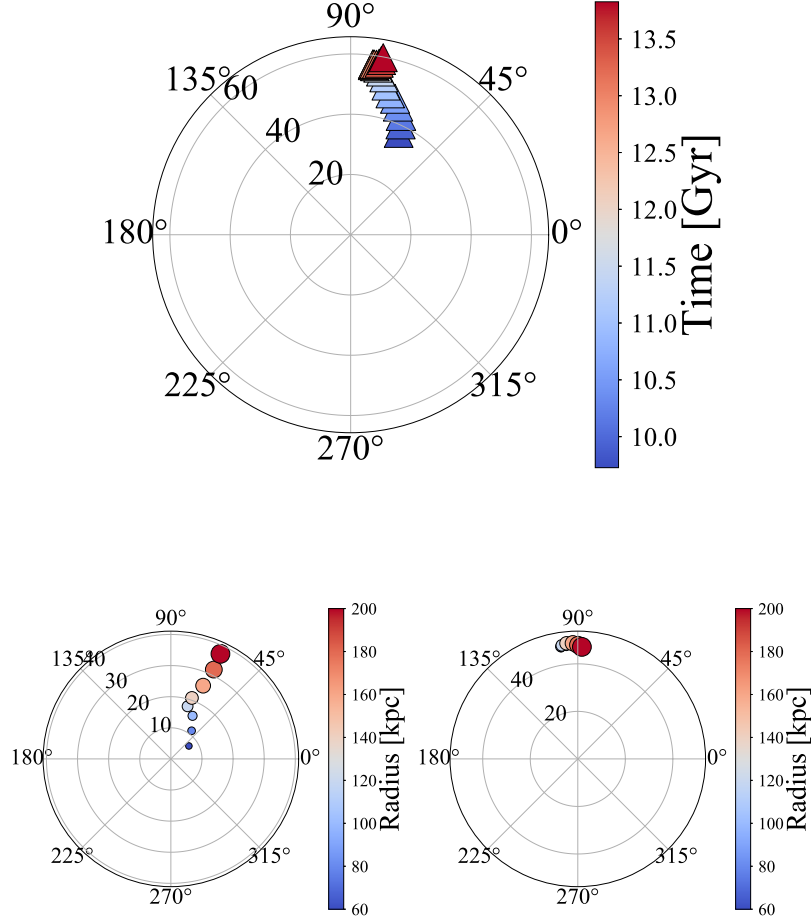


Fig. 4.27 **g2.79e12** - Top: angular momentum of the hot gas ($T > 50,000\text{K}$) beyond 40 kpc L_{corona} within the virial radius ($40\text{kpc} < R_{\text{gas}} < R_{200}$) at each time step, with respect to the angular momentum of the stellar disc at $z \sim 0.3$. Bottom left & right: L_{gas} for hot gas within annuli of increasing radii from 40 to 200 kpc, with a width of 20 kpc, at $z \sim 0.3$ (left) and at $z = 0$ (right). Both bottom panels are shown with respect to the angular momentum of the stellar disc at their respective time steps. The size of each point indicates the magnitude of the angular momentum vector, the colour denotes its position in the time (top) or radial (bottom) sequence, dark blue being the start ($z \sim 0.3$ or $R = 40$ kpc) and dark red being the end ($z = 0$ or $R = 200$ kpc). The angular momentum of the hot gas corona is aligned with the tilting direction of the disc.

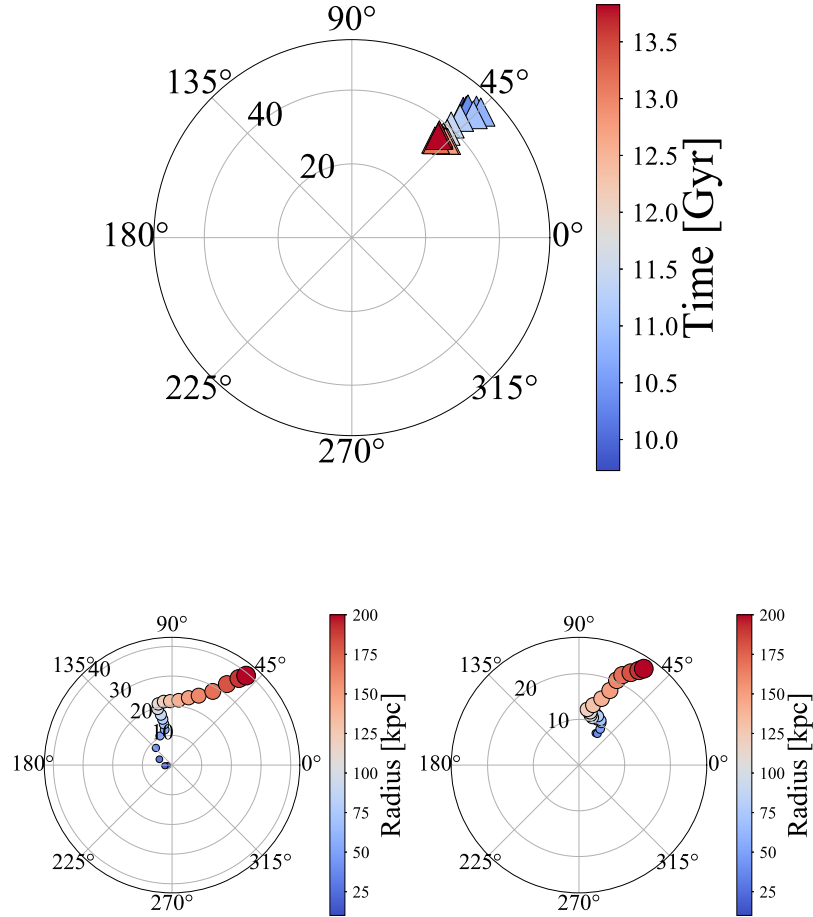


Fig. 4.28 **g2.79e12** - Top: angular momentum of the halo L_{dark} within the virial radius ($R_{\text{dark}} < R_{200}$) at each time step, with respect to the angular momentum of the stellar disc at $z \sim 0.3$. Bottom left & right: L_{dark} within annuli of increasing radii from 10 to 200 kpc, with a width of 10 kpc, at $z \sim 0.3$ (left) and at $z = 0$ (right). Both bottom panels are shown with respect to the angular momentum of the stellar disc at their respective time steps. The size of each point indicates the magnitude of the angular momentum vector, the colour denotes its position in the time (top) or radial (bottom) sequence, dark blue being the start ($z \sim 0.3$ or $R = 10$ kpc) and dark red being the end ($z = 0$ or $R = 200$ kpc). The angular momentum of the dark matter halo is not well aligned with the tilting direction of the disc.

g2.79e12: integrated net gas flow

Figure 4.29 shows the net flow of angular momentum in gas ($\mathbf{L}_{\text{flow,gas}}$) crossing shells of increasing radius from 5 to 30 kpc, with a separation of 5 kpc (top), with respect to $\mathbf{L}_{\text{disc,*}}$ at $z \sim 0.3$. This panel shows that $\mathbf{L}_{\text{flow,gas}}$ is aligned with \mathbf{L}_{warp} at lower radii and with $\mathbf{L}_{\text{corona}}$ at higher radii. Such a flow of gas in this manner would result in a change in $\mathbf{L}_{\text{disc,*}}$, in the direction that has been measured. The magnitude of the angular momentum in this flow is large, with values of $|\mathbf{L}_{\text{flow,gas}}| \sim 1.8 \times 10^{14} M_{\odot} \text{ kpc km s}^{-1}$ at 15 kpc. The bottom left plot shows the same plot extended to higher radii, starting at 40 kpc and ending at 160 kpc with a spacing of 30 kpc. Again, one can see that $\mathbf{L}_{\text{flow,gas}}$ is aligned with $\mathbf{L}_{\text{corona}}$ for low radii, at higher radii, it becomes even more misaligned than the corona itself. This could possibly be the cause of the change in $\mathbf{L}_{\text{corona}}$ as a whole.

g2.79e12: summary

This galaxy exhibits tilting in the direction of the cool gas warp, hot gas corona and the ongoing inflow of angular momentum coming in the form of gas. The amount of angular momentum reaching the disc in the form of gas is much higher than any other galaxy in sample A. The warp starts aligned with the tilting direction of the disc and over the period becomes more coherent, with increasing misalignment with radii in the same direction at every radial bin. This galaxy has the largest amount of gas flowing into the disc, therefore, it is not surprising that its tilting would be dominated by this process. If this process is driving the stellar disc to tilt in the MW, one would be able to predict the tilting direction by the orientation of the HI warp.

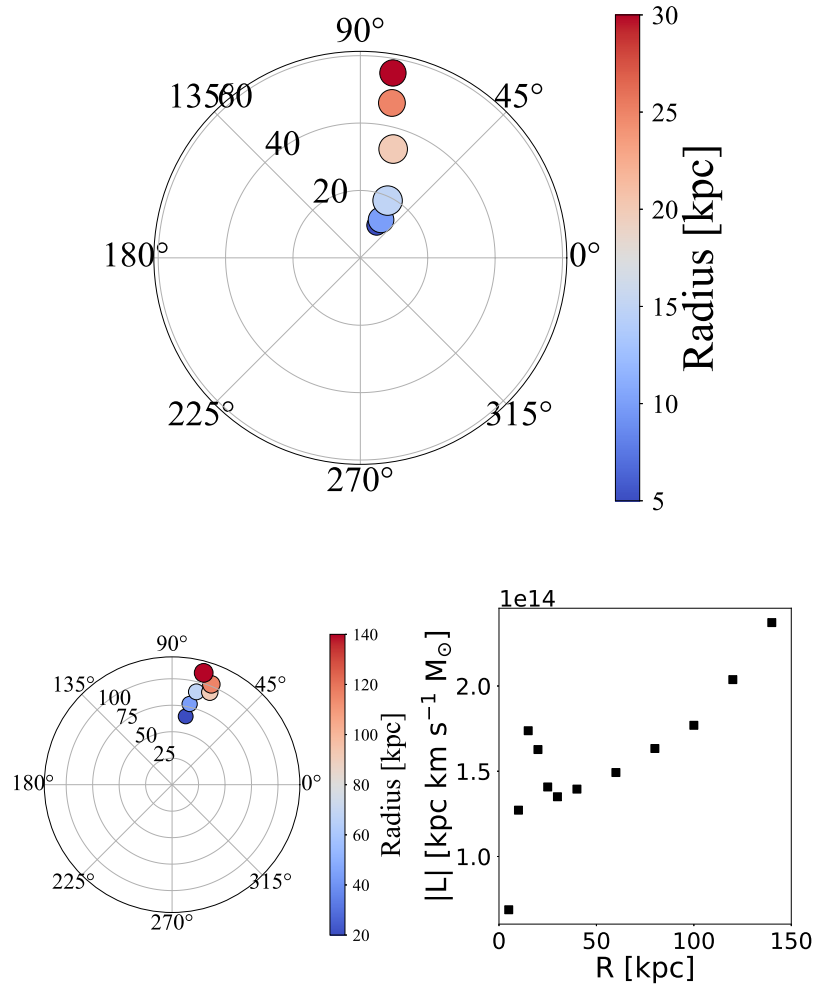


Fig. 4.29 **$g2.79e12$** - Top: integrated net flow of angular momentum in gas $\mathbf{L}_{\text{flow,gas}}$ crossing shells of increasing radius from 5 to 30 kpc, with a separation of 5 kpc at each time step, with respect to the angular momentum of the stellar disc at $z \sim 0.3$. Bottom left & right: $\mathbf{L}_{\text{flow,gas}}$ crossing shells of increasing radius from 40 to 140 kpc, with a separation of 20 kpc at each time step (left), with respect to the angular momentum of the stellar disc at $z \sim 0.3$ and the magnitude of the angular momentum vectors $|\mathbf{L}_{\text{flow,gas}}|$ versus the shell radius (right). The size of each point indicates the magnitude of the angular momentum vector, the colour denotes its position in the radial sequence, dark blue being the smallest radius and dark red being the largest radius. The angular momentum of inflowing gas is aligned with the tilting direction of the disc.

4.4 Gas driven tilting

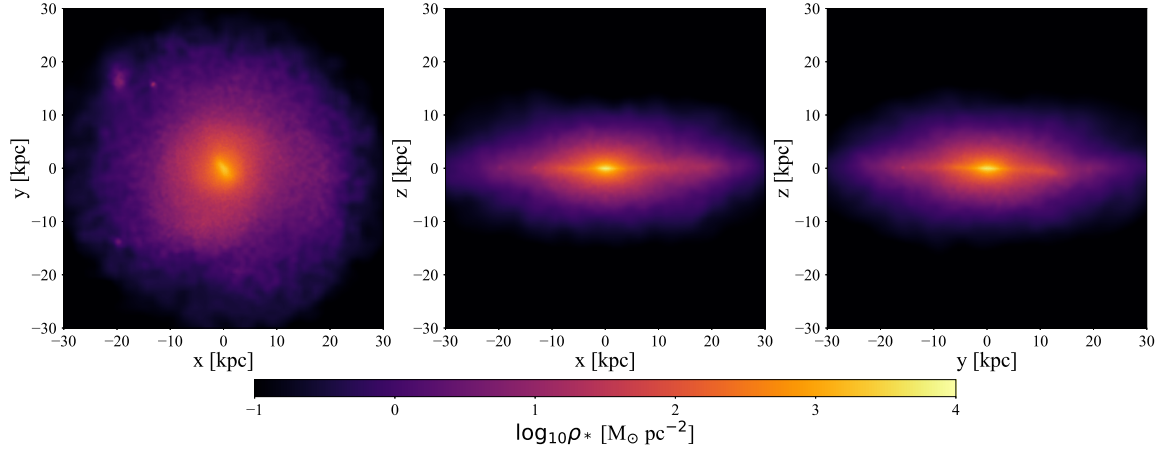


Fig. 4.30 **g7.55e11** - Stellar surface density maps at $z = 0$, projected into the x - y -, x - z - and y - z -planes.

4.4.2 Galaxy: g7.55e11

The stellar disc of g7.55e11 is the second largest in the sample with the warp starting at $R_{\text{warp}} = 25$ kpc. At $z = 0$ it has the lowest stellar mass in the sample, with $M_{\text{disc},*} = 3 \times 10^{10} M_{\odot}$. It has the median tilting rate for gas driven galaxies, with $\Delta\theta/\Delta t \sim 2.1^{\circ} \text{ Gyr}^{-1}$. Figure 4.30 shows the stellar surface density of g7.55e11.

g7.55e11: stellar disc and satellites

Figure 4.31 shows the angular momentum of the stars in the stellar disc (inside 25 kpc) $\mathbf{L}_{\text{disc},*}$ plotted at each time step (top), with respect to $\mathbf{L}_{\text{disc},*}$ at $z \sim 0.3$. This figure shows that the tilting direction of the disc is not consistent with two changes in direction over the time period. The bottom two plots show $\mathbf{L}_{\text{disc},*}$ within annuli of increasing radius from 5 to 30 kpc, within a width of 2 kpc, at $z \sim 0.3$ (left) and $z = 0$ (right). These plots show that $\mathbf{L}_{\text{disc},*}$ at $z \sim 0.3$ varies by about half the total tilting between $z \sim 0.3$ and 0, this value reduces to a final variance of ~ 20 per cent at $z = 0$. The magnitude of the angular momentum of the stellar disc $|\mathbf{L}_{\text{disc},*}|$ goes from 7.1 to $15 \times 10^{12} M_{\odot} \text{ kpc km s}^{-1}$ over the same time, with most of the change in angular momentum residing at higher radii with the outermost

annulus, starting at $1 \times 10^{11} M_{\odot} \text{ km s}^{-1}$ and increasing by a factor of three by $z = 0$.

This galaxy has the largest stellar mass fraction in satellites with four per cent of the total stellar mass, at $z \sim 0.3$. Figure 4.32 shows the angular momentum of all stars outside 25 kpc and within the virial radius (top) at each time step, with respect to $\mathbf{L}_{\text{disc},*}$ at $z \sim 0.3$. At $z \sim 0.3$ the total stellar angular momentum \mathbf{L}_* is aligned with the disc, however, in the very next time step this changes by $\sim 50^\circ$, hinting at a separate stellar population with high angular momentum. The magnitude of stellar angular momentum $|\mathbf{L}_*|$ outside the disc radius increases over the time interval from 1.7 to $2.9 \times 10^{12} M_{\odot} \text{ kpc km s}^{-1}$. The bottom panels show the angular momentum of stars within the virial radius at each time step (left) and within annuli of radius 10 to 160 kpc, with a width of 10 kpc, at $z = 0$ (right). The total $|\mathbf{L}_*|$ for all stars inside the virial radius also increased between the time interval, from 8.9 to $17.5 \times 10^{12} M_{\odot} \text{ kpc km s}^{-1}$, slightly more than the change in $|\mathbf{L}_{\text{disc},*}|$ over the same time. At $z = 0$, $|\mathbf{L}_*|$ decreases rapidly with radius from 4.6 to $0.01 \times 10^{12} M_{\odot} \text{ kpc km s}^{-1}$, at $R = 10$ and 160 kpc, respectively. The increase in $|\mathbf{L}_*|$ for stars outside the disc might be due to the transfer of angular momentum, or due to just star formation outside of the disc. When looking at the stellar density at each time step, one can see that this galaxy appears to have just one satellite with stellar content which orbits the central galaxy.

g7.55e11: gas disc, warp and hot corona

Figure 4.33 shows the column density of HI in g7.55e11 and Figure 4.34 shows the axis ratios, b/a (black) and c/a (red) for the hot gas at $z = 0.3$ (left). There is a transition between a more oblate and a more spheroidal shape for the hot gas, between 10 and 20 kpc. The right panel shows the angle between the angular momentum vectors of the cool and hot gas at $z = 0.3$ (black) and 0 (red). In this panel, there is a transition between a strong and weak alignment at ~ 20 kpc.

Figure 4.35 shows the change in angular momentum of cool gas in the warp \mathbf{L}_{warp} at each

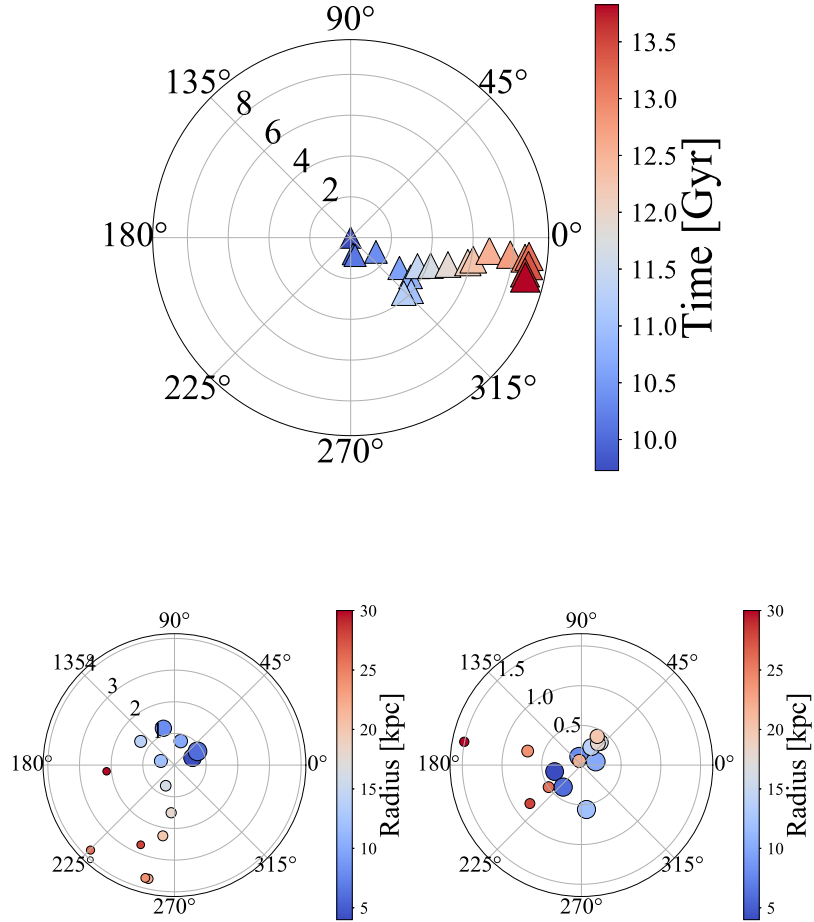


Fig. 4.31 **g7.55e11** - Top: angular momentum of the stellar disc $L_{\text{disc},*}$ at each time step (top), with respect to the angular momentum of the stellar disc at $z \sim 0.3$. Bottom left & right: $L_{\text{disc},*}$ within annuli of increasing radii from 5 to 30 kpc, with a width of 2 kpc, at $z \sim 0.3$ (left) and at $z = 0$ (right). Each bottom panel is shown with respect to the stellar angular momentum of the disc at their respective time steps. The size of each point indicates the magnitude of the angular momentum vector, the colour denotes its position in the time (top) or radial (bottom) sequence, dark blue being the start ($z \sim 0.3$ or $R = 5$ kpc) and dark red being the end ($z = 0$ or $R = 30$ kpc). The tilting direction is close to uniform, and the stellar disc is not warped at either time step.

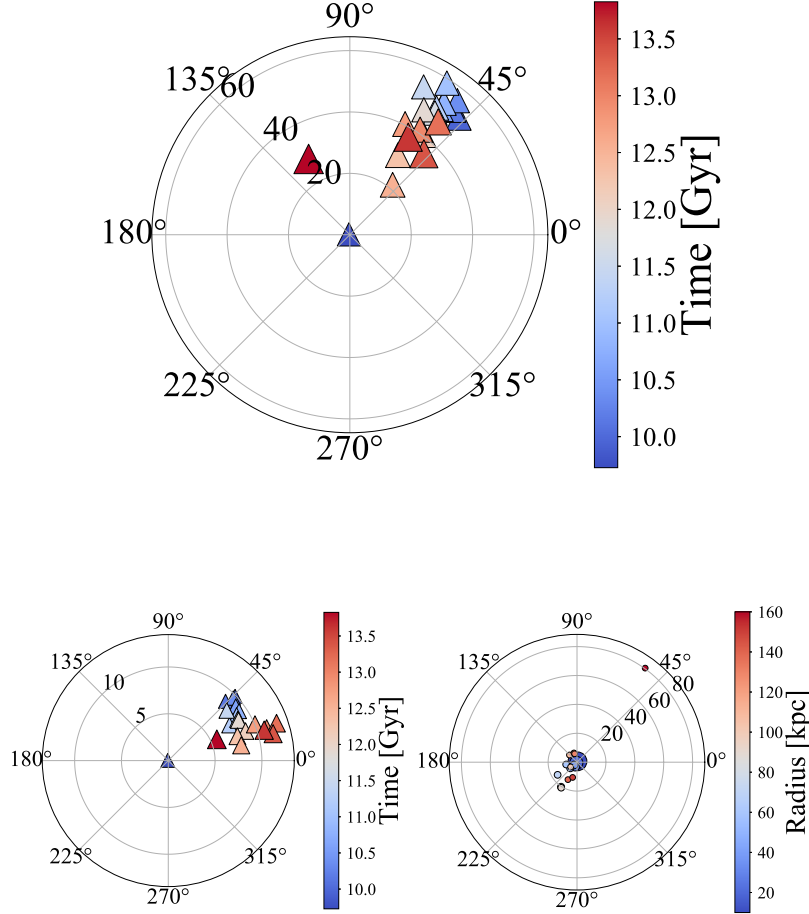


Fig. 4.32 **g7.55e11** - Top: angular momentum of all the stars L_* outside the disc and within the virial radius ($R_{\text{warp}} < R_* < R_{200}$) at each time step, with respect to the angular momentum of the stellar disc at $z \sim 0.3$. Bottom left: L_* for all stars within the virial radius R_{200} at each time step (left), with respect to the angular momentum of the stellar disc at $z \sim 0.3$. Bottom right: L_* within annuli of increasing radii from 10 to 160 kpc, with a width of 10 kpc (right) at $z = 0$, with respect to the angular momentum of the stellar disc at $z = 0$. The size of each point indicates the magnitude of the angular momentum vector, the colour denotes its position in the time (top) or radial (bottom) sequence, dark blue being the start ($z \sim 0.3$ or $R = 10$ kpc) and dark red being the end ($z = 0$ or $R = 160$ kpc). The angular momentum of all stars inside the virial radius is not aligned with the tilting direction of the disc.

4.4 Gas driven tilting

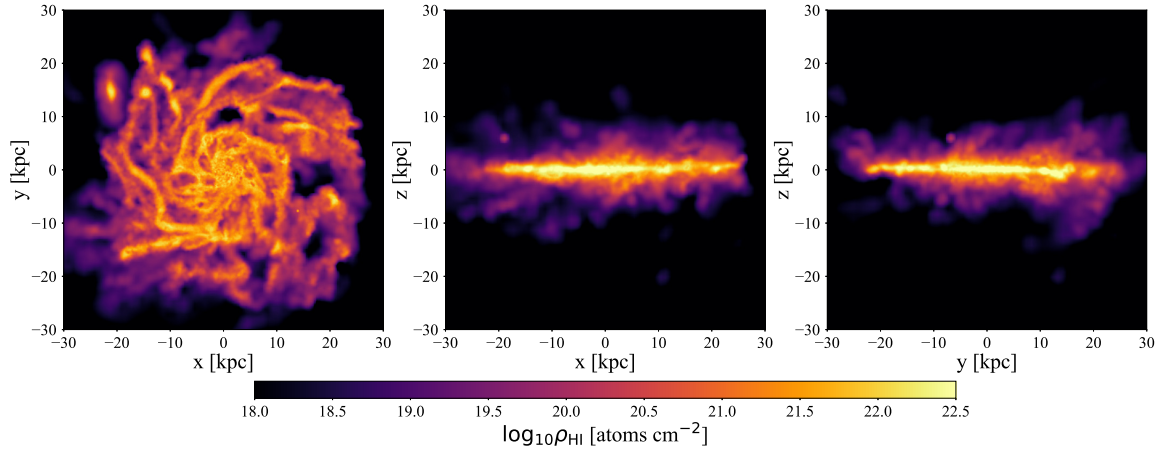


Fig. 4.33 **g7.55e11** - HI column density maps at $z = 0$, projected into the x - y -, x - z - and y - z -planes.

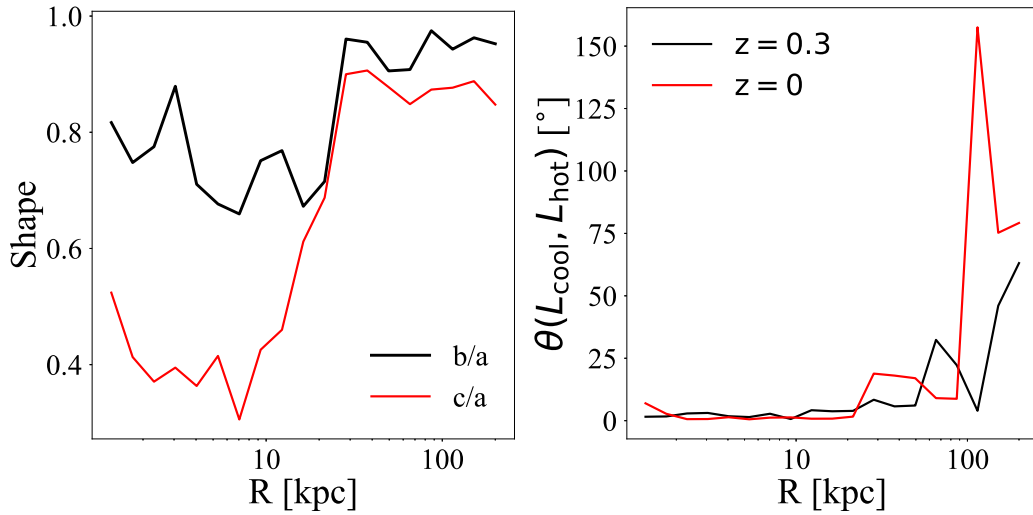


Fig. 4.34 **g7.55e11** - Left: the axis ratios b/a (black) and c/a (red) at $z \sim 0.3$, right: the angle between the cool ($T < 20,000\text{K}$) and hot ($T > 50,000\text{K}$) gas's angular momentum vectors, at $z \sim 0.3$ (black) and $z = 0$ (red). The transition between oblate and spheroidal happens between 10 and 20 kpc.

time step (top), with respect to $\mathbf{L}_{\text{disc},*}$ at $z \sim 0.3$. This figure shows that that \mathbf{L}_{warp} is aligned with $\mathbf{L}_{\text{disc},*}$ starting with just a $\sim 3^\circ$ offset and ending with a $\sim 1^\circ$ offset. The warp becomes more aligned with the disc over time, however, the final time does show that the warp has tilted further in roughly the same direction as the disc. Between $z \sim 0.3$ and 0, the magnitude of the angular momentum in the warp $|\mathbf{L}_{\text{warp}}|$ slightly falls from 7.2 to $7.1 \times 10^{12} M_\odot \text{ kpc km s}^{-1}$. Similarly to the stellar disc, \mathbf{L}_{warp} at different radii becomes more aligned over time, at $z \sim 0.3$ the angular momentum varies by as much as $\sim 4^\circ$, whereas at $z = 0$ this is reduced to just $\sim 1.5^\circ$. The magnitude of the angular momentum in these radial bins increases for the small and intermediate radii but falls for larger radii (roughly the warp radius). For the smallest annulus the total angular momentum goes from 4.2 to $5 \times 10^{12} M_\odot \text{ kpc km s}^{-1}$, the average increases from 5.8 to $6.8 \times 10^{12} M_\odot \text{ kpc km s}^{-1}$ and the largest annulus falls from 2 to $1.5 \times 10^{12} M_\odot \text{ kpc km s}^{-1}$. The loss of angular momentum at higher radii is possibly due to gas from the warp falling into the disc, resulting in the measured increase in angular momentum at lower radii.

Figure 4.36 shows the angular momentum of the hot gas corona $\mathbf{L}_{\text{corona}}$ at each time step (top), with respect to $\mathbf{L}_{\text{disc},*}$ at $z \sim 0.3$. The bottom left and right panels show $\mathbf{L}_{\text{corona}}$ in radial annuli from 40 to 200 kpc, with a width of 20 kpc, at $z \sim 0.3$ (left) and at $z = 0$ (right). The direction of $\mathbf{L}_{\text{corona}}$ changes with time and the tilting direction is not constant, with a change in tilting direction occurring roughly halfway through the interval. The magnitude of the angular momentum $|\mathbf{L}_{\text{corona}}|$ is far larger than $|\mathbf{L}_{\text{disc},*}|$ or $|\mathbf{L}_{\text{warp}}|$ and increases over the time interval, starting at 1.1 and ending at $1.3 \times 10^{14} M_\odot \text{ kpc km s}^{-1}$. The bottom two panels of the plot show $\mathbf{L}_{\text{corona}}$ at increasing radii, showing that for lower radii the direction changes far more than at higher radii. The amount of angular momentum in each radial bin does the opposite to the warp, with $|\mathbf{L}_{\text{corona}}|$ in the innermost bins and the average falling, whereas for the outer most radii, there is a gain in angular momentum.

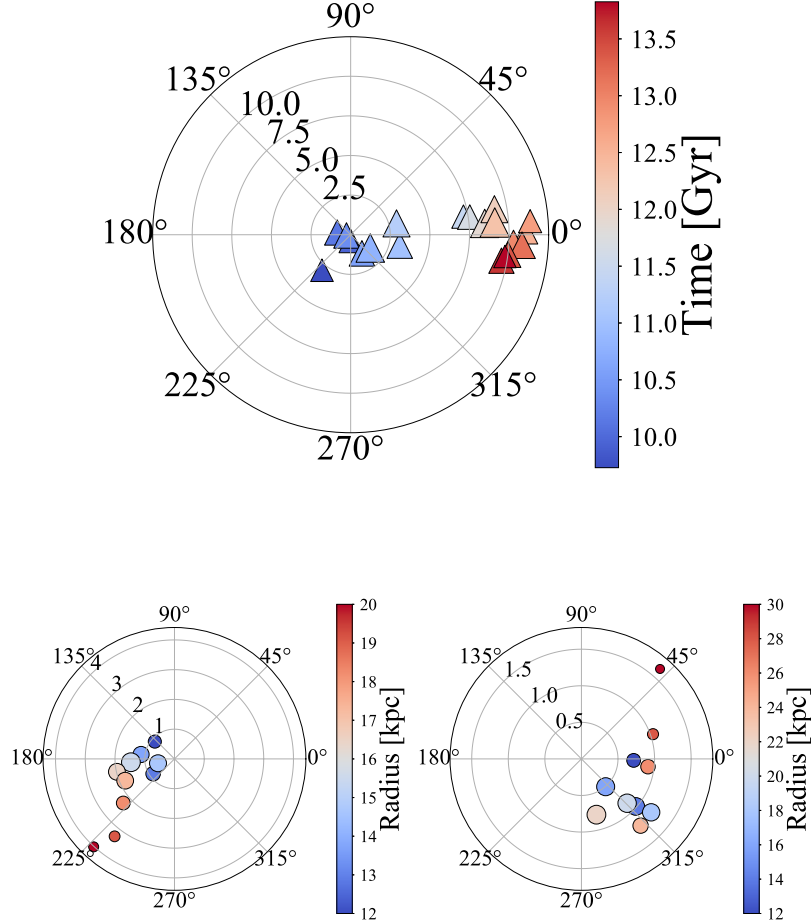


Fig. 4.35 **g7.55e11** - Top: angular momentum of the cool gas ($T < 20,000\text{K}$) beyond the stellar disc L_{warp} within 30 kpc ($R_{\text{warp}} < R_{\text{gas}} < 30$ kpc) at each time step, with respect to the angular momentum of the stellar disc at $z \sim 0.3$. Bottom left & right: L_{gas} for cool gas within annuli of increasing radii from 10 to 30 kpc, with a width of 2 kpc, at $z \sim 0.3$ (left) and at $z = 0$ (right). Both bottom panels are shown with respect to the angular momentum of the stellar disc at their respective time steps. The size of each point indicates the magnitude of the angular momentum vector, the colour denotes its position in the time (top) or radial (bottom) sequence, dark blue being the start ($z \sim 0.3$ or $R = 5$ kpc) and dark red being the end ($z = 0$ or $R = 30$ kpc). The angular momentum of the cool gas does seem to be aligned with the tilting direction of the disc.

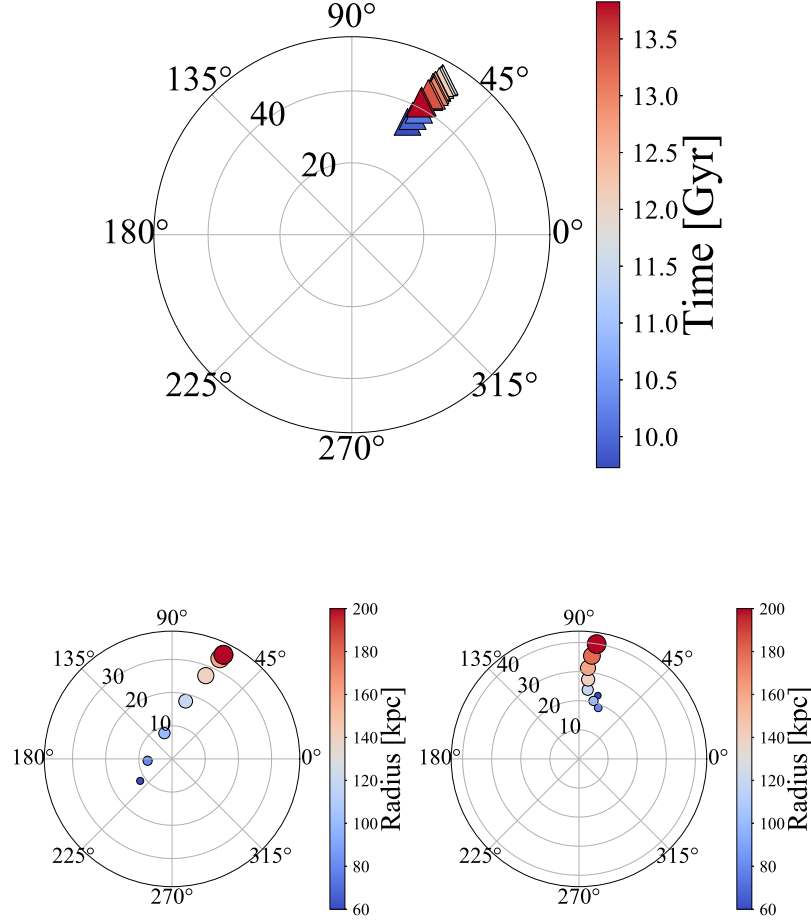


Fig. 4.36 **g7.55e11** - Top: angular momentum of the hot gas ($T > 50,000\text{K}$) beyond 40 kpc L_{corona} within the virial radius ($40\text{kpc} < R_{\text{gas}} < R_{200}$) at each time step, with respect to the angular momentum of the stellar disc at $z \sim 0.3$. Bottom left & right: L_{gas} for hot gas within annuli of increasing radii from 40 to 200 kpc, with a width of 20 kpc, at $z \sim 0.3$ (left) and at $z = 0$ (right). Both bottom panels are shown with respect to the angular momentum of the stellar disc at their respective time steps. The size of each point indicates the magnitude of the angular momentum vector, the colour denotes its position in the time (top) or radial (bottom) sequence, dark blue being the start ($z \sim 0.3$ or $R = 40$ kpc) and dark red being the end ($z = 0$ or $R = 200$ kpc). The angular momentum of the hot gas corona is not aligned with the tilting direction of the disc.

g7.55e11: dark matter halo

Figure 4.37 shows the angular momentum of the dark matter halo \mathbf{L}_{dark} at each time step (top) and within radial bins from 10 to 200 kpc, with a width of 10 kpc, at $z \sim 0.3$ (bottom left) and at $z = 0$ (bottom right), with respect to $\mathbf{L}_{\text{disc},*}$ at $z \sim 0.3$. This figure shows that \mathbf{L}_{dark} changes by $\sim 90^\circ$ over the time interval, with a clear change in direction roughly halfway through, similar to $\mathbf{L}_{\text{corona}}$. The magnitude of the dark matters angular momentum $|\mathbf{L}_{\text{dark}}|$ is even greater than the corona, starting at 1 and finishing at $1.7 \times 10^{15} M_\odot \text{ kpc km s}^{-1}$. The bottom two plots show \mathbf{L}_{dark} kinks at similar radii and with similar misalignments, however, the misalignment at higher radii increases by $\sim 20^\circ$. These features in the angular momentum versus radius Briggs figures are symptoms of a satellite.

g7.55e11: integrated net gas flow

Figure 4.38 shows the net flow of angular momentum in gas $\mathbf{L}_{\text{flow,gas}}$ crossing increasing shells of increasing radius from 5 to 30 kpc, with 5 kpc separation, between $z \sim 0.3$ and 0 (top), with respect to $\mathbf{L}_{\text{disc},*}$ at $z \sim 0.3$. This panel shows that $\mathbf{L}_{\text{flow,gas}}$ moving within the disc radius is aligned with the tilting direction for radii $R \lesssim 15$ kpc, however, at higher radii ($R \gtrsim 15$ kpc) $\mathbf{L}_{\text{flow,gas}}$ is more aligned with the hot gas corona. The bottom left panel continues this plot with shells of higher radii ranging from 40 to 120 kpc with 20 kpc spacing, showing that at low and intermediate radii $\mathbf{L}_{\text{flow,gas}}$ is roughly aligned with $\mathbf{L}_{\text{corona}}$, however, at the largest radii this alignment breaks down. Finally, the lower right panel shows the total magnitude of angular momentum $|\mathbf{L}_{\text{flow,gas}}|$ crossing each shell. The flow is strongest between $R = 10$ and 40 kpc reaching a maximum of $\sim 4.9 \times 10^{13} M_\odot \text{ kpc km s}^{-1}$. This chapter previously mentioned that the amount of angular momentum in the gas around the radius of the warp decreased between $z \sim 0.3$ and 0. One must account for star formation, which directly transfers angular momentum from gas to star particles. The angular momentum of stars around the warp radius increased, alluding to the possible

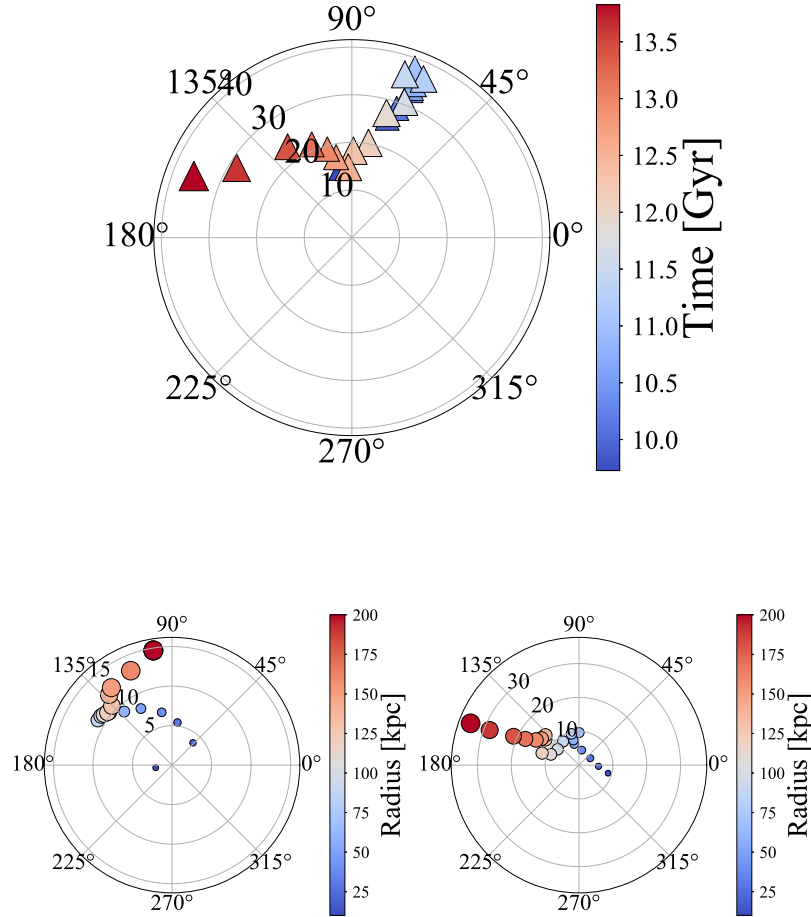


Fig. 4.37 **g7.55e11** - Top: angular momentum of the halo L_{dark} within the virial radius ($R_{\text{dark}} < R_{200}$) at each time step, with respect to the angular momentum of the stellar disc at $z \sim 0.3$. Bottom left & right: L_{dark} within annuli of increasing radii from 10 to 200 kpc, with a width of 10 kpc, at $z \sim 0.3$ (left) and at $z = 0$ (right). Both bottom panels are shown with respect to the angular momentum of the stellar disc at their respective time steps. The size of each point indicates the magnitude of the angular momentum vector, the colour denotes its position in the time (top) or radial (bottom) sequence, dark blue being the start ($z \sim 0.3$ or $R = 10$ kpc) and dark red being the end ($z = 0$ or $R = 200$ kpc). The angular momentum of the dark matter halo is not aligned with the tilting direction of the disc.

4.4 Gas driven tilting

formation of stars at this radius, which might explain this apparent dichotomy.

g7.55e11: summary

The two possible drivers for tilting in this galaxy are the accretion of cool gas with angular momentum misaligned with the disc, or the interaction between the central galaxy and its main satellite. The interaction with the satellite is most likely not the principle driver, as the angular momentum of the satellite and the tilting direction of the disc are not aligned. The angular momentum of gas falling to radii between 5 and 15 kpc is aligned with the tilting direction of the disc, suggesting that the infall of this gas is dictating the tilting direction of the stellar disc. The warp of this galaxy changes its angular momentum in a similar manner to the stellar disc, becoming aligned with the tilting direction of the stellar disc and the inflowing angular momentum of gas. Again, this scenario in the MW would be predictable using the angular momentum of the warp in the HI gas disc.

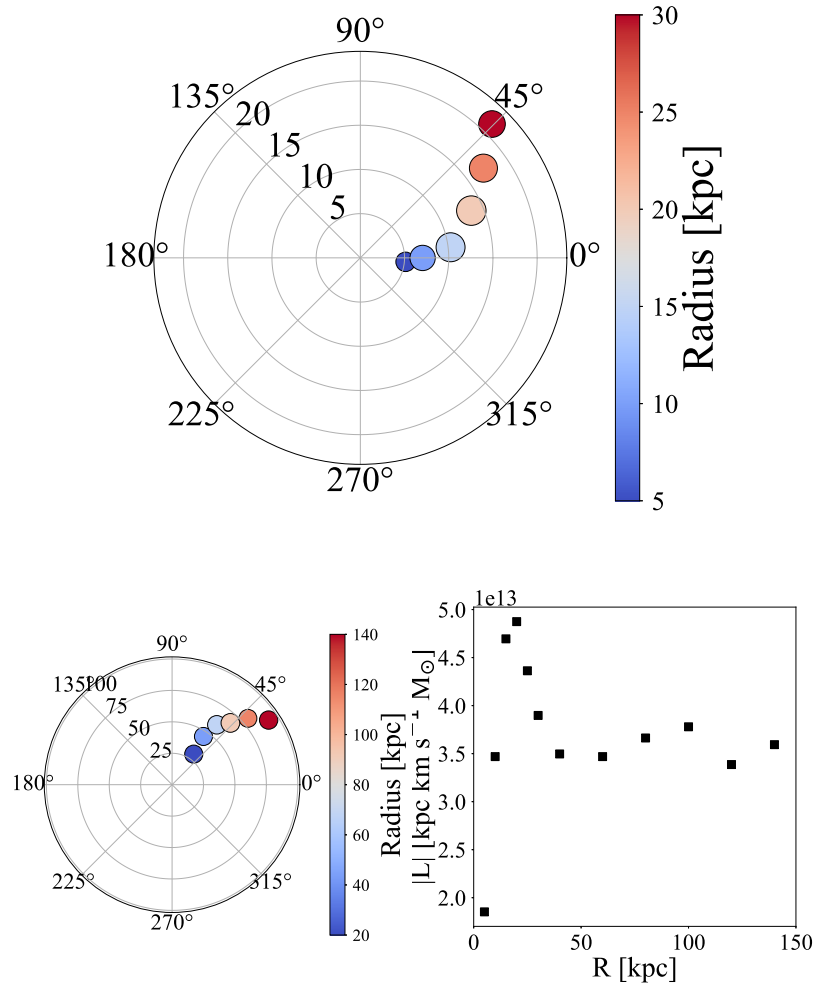


Fig. 4.38 **g7.55e11** - Top: integrated net flow of angular momentum in gas $\mathbf{L}_{\text{flow,gas}}$ crossing shells of increasing radius from 5 to 30 kpc, with a separation of 5 kpc at each time step, with respect to the angular momentum of the stellar disc at $z \sim 0.3$. Bottom left & right: $\mathbf{L}_{\text{flow,gas}}$ crossing shells of increasing radius from 40 to 140 kpc, with a separation of 20 kpc at each time step (left), with respect to the angular momentum of the stellar disc at $z \sim 0.3$ and the magnitude of the angular momentum vectors $|\mathbf{L}_{\text{flow,gas}}|$ versus the shell radius (right). The size of each point indicates the magnitude of the angular momentum vector, the colour denotes its position in the radial sequence, dark blue being the smallest radius and dark red being the largest radius. The angular momentum of inflowing gas is aligned with the tilting direction of the disc inside 15 kpc.

4.4 Gas driven tilting

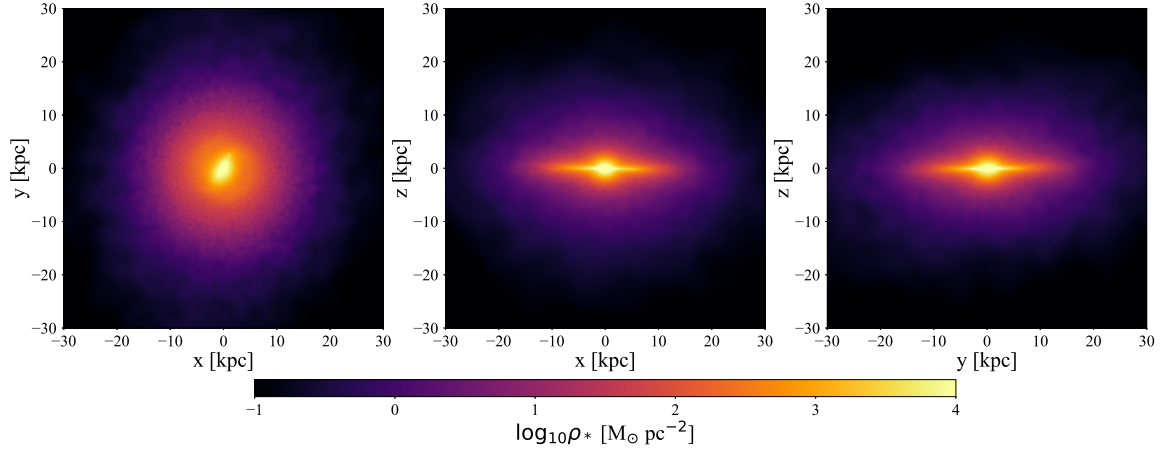


Fig. 4.39 **g1.92e12** - Stellar surface density maps at $z = 0$, projected into the x - y -, x - z - and y - z -planes.

4.4.3 Galaxy: g1.92e12

Galaxy g1.92e12 is the second most massive in stellar mass, $M_{\text{disc}} = 1.5 \times 10^{11} \text{M}_\odot$. Similar to g7.66e11 it has a very small disc, with a radius of just 13 kpc. It has the lowest tilting rate of all gas driven and hierarchically driven galaxies, with $\Delta\theta/\Delta t \sim 1.4^\circ \text{Gyr}^{-1}$. Figure 4.39 shows the stellar surface density of g1.92e12.

g1.92e12: stellar disc and satellites

Figure 4.40 shows the angular momentum of the stellar disc ($\mathbf{L}_{\text{disc},*}$) at each time step (top), with respect to $\mathbf{L}_{\text{disc},*}$ at $z \sim 0.3$. The direction of tilting for this galaxy is steady but changes direction at roughly $z = 0.13$. The magnitude of the angular momentum also increases with time, from 8.1 to $10.8 \times 10^{13} \text{M}_\odot \text{kpc km s}^{-1}$. The bottom right and left panels show $\mathbf{L}_{\text{disc},*}$ within annuli of increasing radius, from 5 to 30 kpc, with widths of 2 kpc at $z \sim 0.3$ and 0, respectively. Here it is hard to see, but for $z \sim 0.3$ $\mathbf{L}_{\text{disc},*}$ within the inner annuli are slightly more misaligned with each other than at $z = 0$, however, it is easier to see that the misalignment at higher radii becomes much larger. The inner few bins contain the vast majority of $|\mathbf{L}_{\text{disc},*}|$, this increases between the interval from 3.5 to $3.1 \times 10^{13} \text{M}_\odot \text{kpc km}$

s^{-1} . At higher radii $|\mathbf{L}_{\text{disc},*}|$ also increases slightly, from 5 to $6 \times 10^{10} M_{\odot} \text{ kpc km s}^{-1}$.

Figure 4.41 shows the angular momentum of all stars outside the disc radius, but within the virial radius (\mathbf{L}_*) at each time step (top), with respect to $\mathbf{L}_{\text{disc},*}$ at $z \sim 0.3$. This panel shows that \mathbf{L}_* , outside the disc, is very steady and populated just one location on the plot with some scatter—which is larger for the first few time steps. The bottom left plot shows \mathbf{L}_* of all stars within the virial radius, where the plot shows the expected result that the disc dominates the evolution of the angular momentum, but is slightly offset by the stars outside the disc. The final panel (bottom right) shows \mathbf{L}_* in annuli of increasing radius from 10 to 160 kpc with widths of 10 kpc. Here one can see that the angular momentum of the stellar disc dwarfs that of any of the galaxies satellites, with the magnitude of stellar angular momentum dropping rapidly from $7.8 \times 10^{13} M_{\odot} \text{ kpc km s}^{-1}$ for the inner annulus and $1.7 \times 10^{11} M_{\odot} \text{ kpc km s}^{-1}$ for the outer annulus.

g1.92e12: gas disc, warp and hot corona

Figure 4.42 shows the column density of HI in g1.92e12 and Figure 4.43 shows the axis ratios, b/a (black) and c/a (red) for the hot gas at $z = 0.3$ (left). There is a clear transition between an oblate and a more spheroidal shape at ~ 5 kpc. The right panel shows the angle between the angular momentum vectors of the cool and hot gas at $z = 0.3$ (black) and 0 (red). In this panel, there is a clear transition at 7 kpc for $z = 0$, for $z = 0.3$ this transition is more gradual between 10 and 20 kpc.

The compact disc of this galaxy has a very large amount of angular momentum compared to its hot gas corona, with a ratio of 0.77 far below anything else in this sample. Figure 4.44 shows the angular momentum of the gas warp (\mathbf{L}_{warp}) at each time step (top), with respect to $\mathbf{L}_{\text{disc},*}$ at $z \sim 0.3$. Here one can see that there appears to be no alignment between the highly misaligned \mathbf{L}_{warp} and the tilting direction of the stellar disc. The amount of angular momentum in the warp decreases with time starting at $|\mathbf{L}_{\text{warp}}| = 5$ and finishing

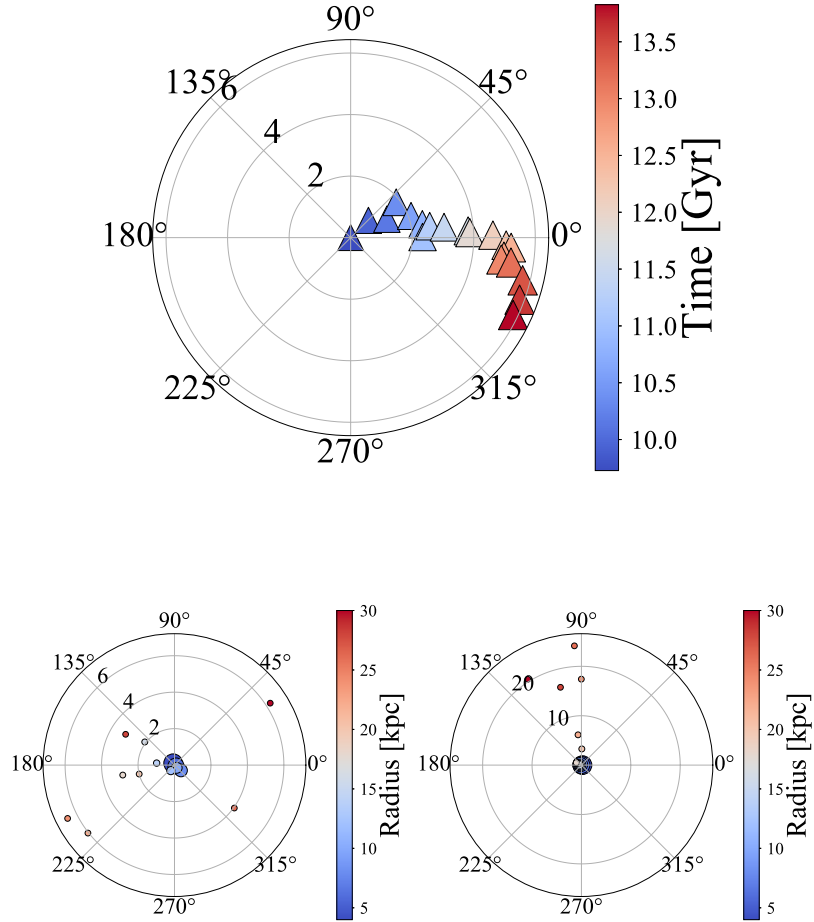


Fig. 4.40 **g1.92e12** - Top: angular momentum of the stellar disc $L_{\text{disc},*}$ at each time step (top), with respect to the angular momentum of the stellar disc at $z \sim 0.3$. Bottom left & right: $L_{\text{disc},*}$ within annuli of increasing radii from 5 to 30 kpc, with a width of 2 kpc, at $z \sim 0.3$ (left) and at $z = 0$ (right). Each bottom panel is shown with respect to the stellar angular momentum of the disc at their respective time steps. The size of each point indicates the magnitude of the angular momentum vector, the colour denotes its position in the time (top) or radial (bottom) sequence, dark blue being the start ($z \sim 0.3$ or $R = 5$ kpc) and dark red being the end ($z = 0$ or $R = 30$ kpc). The tilting direction is fairly uniform, the majority of the stellar angular momentum is within 15 kpc and is not warped.

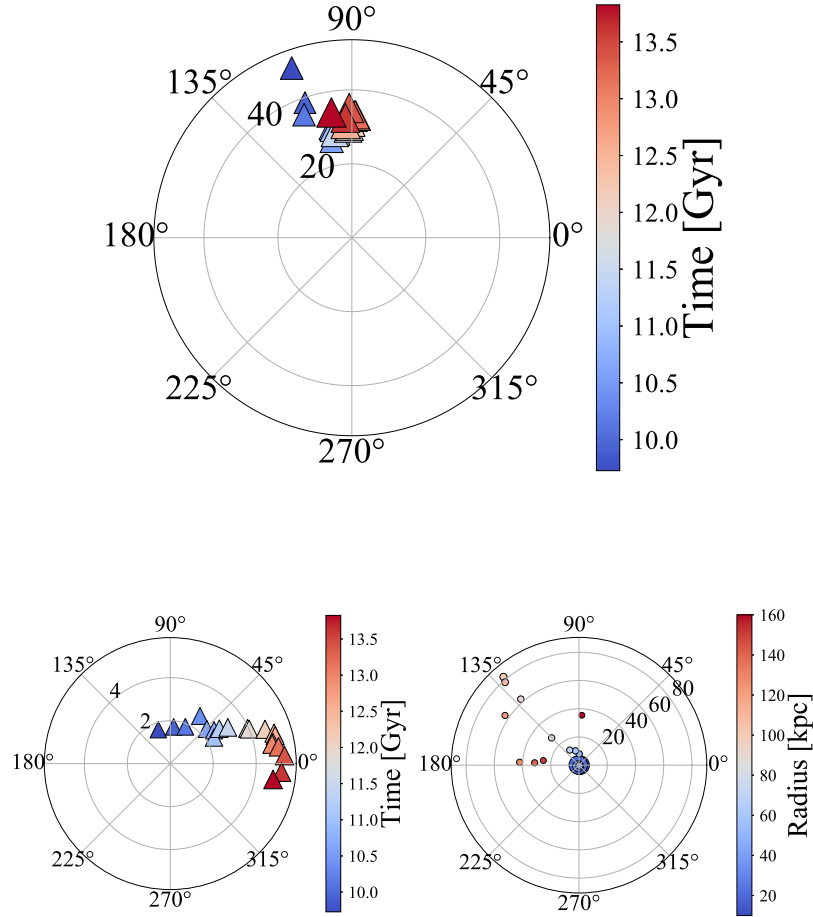


Fig. 4.41 **g1.92e12** - Top: angular momentum of all the stars L_* outside the disc and within the virial radius ($R_{\text{warp}} < R_* < R_{200}$) at each time step, with respect to the angular momentum of the stellar disc at $z \sim 0.3$. Bottom left: L_* for all stars within the virial radius R_{200} at each time step (left), with respect to the angular momentum of the stellar disc at $z \sim 0.3$. Bottom right: L_* within annuli of increasing radii from 10 to 160 kpc, with a width of 10 kpc (right) at $z = 0$, with respect to the angular momentum of the stellar disc at $z = 0$. The size of each point indicates the magnitude of the angular momentum vector, the colour denotes its position in the time (top) or radial (bottom) sequence, dark blue being the start ($z \sim 0.3$ or $R = 10$ kpc) and dark red being the end ($z = 0$ or $R = 160$ kpc). The angular momentum of all stars within the virial radius is not aligned with the tilting direction of the stellar disc.

4.4 Gas driven tilting

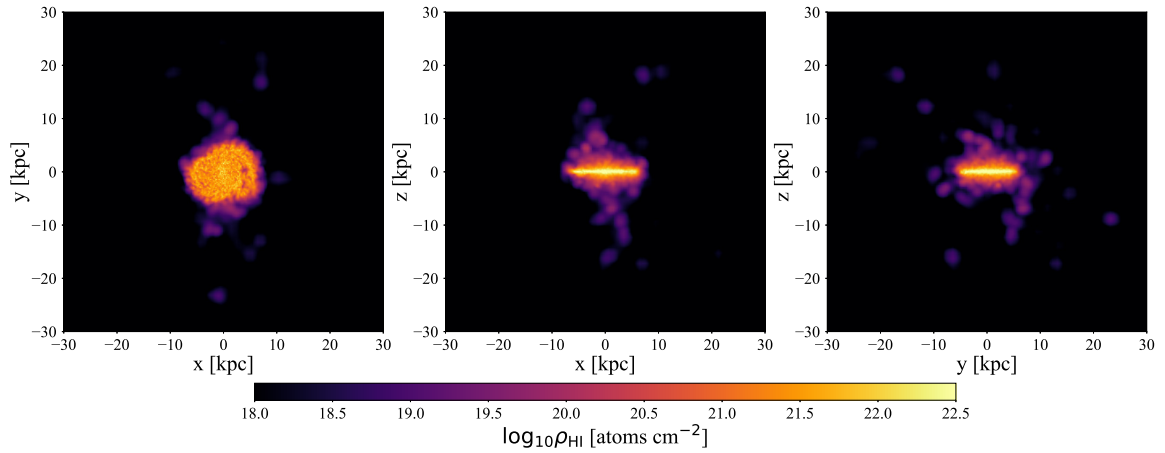


Fig. 4.42 **g1.92e12** - HI column density maps at $z = 0$, projected into the x - y -, x - z - and y - z -planes.

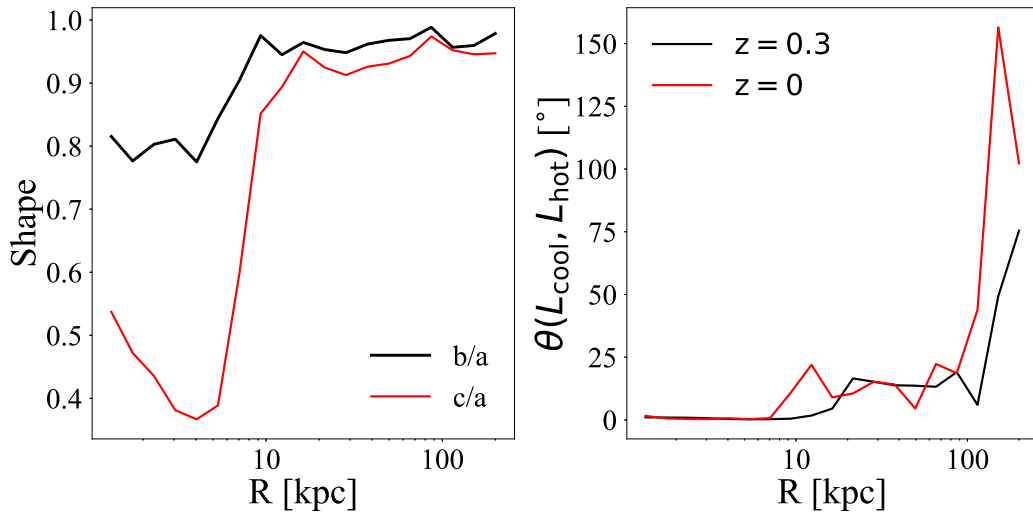


Fig. 4.43 **g1.92e12** - Left: the axis ratios b/a (black) and c/a (red) at $z \sim 0.3$, right: the angle between the cool ($T < 20,000\text{K}$) and hot ($T > 50,000\text{K}$) gas's angular momentum vectors, at $z \sim 0.3$ (black) and $z = 0$ (red). There is a clear transition between an oblate and a more spheroidal shape at ~ 5 kpc.

at $1.6 \times 10^{12} \text{ km s}^{-1}$. The bottom panels show the angular momentum of the cool gas within annuli of increasing radius from 5 to 30 kpc with widths of 2 kpc at $z \sim 0.3$ and 0, respectively. Here one can see that at $z \sim 0.3$ there is a large amount of angular momentum in the very centre of the galaxy that is aligned with $\mathbf{L}_{\text{disc},*}$, however this rapidly drops in angular momentum from $7.7 \times 10^{12} M_{\odot} \text{ kpc km s}^{-1}$ to $3.3 \times 10^{11} M_{\odot} \text{ kpc km s}^{-1}$. Not only does the total angular momentum of the cool gas drop drastically, its alignment also changes becoming aligned with \mathbf{L}_{warp} , not the stellar disc at $z = 0$. Moreover, at $z = 0$ even the gas within 10 kpc has become completely misaligned with the stellar disc.

Figure 4.45 shows the angular momentum of the hot gas corona $\mathbf{L}_{\text{corona}}$ at each time step (top), with respect to $\mathbf{L}_{\text{disc},*}$ at $z \sim 0.3$. The orientation of $\mathbf{L}_{\text{corona}}$ changes at a steady rate but does change its tilting direction roughly halfway through the interval. The magnitude of $\mathbf{L}_{\text{corona}}$ also falls by a factor of two, ending with the value of $8.3 \times 10^{13} M_{\odot} \text{ kpc km s}^{-1}$. The bottom left and bottom right plots show the angular momentum of the hot gas in annuli of increasing radius from 40 kpc to 200 kpc, with a width of 20 kpc, at $z \sim 0.3$ and 0, respectively. Here one can see the angular momentum of hot gas becomes much more uniform throughout the halo with both \mathbf{L}_{warp} and $\mathbf{L}_{\text{corona}}$ becoming well aligned at $z = 0$. As in the case of the corona, $|\mathbf{L}_{\text{corona}}|$ becomes smaller in every annuli, with the inner annulus falling from 1.3 to $0.88 \times 10^{13} M_{\odot} \text{ km s}^{-1}$.

g1.92e12: dark matter halo

Figure 4.46 shows the angular momentum of the dark matter halo (\mathbf{L}_{dark}) at each time step (top), with respect to $\mathbf{L}_{\text{disc},*}$ at $z \sim 0.3$. Here one can see that \mathbf{L}_{dark} is tilting, but in a direction not related to any of the stellar or the gas components. The bottom left and right panels show \mathbf{L}_{dark} in annuli of increasing radius, from 10 to 200 kpc with a width of 10 kpc, at $z \sim 0.3$ and 0, respectively. The angular momentum is aligned similarly at both time steps, with the only difference being at lower radii. At $z = 0$, the inner halo becomes more aligned with

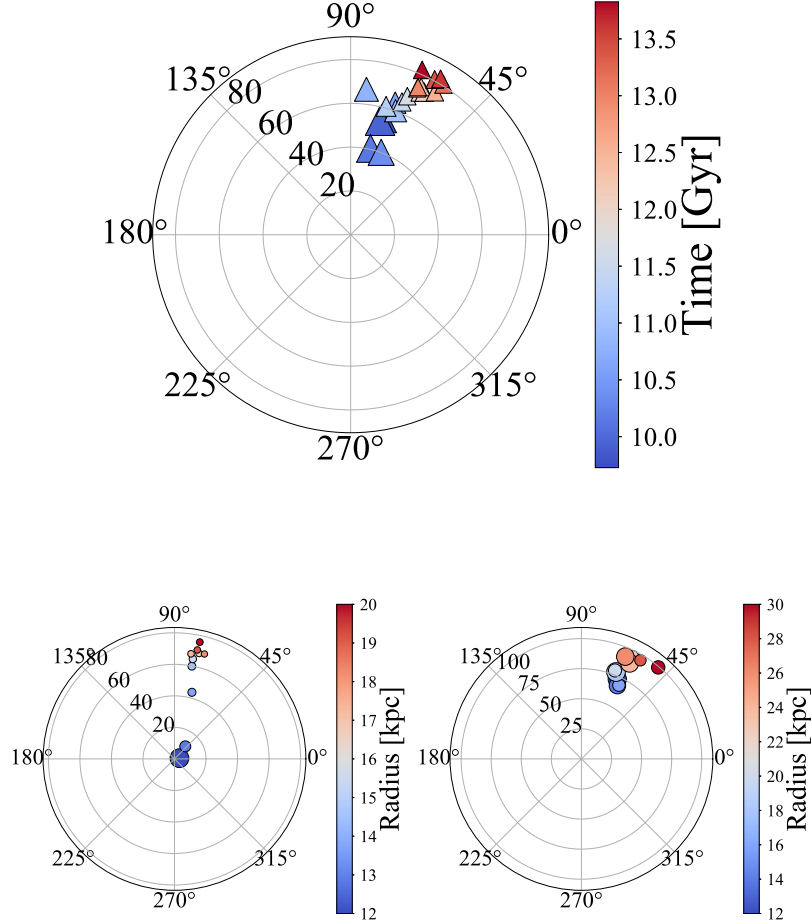


Fig. 4.44 **g1.92e12** - Top: angular momentum of the cool gas ($T < 20,000\text{K}$) beyond the stellar disc L_{warp} within 30 kpc ($R_{\text{warp}} < R_{\text{gas}} < 30$ kpc) at each time step, with respect to the angular momentum of the stellar disc at $z \sim 0.3$. Bottom left & right: L_{gas} for cool gas within annuli of increasing radii from 10 to 30 kpc, with a width of 2 kpc, at $z \sim 0.3$ (left) and at $z = 0$ (right). Both bottom panels are shown with respect to the angular momentum of the stellar disc at their respective time steps. The size of each point indicates the magnitude of the angular momentum vector, the colour denotes its position in the time (top) or radial (bottom) sequence, dark blue being the start ($z \sim 0.3$ or $R = 5$ kpc) and dark red being the end ($z = 0$ or $R = 30$ kpc). The angular momentum of the cool gas does not appear to be aligned with the tilting direction of the disc.

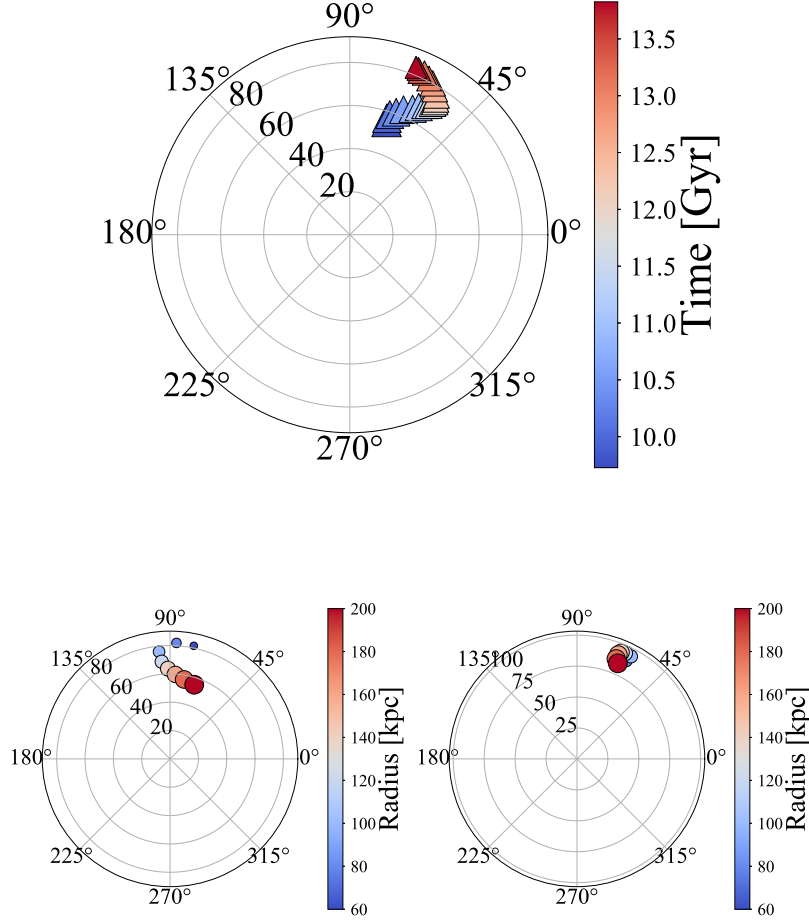


Fig. 4.45 **g1.92e12** - Top: angular momentum of the hot gas ($T > 50,000\text{K}$) beyond 40 kpc L_{corona} within the virial radius ($40\text{kpc} < R_{\text{gas}} < R_{200}$) at each time step, with respect to the angular momentum of the stellar disc at $z \sim 0.3$. Bottom left & right: L_{gas} for hot gas within annuli of increasing radii from 40 to 200 kpc, with a width of 20 kpc, at $z \sim 0.3$ (left) and at $z = 0$ (right). Both bottom panels are shown with respect to the angular momentum of the stellar disc at their respective time steps. The size of each point indicates the magnitude of the angular momentum vector, the colour denotes its position in the time (top) or radial (bottom) sequence, dark blue being the start ($z \sim 0.3$ or $R = 40$ kpc) and dark red being the end ($z = 0$ or $R = 200$ kpc). The angular momentum of the hot gas corona is not aligned with the tilting direction of the disc.

4.4 Gas driven tilting

$L_{\text{disc},*}$. The magnitude of angular momentum in the dark matter increases at all radii over the time interval.

g1.92e12: integrated net gas flow

Figure 4.47 shows the net flow of angular momentum in gas ($L_{\text{flow,gas}}$) crossing shells of increasing radius from 5 to 30 kpc with a 5 kpc separation (top), with respect to $L_{\text{disc},*}$ at $z \sim 0.3$. The bottom left panel extends this plot to higher radii starting at 40 kpc and ending at 140 kpc, with a spacing of 20 kpc. The angular momentum flowing across these shells does not appear to be related to the tilting direction of the stellar disc. The bottom right panel shows the magnitude of $L_{\text{flow,gas}}$, here one can see that there is a higher flow of angular momentum at higher radii.

g1.92e12: realignment of cool gas

Figure 4.48 shows the angular momentum of hot (diamonds) and cool gas (circles), in annuli of increasing radius, from 1 to 10 kpc (left) and 11 to 20 kpc (right), both with annular widths of 1 kpc, at $z = 0.3$. Comparing the two panels, at lower radii the hot and cool gas are much more aligned at higher radii—as seen in the right panel of Figure 4.43. The alignment becomes far closer at radii $R < 10$ kpc, at which point the hot and cool gas components are very well aligned. Within this radius, both hot and cool gas is aligned with the direction of tilting. These panels highlight the results found previously in Roškar et al. (2010), that by the time the cool gas reaches the disc it is completely aligned with the hot gas. However, the angular momentum of the hot gas at the disc radius is not aligned with the global angular momentum of the halo.

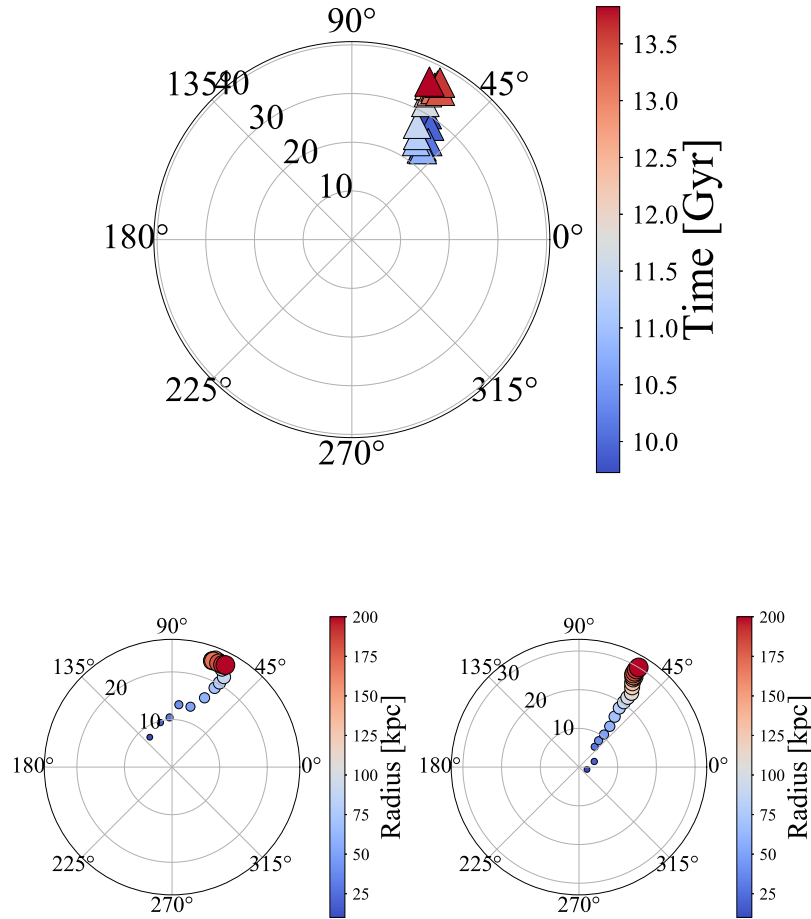


Fig. 4.46 **g1.92e12** - Top: angular momentum of the halo L_{dark} within the virial radius ($R_{\text{dark}} < R_{200}$) at each time step, with respect to the angular momentum of the stellar disc at $z \sim 0.3$. Bottom left & right: L_{dark} within annuli of increasing radii from 10 to 200 kpc, with a width of 10 kpc, at $z \sim 0.3$ (left) and at $z = 0$ (right). Both bottom panels are shown with respect to the angular momentum of the stellar disc at their respective time steps. The size of each point indicates the magnitude of the angular momentum vector, the colour denotes its position in the time (top) or radial (bottom) sequence, dark blue being the start ($z \sim 0.3$ or $R = 10$ kpc) and dark red being the end ($z = 0$ or $R = 200$ kpc). The angular momentum of the dark matter halo is not aligned with the tilting direction of the disc.

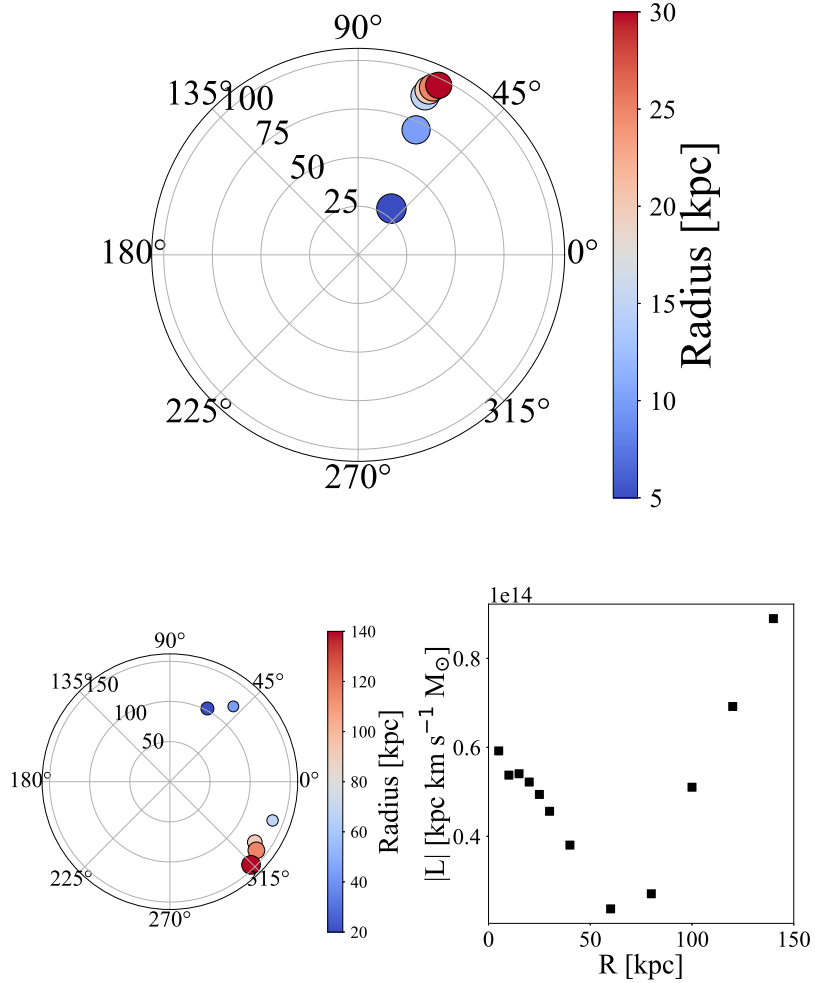


Fig. 4.47 Top: integrated net flow of angular momentum in gas $\mathbf{L}_{\text{flow,gas}}$ crossing shells of increasing radius from 5 to 30 kpc, with a separation of 5 kpc at each time step, with respect to the angular momentum of the stellar disc at $z \sim 0.3$. Bottom left & right: $\mathbf{L}_{\text{flow,gas}}$ crossing shells of increasing radius from 40 to 140 kpc, with a separation of 20 kpc at each time step (left), with respect to the angular momentum of the stellar disc at $z \sim 0.3$ and the magnitude of the angular momentum vectors $|\mathbf{L}_{\text{flow,gas}}|$ versus the shell radius (right). The size of each point indicates the magnitude of the angular momentum vector, the colour denotes its position in the radial sequence, dark blue being the smallest radius and dark red being the largest radius. The angular momentum of the infalling gas is not aligned with the tilting direction of the disc.

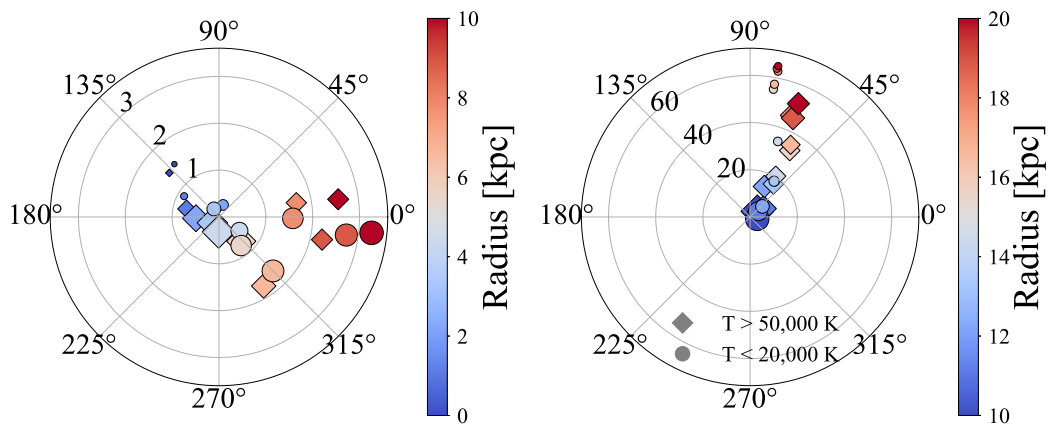


Fig. 4.48 Angular momentum of hot (diamonds) and cool gas (circles), in annuli of increasing radius, from 1 to 10 kpc (left) and 11 to 20 kpc (right), both with annular widths of 1 kpc, with respect to the angular momentum of the stellar disc, at $z = 0.3$. The colours denote the position in the radial series, blue being the lowest radius and red being the highest. The size of the points denotes the amount of angular momentum in each annulus, normalised to each panel. The cool gas within 10 kpc is aligned with both the hot gas within 10 kpc and the tilting direction of the disc. The angular momentum of both hot and cool gas outside 10 kpc are aligned with each other, but not with the tilting direction of the disc.

g1.92e12: summary

The galaxy has undergone interactions with satellites over the period, however, the angular momenta of these interactions are not aligned with the tilting direction. When looking at the accretion of star particles, again there is no alignment between the misaligned angular momentum contributed and the tilting direction. Comparing the angular momentum of the hot and cool gas in annuli ranging from 1 kpc to 20, there is a trend for the cool gas to become aligned with the hot gas by the time it reaches the disc. The angular momentum of this cool gas is aligned with the tilting direction of the stellar disc and most likely the primary driver for the tilting of the stellar disc. In this scenario, to determine the tilting direction of the MW, one could consider the angular momentum in the HI gas. If there is a small warp, like in this galaxy, then one would be able to predict the tilting direction of the stellar disc.

4.5 Chapter summary

4.5.1 Hierarchical processes

This chapter has presented two galaxies that tilt due to hierarchical processes, g7.66e11 and g8.26e11. The first galaxy, g7.66e11, has a very high tilting rate which is driven by the interaction of a satellite. During the interaction, the stellar disc becomes warped in the direction of the angular momentum of the satellite. Bailin (2003) proposed a similar scenario for the formation of the MW's stellar warp. If this is the case, then the direction in which the MW's disc is tilting would be predictable using the angular momentum of the stellar warp. On the other hand, if the warp of the MW is not caused by a satellite but the tilting is, using the angular momentum of the satellite one could predict the tilting direction of the stellar disc. The second galaxy, g8.26e11, has a much lower tilting rate which is driven by interactions and the accretion of dark matter. The amount of angular momentum

that builds up within ~ 40 kpc is very large compared to other galaxies within this sample. In this case, it would be harder to predict the direction of the MW's tilt.

4.5.2 Accretion of misaligned gas

This chapter has also presented three galaxies from sample B that have tilting that is driven by the accretion of misaligned gas, g2.79e12, g7.55e11 and g1.92e12. The first, g2.79e12, is being driven by gas from the hot corona cooling and falling onto the disc, forming a warp and contributing misaligned angular momentum to the stellar disc. The second, g7.55e11, is tilting in the direction of the cool gas warp, as a result of the accretion of gas with misaligned angular momentum. Finally, g1.92e12, which is the slowest tilting galaxy in all of sample B, is also tilting due to the accretion of misaligned gas. In the case of this galaxy, the warp is much harder to determine, but the cool gas is being affected by torques imposed by the hot gas within the disc radius. For all three of these cases, if a scenario like this was causing the MW to tilt, one could make a prediction for the tilting direction using the angular momentum the HI disc.

Chapter 5

Conclusions and Future Work

5.1 Conclusions

5.1.1 Tilting rate and Gaia limit

This thesis presents the tilting rates for galaxies in two, separate, fully cosmological hydrodynamical simulations. Chapter 2 presents the tilting rate of galaxies with halo masses comparable to the MW, finding significant tilting with an error weighted mean rate of $7.6^\circ \text{ Gyr}^{-1}$ and a standard deviation of $4.5^\circ \text{ Gyr}^{-1}$. This sample was further restricted to galaxies with low relative stellar accretion, and a maximum stellar mass fraction in satellites of 40 per cent, finding a lower mean tilting rate of $6.2^\circ \text{ Gyr}^{-1}$, with a range from 0.65 to $24.6^\circ \text{ Gyr}^{-1}$. In both samples, all the galaxies display significant tilting, with rates higher than the detection limit of *Gaia* (Perryman et al., 2014). However, this simulation suffered from over-cooling. Due to this more stars were able to form in lower mass galaxies resulting in galaxies that do not follow abundance matching relationships.

Chapter 3 presents the tilting rates for galaxies in the NIHAO simulation suite (Wang et al., 2015) which does not suffer from the over-cooling problem, finding an average tilting rate of $7.8^\circ \text{ Gyr}^{-1}$ and a standard deviation of $9.8^\circ \text{ Gyr}^{-1}$. When the sample is restricted to

galaxies with virial mass $M_{200} > 9 \times 10^{12} M_{\odot}$, the average tilting rate drops to $4.7^{\circ} \text{Gyr}^{-1}$ and has a standard deviation of $5^{\circ} \text{Gyr}^{-1}$. All the galaxies in the NIHAO sample, with well determined tilting rates, tilt with a rate that is comparable to the galaxies studied in Chapter 2, and that would also be detectable by *Gaia*.

5.1.2 Environmental factors

Local density

Chapter 2 investigated the effect of the local environment on the tilting rate of the disc. By comparing the total local density to the tilting rate, it was shown that the tilting rate does not correlate with the normalized local density within 3Mpc for subsample VICTOR:A. However, for subsample VICTOR:B, there is a correlation. When considering larger radii, there is a correlation between the tilting rate and the local environment for both subsamples. Chapter 3 verified this result using the NIHAO simulations, finding correlation coefficients of $p = 0.59, 0.63, 0.65$ & 0.86 for the radii, 3, 4, 5 & 6 Mpc, respectively. The strongest correlation is at the largest radius, and contains galaxies of a wide range of masses and environmental configurations, implying that on average the smaller scale structure is not the primary driver for most galaxies. Galaxies in denser regions generally tilt at higher rates than galaxies in lower density regions, irrespective of the galaxies stellar mass accretion, or stellar mass.

Massive neighbours

The MW has a close, similar mass, neighbour M31. Chapter 2 compared galaxies to the MW's configuration, by measuring the distances to the nearest massive galaxy and determining their correlation with the tilting rates. There is almost no correlation for subsample VICTOR:A; however, for subsample VICTOR:B, we do find very weak anti-correlation, suggesting that the local configuration is unlikely to be a large contributing factor when the disc

5.1 Conclusions

is accreting significant stellar mass. The sample contains galaxies in similar configurations to the MW with companion galaxies within a few hundred kpc; these galaxies exhibit tilting rates similar to more isolated galaxies. Such a comparison was not possible in the NIHAO suite, due to the strict isolation criterion imposed on the sample. However, comparable tilting rates are found for these galaxies, which all lack massive neighbouring galaxies, again emphasising that the local configuration is not a primary driver of disc tilting.

Interactions and minor mergers

Mergers with other galaxies are among the most violent processes, which could result in a drastic change in the disc's angular momentum over a short period. Both Chapters 2 and 3 showed that even when excluding galaxies that gain a large amount of stellar mass from such events, the measured tilting is still significant. In Chapter 4 two of the galaxies in the NIHAO suite are shown to exhibit tilting caused by the interaction with a satellite and by the accretion of a large amount of angular momentum in the form of dark matter. In first of these two cases, where the interaction with the satellite caused the tilting of the stellar disc, a very high tilting rate was measured. Therefore, interactions with satellites containing large amounts of angular momentum can drastically change the angular momentum of the disc over a very short time, also resulting in a warped stellar disc. In the second case, where the accretion of dark matter with misaligned angular momentum was the primary driver, the tilting rate was very similar to galaxies tilting solely due to the accretion of misaligned cool gas.

5.1.3 Secular processes

Specific star formation

Debattista et al. (2015) found that red galaxies tend to have angular momentum aligned with the minor axis of their dark matter halo, whereas, blue galaxies are found to have random

orientations. Both Chapters 2 and 3 compared the tilting rate of the disc to the star formation rate, finding that galaxies with higher star formation tilt faster. Of all the correlations that are reported in Chapter 3, the one between the sSFR and tilting rate was the strongest, with a value of $p=0.77$ for $\text{sSFR}(z=0)$ and $p=0.9$ for $\langle \text{sSFR} \rangle$. These correlations help explain the random orientations of blue galaxies. As the sSFR increases, the tilting becomes more rapid, perturbing the galaxy away from a stable orientation, irrespective of the driving mechanism. Moreover, Chapter 3 measured the alignment between the stellar disc and the minor, intermediate and major axes of the halo for the predominantly blue galaxies within the NIHAO sample. In agreement with Debattista et al. (2015), no preferential alignments are found.

Dark matter halo

Yurin and Springel (2015) inserted model stellar discs into dark matter haloes within a cosmological N-body simulation. The authors report tilting rates for their stellar discs comparable to the tilting rates presented in this thesis. In such a scenario the tilting of the stellar disc is driven by the torques, dynamical friction and interactions imposed by the tumbling parent halo and surrounding substructure. In the case of torquing from the dark matter halo, less spheroidal haloes exert greater torques on the disc. To test this Chapter 3 compared the tilting rate of the stellar disc to the axis ratios, b/a and c/a of the halo, finding weak anti-correlations for both. The triaxiality of the halo was also measured and compared to the tilting rate of the stellar disc, however, no correlation was found. Although there is a weak correlation, and the comparable tilting rates presented in Yurin and Springel (2015), when looking at individual galaxies in the NIHAO sample, none of them are found to be tilting due to the torques imposed by the dark matter halo.

Hot gas corona

In an attempt to determine the effect of misaligned gas accretion from the hot gas corona, Chapters 2 and 3 measured both the tilting rate of the hot gas corona and the angular misalignment between the stellar disc and the corona. Both chapters find no correlations between the tilting rates of the two different components. In Chapter 2, when comparing the tilting rate of the disc to the angular momentum misalignment between the two components: a weak correlation was found for subsample VICTOR:A and a slightly stronger correlation was found for subsample VICTOR:B. Chapter 3 did not find such a correlation for either sample with a correlation coefficient of just 0.21. When looking at individual galaxies from the NIHAO suite, only one galaxy tilted in the direction of the hot gas corona. However, when looking in more detail as cool gas fell further into the halo it became more aligned with the hot gas, as shown by Roškar et al. (2010). The hot gas near the disc is much more oblate and misaligned with the global angular momentum of the corona. It is possible that the more oblate shape induces larger torques on the infalling gas, it will change the angular momentum of the cool gas much more efficiently. However, further investigation is needed to understand the structure and angular momentum of the hot gas at different radii.

Warps

Chapter 3 presents a comparison between the misalignment of the gas disc with the tilting rate of the stellar disc, finding a weak correlation. Subsequently, Chapter 4 compared the angular momentum of the cool gas at various radii with the tilting direction of the stellar disc. In all three cases where the accretion of cool gas is the primary driver of tilting, the cool gas is misaligned in the direction of tilting. Roškar et al. (2010) argued for the creation of warps due to the ongoing feeding of misaligned cool gas to the disc, which would explain why these three galaxies, with tilting driven by cool gas accretion, have a warped gas disc.

5.2 Predictions for the Milky Way

This thesis presents tilting rates for galaxies in fully cosmological simulations and compares them to the predicted observational limit of *Gaia* (Perryman et al., 2014). If the MW is tilting at a similar rate to the galaxies investigated, it would be detectable. The next question is, in which direction is the disc tilting?

5.2.1 Using the warp

Three of the galaxies in the NIHAO suite tilt due to the ongoing accretion of misaligned angular momentum, in the form of cool gas. In all these cases the cool gas disc is warped with its angular momentum vector aligned towards the tilting direction of the stellar disc. Levine et al. (2006) reported the height of the MW's HI disc, finding that for $R = 16, 22$ and 28 kpc their fit yielded peaks in height out of the plane of $\sim 1.3, 3.7$ and 6.4 kpc, located at $l = 53^\circ, 57^\circ$ and 59° , respectively. If this is the case then the angular momentum of the HI is misaligned with the stellar disc of the MW, with a contribution in a direction towards $121^\circ \lesssim l \lesssim 127^\circ$. In such a scenario one would expect the MW to be tilting such that stars at longitude $53^\circ \lesssim l \lesssim 59^\circ$ would move preferentially towards positive heights and stars with longitude $121^\circ \lesssim l \lesssim 127^\circ$ would move towards negative heights, relative to the inertial frame of *Gaia*.

In the case of one of the galaxies in the NIHAO sample, the tilting is driven by the interaction with a satellite. After the interaction, the stellar disc of the galaxy has become aligned with the tilting direction. Bailin (2003) argued that because the angular momentum of the Galactic warp and Sgr dSph are aligned, and that the infall of the dwarf galaxy may have caused the warp to form. If this is the case, such a scenario is similar to the simulated galaxy, and one would predict a tilting direction using the stellar warp. Recently, Laporte et al. (2018) presented results from a set of N-body and hydrodynamical simulations of

the LMC and MW disc. Their simulations are able to create a warp in the stellar and gas discs, and the authors proposed that the current structure of the MW disc is caused by the interaction with the LMC. Past authors have claimed a similar connection between the LMC and Galactic warp (e.g. Weinberg and Blitz, 2006b). Again, in such a paradigm the tilting direction of the stellar disc would be predictable using the stellar or HI warp, as the main contribution of angular momentum will be aligned with the angular momentum of the infalling satellite, and the resulting stellar and gas warps.

5.3 Future work

5.3.1 Sample improvements

The logical extension is to improve the statistics by investigating the driving mechanism behind the measured tilting rates in the rest of NIHAO sample NIHAO:A. Because the galaxies in NIHAO have a roughly constant relative resolution, extending the sample to lower mass should not result in resolution issues, which would have been a hindrance in the cosmological simulation presented in Chapter 2.

The correlation between the sSFR and tilting rate of the stellar disc is tantalising, not only because it is the strongest found in this thesis. If the accretion of misaligned cool gas is the predominant driver behind the tilting rate of the stellar disc, galaxies with higher star formation would require the accretion of more gas, and would, therefore, tilt faster, explaining this correlation. However, in Chapter 4, two galaxies are presented where the dominant driver was not the accretion of cool gas. Extending this investigation to the remaining NIHAO galaxies would go a long way in unveiling the links between gas accretion, star formation and tilting rates.

5.3.2 More details about the corona

Chapter 4 showed the shape of the hot gas and the alignment between the angular momentum of the hot and cool gas. There is a clear transition between a more oblate and a more spheroidal shape near the radius of the stellar disc. The shape transition is likely driven by the potential well of the stellar disc, but the impact of the shape on the flow of cool gas has not been investigated. Cool gas passing through a spheroidal gas cloud could be torqued differently than gas passing through a more oblate distribution of gas. The angular momentum of the hot gas corona is not always aligned with the hot gas closer to the disc. More work needs to be carried out to investigate the cause of this angular momentum substructure, and the role both the substructure, shape and hydrodynamical forces play in the reorientation of the infalling cool gas's angular momentum.

References

- Agertz, O., Moore, B., Stadel, J., Potter, D., Miniati, F., Read, J., Mayer, L., Gawryszczak, A., Kravtsov, A., Nordlund, Å., Pearce, F., Quilis, V., Rudd, D., Springel, V., Stone, J., Tasker, E., Teyssier, R., Wadsley, J., and Walder, R. (2007). Fundamental differences between SPH and grid methods. *MNRAS*, 380:963–978.
- Aguerri, J. A. L., Méndez-Abreu, J., and Corsini, E. M. (2009). The population of barred galaxies in the local universe. I. Detection and characterisation of bars. *A&A*, 495:491–504.
- Agustsson, I. and Brainerd, T. G. (2006). The Locations of Satellite Galaxies in a Λ CDM Universe. *ApJ*, 650:550–559.
- Allgood, B., Flores, R. A., Primack, J. R., Kravtsov, A. V., Wechsler, R. H., Faltenbacher, A., and Bullock, J. S. (2006). The shape of dark matter haloes: dependence on mass, redshift, radius and formation. *MNRAS*, 367:1781–1796.
- Anderson, M. E. and Bregman, J. N. (2010). Do Hot Halos Around Galaxies Contain the Missing Baryons? *ApJ*, 714:320–331.
- Anderson, M. E. and Bregman, J. N. (2011). Detection of a Hot Gaseous Halo around the Giant Spiral Galaxy NGC 1961. *ApJ*, 737:22.
- Anderson, M. E., Churazov, E., and Bregman, J. N. (2016). A deep XMM-Newton study of the hot gaseous halo around NGC 1961. *MNRAS*, 455:227–243.
- Aragón-Calvo, M. A., van de Weygaert, R., Jones, B. J. T., and van der Hulst, J. M. (2007). Spin Alignment of Dark Matter Halos in Filaments and Walls. *ApJ*, 655:L5–L8.
- Athanassoula, E. (1992). The existence and shapes of dust lanes in galactic bars. *MNRAS*, 259:345–364.
- Athanassoula, E. (2005). On the nature of bulges in general and of box/peanut bulges in particular: input from N-body simulations. *MNRAS*, 358:1477–1488.
- Azzaro, M., Patiri, S. G., Prada, F., and Zentner, A. R. (2007). Angular distribution of satellite galaxies from the Sloan Digital Sky Survey Data Release 4. *MNRAS*, 376:L43–L47.
- Babcock, H. W. (1939). The rotation of the Andromeda Nebula. *Lick Observatory Bulletin*, 19:41–51.

- Bailin, J. (2003). Evidence for Coupling between the Sagittarius Dwarf Galaxy and the Milky Way Warp. *ApJ*, 583:L79–L82.
- Bailin, J., Kawata, D., Gibson, B. K., Steinmetz, M., Navarro, J. F., Brook, C. B., Gill, S. P. D., Ibata, R. A., Knebe, A., Lewis, G. F., and Okamoto, T. (2005). Internal Alignment of the Halos of Disk Galaxies in Cosmological Hydrodynamic Simulations. *ApJ*, 627:L17–L20.
- Bailin, J. and Steinmetz, M. (2004). Figure Rotation of Cosmological Dark Matter Halos. *ApJ*, 616:27–39.
- Bailin, J. and Steinmetz, M. (2005). Internal and External Alignment of the Shapes and Angular Momenta of Λ CDM Halos. *ApJ*, 627:647–665.
- Barazza, F. D., Jogee, S., and Marinova, I. (2008). Bars in Disk-dominated and Bulge-dominated Galaxies at $z \sim 0$: New Insights from ~ 3600 SDSS Galaxies. *ApJ*, 675:1194–1212.
- Bardeen, J. M., Bond, J. R., Kaiser, N., and Szalay, A. S. (1986). The statistics of peaks of Gaussian random fields. *ApJ*, 304:15–61.
- Barnes, J. and Efstathiou, G. (1987). Angular momentum from tidal torques. *ApJ*, 319:575–600.
- Barnes, J. and Hut, P. (1986). A hierarchical $O(N \log N)$ force-calculation algorithm. *Nature*, 324:446–449.
- Behroozi, P. S., Wechsler, R. H., and Conroy, C. (2013). The Average Star Formation Histories of Galaxies in Dark Matter Halos from $z = 0-8$. *ApJ*, 770:57.
- Bekki, K. (1998). Formation of a Polar Ring Galaxy in a Galaxy Merger. *ApJ*, 499:635–649.
- Bell, E. F. and de Jong, R. S. (2000). The stellar populations of spiral galaxies. *MNRAS*, 312:497–520.
- Bell, E. F., Wolf, C., Meisenheimer, K., Rix, H.-W., Borch, A., Dye, S., Kleinheinrich, M., Wisotzki, L., and McIntosh, D. H. (2004). Nearly 5000 Distant Early-Type Galaxies in COMBO-17: A Red Sequence and Its Evolution since $z \sim 1$. *ApJ*, 608:752–767.
- Bett, P., Eke, V., Frenk, C. S., Jenkins, A., and Okamoto, T. (2010). The angular momentum of cold dark matter haloes with and without baryons. *MNRAS*, 404:1137–1156.
- Bett, P. E. and Frenk, C. S. (2012). Spin flips - I. Evolution of the angular momentum orientation of Milky Way-mass dark matter haloes. *MNRAS*, 420:3324–3333.
- Bett, P. E. and Frenk, C. S. (2016). Spin flips - II. Evolution of dark matter halo spin orientation, and its correlation with major mergers. *MNRAS*, 461:1338–1355.
- Binggeli, B. (1982). The shape and orientation of clusters of galaxies. *A&A*, 107:338–349.
- Binney, J., Nipoti, C., and Fraternali, F. (2009). Do high-velocity clouds form by thermal instability? *MNRAS*, 397:1804–1815.

References

- Binney, J. and Petrou, M. (1985). Structure of box-shaped bulges and other spheroidal components. *MNRAS*, 214:449–462.
- Binney, J. and Tremaine, S. (2008). *Galactic Dynamics: Second Edition*. Princeton University Press.
- Bland-Hawthorn, J. and Gerhard, O. (2016). The Galaxy in Context: Structural, Kinematic, and Integrated Properties. *ARAA*, 54:529–596.
- Bogdán, Á., Forman, W. R., Kraft, R. P., and Jones, C. (2013). Detection of a Luminous Hot X-Ray Corona around the Massive Spiral Galaxy NGC 266. *ApJ*, 772:98.
- Bosma, A. (1978). *The distribution and kinematics of neutral hydrogen in spiral galaxies of various morphological types*. PhD thesis, PhD Thesis, Groningen Univ., (1978).
- Bouwens, R. J., Illingworth, G. D., Blakeslee, J. P., Broadhurst, T. J., and Franx, M. (2004). Galaxy Size Evolution at High Redshift and Surface Brightness Selection Effects: Constraints from the Hubble Ultra Deep Field. *ApJ*, 611:L1–L4.
- Bovy, J. and Rix, H.-W. (2013). A Direct Dynamical Measurement of the Milky Way’s Disk Surface Density Profile, Disk Scale Length, and Dark Matter Profile at $4 \text{ kpc} < \tilde{R} < \sim 9 \text{ kpc}$. *ApJ*, 779:115.
- Brainerd, T. G. (2005). Anisotropic Distribution of SDSS Satellite Galaxies: Planar (Not Polar) Alignment. *ApJ*, 628:L101–L104.
- Briggs, F. H. (1990). Rules of behavior for galactic WARPS. *ApJ*, 352:15–29.
- Brook, C. B., Governato, F., Quinn, T., Wadsley, J., Brooks, A. M., Willman, B., Stilp, A., and Jonsson, P. (2008). The Formation of Polar Disk Galaxies. *ApJ*, 689:678–686.
- Brook, C. B., Kawata, D., Gibson, B. K., and Freeman, K. C. (2004). The Emergence of the Thick Disk in a Cold Dark Matter Universe. *ApJ*, 612:894–899.
- Brook, C. B., Stinson, G., Gibson, B. K., Roškar, R., Wadsley, J., and Quinn, T. (2012). Hierarchical formation of bulgeless galaxies - II. Redistribution of angular momentum via galactic fountains. *MNRAS*, 419:771–779.
- Brooks, A. M., Governato, F., Quinn, T., Brook, C. B., and Wadsley, J. (2009). The Role of Cold Flows in the Assembly of Galaxy Disks. *ApJ*, 694:396–410.
- Bryan, S. E. and Cress, C. M. (2007). Figure rotation of dark haloes in cold dark matter simulations. *MNRAS*, 380:657–664.
- Buck, T., Dutton, A. A., and Macciò, A. V. (2016). Simulated Λ CDM analogues of the thin plane of satellites around the Andromeda galaxy are not kinematically coherent structures. *MNRAS*, 460:4348–4365.
- Burbidge, E. M. and Burbidge, G. R. (1959). Three Unusual so Galaxies. *ApJ*, 130:20.
- Bureau, M., Freeman, K. C., Pfizner, D. W., and Meurer, G. R. (1999). The Shape and Figure Rotation of the Dark Halo of NGC 2915. *AJ*, 118:2158–2171.

- Burton, W. B. (1988). *The structure of our Galaxy derived from observations of neutral hydrogen*, pages 295–358. Springer, New York, NY.
- Buta, R. J., Byrd, G. G., and Freeman, T. (2003). The Ringed Spiral Galaxy NGC 4622. I. Photometry, Kinematics, and the Case for Two Strong Leading Outer Spiral Arms. *AJ*, 125:634–666.
- Buta, R. J., Sheth, K., Athanassoula, E., Bosma, A., Knapen, J. H., Laurikainen, E., Salo, H., Elmegreen, D., Ho, L. C., Zaritsky, D., Courtois, H., Hinz, J. L., Muñoz-Mateos, J.-C., Kim, T., Regan, M. W., Gadotti, D. A., Gil de Paz, A., Laine, J., Menéndez-Delmestre, K., Comerón, S., Erroz Ferrer, S., Seibert, M., Mizusawa, T., Holwerda, B., and Madore, B. F. (2015). A Classical Morphological Analysis of Galaxies in the Spitzer Survey of Stellar Structure in Galaxies (S4G). *ApJS*, 217:32.
- Butsky, I., Macciò, A. V., Dutton, A. A., Wang, L., Obreja, A., Stinson, G. S., Penzo, C., Kang, X., Keller, B. W., and Wadsley, J. (2016). NIHAO project II: halo shape, phase-space density and velocity distribution of dark matter in galaxy formation simulations. *MNRAS*, 462:663–680.
- Camelio, G. and Lombardi, M. (2015). On the origin of intrinsic alignment in cosmic shear measurements: an analytic argument. *A&A*, 575:A113.
- Catelan, P., Kamionkowski, M., and Blandford, R. D. (2001). Intrinsic and extrinsic galaxy alignment. *MNRAS*, 320:L7–L13.
- Catelan, P. and Porciani, C. (2001). Correlations of cosmic tidal fields. *MNRAS*, 323:713–717.
- Cen, R. (2014). Evolution of Cold Streams and the Emergence of the Hubble Sequence. *ApJ*, 789:L21.
- Chemin, L., Balkowski, C., Cayatte, V., Carignan, C., Amram, P., Garrido, O., Hernandez, O., Marcelin, M., Adami, C., Boselli, A., and Boulesteix, J. (2006). A Virgo high-resolution H α kinematical survey - II. The Atlas. *MNRAS*, 366:812–857.
- Chen, D. N., Jing, Y. P., and Yoshikaw, K. (2003). Angular Momentum Distribution of Hot Gas and Implications for Disk Galaxy Formation. *ApJ*, 597:35–47.
- Cheung, E., Athanassoula, E., Masters, K. L., Nichol, R. C., Bosma, A., Bell, E. F., Faber, S. M., Koo, D. C., Lintott, C., Melvin, T., Schawinski, K., Skibba, R. A., and Willett, K. W. (2013). Galaxy Zoo: Observing Secular Evolution through Bars. *ApJ*, 779:162.
- Claeskens, J.-F., Smette, A., Vandenbulcke, L., and Surdej, J. (2006). Identification and redshift determination of quasi-stellar objects with medium-band photometry: application to Gaia. *MNRAS*, 367:879–904.
- Clowe, D., Bradač, M., Gonzalez, A. H., Markevitch, M., Randall, S. W., Jones, C., and Zaritsky, D. (2006). A Direct Empirical Proof of the Existence of Dark Matter. *ApJ*, 648:L109–L113.

References

- Codis, S., Pichon, C., Devriendt, J., Slyz, A., Pogosyan, D., Dubois, Y., and Sousbie, T. (2012). Connecting the cosmic web to the spin of dark haloes: implications for galaxy formation. *MNRAS*, 427:3320–3336.
- Colless, M., Dalton, G., Maddox, S., Sutherland, W., Norberg, P., Cole, S., Bland-Hawthorn, J., Bridges, T., Cannon, R., Collins, C., Couch, W., Cross, N., Deeley, K., De Propriis, R., Driver, S. P., Efstathiou, G., Ellis, R. S., Frenk, C. S., Glazebrook, K., Jackson, C., Lahav, O., Lewis, I., Lumsden, S., Madgwick, D., Peacock, J. A., Peterson, B. A., Price, I., Seaborne, M., and Taylor, K. (2001). The 2dF Galaxy Redshift Survey: spectra and redshifts. *MNRAS*, 328:1039–1063.
- Combes, F. and Sanders, R. H. (1981). Formation and properties of persisting stellar bars. *A&A*, 96:164–173.
- Conn, A. R., Lewis, G. F., Ibata, R. A., Parker, Q. A., Zucker, D. B., McConnachie, A. W., Martin, N. F., Valls-Gabaud, D., Tanvir, N., Irwin, M. J., Ferguson, A. M. N., and Chapman, S. C. (2013). The Three-dimensional Structure of the M31 Satellite System; Strong Evidence for an Inhomogeneous Distribution of Satellites. *ApJ*, 766:120.
- Corbelli, E. and Salucci, P. (2000). The extended rotation curve and the dark matter halo of M33. *MNRAS*, 311:441–447.
- Crittenden, R. G., Natarajan, P., Pen, U.-L., and Theuns, T. (2001). Spin-induced Galaxy Alignments and Their Implications for Weak-Lensing Measurements. *ApJ*, 559:552–571.
- Croft, R. A. C., Di Matteo, T., Springel, V., and Hernquist, L. (2009). Galaxy morphology, kinematics and clustering in a hydrodynamic simulation of a Λ cold dark matter universe. *MNRAS*, 400:43–67.
- Croft, R. A. C. and Metzler, C. A. (2000). Weak-Lensing Surveys and the Intrinsic Correlation of Galaxy Ellipticities. *ApJ*, 545:561–571.
- Cuesta, A. J., Betancort-Rijo, J. E., Gottlöber, S., Patiri, S. G., Yepes, G., and Prada, F. (2008). Spin alignment of dark matter haloes in the shells of the largest voids. *MNRAS*, 385:867–874.
- Dahlem, M. (1997). Gaseous Halos of Late-Type Spiral Galaxies. *PASP*, 109:1298–1320.
- Dai, X., Anderson, M. E., Bregman, J. N., and Miller, J. M. (2012). XMM-Newton Detects a Hot Gaseous Halo in the Fastest Rotating Spiral Galaxy UGC 12591. *ApJ*, 755:107.
- Dale, D. A., Beltz-Mohrmann, G. D., Egan, A. A., Hatlestad, A. J., Herzog, L. J., Leung, A. S., McLane, J. N., Phenicie, C., Roberts, J. S., Barnes, K. L., Boquien, M., Calzetti, D., Cook, D. O., Kobulnicky, H. A., Staudaher, S. M., and van Zee, L. (2016). Radial Star Formation Histories in 15 Nearby Galaxies. *AJ*, 151:4.
- Davies, R. L., Efstathiou, G., Fall, S. M., Illingworth, G., and Schechter, P. L. (1983). The kinematic properties of faint elliptical galaxies. *ApJ*, 266:41–57.
- de Jong, R. S. (1996). Near-infrared and optical broadband surface photometry of 86 face-on disk dominated galaxies. IV. Using color profiles to study stellar and dust content of galaxies. *A&A*, 313:377–395.

- de Vaucouleurs, G. (1948). Recherches sur les Nebuleuses Extragalactiques. *Annales d'Astrophysique*, 11:247.
- de Vaucouleurs, G. (1974). Structures of Central Bulges and Nuclei of Galaxies. In Shakeshaft, J. R., editor, *The Formation and Dynamics of Galaxies*, volume 58 of *IAU Symposium*, page 335.
- de Zeeuw, T. and Franx, M. (1991). Structure and dynamics of elliptical galaxies. *ARAA*, 29:239–274.
- Debattista, V. P., Carollo, C. M., Mayer, L., and Moore, B. (2004). Bulges or Bars from Secular Evolution? *ApJ*, 604:L93–L96.
- Debattista, V. P., Mayer, L., Carollo, C. M., Moore, B., Wadsley, J., and Quinn, T. (2006). The Secular Evolution of Disk Structural Parameters. *ApJ*, 645:209–227.
- Debattista, V. P., Moore, B., Quinn, T., Kazantzidis, S., Maas, R., Mayer, L., Read, J., and Stadel, J. (2008). The Causes of Halo Shape Changes Induced by Cooling Baryons: Disks versus Substructures. *ApJ*, 681:1076–1088.
- Debattista, V. P., Roškar, R., Valluri, M., Quinn, T., Moore, B., and Wadsley, J. (2013). What's up in the Milky Way? The orientation of the disc relative to the triaxial halo. *MNRAS*, 434:2971–2981.
- Debattista, V. P. and Sellwood, J. A. (1999). Warped Galaxies from Misaligned Angular Momenta. *ApJ*, 513:L107–L110.
- Debattista, V. P. and Sellwood, J. A. (2000). Constraints from Dynamical Friction on the Dark Matter Content of Barred Galaxies. *ApJ*, 543:704–721.
- Debattista, V. P., van den Bosch, F. C., Roškar, R., Quinn, T., Moore, B., and Cole, D. R. (2015). Internal alignments of red versus blue discs in dark matter haloes. *MNRAS*, 452:4094–4110.
- Deg, N. and Widrow, L. (2013). The Sagittarius stream and halo triaxiality. *MNRAS*, 428:912–922.
- Dehnen, W. and Aly, H. (2012). Improving convergence in smoothed particle hydrodynamics simulations without pairing instability. *MNRAS*, 425:1068–1082.
- Diehl, R., Halloin, H., Kretschmer, K., Lichti, G. G., Schönfelder, V., Strong, A. W., von Kienlin, A., Wang, W., Jean, P., Knödlseher, J., Roques, J.-P., Weidenspointner, G., Schanne, S., Hartmann, D. H., Winkler, C., and Wunderer, C. (2006). Radioactive ^{26}Al from massive stars in the Galaxy. *Nature*, 439:45–47.
- Djorgovski, S. and Davis, M. (1987). Fundamental properties of elliptical galaxies. *ApJ*, 313:59–68.
- Dong, X. C., Lin, W. P., Kang, X., Ocean Wang, Y., Dutton, A. A., and Macciò, A. V. (2014). The Distribution of Satellites around Central Galaxies in a Cosmological Hydrodynamical Simulation. *ApJ*, 791:L33.

References

- Drory, N. and Fisher, D. B. (2007). A Connection between Bulge Properties and the Bimodality of Galaxies. *ApJ*, 664:640–649.
- Dubinski, J. (1992). Cosmological tidal shear. *ApJ*, 401:441–454.
- Dubinski, J. and Carlberg, R. G. (1991a). The structure of cold dark matter halos. *ApJ*, 378:496–503.
- Dubinski, J. and Carlberg, R. G. (1991b). The structure of cold dark matter halos. *ApJ*, 378:496–503.
- Dubinski, J. and Chakrabarty, D. (2009). Warps and Bars from the External Tidal Torques of Tumbling Dark Halos. *ApJ*, 703:2068–2081.
- Dubinski, J. and Kuijken, K. (1995). The settling of warped disks in oblate dark halos. *ApJ*, 442:492–503.
- Dutton, A. A. and Macciò, A. V. (2014). Cold dark matter haloes in the Planck era: evolution of structural parameters for Einasto and NFW profiles. *MNRAS*, 441:3359–3374.
- Einstein, A. (1936). Lens-Like Action of a Star by the Deviation of Light in the Gravitational Field. *Science*, 84:506–507.
- Erwin, P. (2017). The Dependence of Bar Frequency on Galaxy Mass, Colour, and Gas Content – and Angular Resolution – in the Local Universe. *ArXiv e-prints*.
- Erwin, P. and Debattista, V. P. (2017). The frequency and stellar-mass dependence of boxy/peanut-shaped bulges in barred galaxies. *MNRAS*, 468:2058–2080.
- Fall, S. M. and Efstathiou, G. (1980a). Formation and rotation of disc galaxies with haloes. *MNRAS*, 193:189–206.
- Fall, S. M. and Efstathiou, G. (1980b). Formation and rotation of disc galaxies with haloes. *MNRAS*, 193:189–206.
- Faltenbacher, A., Allgood, B., Gottlöber, S., Yepes, G., and Hoffman, Y. (2005). Imprints of mass accretion on properties of galaxy clusters. *MNRAS*, 362:1099–1108.
- Faltenbacher, A., Jing, Y. P., Li, C., Mao, S., Mo, H. J., Pasquali, A., and van den Bosch, F. C. (2008). Spatial and Kinematic Alignments between Central and Satellite Halos. *ApJ*, 675:146–155.
- Faltenbacher, A., Li, C., Mao, S., van den Bosch, F. C., Yang, X., Jing, Y. P., Pasquali, A., and Mo, H. J. (2007). Three Different Types of Galaxy Alignment within Dark Matter Halos. *ApJ*, 662:L71–L74.
- Faltenbacher, A., Li, C., White, S. D. M., Jing, Y.-P., Shu-DeMao, and Wang, J. (2009). Alignment between galaxies and large-scale structure. *Research in Astronomy and Astrophysics*, 9:41–58.
- Fiacconi, D., Feldmann, R., and Mayer, L. (2015). The Argo simulation - II. The early build-up of the Hubble sequence. *MNRAS*, 446:1957–1972.

- Fisher, D. B. and Drory, N. (2011). Demographics of Bulge Types within 11 Mpc and Implications for Galaxy Evolution. *ApJ*, 733:L47.
- Fraternali, F. (2017). Gas Accretion via Condensation and Fountains. In Fox, A. and Davé, R., editors, *Gas Accretion onto Galaxies*, volume 430 of *Astrophysics and Space Science Library*, page 323.
- Frenk, C. S., White, S. D. M., Davis, M., and Efstathiou, G. (1988). The formation of dark halos in a universe dominated by cold dark matter. *ApJ*, 327:507–525.
- Frenk, C. S., White, S. D. M., Efstathiou, G., and Davis, M. (1985). Cold dark matter, the structure of galactic haloes and the origin of the Hubble sequence. *Nature*, 317:595–597.
- Fukugita, M. and Peebles, P. J. E. (2006). Massive Coronae of Galaxies. *ApJ*, 639:590–599.
- Gadotti, D. A. (2009). Structural properties of pseudo-bulges, classical bulges and elliptical galaxies: a Sloan Digital Sky Survey perspective. *MNRAS*, 393:1531–1552.
- García-Ruiz, I., Sancisi, R., and Kuijken, K. (2002). Neutral hydrogen and optical observations of edge-on galaxies: Hunting for warps. *A&A*, 394:769–789.
- Gatto, A., Fraternali, F., Read, J. I., Marinacci, F., Lux, H., and Walch, S. (2013). Unveiling the corona of the Milky Way via ram-pressure stripping of dwarf satellites. *MNRAS*, 433:2749–2763.
- Gill, S. P. D., Knebe, A., and Gibson, B. K. (2004). The evolution of substructure - I. A new identification method. *MNRAS*, 351:399–409.
- Gingold, R. A. and Monaghan, J. J. (1977). Smoothed particle hydrodynamics - Theory and application to non-spherical stars. *MNRAS*, 181:375–389.
- Gnedin, O. Y., Goodman, J., and Frei, Z. (1995). Measuring Spiral Arm Torques: Results for M100. *AJ*, 110:1105.
- Gogarten, S. M., Dalcanton, J. J., Williams, B. F., Roškar, R., Holtzman, J., Seth, A. C., Dolphin, A., Weisz, D., Cole, A., Debattista, V. P., Gilbert, K. M., Olsen, K., Skillman, E., de Jong, R. S., Karachentsev, I. D., and Quinn, T. R. (2010). The Advanced Camera for Surveys Nearby Galaxy Survey Treasury. V. Radial Star Formation History of NGC 300. *ApJ*, 712:858–874.
- Goldreich, P. and Lynden-Bell, D. (1965). II. Spiral arms as sheared gravitational instabilities. *MNRAS*, 130:125.
- Gómez, F. A., Besla, G., Carpintero, D. D., Villalobos, Á., O'Shea, B. W., and Bell, E. F. (2015). And Yet it Moves: The Dangers of Artificially Fixing the Milky Way Center of Mass in the Presence of a Massive Large Magellanic Cloud. *ApJ*, 802:128.
- Governato, F., Brook, C., Mayer, L., Brooks, A., Rhee, G., Wadsley, J., Jonsson, P., Willman, B., Stinson, G., Quinn, T., and Madau, P. (2010). Bulgeless dwarf galaxies and dark matter cores from supernova-driven outflows. *Nature*, 463:203–206.

References

- Governato, F., Willman, B., Mayer, L., Brooks, A., Stinson, G., Valenzuela, O., Wadsley, J., and Quinn, T. (2007). Forming disc galaxies in Λ CDM simulations. *MNRAS*, 374:1479–1494.
- Grosbøl, P., Patsis, P. A., and Pompei, E. (2004). Spiral galaxies observed in the near-infrared K band. I. Data analysis and structural parameters. *A&A*, 423:849–859.
- Haardt, F. and Madau, P. (1996). Radiative Transfer in a Clumpy Universe. II. The Ultraviolet Extragalactic Background. *ApJ*, 461:20.
- Hahn, O., Carollo, C. M., Porciani, C., and Dekel, A. (2007a). The evolution of dark matter halo properties in clusters, filaments, sheets and voids. *MNRAS*, 381:41–51.
- Hahn, O., Porciani, C., Carollo, C. M., and Dekel, A. (2007b). Properties of dark matter haloes in clusters, filaments, sheets and voids. *MNRAS*, 375:489–499.
- Hahn, O., Teyssier, R., and Carollo, C. M. (2010). The large-scale orientations of disc galaxies. *MNRAS*, 405:274–290.
- Hammer, F., Flores, H., Puech, M., Yang, Y. B., Athanassoula, E., Rodrigues, M., and Delgado, R. (2009). The Hubble sequence: just a vestige of merger events? *A&A*, 507:1313–1326.
- Harvey, D., Massey, R., Kitching, T., Taylor, A., and Tittley, E. (2015). The nongravitational interactions of dark matter in colliding galaxy clusters. *Science*, 347:1462–1465.
- Heavens, A., Refregier, A., and Heymans, C. (2000). Intrinsic correlation of galaxy shapes: implications for weak lensing measurements. *MNRAS*, 319:649–656.
- Hernquist, L. and Katz, N. (1989). TREESPH - A unification of SPH with the hierarchical tree method. *ApJS*, 70:419–446.
- Hirata, C. M., Mandelbaum, R., Ishak, M., Seljak, U., Nichol, R., Pimblet, K. A., Ross, N. P., and Wake, D. (2007). Intrinsic galaxy alignments from the 2SLAQ and SDSS surveys: luminosity and redshift scalings and implications for weak lensing surveys. *MNRAS*, 381:1197–1218.
- Hobbs, A., Read, J., and Nicola, A. (2015). Growing galaxies via superbubble-driven accretion flows. *MNRAS*, 452:3593–3609.
- Hobbs, A., Read, J., Power, C., and Cole, D. (2013). Thermal instabilities in cooling galactic coronae: fuelling star formation in galactic discs. *MNRAS*, 434:1849–1868.
- Hoffman, Y. (1988). On the formation and structure of galactic halos. *ApJ*, 328:489–498.
- Hoffman, Y. and Shaham, J. (1985). Local density maxima - Progenitors of structure. *ApJ*, 297:16–22.
- Hohl, F. (1971). Numerical Experiments with a Disk of Stars. *ApJ*, 168:343.
- Holmberg, E. (1941). On the Clustering Tendencies among the Nebulae. II. a Study of Encounters Between Laboratory Models of Stellar Systems by a New Integration Procedure. *ApJ*, 94:385.

- Holmberg, E. (1969). A study of physical groups of galaxies. *Arkiv for Astronomi*, 5:305–343.
- Hopkins, P. F. (2013). A general class of Lagrangian smoothed particle hydrodynamics methods and implications for fluid mixing problems. *MNRAS*, 428:2840–2856.
- Huang, S. and Carlberg, R. G. (1997). Sinking Satellites and Tilting Disk Galaxies. *ApJ*, 480:503–523.
- Hubble, E. P. (1926). Extragalactic nebulae. *ApJ*, 64.
- Jiang, I.-G. and Binney, J. (1999). WARPS and cosmic infall. *MNRAS*, 303:L7–L10.
- Jiang, I.-G. and Binney, J. (2000). The orbit and mass of the Sagittarius dwarf galaxy. *MNRAS*, 314:468–474.
- Jing, Y. P. (2002). Intrinsic correlation of halo ellipticity and its implications for large-scale weak lensing surveys. *MNRAS*, 335:L89–L93.
- Jing, Y. P. and Suto, Y. (2002). Triaxial Modeling of Halo Density Profiles with High-Resolution N-Body Simulations. *ApJ*, 574:538–553.
- Joung, M. R., Bryan, G. L., and Putman, M. E. (2012). Gas Condensation in the Galactic Halo. *ApJ*, 745:148.
- Jurić, M., Ivezić, Ž., Brooks, A., Lupton, R. H., Schlegel, D., Finkbeiner, D., Padmanabhan, N., Bond, N., Sesar, B., Rockosi, C. M., Knapp, G. R., Gunn, J. E., Sumi, T., Schneider, D. P., Barentine, J. C., Brewington, H. J., Brinkmann, J., Fukugita, M., Harvanek, M., Kleinman, S. J., Krzesinski, J., Long, D., Neilsen, Jr., E. H., Nitta, A., Snedden, S. A., and York, D. G. (2008). The Milky Way Tomography with SDSS. I. Stellar Number Density Distribution. *ApJ*, 673:864–914.
- Kallivayalil, N., van der Marel, R. P., Besla, G., Anderson, J., and Alcock, C. (2013). Third-epoch Magellanic Cloud Proper Motions. I. Hubble Space Telescope/WFC3 Data and Orbit Implications. *ApJ*, 764:161.
- Katz, N. (1992). Dissipational galaxy formation. II - Effects of star formation. *ApJ*, 391:502–517.
- Kazantzidis, S., Kravtsov, A. V., Zentner, A. R., Allgood, B., Nagai, D., and Moore, B. (2004). The Effect of Gas Cooling on the Shapes of Dark Matter Halos. *ApJ*, 611:L73–L76.
- Kennicutt, Jr., R. C. (1998). The Global Schmidt Law in Star-forming Galaxies. *ApJ*, 498:541–552.
- Kennicutt, Jr., R. C., Tamblyn, P., and Congdon, C. E. (1994). Past and future star formation in disk galaxies. *ApJ*, 435:22–36.
- Kereš, D., Katz, N., Weinberg, D. H., and Davé, R. (2005). How do galaxies get their gas? *MNRAS*, 363:2–28.

References

- Kerr, F. J., Bowers, P. F., Jackson, P. D., and Kerr, M. (1986). Fully sampled neutral hydrogen survey of the southern Milky Way. *A&AS*, 66:373–504.
- Kim, J., Park, C., Rossi, G., Lee, S. M., and Gott, III, J. R. (2011). The New Horizon Run Cosmological N-Body Simulations. *Journal of Korean Astronomical Society*, 44:217–234.
- Kim, W.-T. and Stone, J. M. (2012). Two-dimensional Magnetohydrodynamic Simulations of Barred Galaxies. *ApJ*, 751:124.
- Klessen, R. S. and Glover, S. C. O. (2016). Physical Processes in the Interstellar Medium. *Star Formation in Galaxy Evolution: Connecting Numerical Models to Reality, Saas-Fee Advanced Course, Volume 43. ISBN 978-3-662-47889-9. Springer-Verlag Berlin Heidelberg, 2016, p. 85, 43:85.*
- Klypin, A., Zhao, H., and Somerville, R. S. (2002). Λ CDM-based Models for the Milky Way and M31. I. Dynamical Models. *ApJ*, 573:597–613.
- Knapp, G. R., Stark, A. A., and Wilson, R. W. (1985). The global properties of the Galaxy. III - Maps of the (C-12)(O) emission in the first quadrant of the Galaxy. *AJ*, 90:254–300.
- Knollmann, S. R. and Knebe, A. (2009). AHF: Amiga’s Halo Finder. *ApJS*, 182:608–624.
- Koch, A. and Grebel, E. K. (2006). The Anisotropic Distribution of M31 Satellite Galaxies: A Polar Great Plane of Early-type Companions. *AJ*, 131:1405–1415.
- Komatsu, E., Dunkley, J., Nolta, M. R., Bennett, C. L., Gold, B., Hinshaw, G., Jarosik, N., Larson, D., Limon, M., Page, L., Spergel, D. N., Halpern, M., Hill, R. S., Kogut, A., Meyer, S. S., Tucker, G. S., Weiland, J. L., Wollack, E., and Wright, E. L. (2009). Five-Year Wilkinson Microwave Anisotropy Probe Observations: Cosmological Interpretation. *ApJS*, 180:330–376.
- Kormendy, J. (1985). Families of ellipsoidal stellar systems and the formation of dwarf elliptical galaxies. *ApJ*, 295:73–79.
- Kormendy, J., Drory, N., Bender, R., and Cornell, M. E. (2010). Bulgeless Giant Galaxies Challenge Our Picture of Galaxy Formation by Hierarchical Clustering. *ApJ*, 723:54–80.
- Kormendy, J. and Kennicutt, Jr., R. C. (2004). Secular Evolution and the Formation of Pseudobulges in Disk Galaxies. *ARAA*, 42:603–683.
- Kravtsov, A., Vikhlinin, A., and Meshcheryakov, A. (2014). Stellar mass – halo mass relation and star formation efficiency in high-mass halos. *ArXiv e-prints*.
- Laporte, C. F. P., Gómez, F. A., Besla, G., Johnston, K. V., and Garavito-Camargo, N. (2018). Response of the Milky Way’s disc to the Large Magellanic Cloud in a first infall scenario. *MNRAS*, 473:1218–1230.
- Law, D. R. and Majewski, S. R. (2010). The Sagittarius Dwarf Galaxy: A Model for Evolution in a Triaxial Milky Way Halo. *ApJ*, 714:229–254.
- Law, D. R., Majewski, S. R., and Johnston, K. V. (2009). Evidence for a Triaxial Milky Way Dark Matter Halo from the Sagittarius Stellar Tidal Stream. *ApJ*, 703:L67–L71.

- Law, D. R., Shapley, A. E., Steidel, C. C., Reddy, N. A., Christensen, C. R., and Erb, D. K. (2012). High velocity dispersion in a rare grand-design spiral galaxy at redshift $z = 2.18$. *Nature*, 487:338–340.
- Lee, J. and Pen, U.-L. (2007). Comparison between the Blue and Red Galaxy Alignments Detected in the Sloan Digital Sky Survey. *ApJ*, 670:L1–L4.
- Levine, E. S., Blitz, L., and Heiles, C. (2006). The Vertical Structure of the Outer Milky Way HI Disk. *ApJ*, 643:881–896.
- Li, Z., Wang, Y., Yang, X., Chen, X., Xie, L., and Wang, X. (2013). Brightest Satellite Galaxy Alignment of Sloan Digital Sky Survey Galaxy Groups. *ApJ*, 768:20.
- Libeskind, N. I., Hoffman, Y., Knebe, A., Steinmetz, M., Gottlöber, S., Metuki, O., and Yepes, G. (2012). The cosmic web and the orientation of angular momenta. *MNRAS*, 421:L137–L141.
- Licquia, T. C. and Newman, J. A. (2015). Improved Estimates of the Milky Way’s Stellar Mass and Star Formation Rate from Hierarchical Bayesian Meta-Analysis. *ApJ*, 806:96.
- Lilly, S. J., Carollo, C. M., Pipino, A., Renzini, A., and Peng, Y. (2013). Gas Regulation of Galaxies: The Evolution of the Cosmic Specific Star Formation Rate, the Metallicity-Mass-Star-formation Rate Relation, and the Stellar Content of Halos. *ApJ*, 772:119.
- Lin, C. C. and Shu, F. H. (1964). On the Spiral Structure of Disk Galaxies. *ApJ*, 140:646.
- Lindegren, L., Babusiaux, C., Bailer-Jones, C., Bastian, U., Brown, A. G. A., Cropper, M., Høg, E., Jordi, C., Katz, D., van Leeuwen, F., Luri, X., Mignard, F., de Bruijne, J. H. J., and Prusti, T. (2008). The Gaia mission: science, organization and present status. In Jin, W. J., Platais, I., and Perryman, M. A. C., editors, *A Giant Step: from Milli- to Micro-arcsecond Astrometry*, volume 248 of *IAU Symposium*, pages 217–223.
- Lintott, C., Schawinski, K., Bamford, S., Slosar, A., Land, K., Thomas, D., Edmondson, E., Masters, K., Nichol, R. C., Raddick, M. J., Szalay, A., Andreescu, D., Murray, P., and Vandenberg, J. (2011). Galaxy Zoo 1: data release of morphological classifications for nearly 900 000 galaxies. *MNRAS*, 410:166–178.
- Lintott, C. J., Schawinski, K., Slosar, A., Land, K., Bamford, S., Thomas, D., Raddick, M. J., Nichol, R. C., Szalay, A., Andreescu, D., Murray, P., and Vandenberg, J. (2008). Galaxy Zoo: morphologies derived from visual inspection of galaxies from the Sloan Digital Sky Survey. *MNRAS*, 389:1179–1189.
- Lucy, L. B. (1977). A numerical approach to the testing of the fission hypothesis. *AJ*, 82:1013–1024.
- Lynden-Bell, D. (1976). Dwarf galaxies and globular clusters in high velocity hydrogen streams. *MNRAS*, 174:695–710.
- Lynden-Bell, D. (1979). On a mechanism that structures galaxies. *MNRAS*, 187:101–107.
- Lynds, C. R. and Sandage, A. R. (1963). Evidence for an Explosion in the Center of the Galaxy M82. *ApJ*, 137:1005.

References

- MacArthur, L. A., Courteau, S., Bell, E., and Holtzman, J. A. (2004). Structure of Disk-dominated Galaxies. II. Color Gradients and Stellar Population Models. *ApJS*, 152:175–199.
- Macciò, A. V., Dutton, A. A., and van den Bosch, F. C. (2008). Concentration, spin and shape of dark matter haloes as a function of the cosmological model: WMAP1, WMAP3 and WMAP5 results. *MNRAS*, 391:1940–1954.
- Macciò, A. V., Moore, B., and Stadel, J. (2006). The Origin of Polar Ring Galaxies: Evidence for Galaxy Formation by Cold Accretion. *ApJ*, 636:L25–L28.
- Martinez-Valpuesta, I., Shlosman, I., and Heller, C. (2006). Evolution of Stellar Bars in Live Axisymmetric Halos: Recurrent Buckling and Secular Growth. *ApJ*, 637:214–226.
- Masters, K. L., Maraston, C., Nichol, R. C., Thomas, D., Beifiori, A., Bundy, K., Edmondson, E. M., Higgs, T. D., Leauthaud, A., Mandelbaum, R., Pforr, J., Ross, A. J., Ross, N. P., Schneider, D. P., Skibba, R., Tinker, J., Tojeiro, R., Wake, D. A., Brinkmann, J., and Weaver, B. A. (2011). The morphology of galaxies in the Baryon Oscillation Spectroscopic Survey. *MNRAS*, 418:1055–1070.
- Matsuda, T. and Isaka, H. (1980). Response of Gas to an Ovally Deformed Gravitational Potential of a Disk Galaxy. *Progress of Theoretical Physics*, 64:1265–1279.
- McConnachie, A. W. and Irwin, M. J. (2006). The satellite distribution of M31. *MNRAS*, 365:902–914.
- Metz, M., Kroupa, P., and Libeskind, N. I. (2008). The Orbital Poles of Milky Way Satellite Galaxies: A Rotationally Supported Disk of Satellites. *ApJ*, 680:287–294.
- Miller, G. E. and Scalo, J. M. (1979). The initial mass function and stellar birthrate in the solar neighborhood. *ApJS*, 41:513–547.
- Monaghan, J. J. (1992). Smoothed particle hydrodynamics. *ARAAS*, 30:543–574.
- Moore, B., Kazantzidis, S., Diemand, J., and Stadel, J. (2004). The origin and tidal evolution of cuspy triaxial haloes. *MNRAS*, 354:522–528.
- Moster, B. P., Naab, T., and White, S. D. M. (2013). Galactic star formation and accretion histories from matching galaxies to dark matter haloes. *MNRAS*, 428:3121–3138.
- Nair, P. B. and Abraham, R. G. (2010). A Catalog of Detailed Visual Morphological Classifications for 14,034 Galaxies in the Sloan Digital Sky Survey. *ApJS*, 186:427–456.
- Navarro, J. F., Frenk, C. S., and White, S. D. M. (1996). The Structure of Cold Dark Matter Halos. *ApJ*, 462:563.
- Nierenberg, A. M., Auger, M. W., Treu, T., Marshall, P. J., and Fassnacht, C. D. (2011). Luminous Satellites of Early-type Galaxies. I. Spatial Distribution. *ApJ*, 731:44.
- Okumura, T., Jing, Y. P., and Li, C. (2009). Intrinsic Ellipticity Correlation of SDSS Luminous Red Galaxies and Misalignment with Their Host Dark Matter Halos. *ApJ*, 694:214–221.

- Ostriker, E. C. and Binney, J. J. (1989). Warped and tilted galactic discs. *MNRAS*, 237:785–798.
- Pawlowski, M. S., Kroupa, P., and Jerjen, H. (2013). Dwarf galaxy planes: the discovery of symmetric structures in the Local Group. *MNRAS*, 435:1928–1957.
- Paz, D. J., Stasyszyn, F., and Padilla, N. D. (2008). Angular momentum-large-scale structure alignments in Λ CDM models and the SDSS. *MNRAS*, 389:1127–1136.
- Peñarrubia, J., Gómez, F. A., Besla, G., Erkal, D., and Ma, Y.-Z. (2016). A timing constraint on the (total) mass of the Large Magellanic Cloud. *MNRAS*, 456:L54–L58.
- Peebles, P. J. E. (1969). Origin of the Angular Momentum of Galaxies. *ApJ*, 155:393.
- Peebles, P. J. E. (1970). Structure of the Coma Cluster of Galaxies. *AJ*, 75:13.
- Pen, U.-L., Lee, J., and Seljak, U. (2000). Tentative Detection of Galaxy Spin Correlations in the Tully Catalog. *ApJ*, 543:L107–L110.
- Perryman, M., Spergel, D. N., and Lindegren, L. (2014). The Gaia Inertial Reference Frame and the Tilting of the Milky Way Disk. *ApJ*, 789:166.
- Perryman, M. A. C., de Boer, K. S., Gilmore, G., Høg, E., Lattanzi, M. G., Lindegren, L., Luri, X., Mignard, F., Pace, O., and de Zeeuw, P. T. (2001). GAIA: Composition, formation and evolution of the Galaxy. *A&A*, 369:339–363.
- Planck Collaboration, Ade, P. A. R., Aghanim, N., Armitage-Caplan, C., Arnaud, M., Ashdown, M., Atrio-Barandela, F., Aumont, J., Baccigalupi, C., Banday, A. J., and et al. (2014). Planck 2013 results. XVI. Cosmological parameters. *A&A*, 571:A16.
- Planck Collaboration, Ade, P. A. R., Aghanim, N., Arnaud, M., Ashdown, M., Aumont, J., Baccigalupi, C., Banday, A. J., Barreiro, R. B., Bartlett, J. G., and et al. (2016). Planck 2015 results. XIII. Cosmological parameters. *A&A*, 594:A13.
- Plionis, M. (1994). Position angles and alignments of clusters of galaxies. *ApJS*, 95:401–412.
- Porciani, C., Dekel, A., and Hoffman, Y. (2002). Testing tidal-torque theory - I. Spin amplitude and direction. *MNRAS*, 332:325–338.
- Power, C., Navarro, J. F., Jenkins, A., Frenk, C. S., White, S. D. M., Springel, V., Stadel, J., and Quinn, T. (2003). The inner structure of Λ CDM haloes - I. A numerical convergence study. *MNRAS*, 338:14–34.
- Price, D. J. (2008). Modelling discontinuities and Kelvin Helmholtz instabilities in SPH. *Journal of Computational Physics*, 227:10040–10057.
- Prochaska, J. X., Werk, J. K., Worseck, G., Tripp, T. M., Tumlinson, J., Burchett, J. N., Fox, A. J., Fumagalli, M., Lehner, N., Peeples, M. S., and Tejos, N. (2017). The COS-Halos Survey: Metallicities in the Low-redshift Circumgalactic Medium. *ApJ*, 837:169.
- Putman, M. E., Peek, J. E. G., and Jounge, M. R. (2012). Gaseous Galaxy Halos. *ARAA*, 50:491–529.

References

- Quinn, T. and Binney, J. (1992). Galactic accretion and angular momentum re-orientation. *MNRAS*, 255:729–736.
- Raiteri, C. M., Villata, M., and Navarro, J. F. (1996). Simulations of Galactic chemical evolution. I. O and Fe abundances in a simple collapse model. *A&A*, 315:105–115.
- Read, J. I., Hayfield, T., and Agertz, O. (2010). Resolving mixing in smoothed particle hydrodynamics. *MNRAS*, 405:1513–1530.
- Read, J. I., Lake, G., Agertz, O., and Debattista, V. P. (2008). Thin, thick and dark discs in Λ CDM. *MNRAS*, 389:1041–1057.
- Read, J. I., Walker, M. G., and Steger, P. (2018). The case for a cold dark matter cusp in Draco. *ArXiv e-prints*.
- Rees, M. J. and Ostriker, J. P. (1977). Cooling, dynamics and fragmentation of massive gas clouds - Clues to the masses and radii of galaxies and clusters. *MNRAS*, 179:541–559.
- Reshetnikov, V. and Combes, F. (1998). Statistics of optical WARPS in spiral disks. *A&A*, 337:9–16.
- Ribeiro, B., Le Fèvre, O., Tasca, L. A. M., Lemaux, B. C., Cassata, P., Garilli, B., Maccagni, D., Zamorani, G., Zucca, E., Amorín, R., Bardelli, S., Fontana, A., Giavalisco, M., Hathi, N. P., Koekemoer, A., Pforr, J., Tresse, L., and Dunlop, J. (2016). Size evolution of star-forming galaxies with $2 < z < 4.5$ in the VIMOS Ultra-Deep Survey. *A&A*, 593:A22.
- Robertson, B., Bullock, J. S., Cox, T. J., Di Matteo, T., Hernquist, L., Springel, V., and Yoshida, N. (2006). A Merger-driven Scenario for Cosmological Disk Galaxy Formation. *ApJ*, 645:986–1000.
- Rogstad, D. H., Lockhart, I. A., and Wright, M. C. H. (1974). Aperture-synthesis observations of H I in the galaxy M83. *ApJ*, 193:309–319.
- Rogstad, D. H., Wright, M. C. H., and Lockhart, I. A. (1976). Aperture synthesis of neutral hydrogen in the galaxy M33. *ApJ*, 204:703–711.
- Roškar, R., Debattista, V. P., Brooks, A. M., Quinn, T. R., Brook, C. B., Governato, F., Dalcanton, J. J., and Wadsley, J. (2010). Misaligned angular momentum in hydrodynamic cosmological simulations: warps, outer discs and thick discs. *MNRAS*, 408:783–796.
- Rubin, V. C. and Ford, Jr., W. K. (1970). Rotation of the Andromeda Nebula from a Spectroscopic Survey of Emission Regions. *ApJ*, 159:379.
- Sales, L. and Lambas, D. G. (2004). Anisotropy in the distribution of satellites around primary galaxies in the 2dF Galaxy Redshift Survey: the Holmberg effect. *MNRAS*, 348:1236–1240.
- Salpeter, E. E. (1955). The Luminosity Function and Stellar Evolution. *ApJ*, 121:161.
- Sanchez-Saavedra, M. L., Battaner, E., and Florido, E. (1990). Frequency of Warped Spiral Galaxies at Visible Wavelengths. *MNRAS*, 246:458.

- Sancisi, R. (1976). Warped HI Disks in Galaxies. *A&A*, 53:159.
- Sancisi, R. (1983). Gas at large radii. In Athanassoula, E., editor, *Internal Kinematics and Dynamics of Galaxies*, volume 100 of *IAU Symposium*, pages 55–62.
- Sanders, R. H. and Huntley, J. M. (1976). Gas response to oval distortions in disk galaxies. *ApJ*, 209:53–65.
- Sanders, R. H. and Tubbs, A. D. (1980). Gas as a tracer of barred spiral dynamics. *ApJ*, 235:803–820.
- Savage, B. D. and de Boer, K. S. (1979). Observational evidence for a hot gaseous Galactic corona. *ApJ*, 230:L77–L82.
- Schawinski, K., Urry, C. M., Simmons, B. D., Fortson, L., Kaviraj, S., Keel, W. C., Lintott, C. J., Masters, K. L., Nichol, R. C., Sarzi, M., Skibba, R., Treister, E., Willett, K. W., Wong, O. I., and Yi, S. K. (2014). The green valley is a red herring: Galaxy Zoo reveals two evolutionary pathways towards quenching of star formation in early- and late-type galaxies. *MNRAS*, 440:889–907.
- Schmidt, M. (1959a). The Rate of Star Formation. *ApJ*, 129:243.
- Schmidt, M. (1959b). The Rate of Star Formation. *ApJ*, 129:243.
- Schwarz, M. P. (1981). The response of gas in a galactic disk to bar forcing. *ApJ*, 247:77–88.
- Schweizer, F. (1976). Photometric studies of spiral structure. I - The disks and arms of six SB I and SC I galaxies. *ApJS*, 31:313–332.
- Sellwood, J. A. (2014). Secular evolution in disk galaxies. *Reviews of Modern Physics*, 86:1–46.
- Sharma, S. and Steinmetz, M. (2005). The Angular Momentum Distribution of Gas and Dark Matter in Galactic Halos. *ApJ*, 628:21–44.
- Shen, J. and Sellwood, J. A. (2006). Galactic warps induced by cosmic infall. *MNRAS*, 370:2–14.
- Sheth, K., Vogel, S. N., Regan, M. W., Thornley, M. D., and Teuben, P. J. (2005). Secular Evolution via Bar-driven Gas Inflow: Results from BIMA SONG. *ApJ*, 632:217–226.
- Shetty, R., Vogel, S. N., Ostriker, E. C., and Teuben, P. J. (2007). Kinematics of Spiral-Arm Streaming in M51. *ApJ*, 665:1138–1158.
- Shostak, G. S. and van der Kruit, P. C. (1984). Studies of nearly face-on spiral galaxies. II - HI synthesis observations and optical surface photometry of NGC 628. *A&A*, 132:20–32.
- Silk, J. (1977). On the fragmentation of cosmic gas clouds. I - The formation of galaxies and the first generation of stars. *ApJ*, 211:638–648.

References

- Simmons, B. D., Melvin, T., Lintott, C., Masters, K. L., Willett, K. W., Keel, W. C., Smethurst, R. J., Cheung, E., Nichol, R. C., Schawinski, K., Rutkowski, M., Kartaltepe, J. S., Bell, E. F., Casteels, K. R. V., Conselice, C. J., Almaini, O., Ferguson, H. C., Fortson, L., Hartley, W., Kocevski, D., Koekemoer, A. M., McIntosh, D. H., Mortlock, A., Newman, J. A., Ownsworth, J., Bamford, S., Dahlen, T., Faber, S. M., Finkelstein, S. L., Fontana, A., Galametz, A., Grogin, N. A., Grützbauch, R., Guo, Y., Häußler, B., Jek, K. J., Kaviraj, S., Lucas, R. A., Peth, M., Salvato, M., Wiklind, T., and Wuyts, S. (2014). Galaxy Zoo: CANDELS barred discs and bar fractions. *MNRAS*, 445:3466–3474.
- Skibba, R. A., Masters, K. L., Nichol, R. C., Zehavi, I., Hoyle, B., Edmondson, E. M., Bamford, S. P., Cardamone, C. N., Keel, W. C., Lintott, C., and Schawinski, K. (2012). Galaxy Zoo: the environmental dependence of bars and bulges in disc galaxies. *MNRAS*, 423:1485–1502.
- Smargon, A., Mandelbaum, R., Bahcall, N., and Niederste-Ostholt, M. (2012). Detection of intrinsic cluster alignments to $100 \text{ h}^{-1} \text{ Mpc}$ in the Sloan Digital Sky Survey. *MNRAS*, 423:856–861.
- Spitzer, Jr., L. (1956). On a Possible Interstellar Galactic Corona. *ApJ*, 124:20.
- Springel, V., White, S. D. M., Jenkins, A., Frenk, C. S., Yoshida, N., Gao, L., Navarro, J., Thacker, R., Croton, D., Helly, J., Peacock, J. A., Cole, S., Thomas, P., Couchman, H., Evrard, A., Colberg, J., and Pearce, F. (2005). Simulations of the formation, evolution and clustering of galaxies and quasars. *Nature*, 435:629–636.
- Stadel, J. G. (2001). *Cosmological N-body simulations and their analysis*. PhD thesis, UNIVERSITY OF WASHINGTON.
- Stinson, G., Seth, A., Katz, N., Wadsley, J., Governato, F., and Quinn, T. (2006). Star formation and feedback in smoothed particle hydrodynamic simulations - I. Isolated galaxies. *MNRAS*, 373:1074–1090.
- Stinson, G. S., Brook, C., Macciò, A. V., Wadsley, J., Quinn, T. R., and Couchman, H. M. P. (2013). Making Galaxies In a Cosmological Context: the need for early stellar feedback. *MNRAS*, 428:129–140.
- Strateva, I., Ivezić, Ž., Knapp, G. R., Narayanan, V. K., Strauss, M. A., Gunn, J. E., Lupton, R. H., Schlegel, D., Bahcall, N. A., Brinkmann, J., Brunner, R. J., Budavári, T., Csabai, I., Castander, F. J., Doi, M., Fukugita, M., Györy, Z., Hamabe, M., Hennessy, G., Ichikawa, T., Kunszt, P. Z., Lamb, D. Q., McKay, T. A., Okamura, S., Racusin, J., Sekiguchi, M., Schneider, D. P., Shimasaku, K., and York, D. (2001). Color Separation of Galaxy Types in the Sloan Digital Sky Survey Imaging Data. *AJ*, 122:1861–1874.
- Taylor, A. N., Dye, S., Broadhurst, T. J., Benítez, N., and van Kampen, E. (1998). Gravitational Lens Magnification and the Mass of Abell 1689. *ApJ*, 501:539–553.
- Tempel, E. and Libeskind, N. I. (2013). Galaxy Spin Alignment in Filaments and Sheets: Observational Evidence. *ApJ*, 775:L42.
- Tempel, E., Stoica, R. S., and Saar, E. (2013). Evidence for spin alignment of spiral and elliptical/S0 galaxies in filaments. *MNRAS*, 428:1827–1836.

- Thilker, D. A., Bianchi, L., Boissier, S., Gil de Paz, A., Madore, B. F., Martin, D. C., Meurer, G. R., Neff, S. G., Rich, R. M., Schiminovich, D., Seibert, M., Wyder, T. K., Barlow, T. A., Byun, Y.-I., Donas, J., Forster, K., Friedman, P. G., Heckman, T. M., Jelinsky, P. N., Lee, Y.-W., Malina, R. F., Milliard, B., Morrissey, P., Siegmund, O. H. W., Small, T., Szalay, A. S., and Welsh, B. Y. (2005). Recent Star Formation in the Extreme Outer Disk of M83. *ApJ*, 619:L79–L82.
- Thilker, D. A., Bianchi, L., Meurer, G., Gil de Paz, A., Boissier, S., Madore, B. F., Boselli, A., Ferguson, A. M. N., Muñoz-Mateos, J. C., Madsen, G. J., Hameed, S., Overzier, R. A., Forster, K., Friedman, P. G., Martin, D. C., Morrissey, P., Neff, S. G., Schiminovich, D., Seibert, M., Small, T., Wyder, T. K., Donas, J., Heckman, T. M., Lee, Y.-W., Milliard, B., Rich, R. M., Szalay, A. S., Welsh, B. Y., and Yi, S. K. (2007). A Search for Extended Ultraviolet Disk (XUV-Disk) Galaxies in the Local Universe. *ApJS*, 173:538–571.
- Toomre, A. (1977). Theories of spiral structure. *ARAA*, 15:437–478.
- Tremaine, S. and Weinberg, M. D. (1984). A kinematic method for measuring the pattern speed of barred galaxies. *ApJ*, 282:L5–L7.
- Trowland, H. E., Lewis, G. F., and Bland-Hawthorn, J. (2013). The Cosmic History of the Spin of Dark Matter Halos within the Large-scale Structure. *ApJ*, 762:72.
- Tully, R. B. and Fisher, J. R. (1977). A new method of determining distances to galaxies. *A&A*, 54:661–673.
- Tumlinson, J., Peebles, M. S., and Werk, J. K. (2017a). The Circumgalactic Medium. *ARAA*, 55:389–432.
- Tumlinson, J., Peebles, M. S., and Werk, J. K. (2017b). The Circumgalactic Medium. *ARAA*, 55:389–432.
- Tumlinson, J., Thom, C., Werk, J. K., Prochaska, J. X., Tripp, T. M., Weinberg, D. H., Peebles, M. S., O’Meara, J. M., Oppenheimer, B. D., Meiring, J. D., Katz, N. S., Davé, R., Ford, A. B., and Sembach, K. R. (2011). The Large, Oxygen-Rich Halos of Star-Forming Galaxies Are a Major Reservoir of Galactic Metals. *Science*, 334:948.
- van Albada, G. D. and Roberts, Jr., W. W. (1981). A high-resolution study of the gas flow in barred spirals. *ApJ*, 246:740–750.
- van den Bosch, F. C., Abel, T., Croft, R. A. C., Hernquist, L., and White, S. D. M. (2002). The Angular Momentum of Gas in Protogalaxies. I. Implications for the Formation of Disk Galaxies. *ApJ*, 576:21–35.
- van den Bosch, F. C., Burkert, A., and Swaters, R. A. (2001). The angular momentum content of dwarf galaxies: new challenges for the theory of galaxy formation. *MNRAS*, 326:1205–1215.
- Veilleux, S., Cecil, G., and Bland-Hawthorn, J. (2005). Galactic Winds. *ARAA*, 43:769–826.
- Vera-Ciro, C. and Helmi, A. (2013). Constraints on the Shape of the Milky Way Dark Matter Halo from the Sagittarius Stream. *ApJ*, 773:L4.

References

- Verdes-Montenegro, L., Bosma, A., and Athanassoula, E. (2002). Star formation in the warped outer pseudoring of the spiral galaxy NGC 3642. *A&A*, 389:825–835.
- Visser, H. C. D. (1978). The dynamics of the spiral galaxy M81. In Berkhuijsen, E. M. and Wielebinski, R., editors, *Structure and Properties of Nearby Galaxies*, volume 77 of *IAU Symposium*, pages 105–111.
- Volders, L. M. J. S. (1959). Neutral hydrogen in M 33 and M 101. *BAN*, 14:323.
- Wadsley, J. W., Keller, B. W., and Quinn, T. R. (2017). Gasoline2: a modern smoothed particle hydrodynamics code. *MNRAS*, 471:2357–2369.
- Wadsley, J. W., Stadel, J., and Quinn, T. (2004). Gasoline: a flexible, parallel implementation of TreeSPH. *NewAst*, 9:137–158.
- Wadsley, J. W., Veeravalli, G., and Couchman, H. M. P. (2008). On the treatment of entropy mixing in numerical cosmology. *MNRAS*, 387:427–438.
- Walker, S. A., Bagchi, J., and Fabian, A. C. (2015). A deep Chandra observation of the hot gaseous halo around a rare, extremely massive and relativistic jet launching spiral galaxy. *MNRAS*, 449:3527–3534.
- Wang, H., Mo, H. J., Jing, Y. P., Yang, X., and Wang, Y. (2011). Internal properties and environments of dark matter haloes. *MNRAS*, 413:1973–1990.
- Wang, L., Dutton, A. A., Stinson, G. S., Macciò, A. V., Penzo, C., Kang, X., Keller, B. W., and Wadsley, J. (2015). NIHAO project - I. Reproducing the inefficiency of galaxy formation across cosmic time with a large sample of cosmological hydrodynamical simulations. *MNRAS*, 454:83–94.
- Wang, Q. D., Immler, S., Walterbos, R., Lauroesch, J. T., and Breitschwerdt, D. (2001). Chandra Detection of a Hot Gaseous Corona around the Edge-on Galaxy NGC 4631. *ApJ*, 555:L99–L102.
- Wang, Y., Park, C., Hwang, H. S., and Chen, X. (2010). Distribution of Satellite Galaxies in High-redshift Groups. *ApJ*, 718:762–767.
- Wang, Y., Yang, X., Mo, H. J., Li, C., van den Bosch, F. C., Fan, Z., and Chen, X. (2008). Probing the intrinsic shape and alignment of dark matter haloes using SDSS galaxy groups. *MNRAS*, 385:1511–1522.
- Wang, Y. O., Lin, W. P., Kang, X., Dutton, A., Yu, Y., and Macciò, A. V. (2014). Satellite Alignment. I. Distribution of Substructures and their Dependence on Assembly History from N-body Simulations. *ApJ*, 786:8.
- Warren, M. S., Quinn, P. J., Salmon, J. K., and Zurek, W. H. (1992). Dark halos formed via dissipationless collapse. I - Shapes and alignment of angular momentum. *ApJ*, 399:405–425.
- Weinberg, M. D. and Blitz, L. (2006a). A Magellanic Origin for the Warp of the Galaxy. *ApJ*, 641:L33–L36.

- Weinberg, M. D. and Blitz, L. (2006b). A Magellanic Origin for the Warp of the Galaxy. *ApJ*, 641:L33–L36.
- Wendland, H. (1995). Piecewise polynomial, positive definite and compactly supported radial functions of minimal degree. *Advances in Computational Mathematics*, 4(1):389–396.
- White, S. D. M. and Frenk, C. S. (1991). Galaxy formation through hierarchical clustering. *ApJ*, 379:52–79.
- White, S. D. M. and Rees, M. J. (1978). Core condensation in heavy halos - A two-stage theory for galaxy formation and clustering. *MNRAS*, 183:341–358.
- Whitmore, B. C., Lucas, R. A., McElroy, D. B., Steiman-Cameron, T. Y., Sackett, P. D., and Olling, R. P. (1990). New observations and a photographic atlas of polar-ring galaxies. *AJ*, 100:1489–1522.
- Willett, K. W., Lintott, C. J., Bamford, S. P., Masters, K. L., Simmons, B. D., Casteels, K. R. V., Edmondson, E. M., Fortson, L. F., Kaviraj, S., Keel, W. C., Melvin, T., Nichol, R. C., Raddick, M. J., Schawinski, K., Simpson, R. J., Skibba, R. A., Smith, A. M., and Thomas, D. (2013). Galaxy Zoo 2: detailed morphological classifications for 304 122 galaxies from the Sloan Digital Sky Survey. *MNRAS*, 435:2835–2860.
- Williams, B. F., Dalcanton, J. J., Dolphin, A. E., Holtzman, J., and Sarajedini, A. (2009). The Detection of Inside-Out Disk Growth in M33. *ApJ*, 695:L15–L19.
- Yang, X., van den Bosch, F. C., Mo, H. J., Mao, S., Kang, X., Weinmann, S. M., Guo, Y., and Jing, Y. P. (2006). The alignment between the distribution of satellites and the orientation of their central galaxy. *MNRAS*, 369:1293–1302.
- Yoshino, A. and Yamauchi, C. (2015). Box/peanut and bar structures in edge-on and face-on nearby galaxies in the Sloan Digital Sky Survey - I. Catalogue. *MNRAS*, 446:3749–3767.
- Yuan, T., Richard, J., Gupta, A., Federrath, C., Sharma, S., Groves, B. A., Kewley, L. J., Cen, R., Birnboim, Y., and Fisher, D. B. (2017). The most ancient spiral galaxy: a 2.6-Gyr-old disk with a tranquil velocity field. *ArXiv e-prints*.
- Yurin, D. and Springel, V. (2015). The stability of stellar discs in Milky Way-sized dark matter haloes. *MNRAS*, 452:2367–2387.
- Zhang, Y., Yang, X., Faltenbacher, A., Springel, V., Lin, W., and Wang, H. (2009). The Spin and Orientation of Dark Matter Halos Within Cosmic Filaments. *ApJ*, 706:747–761.
- Zhang, Y., Yang, X., Wang, H., Wang, L., Luo, W., Mo, H. J., and van den Bosch, F. C. (2015). Spin Alignments of Spiral Galaxies within the Large-scale Structure from SDSS DR7. *ApJ*, 798:17.
- Zhang, Y., Yang, X., Wang, H., Wang, L., Mo, H. J., and van den Bosch, F. C. (2013). Alignments of Galaxies within Cosmic Filaments from SDSS DR7. *ApJ*, 779:160.
- Zibetti, S., Charlot, S., and Rix, H.-W. (2009). Resolved stellar mass maps of galaxies - I. Method and implications for global mass estimates. *MNRAS*, 400:1181–1198.

References

Zwicky, F. (1933). Die Rotverschiebung von extragalaktischen Nebeln. *Helvetica Physica Acta*, 6:110–127.

Appendix A

Chapter 4 Figures Continued

A.1 g7.55e11

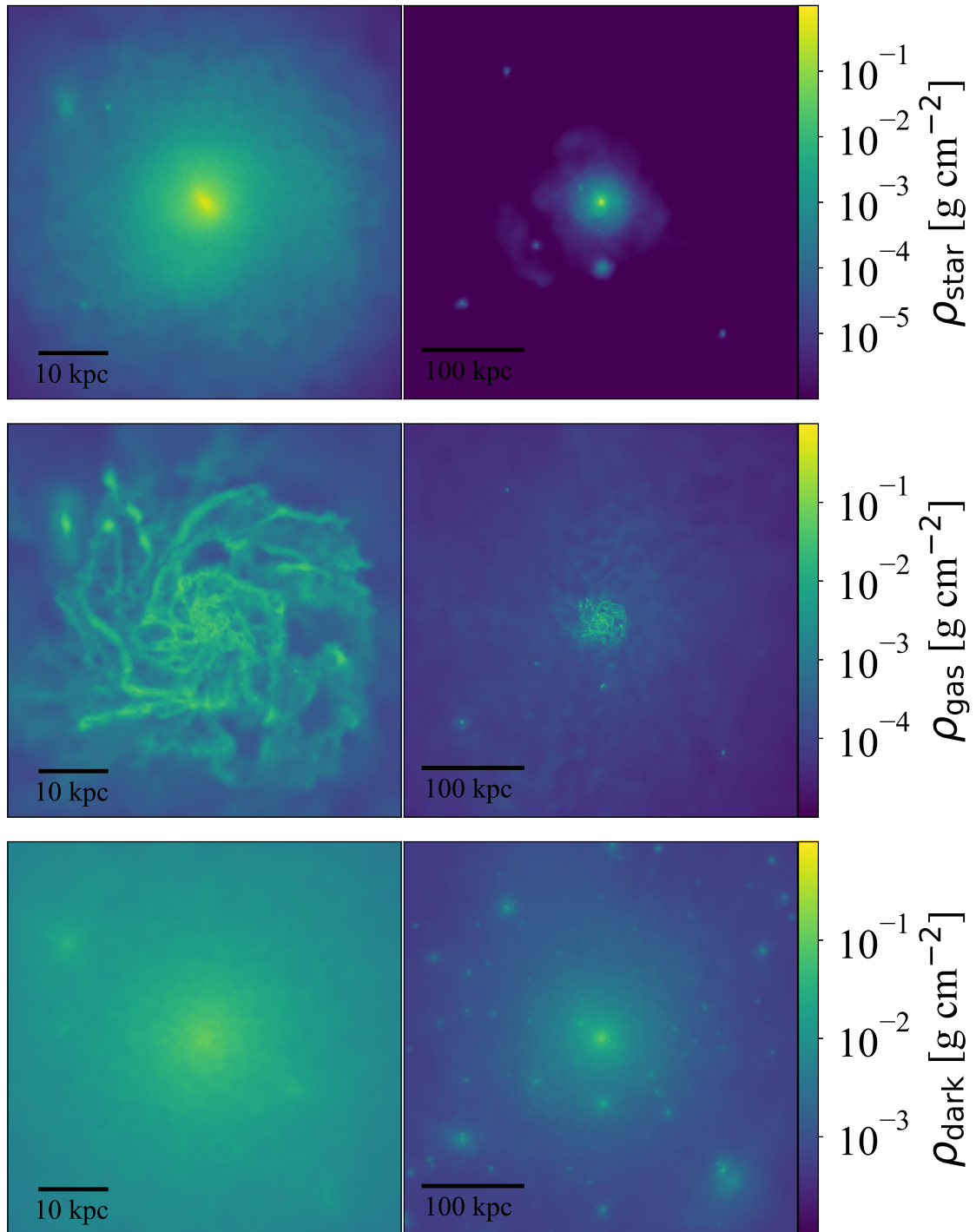


Fig. A.1 g7.55e11: column density of stars (top row), gas (middle row) and dark matter (bottom row), within boxes of widths 60 kpc (left column) and 400 kpc (right column).

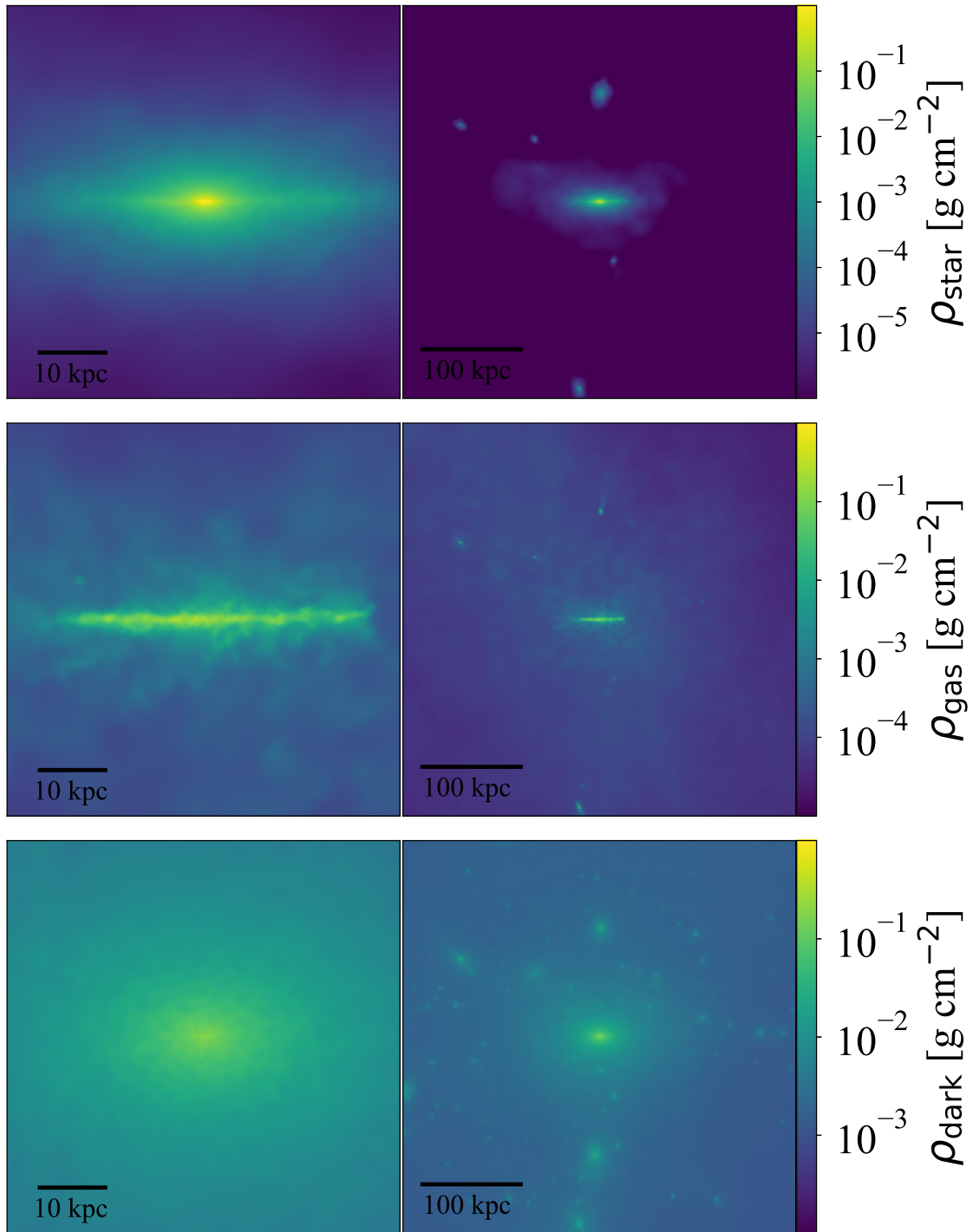


Fig. A.2 g7.55e11: column density of stars (top row), gas (middle row) and dark matter (bottom row), within boxes of widths 60 kpc (left column) and 400 kpc (right column).

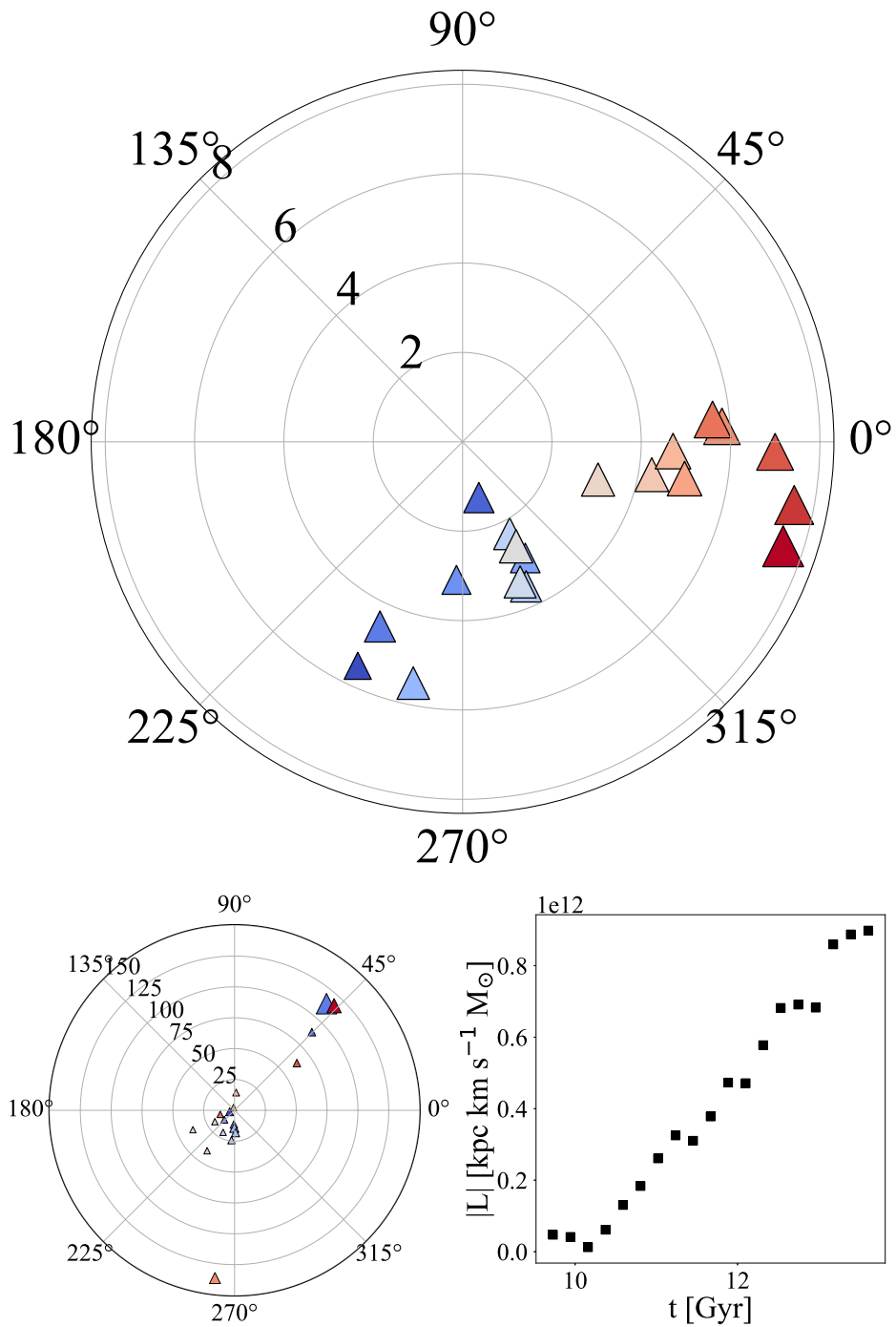


Fig. A.3 g7.55e11: top: total angular momentum of stars entering R_{disc} at each time step, left: total angular momentum of stars entering $0.5R_{200}$ at each time step, right: magnitude of angular momentum entering R_{disc} at each time step.

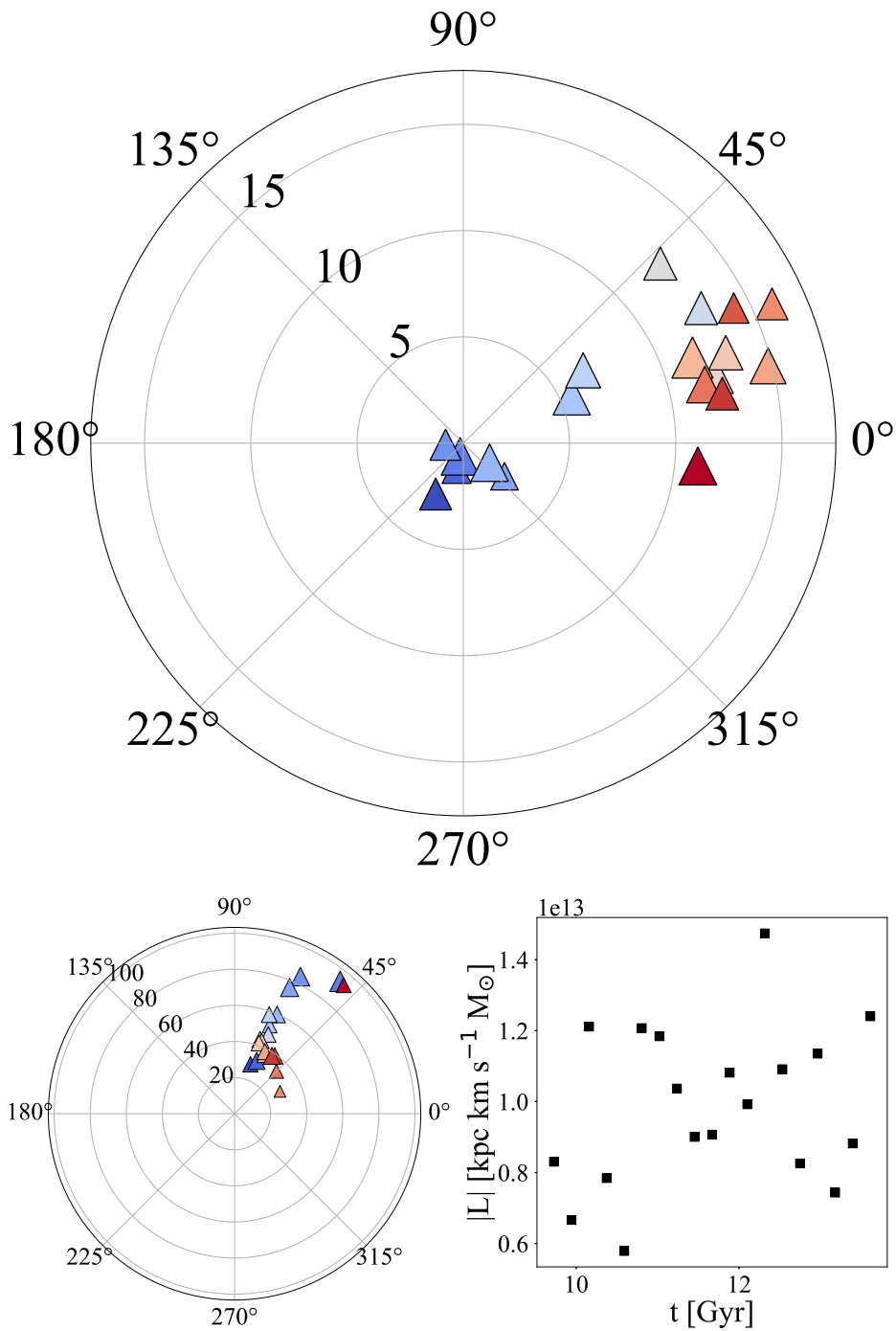


Fig. A.4 g7.55e11: top: total angular momentum of gas entering R_{disc} at each time step, left: total angular momentum of gas entering $0.5R_{200}$ at each time step, right: magnitude of angular momentum entering R_{disc} at each time step.

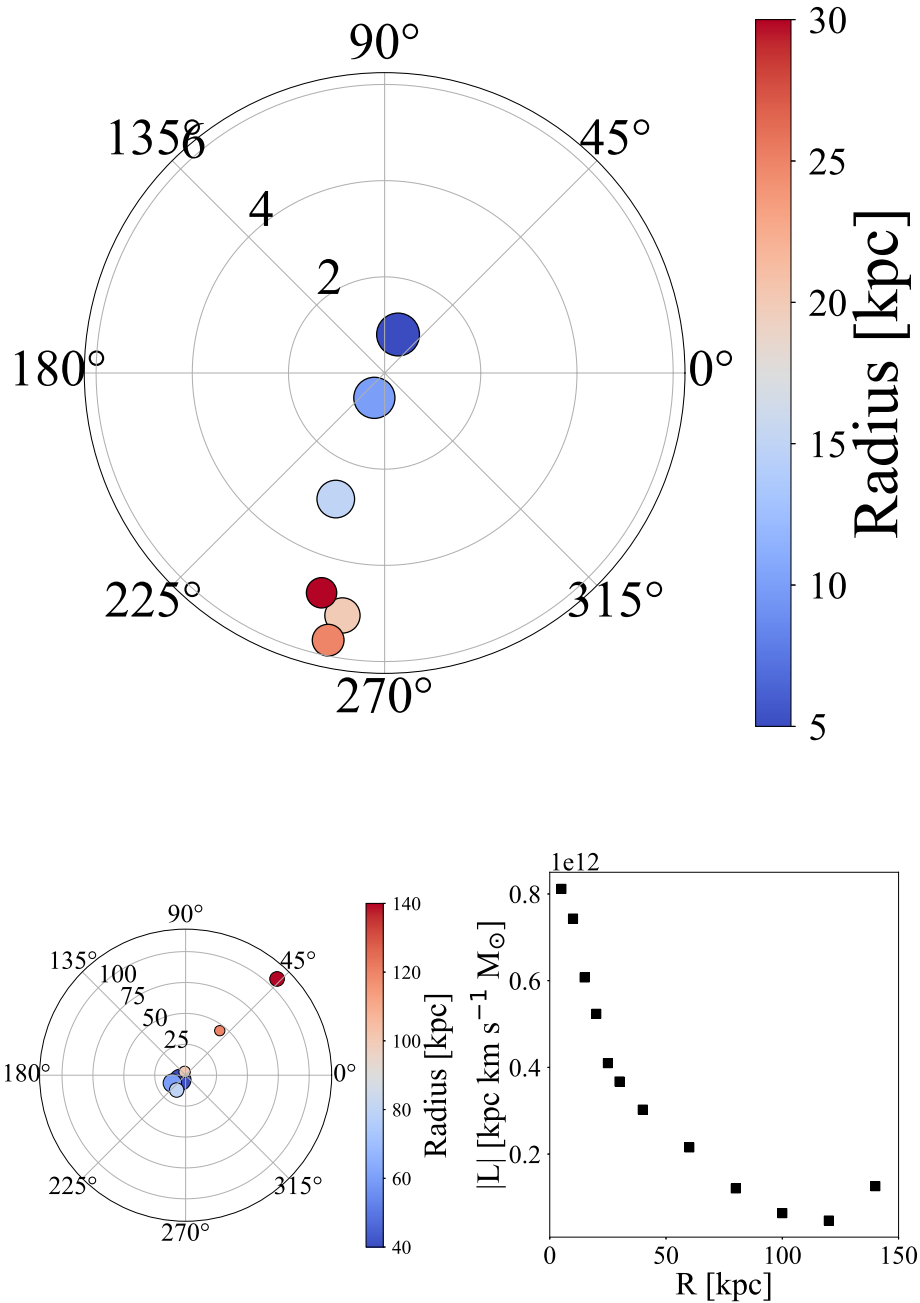


Fig. A.5 g7.55e11: the integrated net angular momentum flow of stars calculated at increasing radii between 5 and 30 kpc with annuli of width 5 kpc (top) and between 40 and 120 kpc with annuli of width 20 kpc (left), and the magnitude of each angular momenta against the interior annular radius (right).

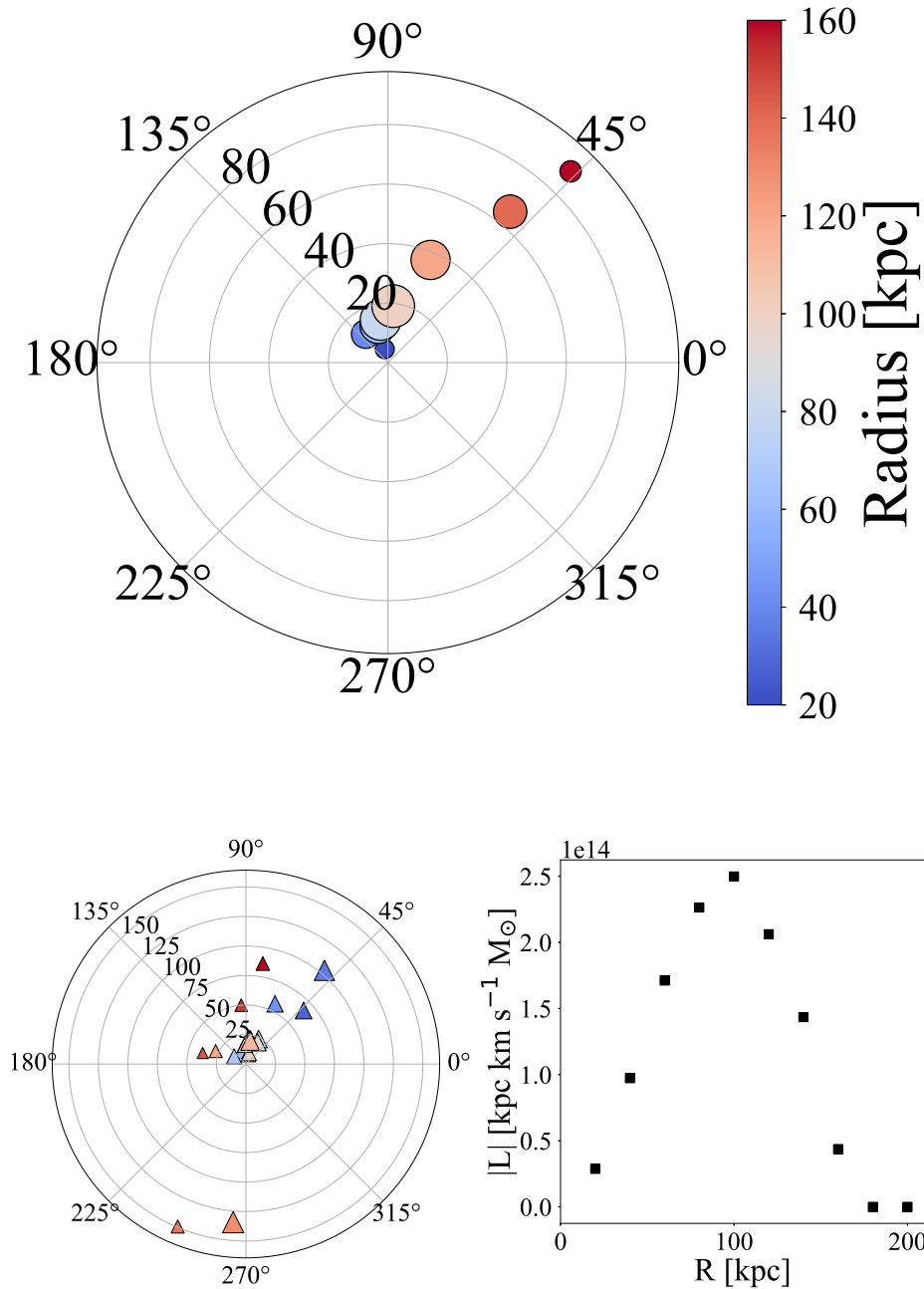


Fig. A.6 g7.55e11: the integrated net angular momentum flow of dark matter calculated at increasing radii between 20 and 200 kpc with annuli of width 20 kpc (top), the total angular momentum of dark matter entering $0.5R_{200}$ at each time step (left), and the magnitude of each angular momenta against the interior annular radius (right).

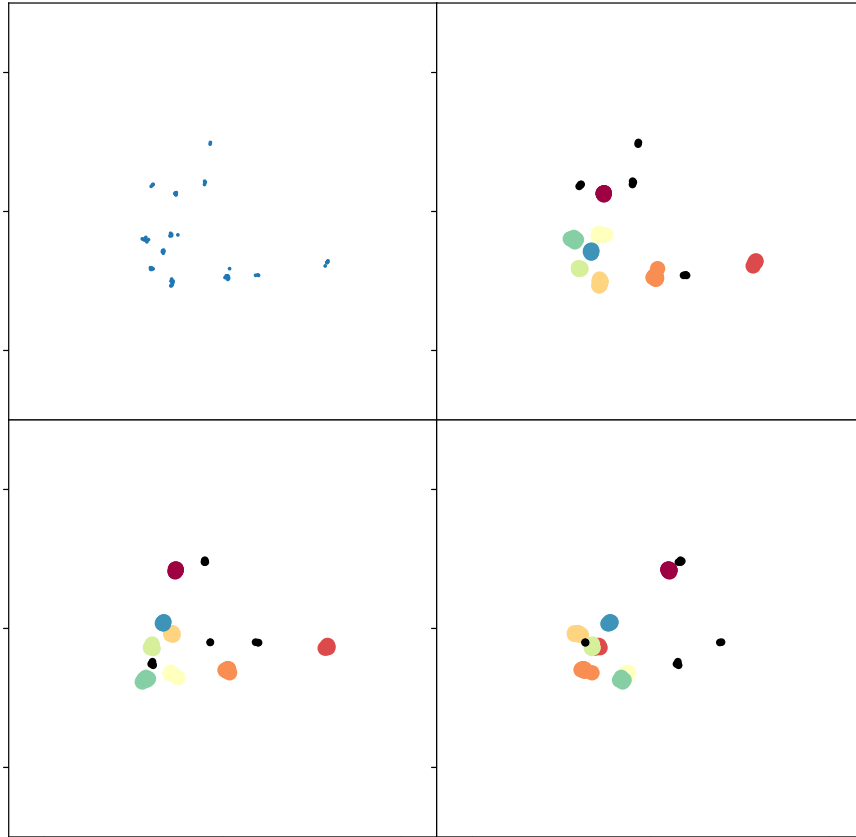


Fig. A.7 g7.55e11: this plot shows the distribution of the gas clouds at $z = 0.3$, each colour represents a different gas cloud that will be tracked. The top left and top right panel show the gas clouds projected in the x - y plane, before (left) and after (right) grouping. The bottom left and bottom right panels show the gas clouds projected in the x - z and y - z planes, respectively.

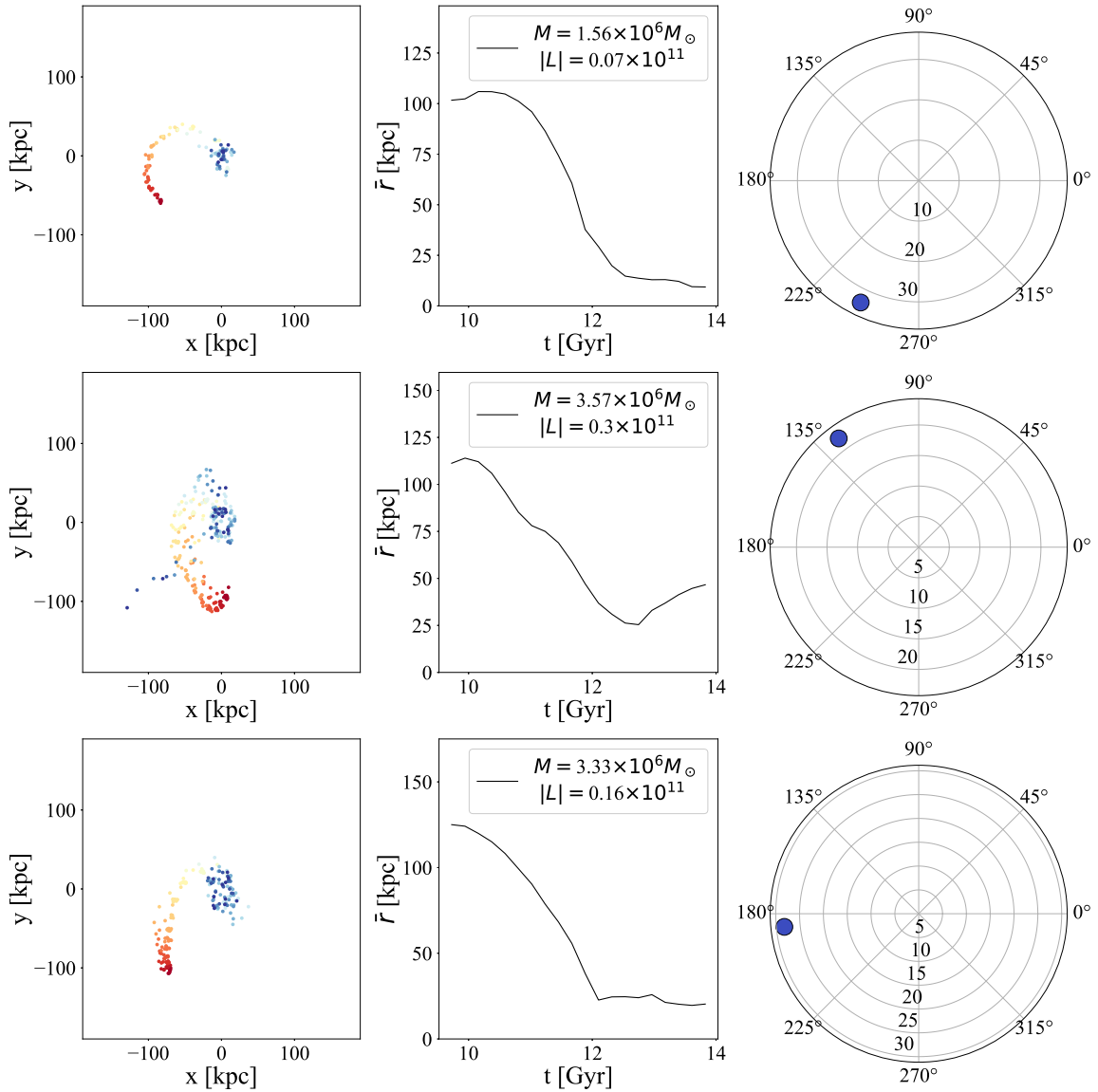


Fig. A.8 Left: the location of all the particles in the gas cloud with $M > 10^6 M_\odot$ & $\bar{R} < 30$ kpc, middle: average distance to the centre of the galaxy with time, right: angular momentum of each gas cloud at $z = 0.3$. The mass and starting angular momentum (in units $M_\odot \text{ km s}^{-1}$) of each cloud is given in middle plot.

A.2 g7.66e11

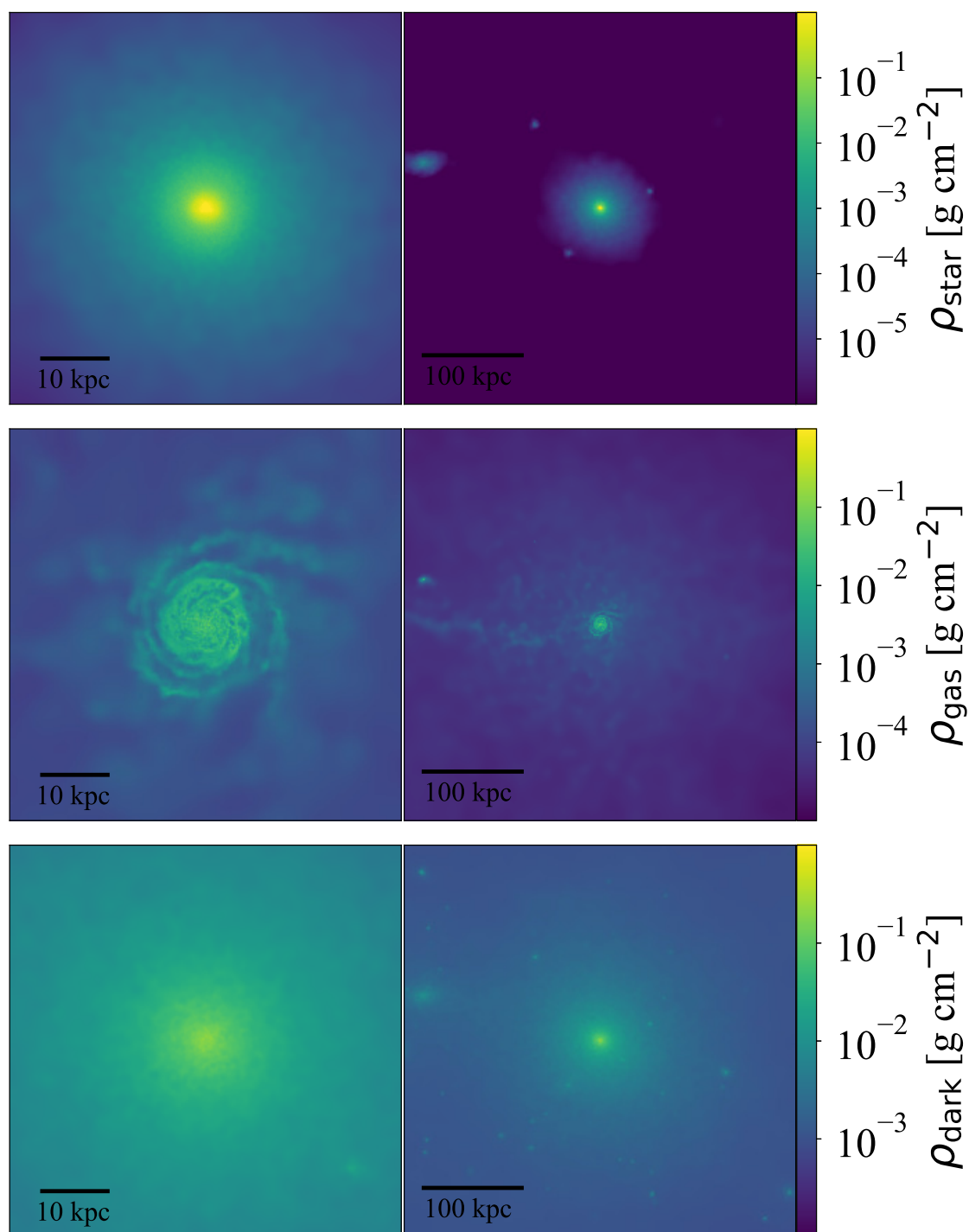


Fig. A.9 g7.66e11: column density of stars (top row), gas (middle row) and dark matter (bottom row), within boxes of widths 60 kpc (left column) and 400 kpc (right column).

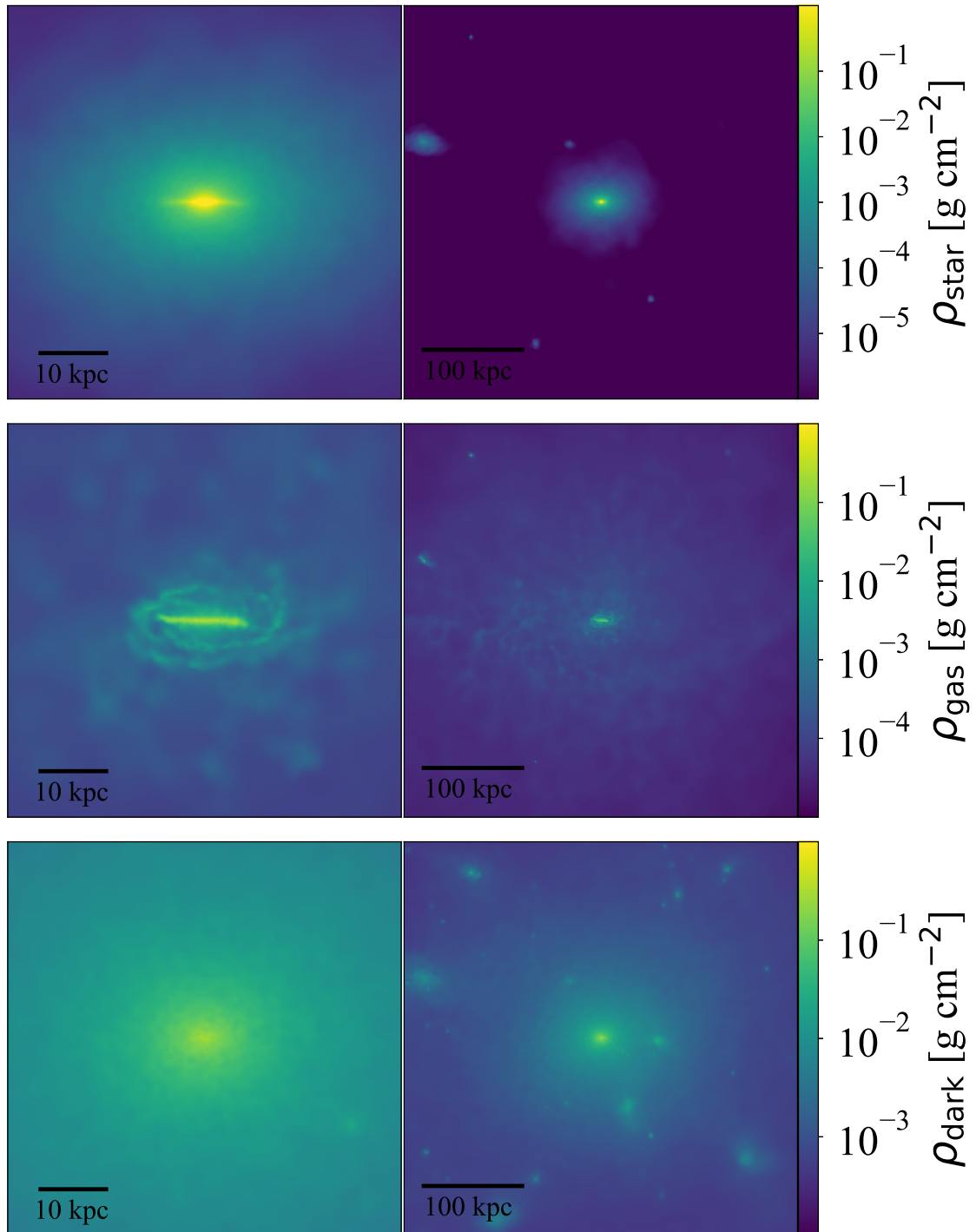


Fig. A.10 g7.66e11: column density of stars (top row), gas (middle row) and dark matter (bottom row), within boxes of widths 60 kpc (left column) and 400 kpc (right column).

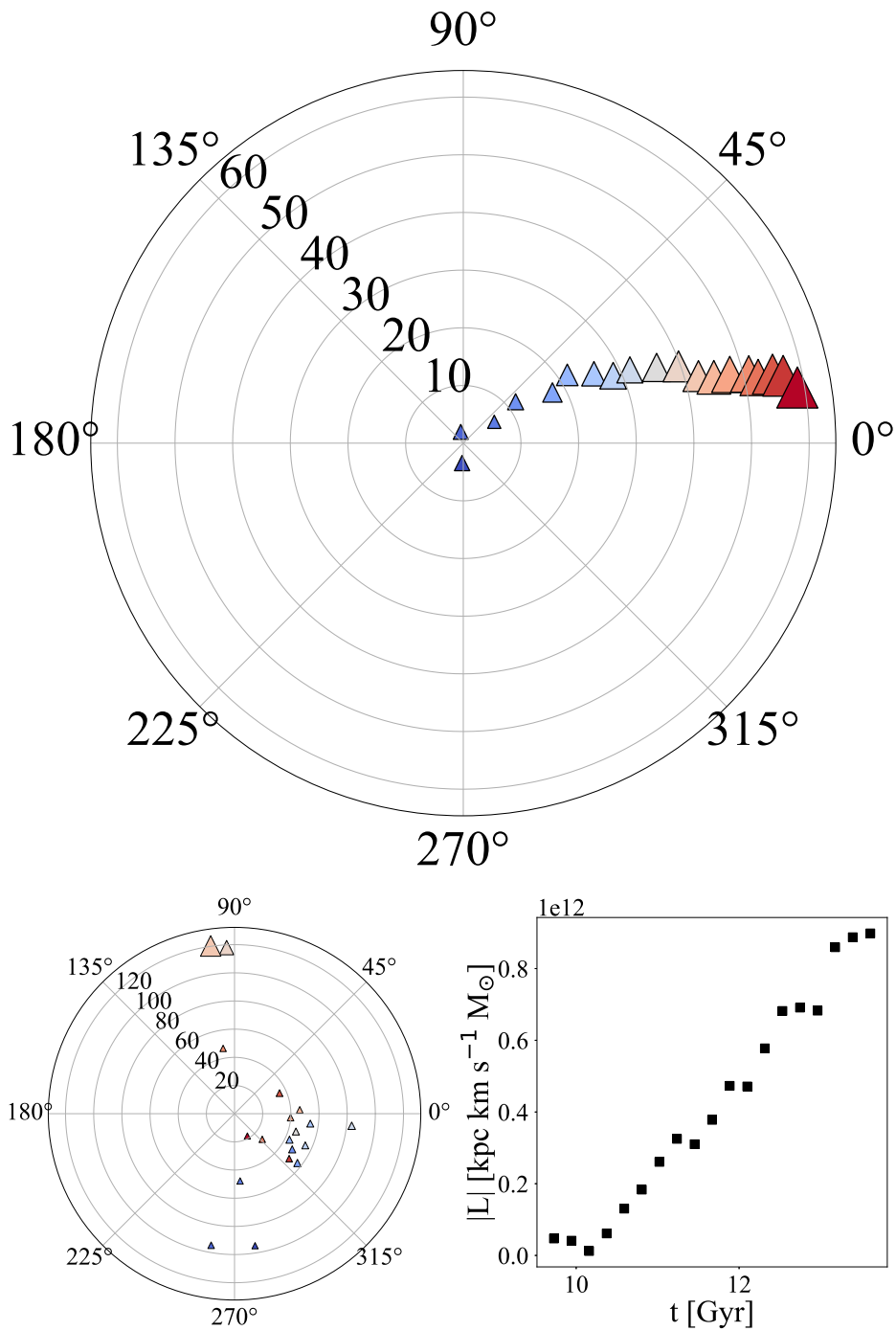


Fig. A.11 g7.66e11: top: total angular momentum of stars entering R_{disc} at each time step, left: total angular momentum of stars entering $0.5R_{200}$ at each time step, right: magnitude of angular momentum entering R_{disc} at each time step.

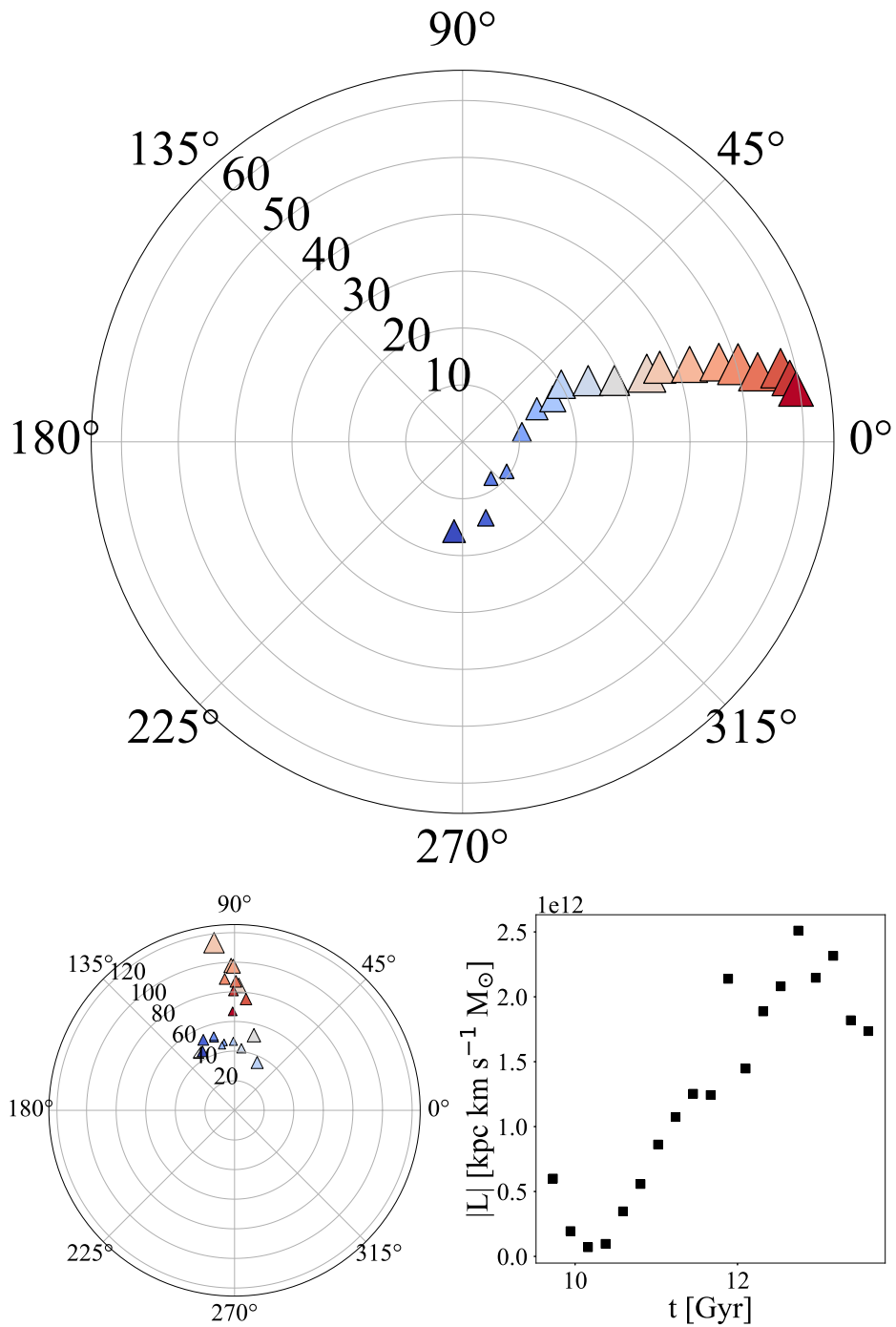


Fig. A.12 g7.66e11: top: total angular momentum of gas entering R_{disc} at each time step, left: total angular momentum of gas entering $0.5R_{200}$ at each time step, right: magnitude of angular momentum entering R_{disc} at each time step.

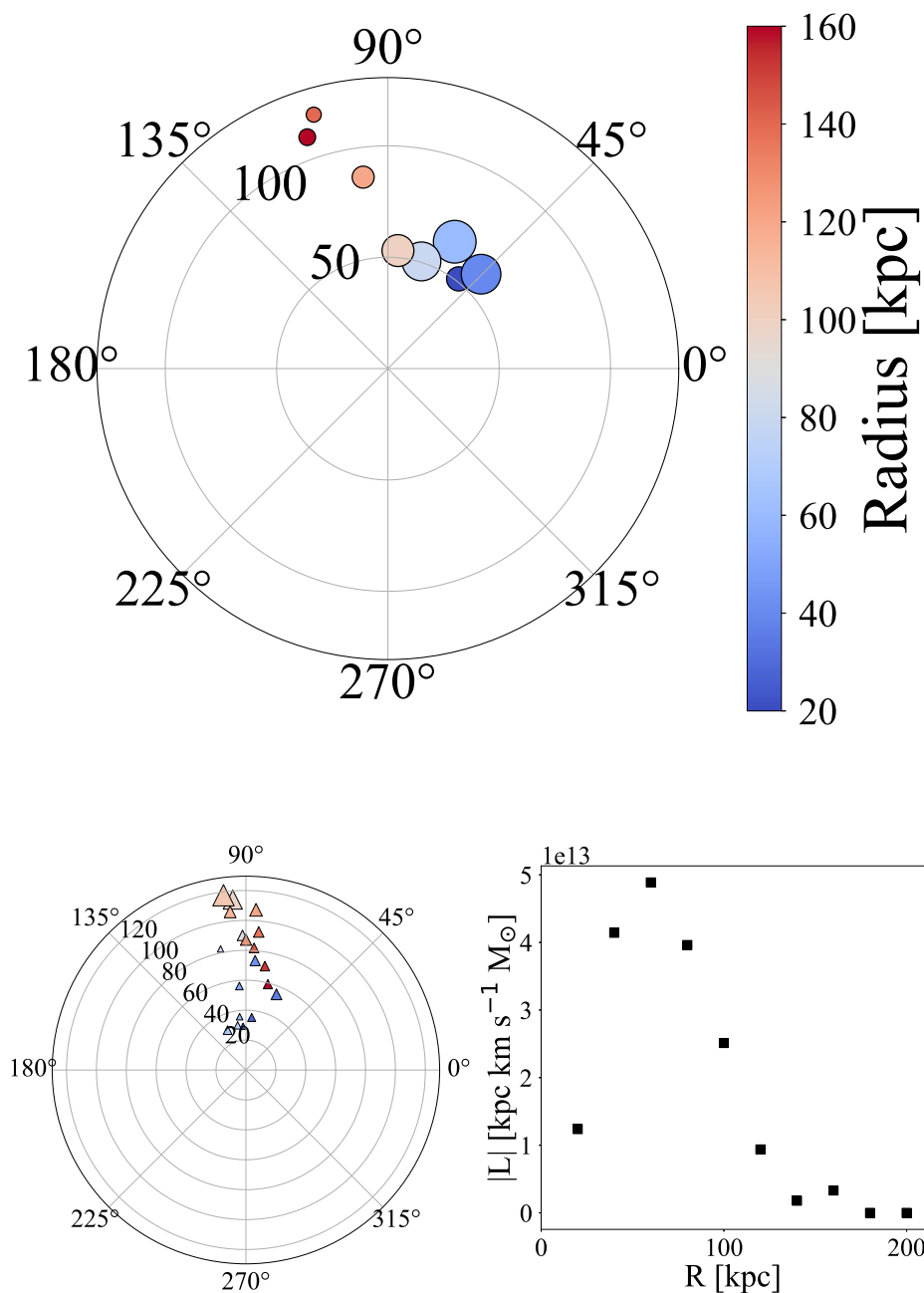


Fig. A.13 g7.66e11: the integrated net angular momentum flow of dark matter calculated at increasing radii between 20 and 200 kpc with annuli of width 20 kpc (top), the total angular momentum of dark matter entering $0.5R_{200}$ at each time step (left), and the magnitude of each angular momenta against the interior annular radius (right).

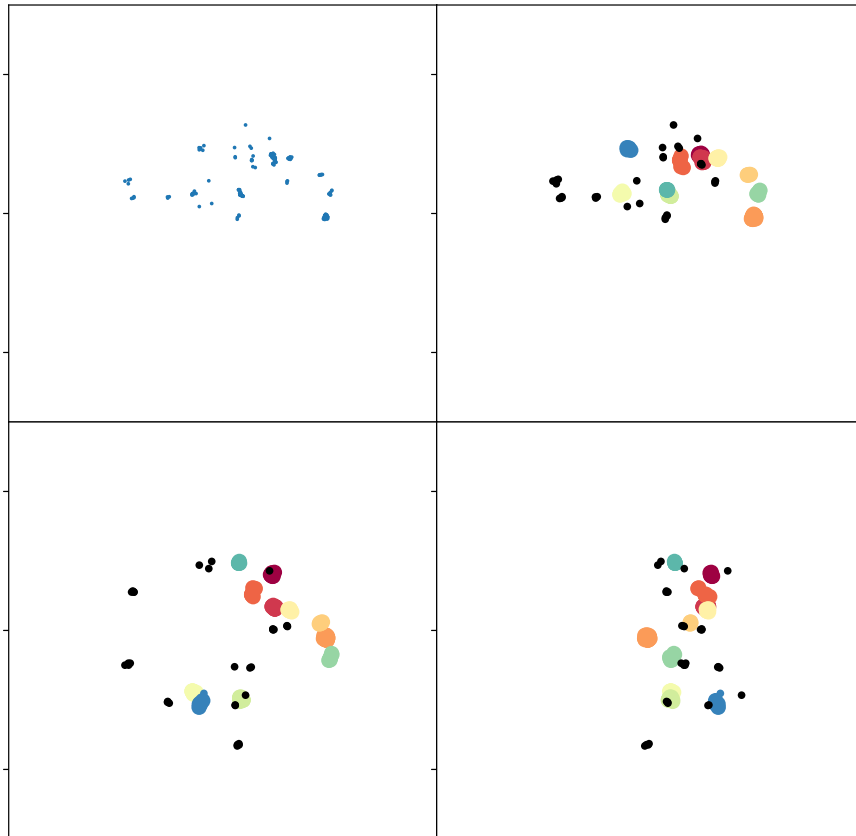
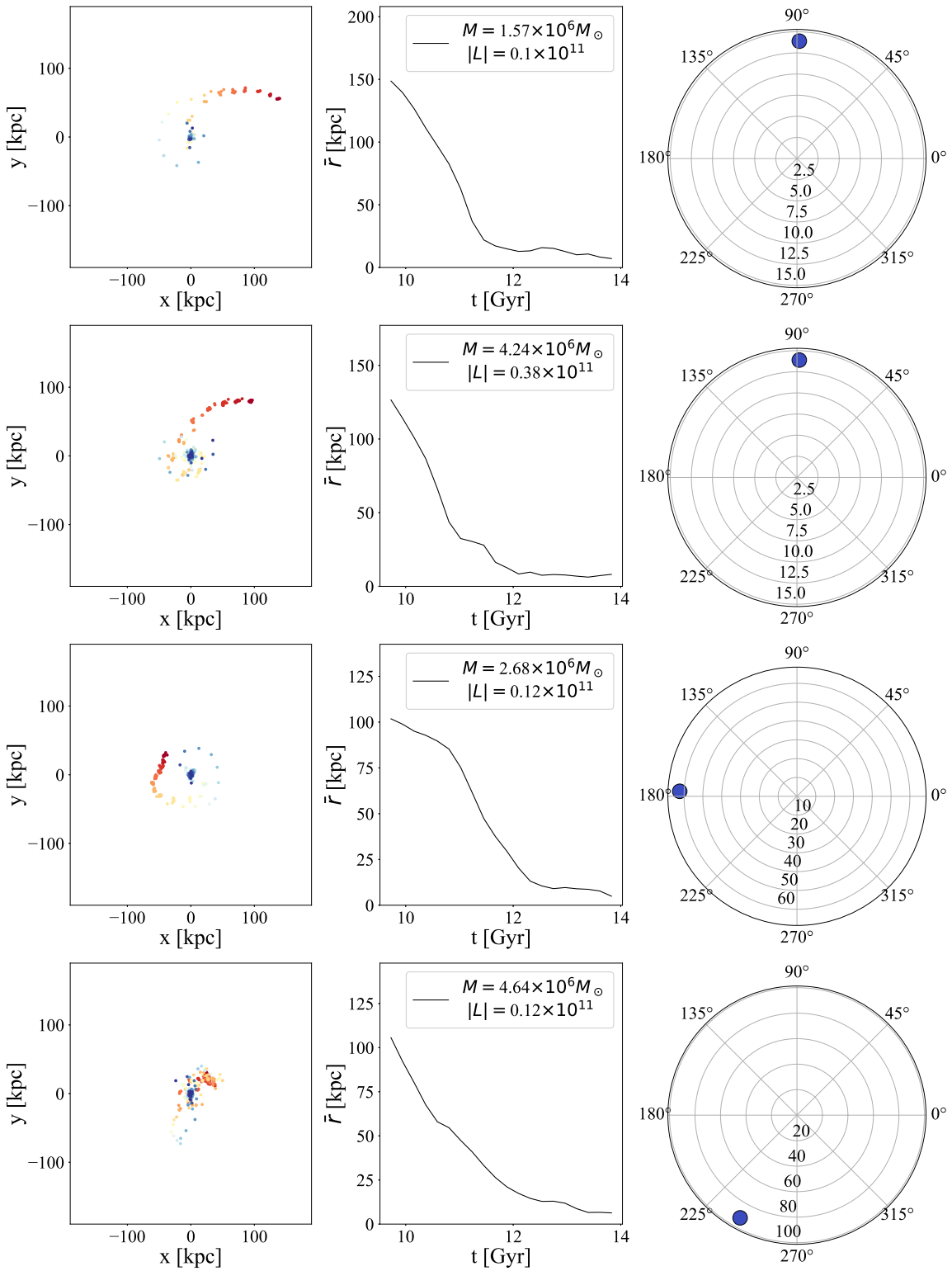
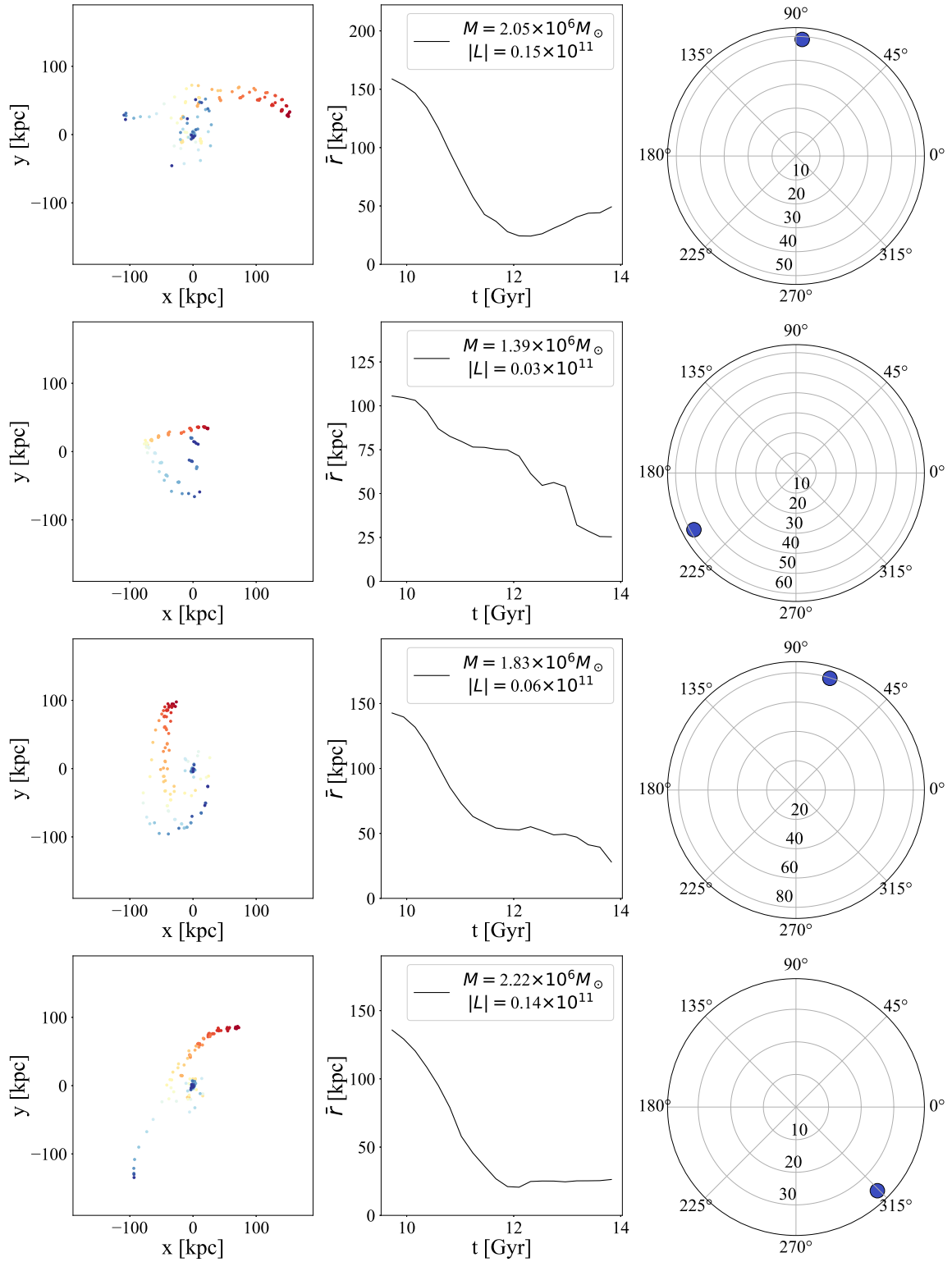


Fig. A.14 g7.66e11: this plot shows the distribution of the gas clouds at $z = 0.3$, each colour represents a different gas cloud that will be tracked. The top left and top right panel show the gas clouds projected in the x - y plane, before (left) and after (right) grouping. The bottom left and bottom right panels show the gas clouds projected in the x - z and y - z planes, respectively.





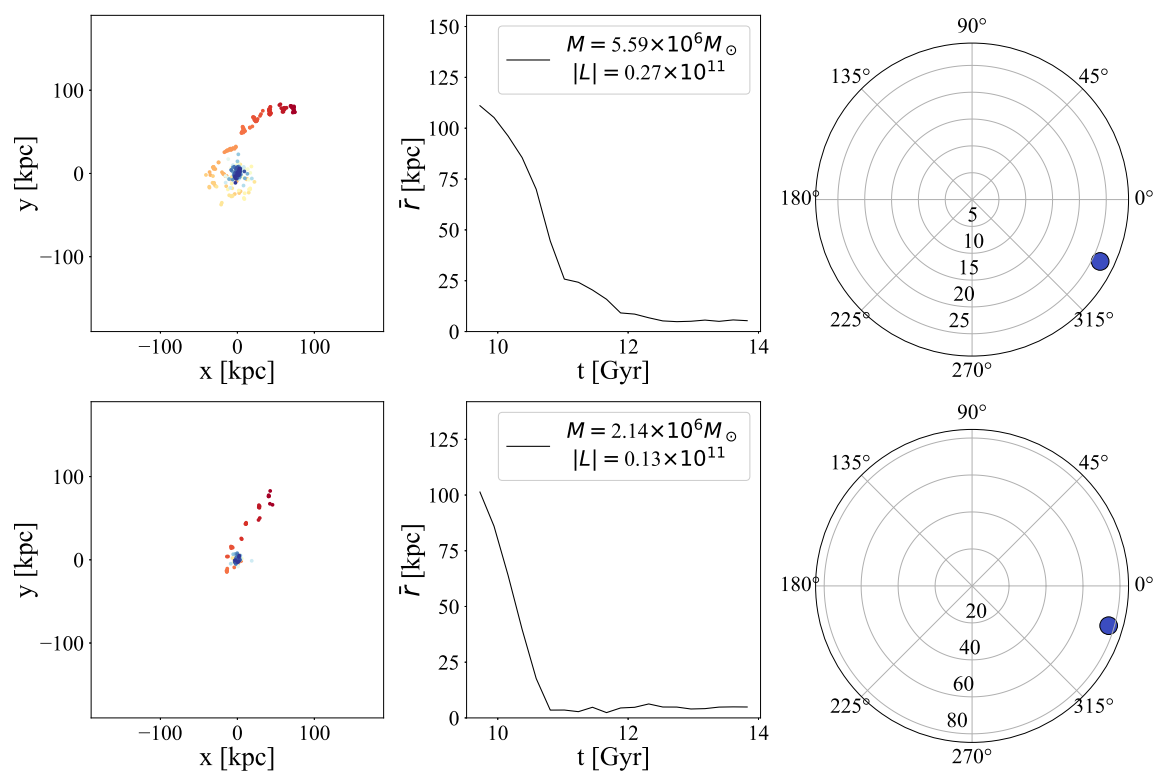


Fig. 13 (Cont.) Left: the location of all the particles in the gas cloud with $M > 10^7 M_\odot$ & $\bar{R} < 30$ kpc, middle: average distance to the centre of the galaxy with time, right: angular momentum of each gas cloud at $z = 0.3$. The mass and starting angular momentum (in units $M_\odot \text{ km s}^{-1}$) of each cloud is given in middle plot.

A.3 g8.26e11

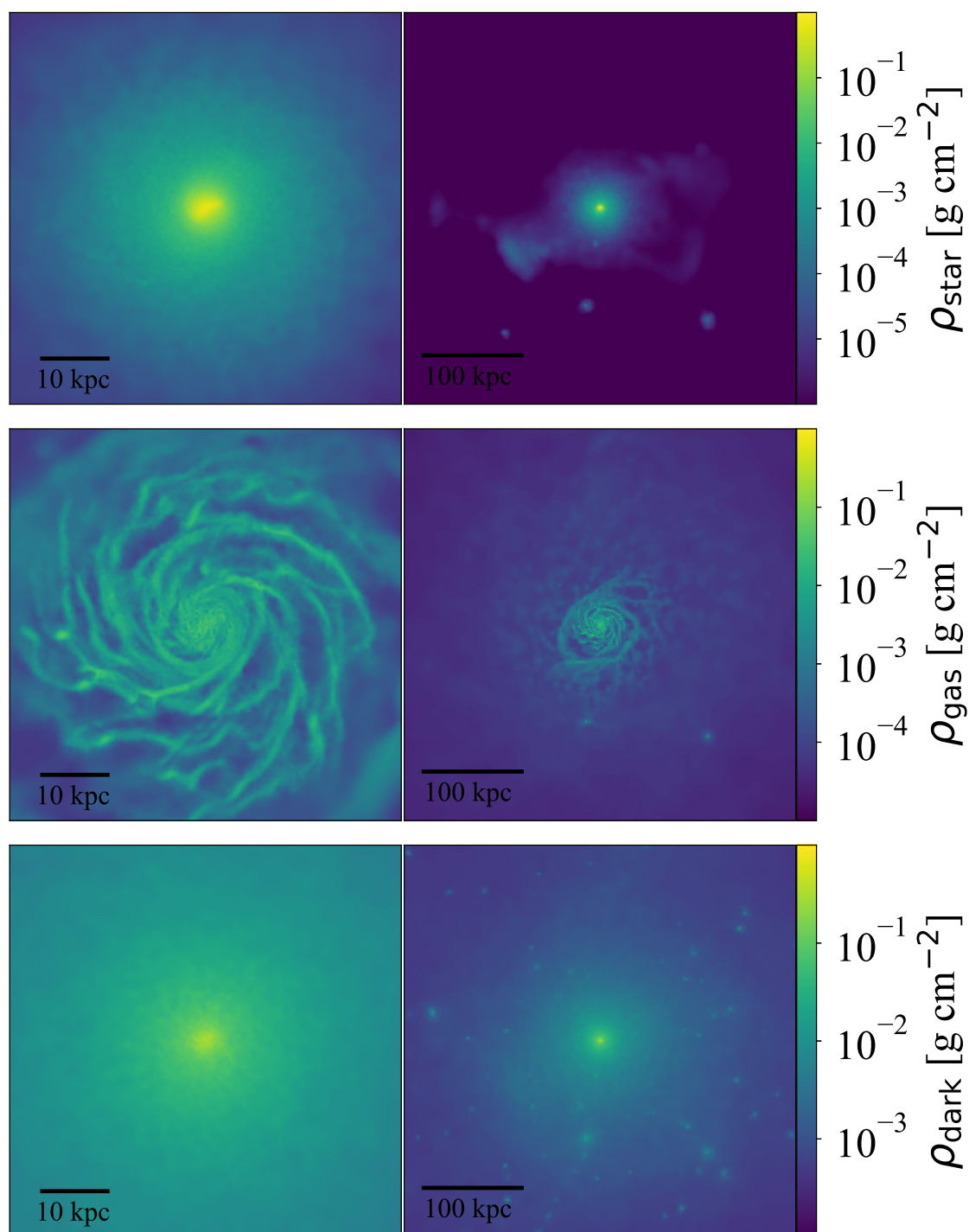


Fig. 14 g8.26e11: column density of stars (top row), gas (middle row) and dark matter (bottom row), within boxes of widths 60 kpc (left column) and 400 kpc (right column).

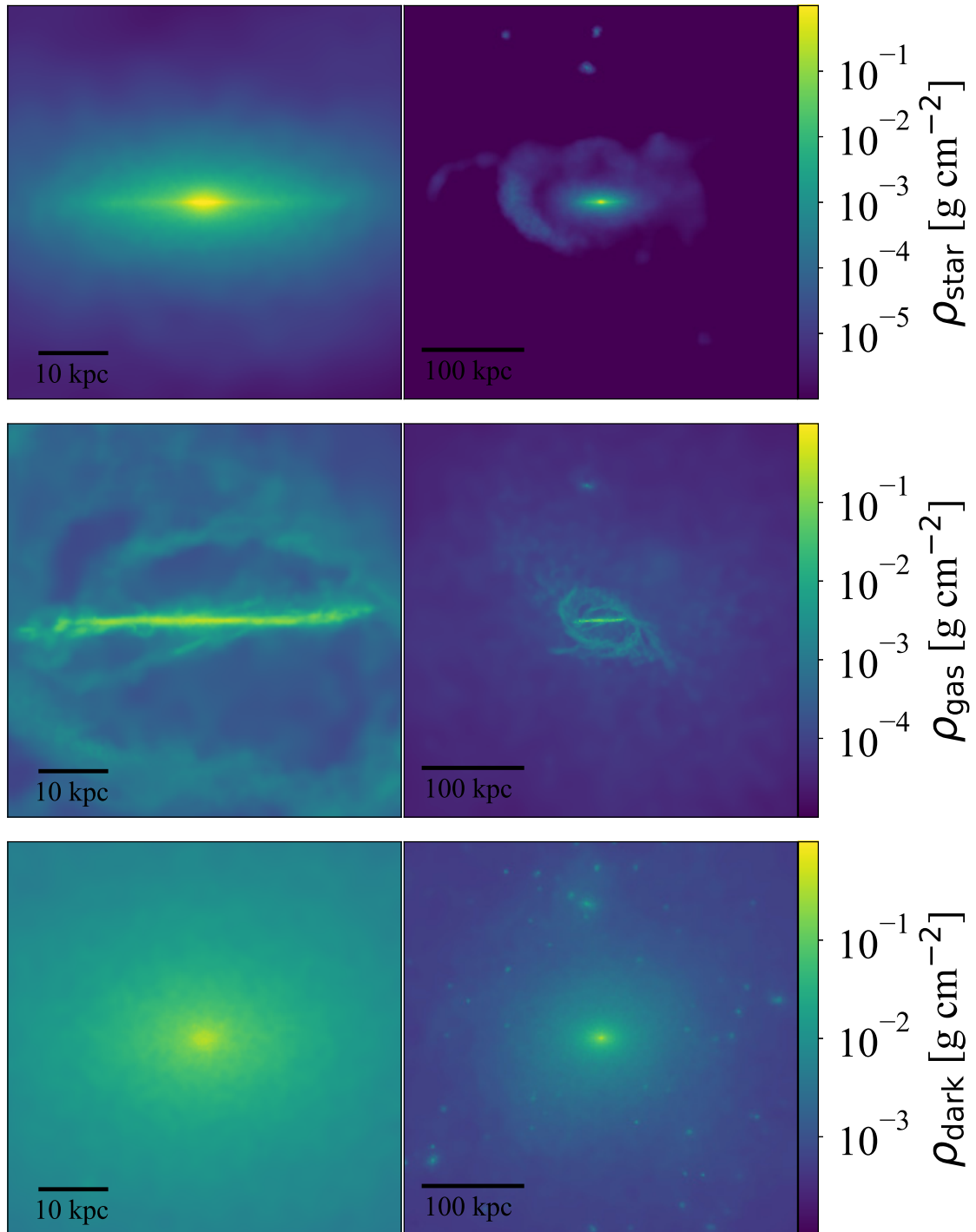


Fig. 15 g8.26e11: column density of stars (top row), gas (middle row) and dark matter (bottom row), within boxes of widths 60 kpc (left column) and 400 kpc (right column).

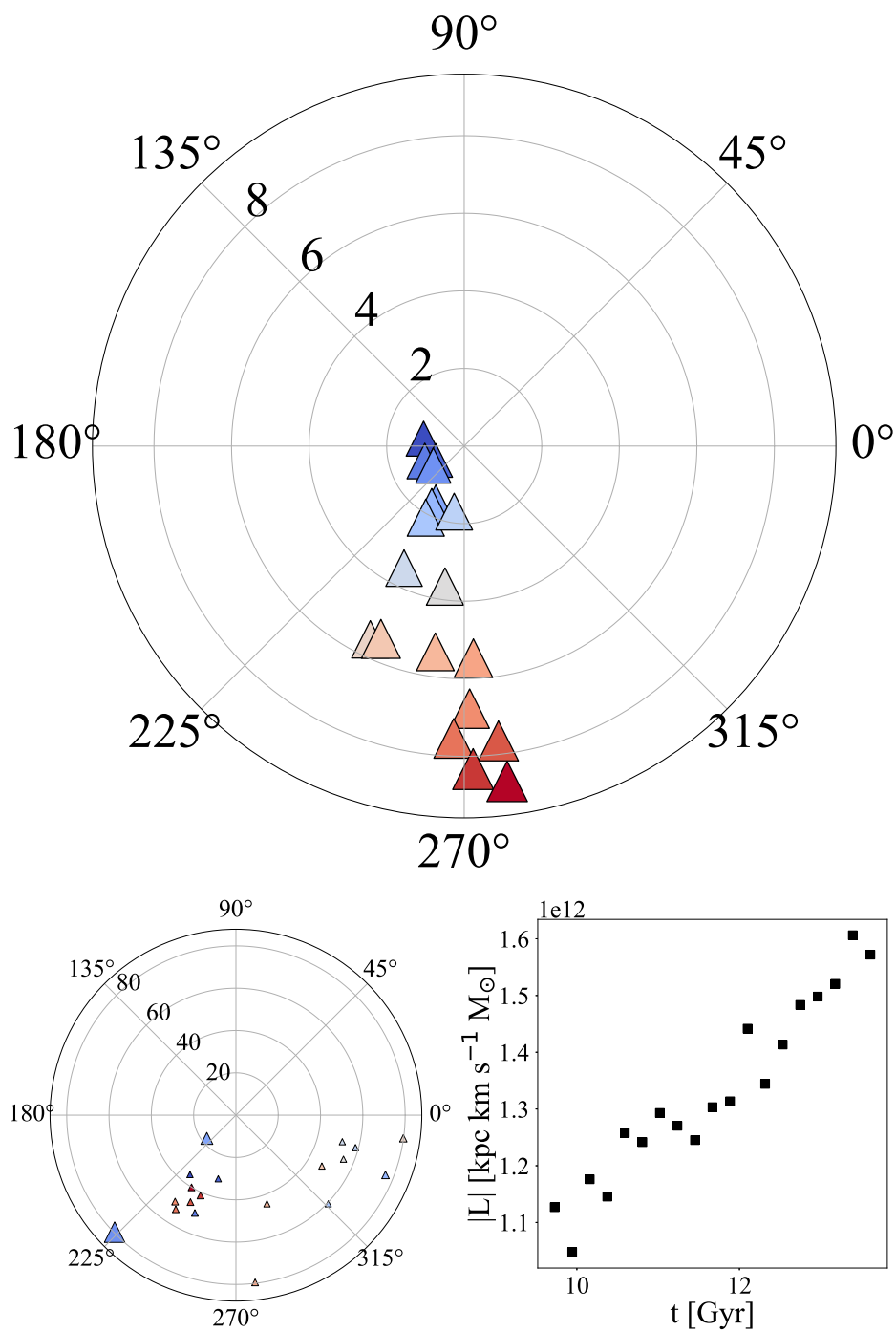


Fig. 16 g8.26e11: top: total angular momentum of stars entering R_{disc} at each time step, left: total angular momentum of stars entering $0.5R_{200}$ at each time step, right: magnitude of angular momentum entering R_{disc} at each time step.

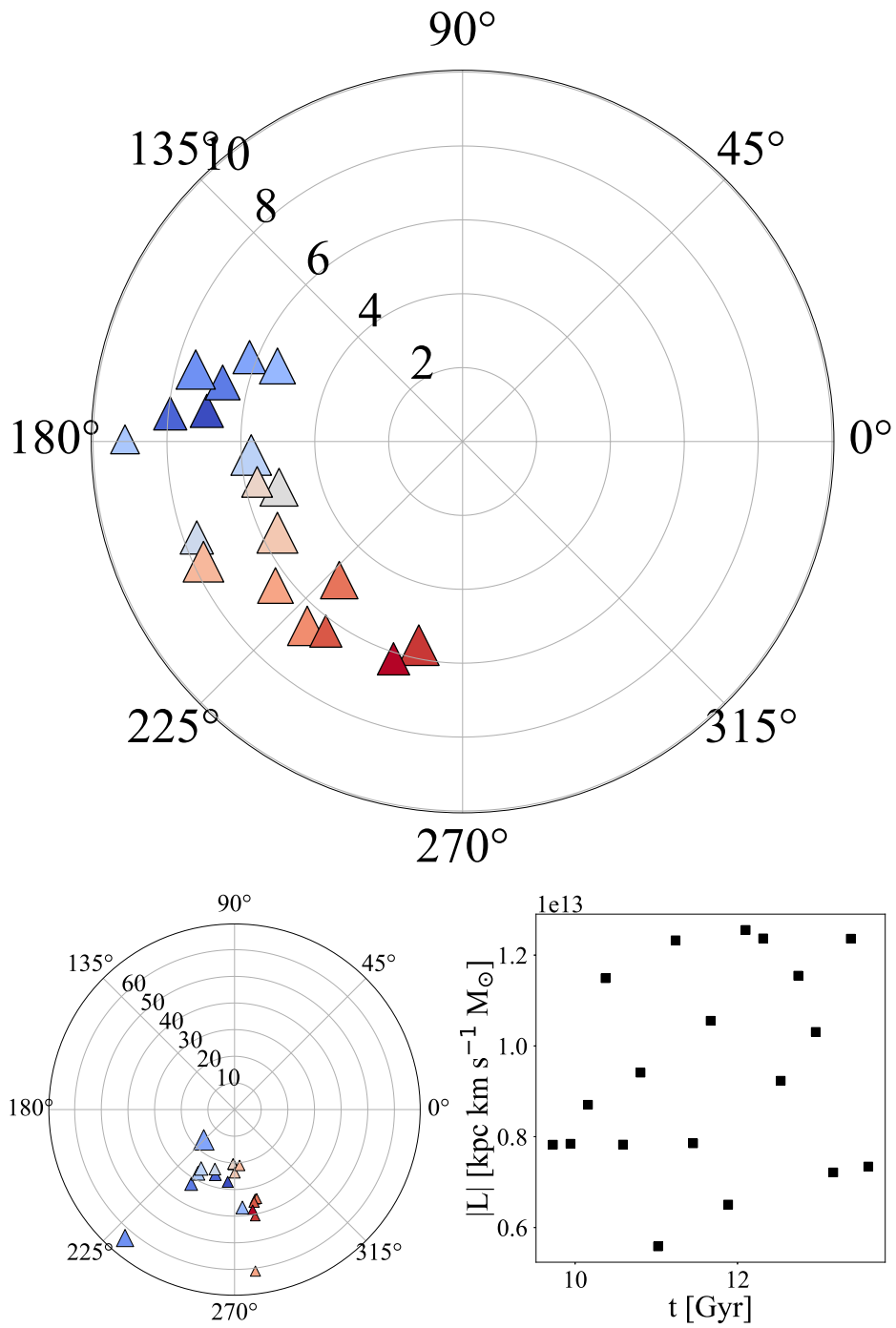


Fig. 17 g8.26e11: top: total angular momentum of gas entering R_{disc} at each time step, left: total angular momentum of gas entering $0.5R_{200}$ at each time step, right: magnitude of angular momentum entering R_{disc} at each time step.

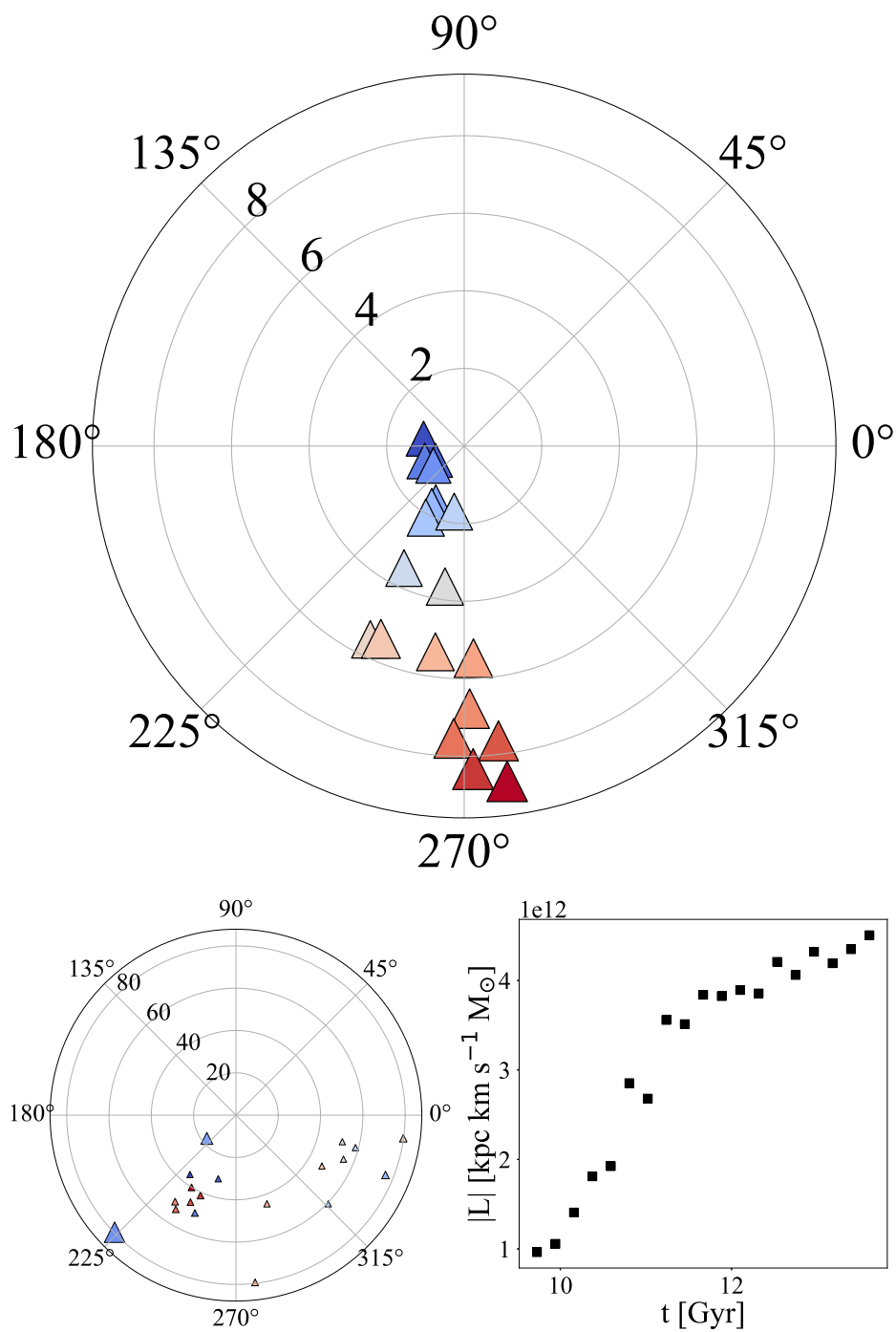


Fig. 18 g8.26e11: top: total angular momentum of stars entering R_{disc} at each time step, left: total angular momentum of stars entering $0.5R_{200}$ at each time step, right: magnitude of angular momentum entering R_{disc} at each time step.

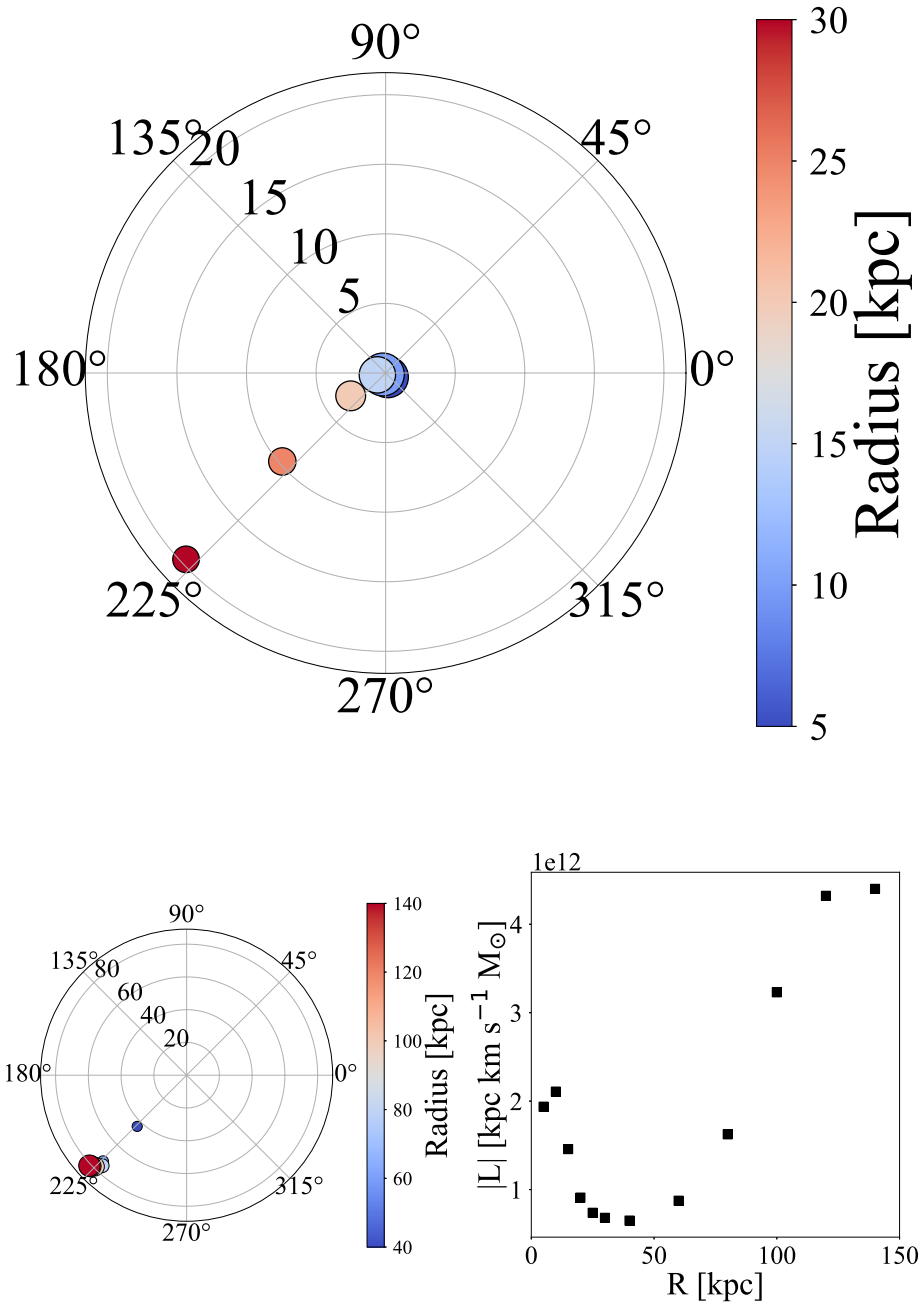


Fig. 19 g8.26e11: the integrated net angular momentum flow of stars calculated at increasing radii between 5 and 30 kpc with annuli of width 5 kpc (top) and between 40 and 120 kpc with annuli of width 20 kpc (left), and the magnitude of each angular momenta against the interior annular radius (right).

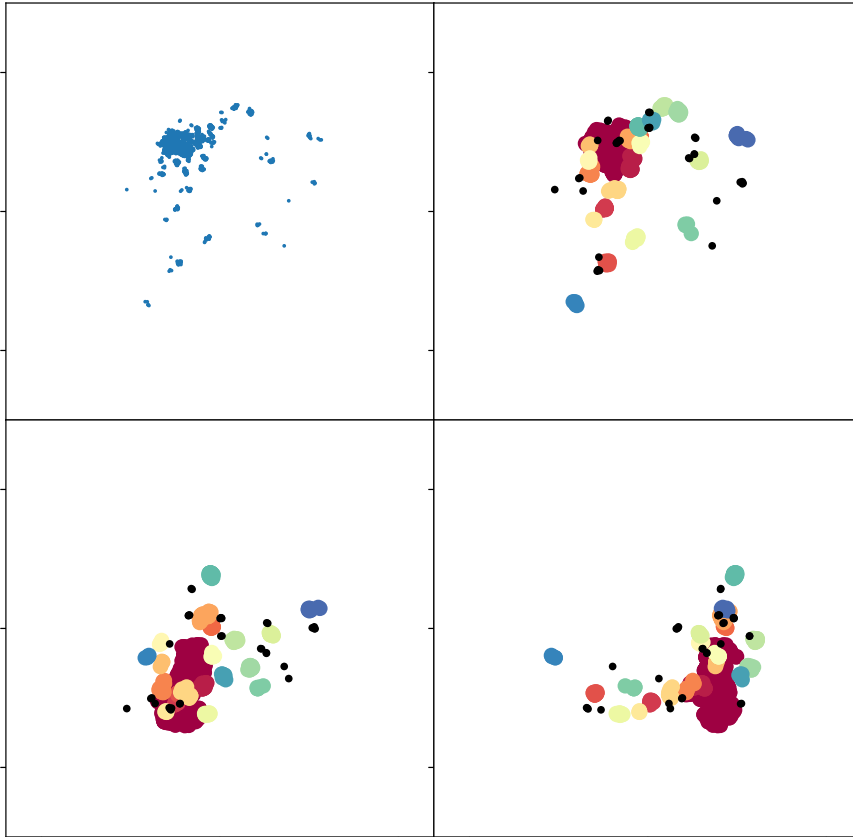


Fig. 20 g8.26e11: this plot shows the distribution of the gas clouds at $z = 0.3$, each colour represents a different gas cloud that will be tracked. The top left and top right panel show the gas clouds projected in the x - y plane, before (left) and after (right) grouping. The bottom left and bottom right panels show the gas clouds projected in the x - z and y - z planes, respectively.

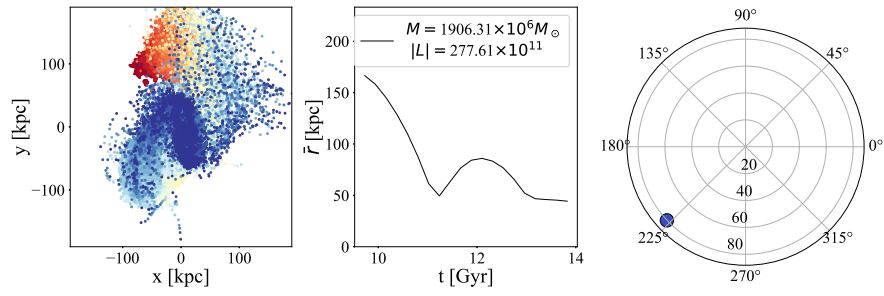


Fig. 21 g8.26e11: left: the location of all the particles in the gas cloud with $M > 10^6 M_{\odot}$ & $\bar{R} < 30$ kpc, middle: average radius of all the particles in the gas cloud with time, right: angular momentum of the gas cloud at $z = 0.3$. The mass and starting angular momentum (in units $M_{\odot} \text{ km s}^{-1}$) of the cloud is given in middle plot.

A.4 g1.92e12

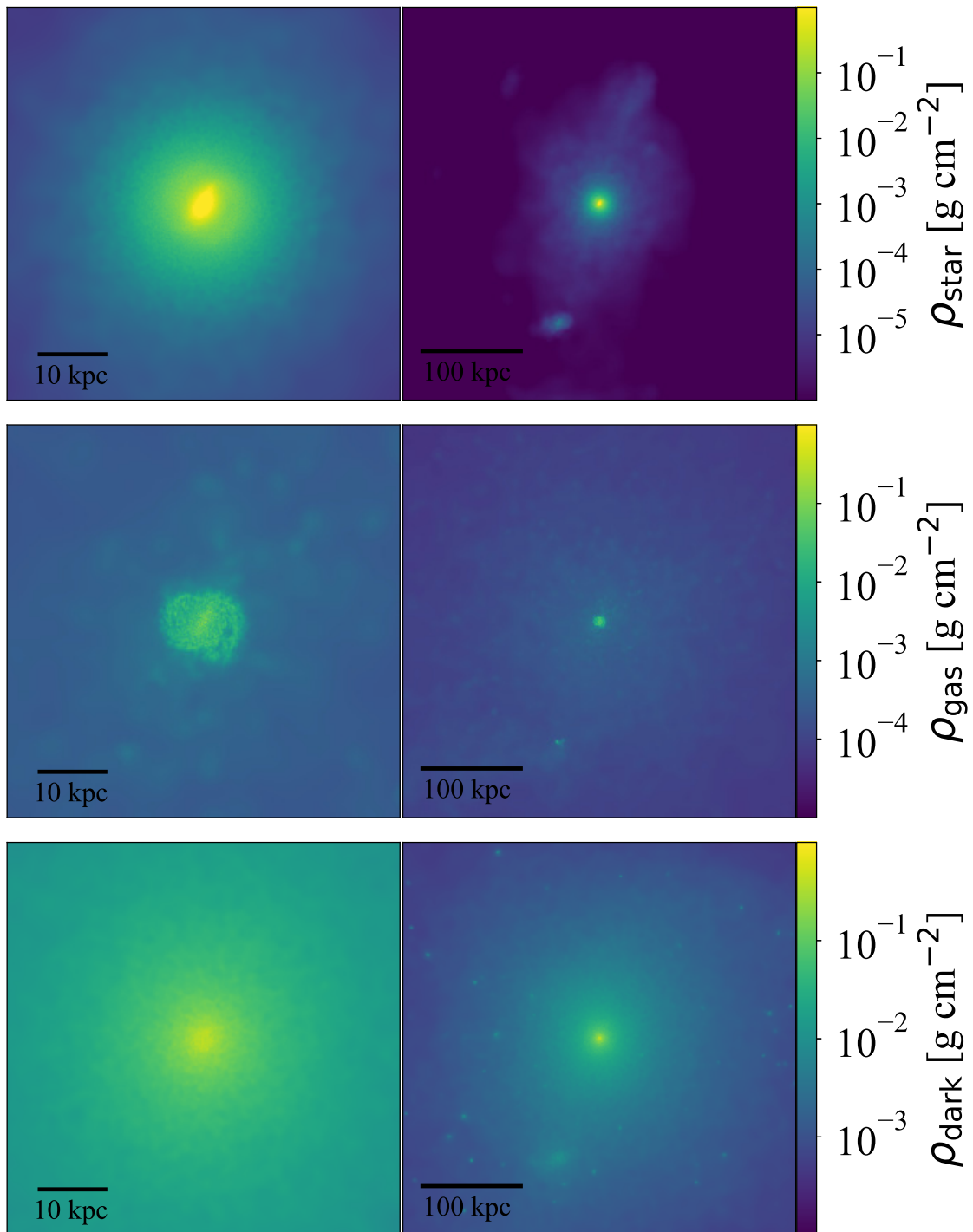


Fig. 22 g1.92e12: column density of stars (top row), gas (middle row) and dark matter (bottom row), within boxes of widths 60 kpc (left column) and 400 kpc (right column).

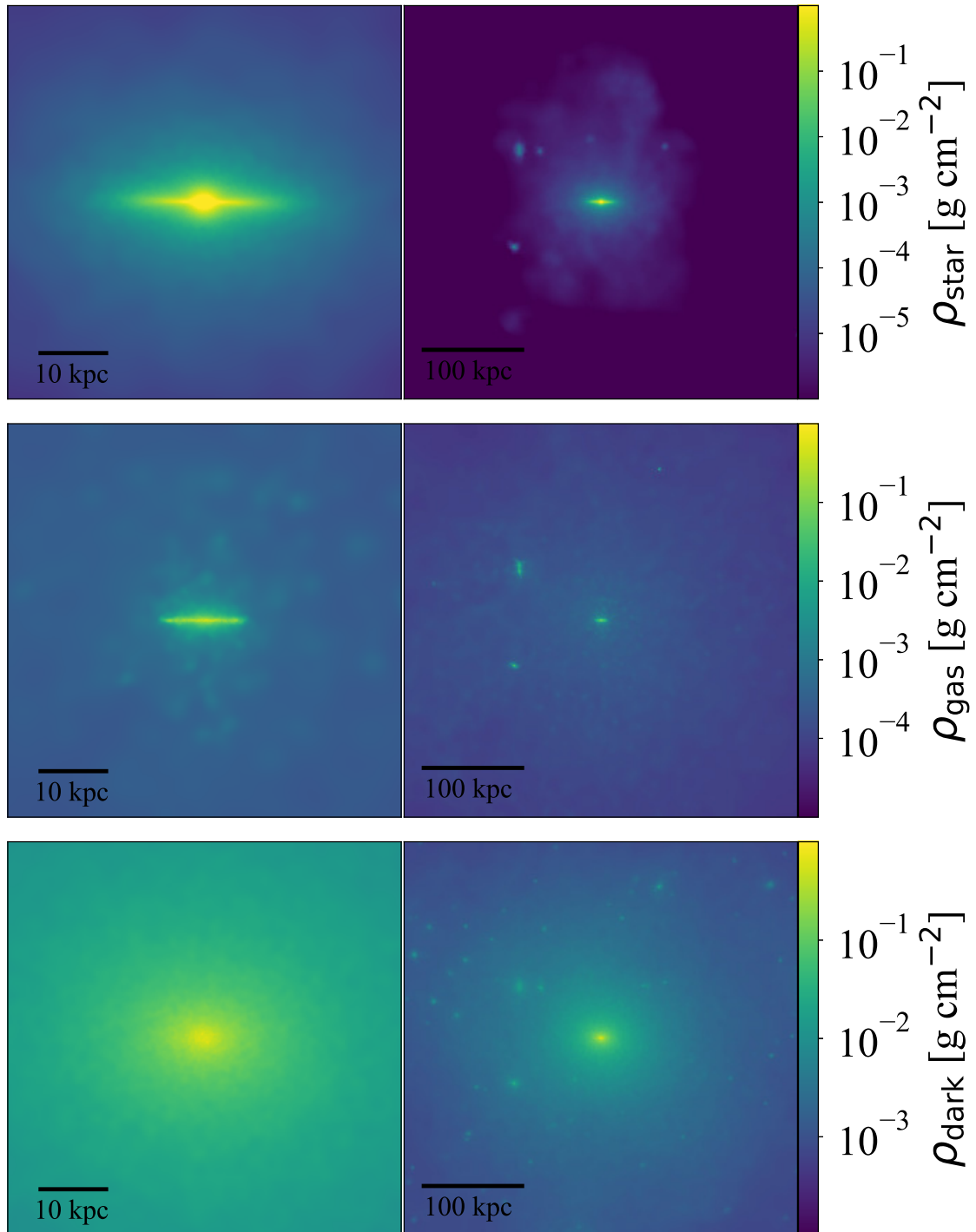


Fig. 23 g1.92e12: column density of stars (top row), gas (middle row) and dark matter (bottom row), within boxes of widths 60 kpc (left column) and 400 kpc (right column).

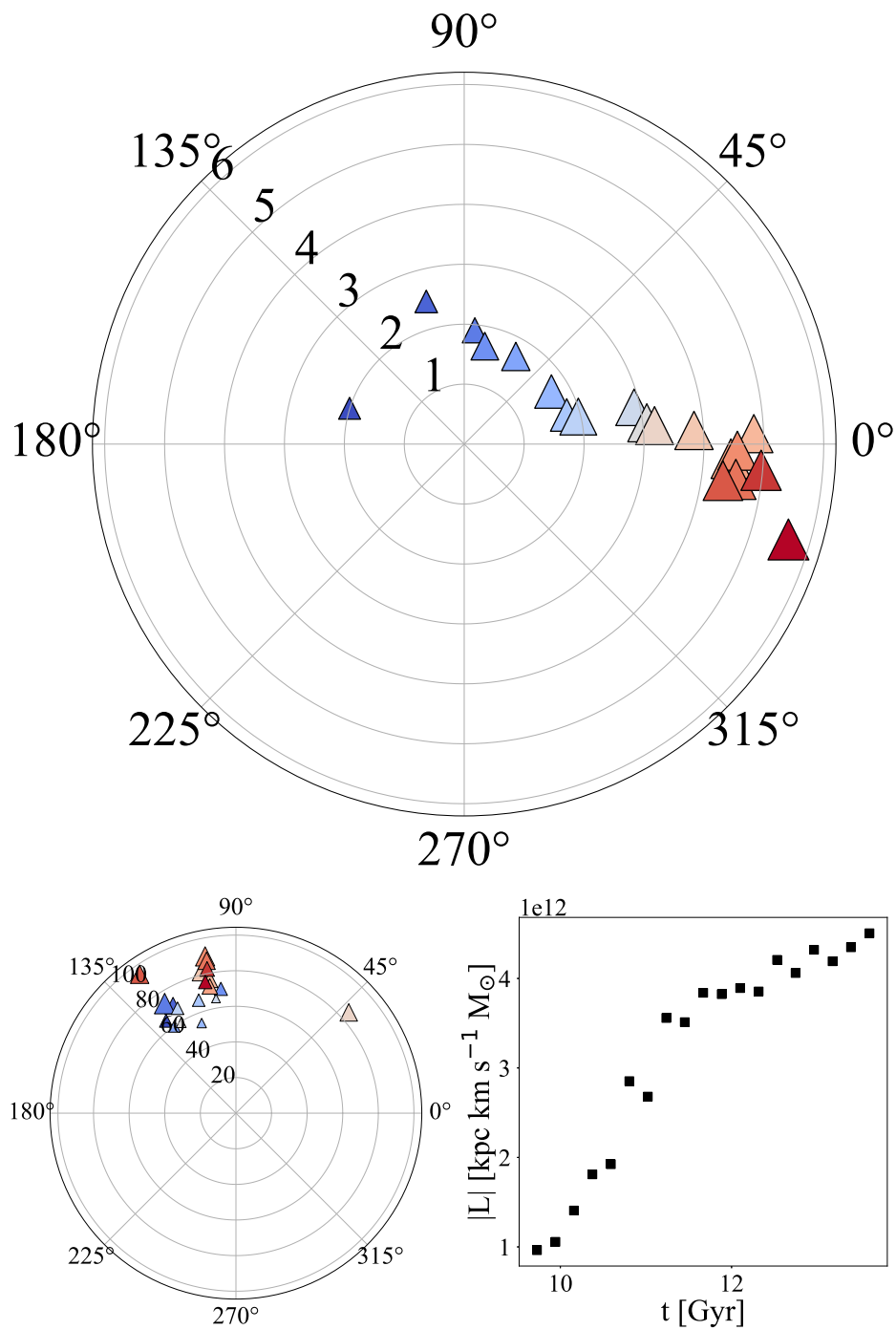


Fig. 24 $g1.92e12$: top: total angular momentum of stars entering R_{disc} at each time step, left: total angular momentum of stars entering $0.5R_{200}$ at each time step, right: magnitude of angular momentum entering R_{disc} at each time step.

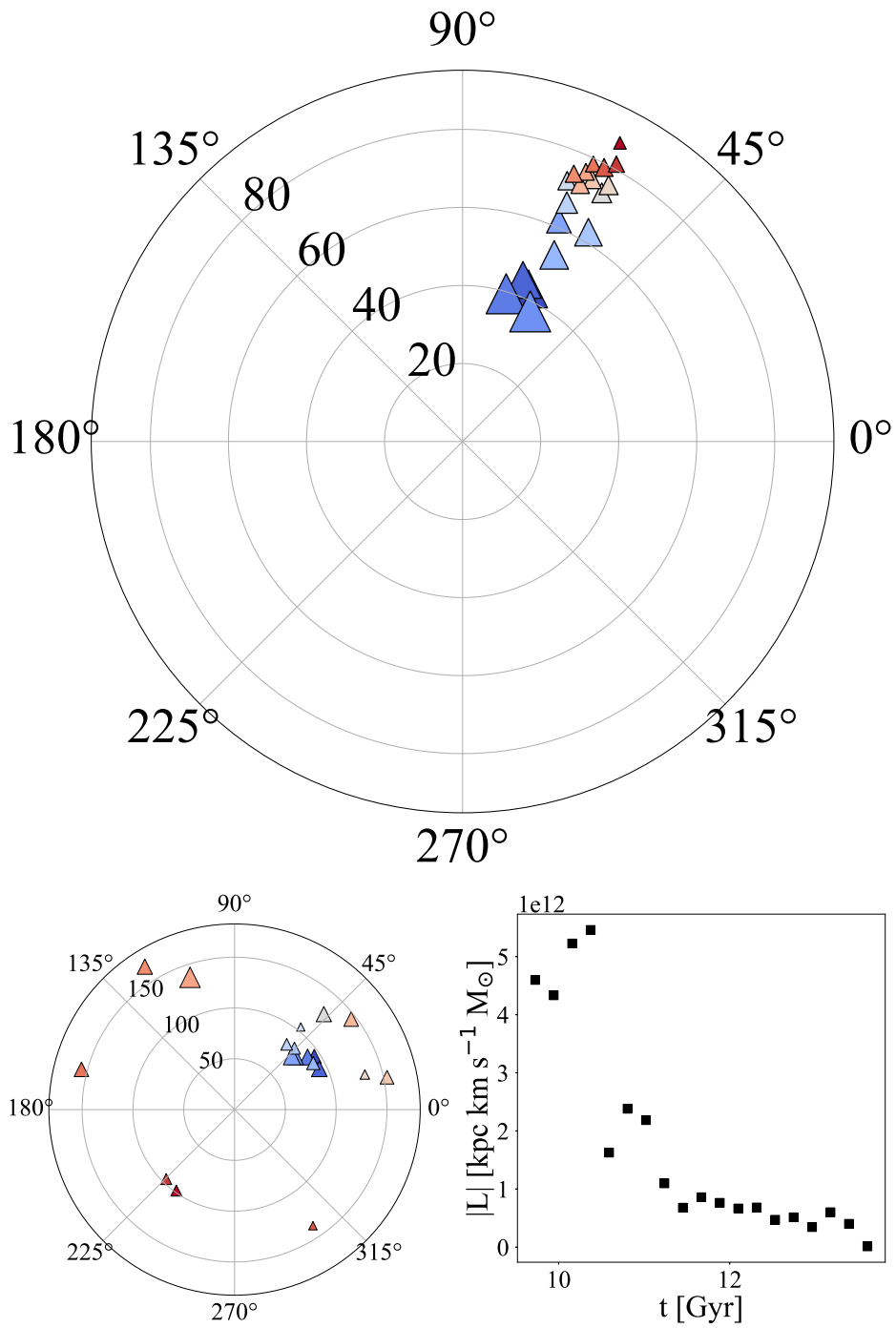


Fig. 25 g1.92e12: top: total angular momentum of gas entering R_{disc} at each time step, left: total angular momentum of gas entering $0.5R_{200}$ at each time step, right: magnitude of angular momentum entering R_{disc} at each time step.

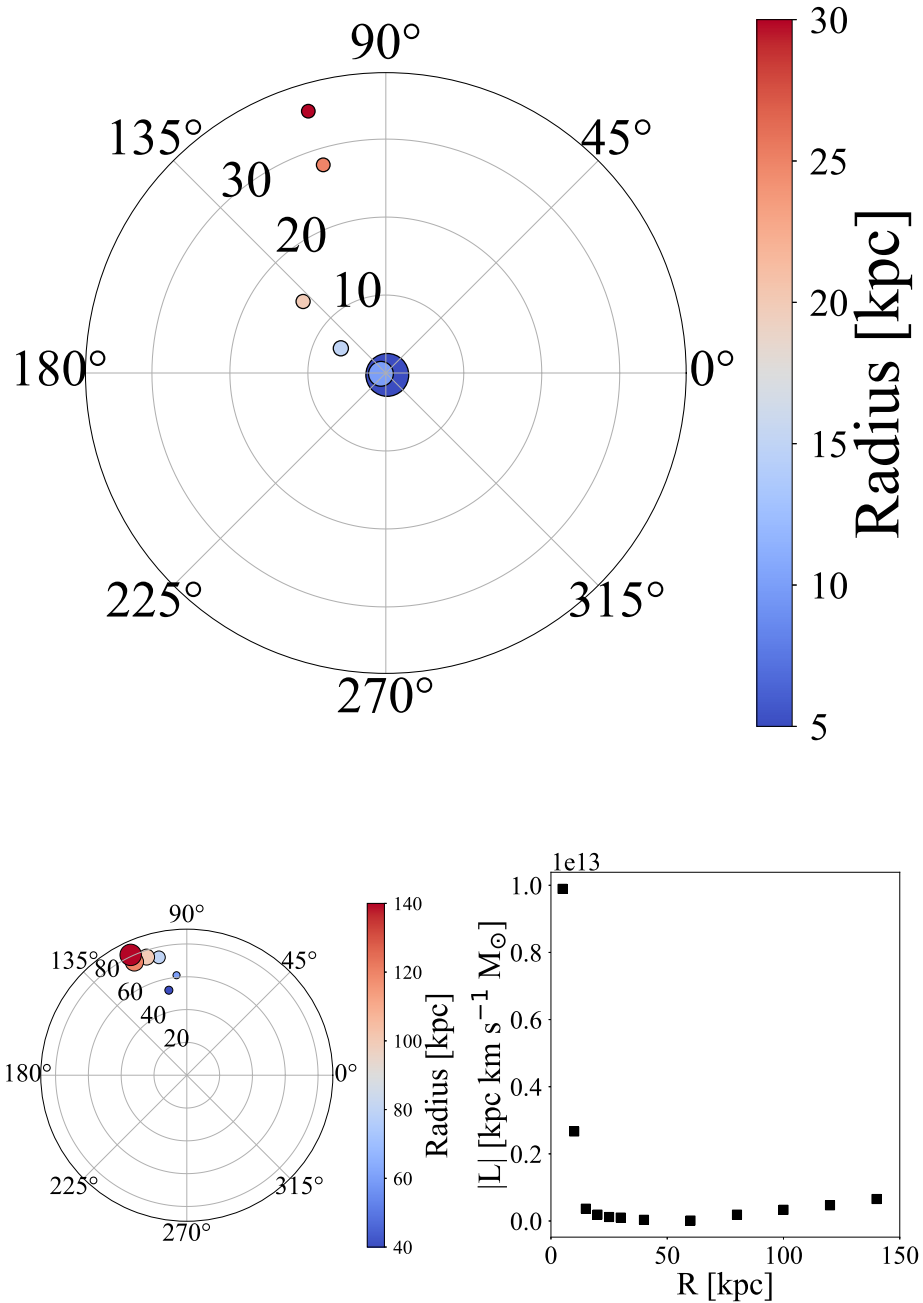


Fig. 26 $g1.92e12$: the integrated net angular momentum flow of stars calculated at increasing radii between 5 and 30 kpc with annuli of width 5 kpc (top) and between 40 and 120 kpc with annuli of width 20 kpc (left), and the magnitude of each angular momenta against the interior annular radius (right).

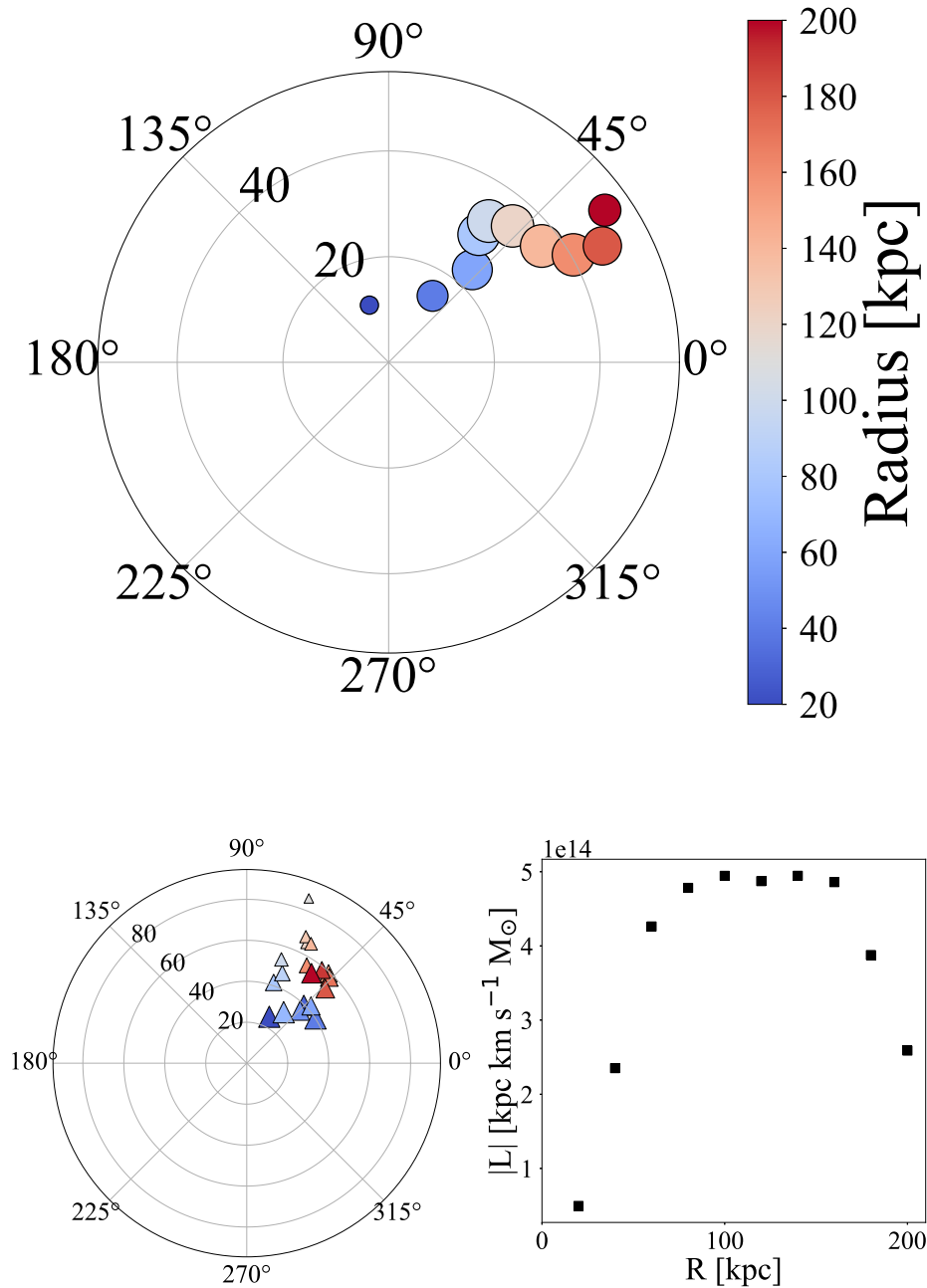


Fig. 27 g1.92e12: the integrated net angular momentum flow of dark matter calculated at increasing radii between 20 and 200 kpc with annuli of width 20 kpc (top), the total angular momentum of dark matter entering $0.5R_{200}$ at each time step (left), and the magnitude of each angular momenta against the interior annular radius (right).

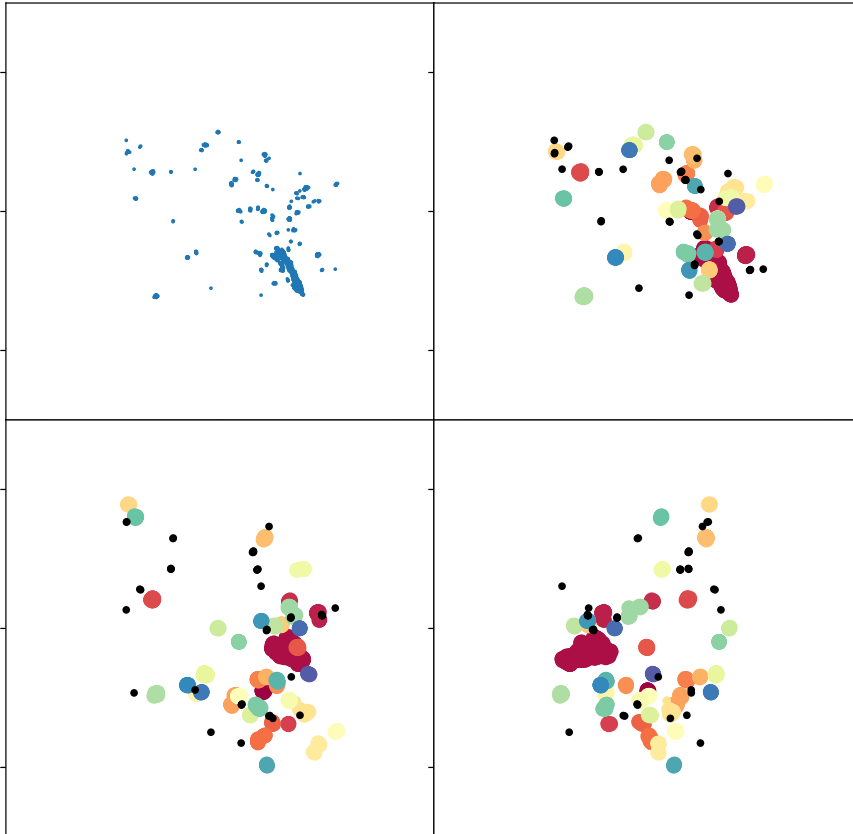


Fig. 28 g1.92e12: this plot shows the distribution of the gas clouds at $z = 0.3$, each colour represents a different gas cloud that will be tracked. The top left and top right panel show the gas clouds projected in the x - y plane, before (left) and after (right) grouping. The bottom left and bottom right panels show the gas clouds projected in the x - z and y - z planes, respectively.

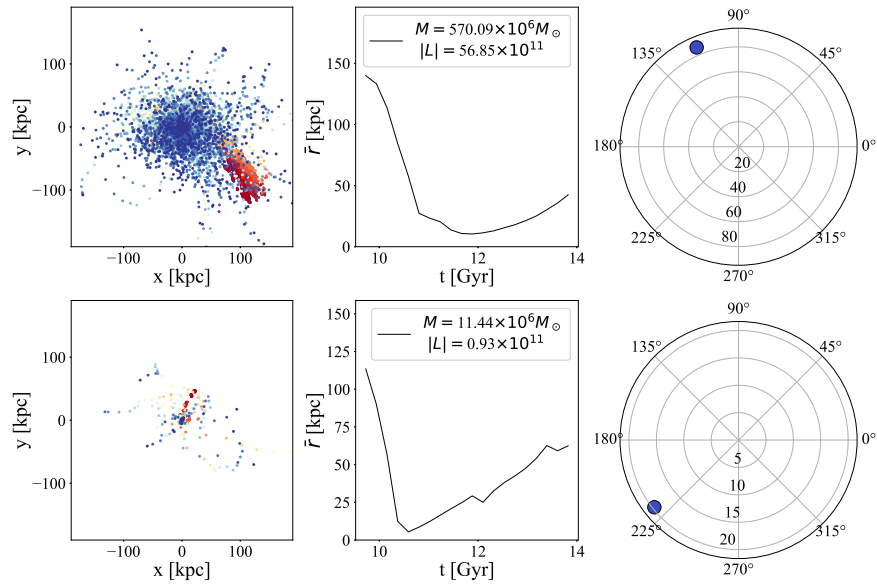


Fig. 29 g1.92e12: left: the location of all the particles in the gas cloud with $M > 10^7 M_{\odot}$ & $\bar{R} < 30$ kpc, middle: average distance to the centre of the galaxy with time, right: angular momentum of each gas cloud at $z = 0.3$. The mass and starting angular momentum (in units $M_{\odot} \text{ km s}^{-1}$) of each cloud is given in middle plot.

A.5 g2.79e12

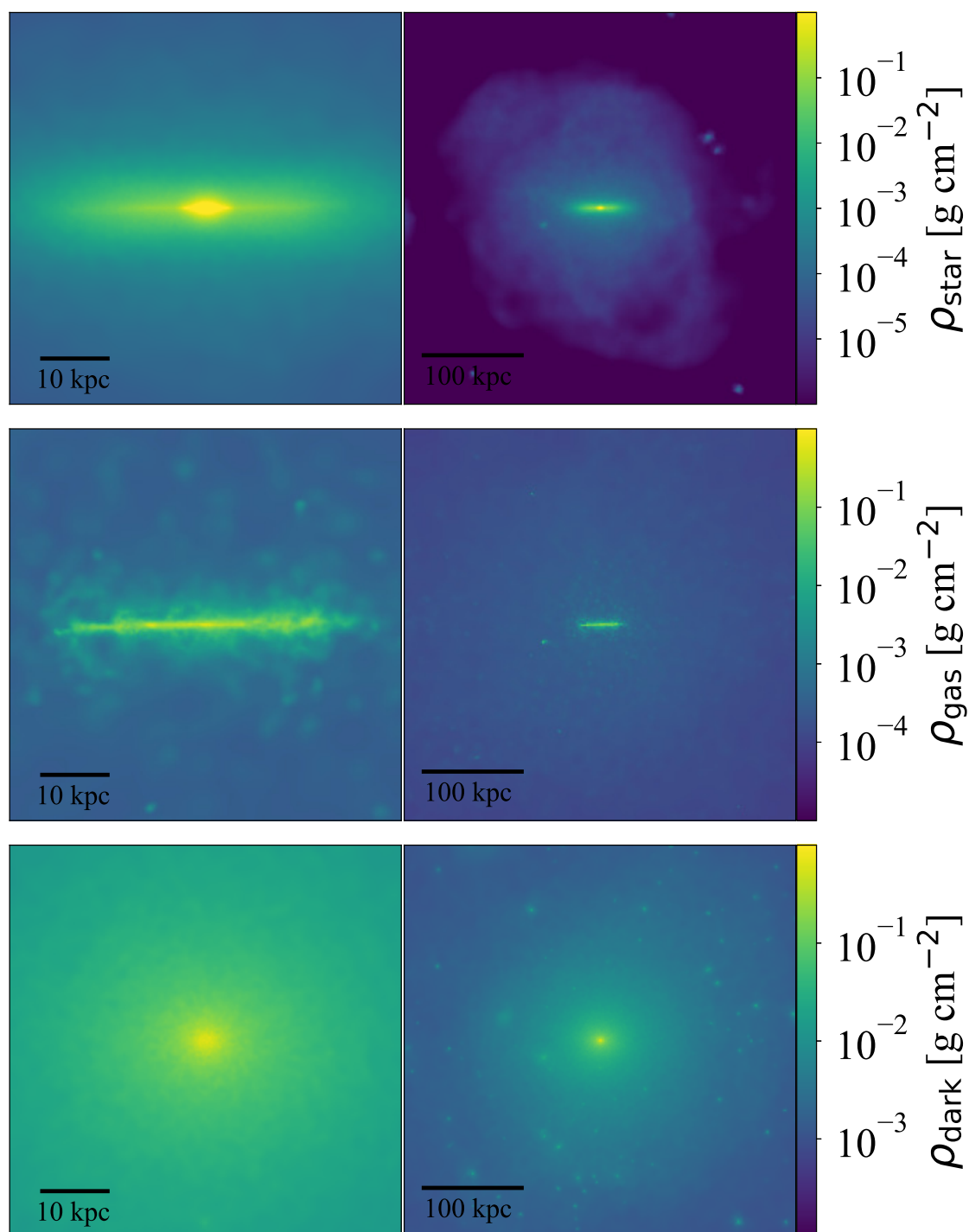


Fig. 30 g2.79e12: column density of stars (top row), gas (middle row) and dark matter (bottom row), within boxes of widths 60 kpc (left column) and 400 kpc (right column).

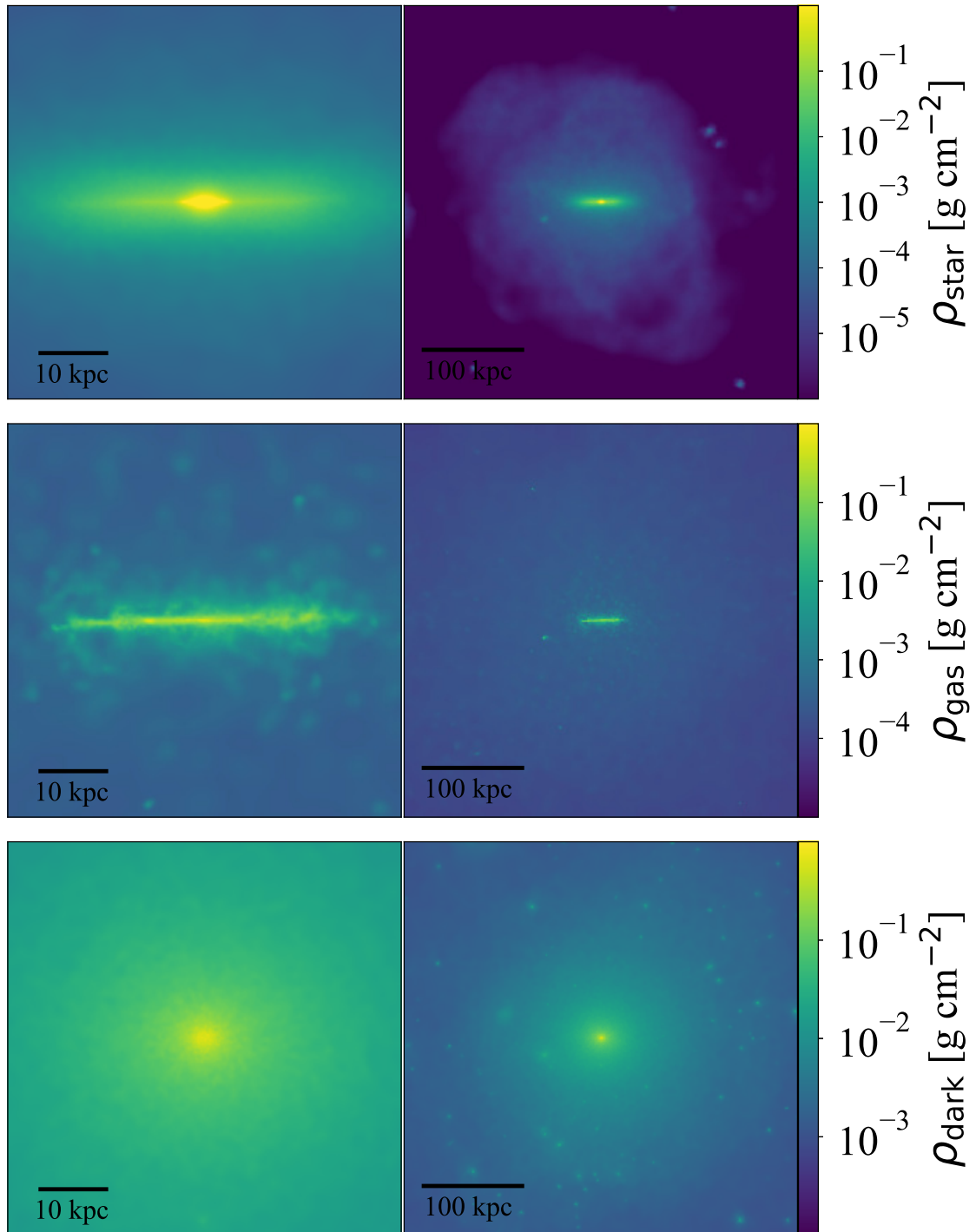


Fig. 31 g2.79e12: column density of stars (top row), gas (middle row) and dark matter (bottom row), within boxes of widths 60 kpc (left column) and 400 kpc (right column).

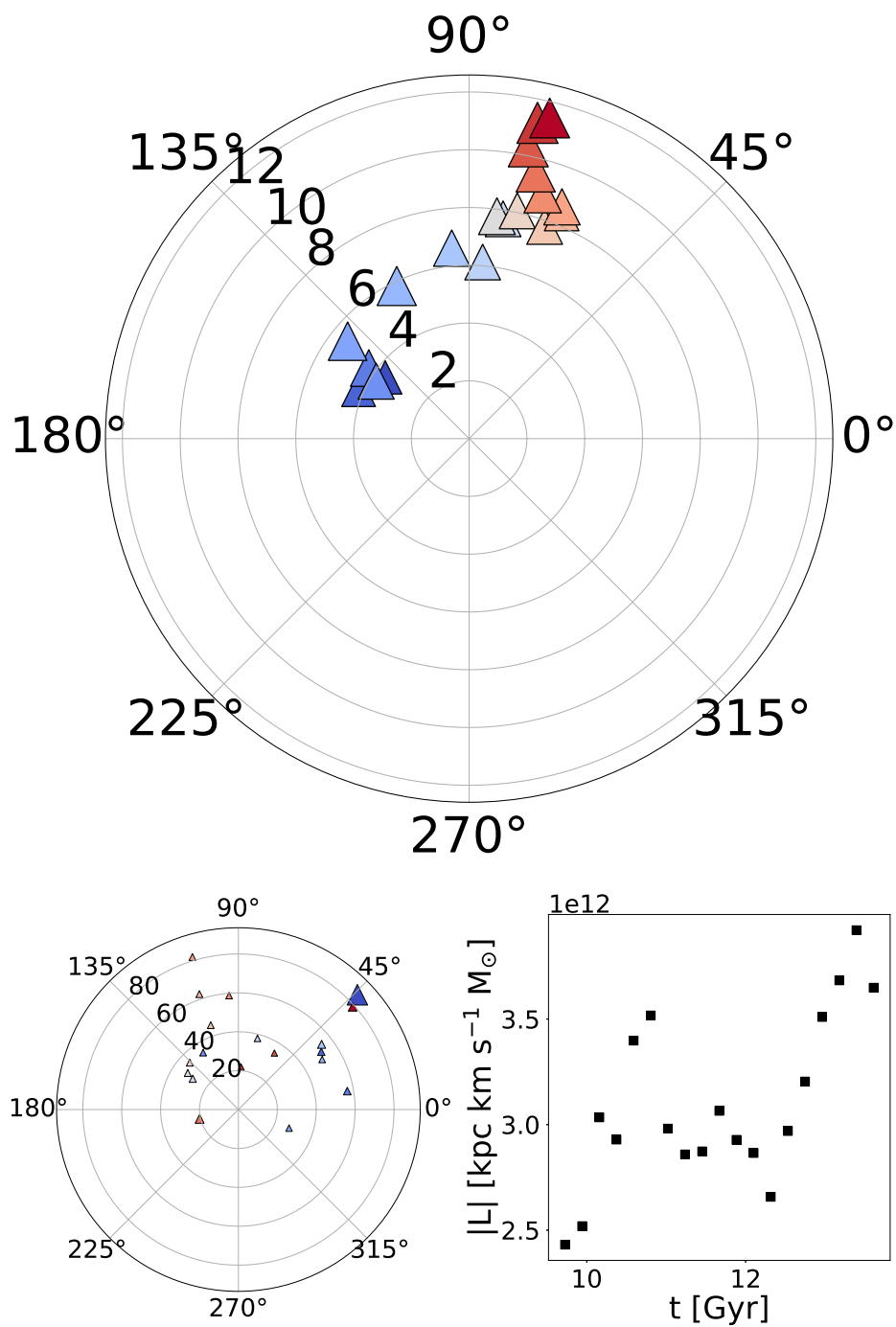


Fig. 32 g2.79e12: top: total angular momentum of stars entering R_{disc} at each time step, left: total angular momentum of stars entering $0.5R_{200}$ at each time step, right: magnitude of angular momentum entering R_{disc} at each time step.

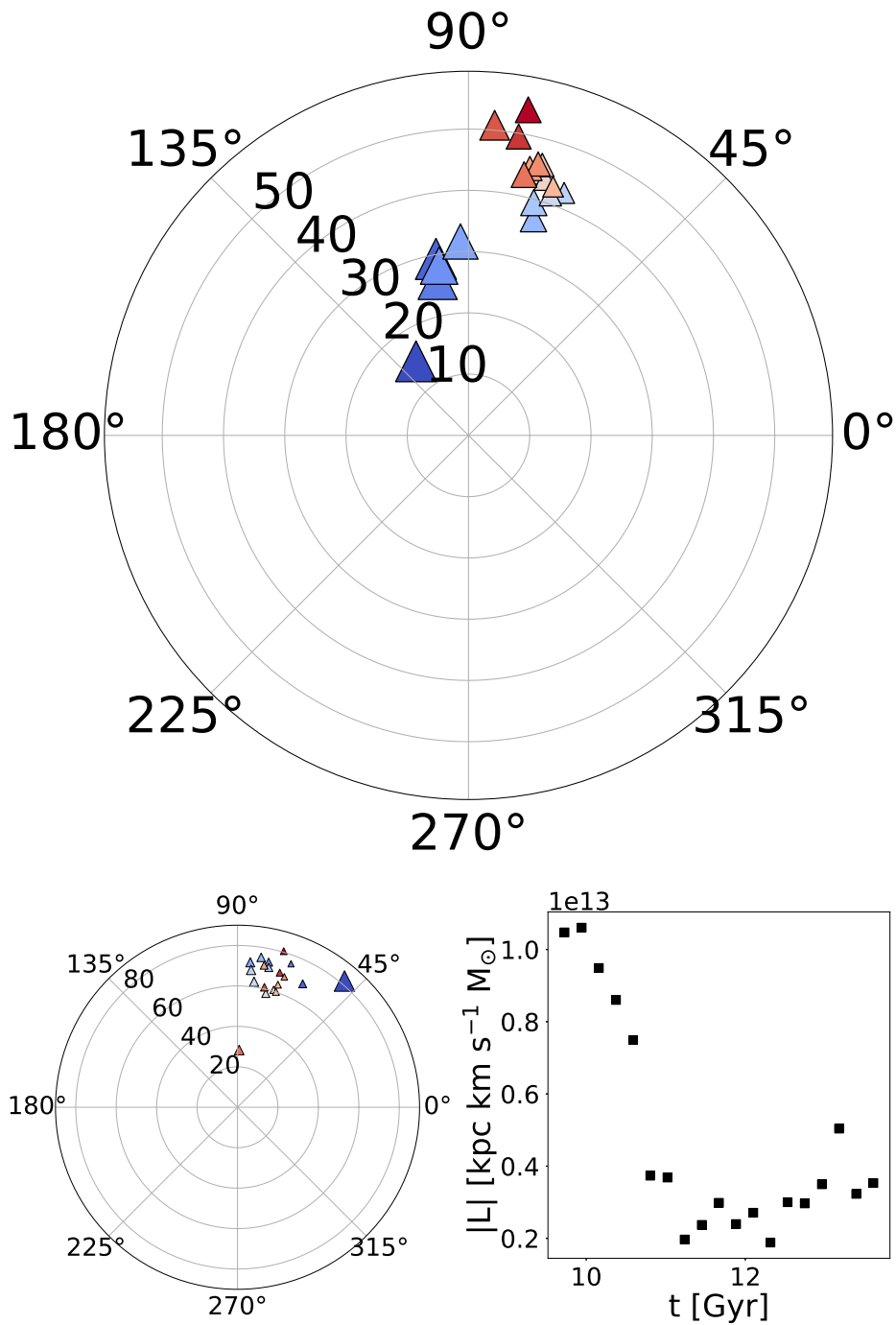


Fig. 33 g2.79e12: top: total angular momentum of gas entering R_{disc} at each time step, left: total angular momentum of gas entering $0.5R_{200}$ at each time step, right: magnitude of angular momentum entering R_{disc} at each time step.

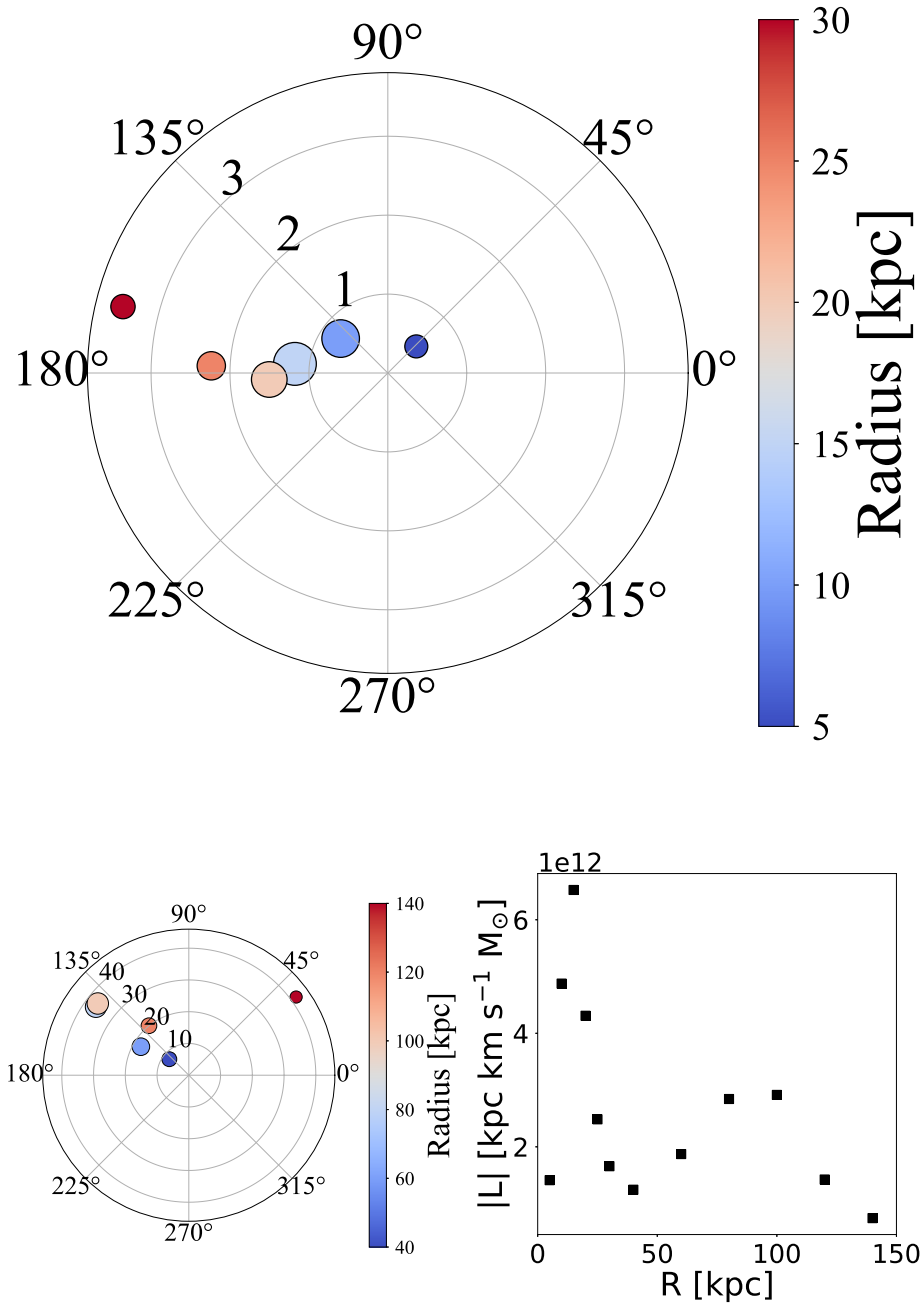


Fig. 34 $g_{2.79e12}$: the integrated net angular momentum flow of stars calculated at increasing radii between 5 and 30 kpc with annuli of width 5 kpc (top) and between 40 and 120 kpc with annuli of width 20 kpc (left), and the magnitude of each angular momenta against the interior annular radius (right).

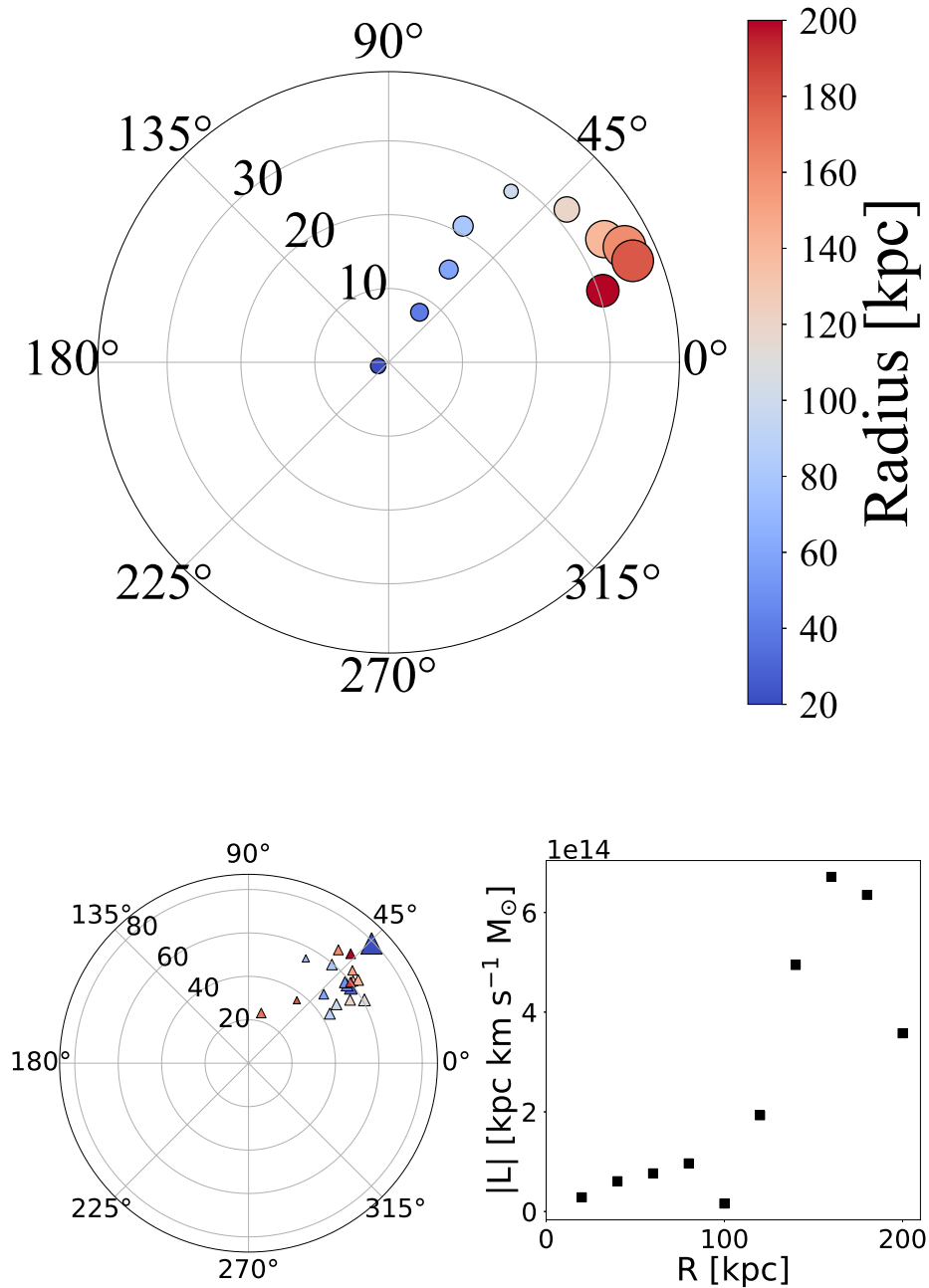


Fig. 35 g2.79e12: the integrated net angular momentum flow of dark matter calculated at increasing radii between 20 and 200 kpc with annuli of width 20 kpc (top), the total angular momentum of dark matter entering $0.5R_{200}$ at each time step (left), and the magnitude of each angular momenta against the interior annular radius (right).

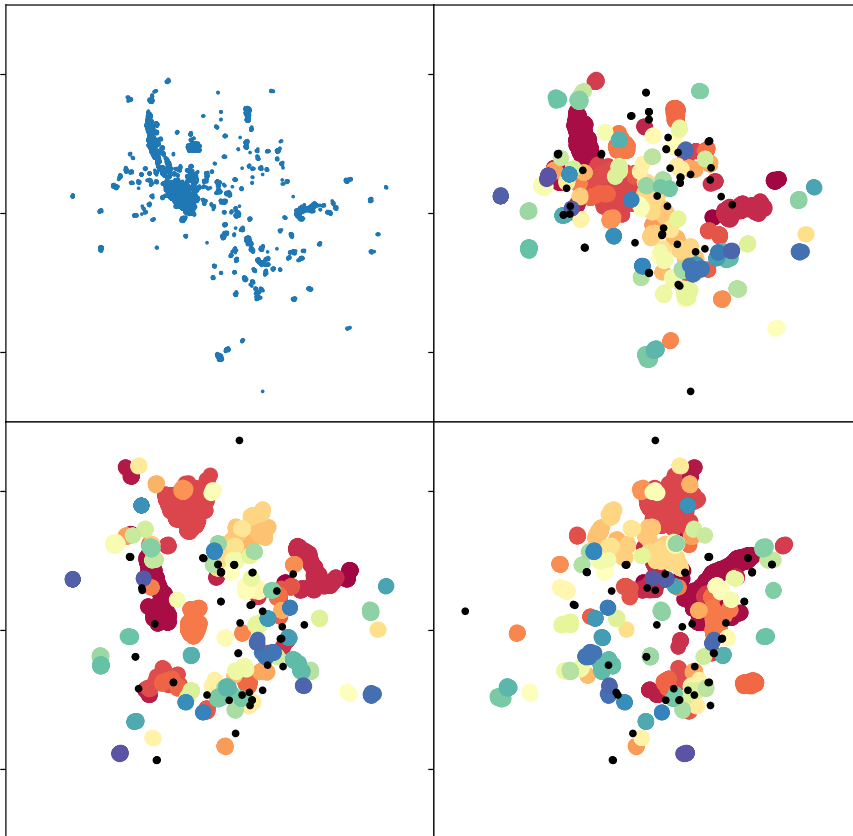
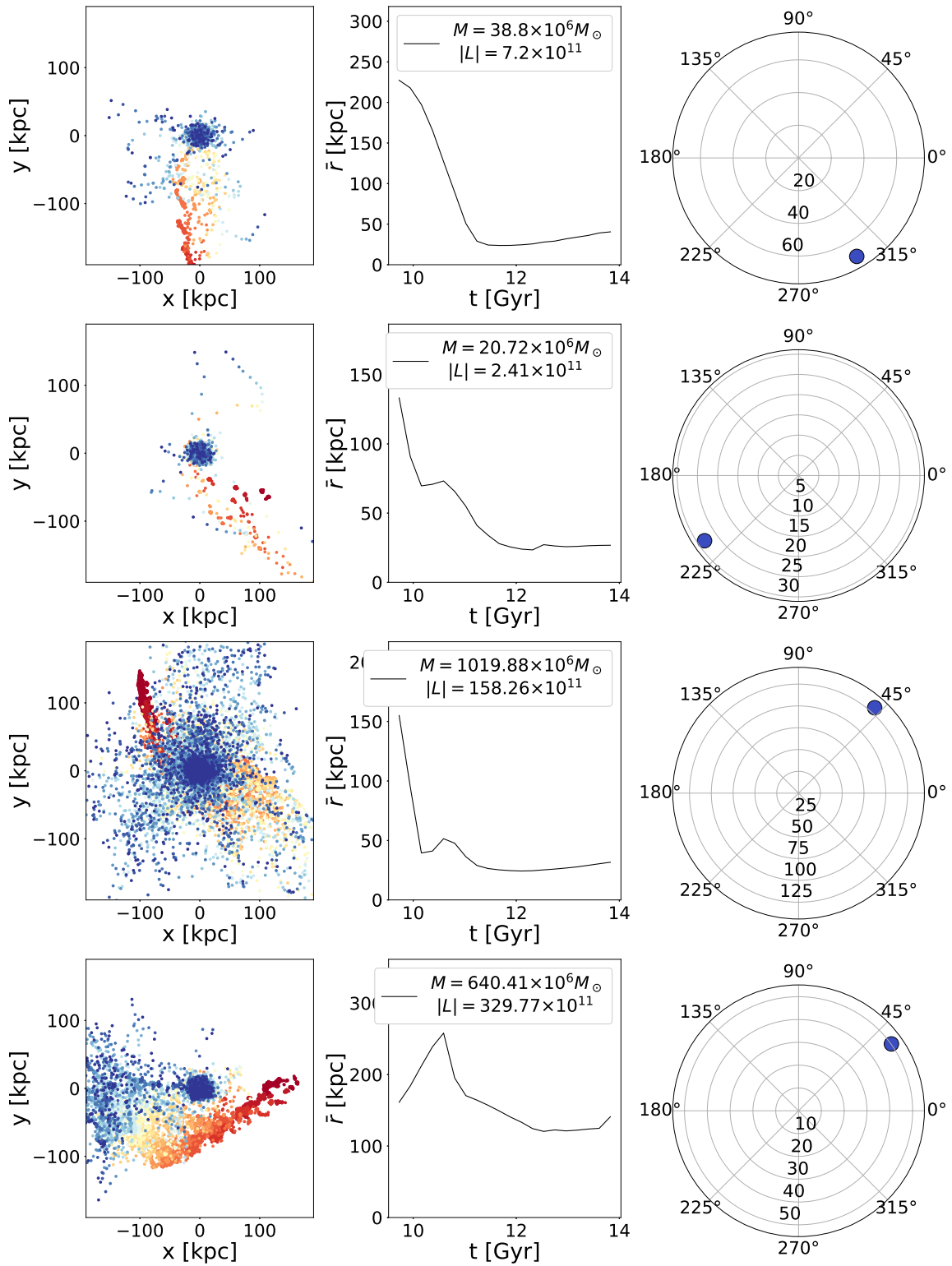
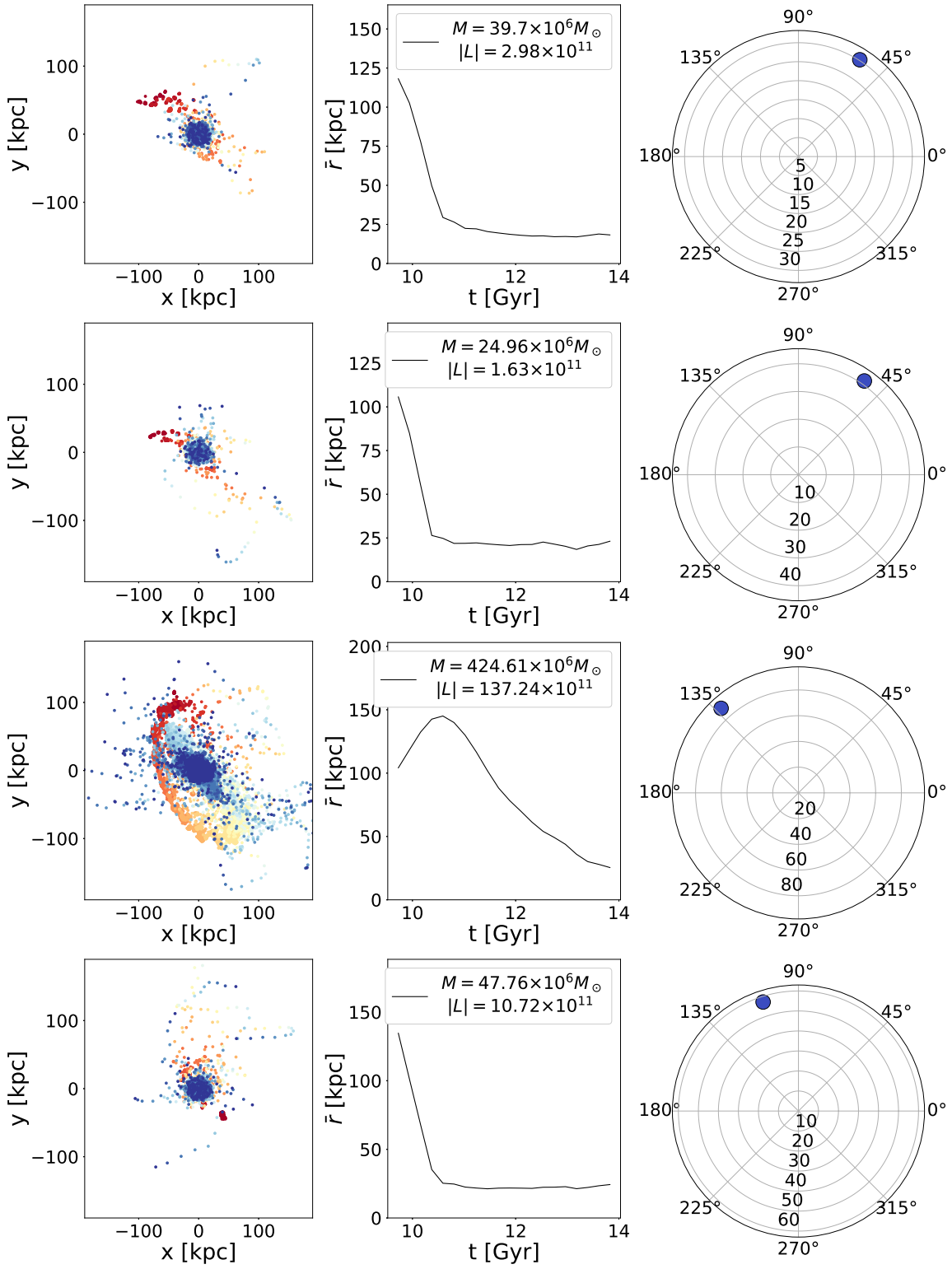
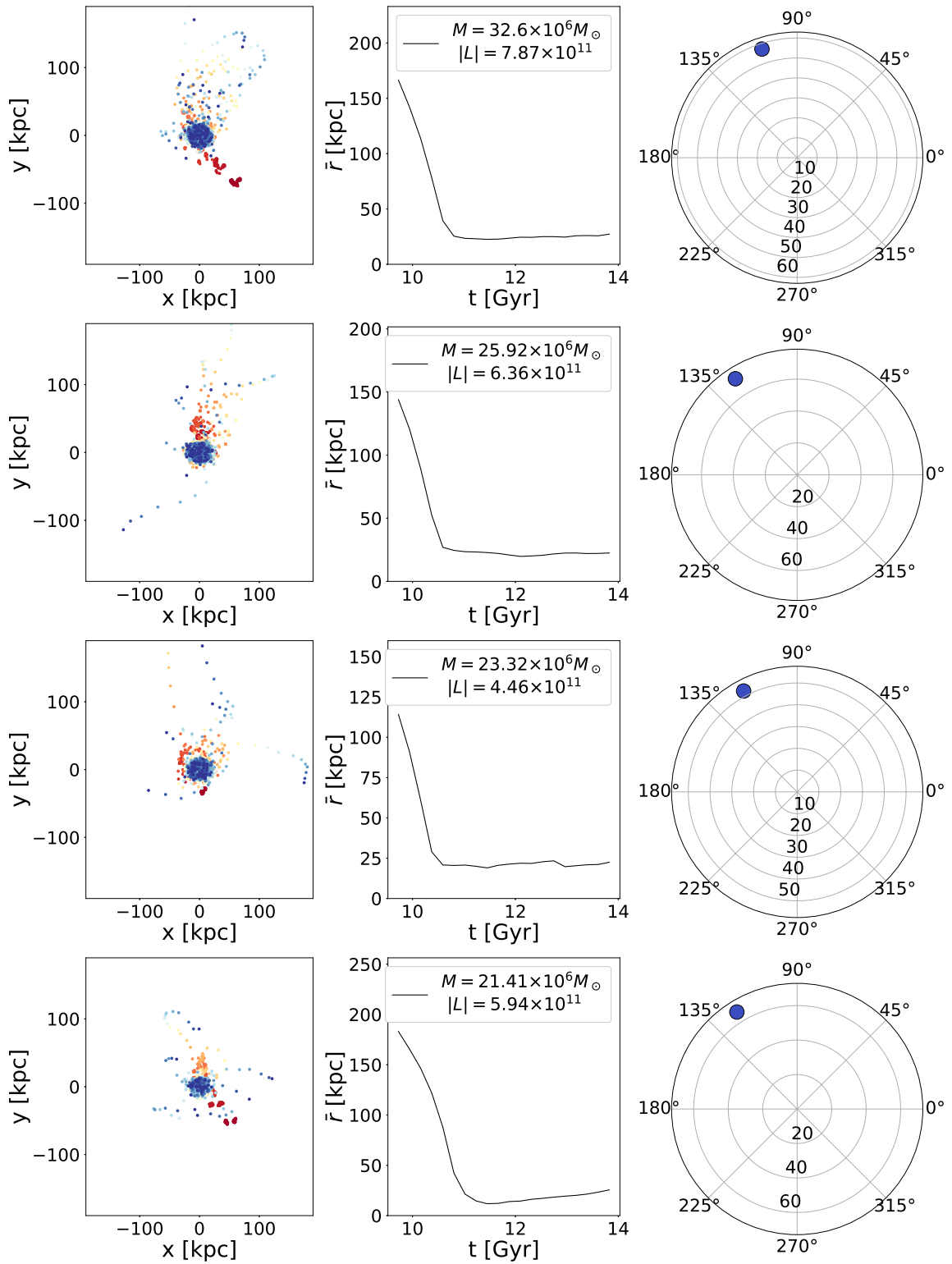


Fig. 36 g2.79e12: this plot shows the distribution of the gas clouds at $z = 0.3$, each colour represents a different gas cloud that will be tracked. The top left and top right panel show the gas clouds projected in the x - y plane, before (left) and after (right) grouping. The bottom left and bottom right panels show the gas clouds projected in the x - z and y - z planes, respectively.







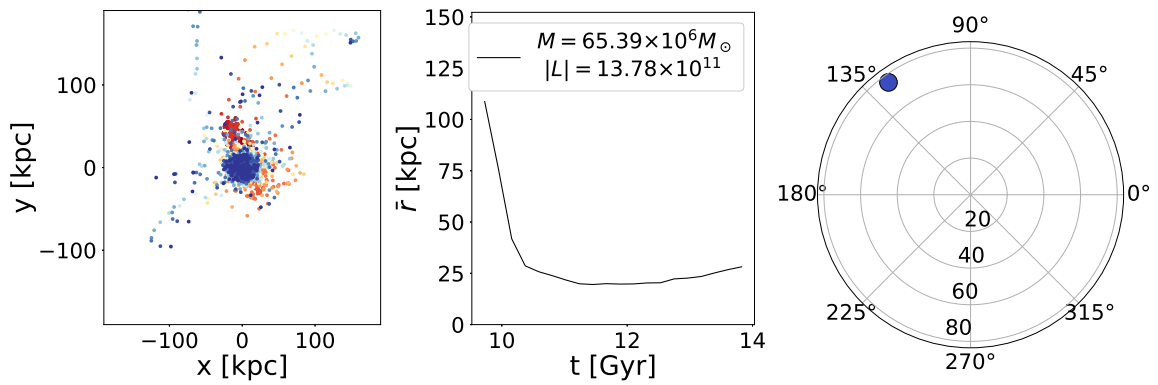


Fig. 34 (Cont.) Left: the location of all the particles in the gas cloud with $M > 10^7 M_{\odot}$ & $\bar{R} < 30$ kpc, middle: average distance to the centre of the galaxy with time, right: angular momentum of the gas cloud at $z = 0.3$. The mass and starting angular momentum (in units $M_{\odot} \text{ km s}^{-1}$) of each cloud is given in middle plot.

Appendix B

Appendix B includes a copy of Earp S. W. F., Debattista V. P., Macciò A. V., Cole D. R., 2017, MNRAS, 469, 4095.



The tilting rate of the Milky Way’s disc

Samuel W. F. Earp,^{1★} Victor P. Debattista,^{1★} Andrea V. Macciò^{2,3} and David R. Cole⁴

¹Jeremiah Horrocks Institute, University of Central Lancashire, Preston, PR1 2HE, UK

²New York University Abu Dhabi, PO Box 129188, Saadiyat Island, Abu Dhabi, UAE

³Max Planck Institute for Astronomy, Königstuhl 17, D-69117 Heidelberg, Germany

⁴Rudolf Peierls Centre for Theoretical Physics, University of Oxford, Keble Road, Oxford OX1 3NP, UK

Accepted 2017 May 9. Received 2017 May 8; in original form 2016 October 13

ABSTRACT

We present tilting rates for galaxies comparable to the Milky Way (MW) in a Λ cold dark matter cosmological hydrodynamical simulation, and compare these with the predicted tilting rate detection limit of the *Gaia* satellite $0.28^\circ \text{Gyr}^{-1}$. We first identify galaxies with mass comparable to the MW ($9 \times 10^{11} \leq M_{200} \leq 1.2 \times 10^{12} M_\odot$) and consider the tilting rates between $z = 0.3$ and 0. This sample yields a tilting rate of $7.6^\circ \pm 4.5^\circ \text{Gyr}^{-1}$. We constrain our sample further to exclude any galaxies that have high stellar accretion during the same time. We still find significant tilting, with an average rate of $6.3^\circ \text{Gyr}^{-1}$. Both subsamples tilt with rates significantly above *Gaia*’s predicted detection limit. We show that our sample of galaxies covers a wide range of environments, including some similar to the MW’s. We find galaxies in denser regions tilt with higher rates than galaxies in less dense regions. We also find correlations between the angular misalignment of the hot gas corona and the tilting rate. *Gaia* is likely to be able to directly measure tilting in the MW. Such a detection will provide an important constraint on the environment of the MW, including the rate of gas cooling on to the disc, the shape and orientation of its dark matter halo, and the mass of the Large Magellanic Cloud. Conversely, failure to detect tilting may suggest the MW is in a very quiet configuration.

Key words: reference systems – Galaxy: disc – Galaxy: evolution – Galaxy: kinematics and dynamics.

1 INTRODUCTION

Disc galaxies such as the Milky Way (MW) are rapidly rotating; the orientation of their spin axis represents the integral of the angular momentum accreted via gas, interactions with satellites or other galaxies, and torques exerted on the disc by the dark matter halo within which they reside. Therefore directly observing disc tilting at the present time provides clues to the nature of each of these processes. The *Gaia* space astrometry mission may soon allow direct measurement of the MW’s disc tilting rate. Precision measurements will enable the construction of stellar position catalogues with accuracies of order 20μ as with respect to distant quasars, which act as the measurement reference frame (Perryman et al. 2001; Lindegren et al. 2008). Perryman, Spergel & Lindegren (2014) estimate that an accuracy better than 1μ as yr^{-1} should be achieved in all the inertial spin components of the *Gaia* reference frame, corresponding to $0.28^\circ \text{Gyr}^{-1}$.

Galaxies tilt for a variety of reasons. The role of interactions in disc tilting has been studied extensively. While major mergers

destroy discs, smaller scale interactions are less violent, and tilt disc galaxies. Huang & Carlberg (1997) showed that infalling satellites tilt discs so that there is a preference for infalling satellites to merge in the plane of the disc. Read et al. (2008) reached a similar conclusion. Bett & Frenk (2012) investigated the effects of minor mergers and flybys on the orientation of spins of dark matter haloes of mass ($12.0 \leq \log_{10}(M/M_\odot)h^{-1} \leq 12.5$) at $z = 0$. They found that the majority of these events only caused small changes in the angular momentum of the entire halo, with only 10.5 per cent of MW mass haloes experiencing changes in their angular momentum by more than 45° over the course of their lifetimes. However, the inner halo is not so stationary, with 47 per cent of inner haloes experiencing a large change in their angular momentum orientation of at least 45° during their lifetimes. Bett & Frenk (2016) extended this study to include a broader range of halo masses ($10.5 \leq \log_{10}(M/M_\odot)h^{-1} \leq 15.5$). They found that 35 per cent of haloes had experienced changes in orientation of at least 45° , at some point in their lifetimes, without a major merger taking place.

In the MW, the most important ongoing interaction is with the Large and Small Magellanic Clouds (LMC and SMC). The mass of the LMC is currently the subject of debate, with mass estimates as high as $M_{\text{LMC}} \sim 2 \times 10^{11} M_\odot$ (Kallivayalil et al. 2013; Gómez

* E-mail: swfearp@gmail.com (SWFE); vpdebattista@gmail.com (VPD)

et al. 2015; Peñarrubia et al. 2016), corresponding to ~ 20 per cent of the mass of the MW. Other estimates are significantly lower ($\sim 5 \times 10^9 M_{\odot}$) (Alves & Nelson 2000; van der Marel et al. 2002). Thus the importance of the LMC on the orientation of the MW's disc spin cannot yet be estimated well.

Another cause of disc tilting is torques from dark matter haloes. In the Λ -cold dark matter (Λ CDM) paradigm, haloes grow hierarchically, becoming triaxial (Bardeen et al. 1986; Barnes & Efstathiou 1987; Frenk et al. 1988; Dubinski & Carlberg 1991; Jing & Suto 2002; Bailin & Steinmetz 2005; Allgood et al. 2006). These triaxial haloes are themselves tilting (Moore et al. 2004). Dubinski (1992) examined the effect of tidal shear on dark matter haloes; he found that in all 14 of his $(1-2) \times 10^{12} M_{\odot}$ haloes, the major axis rotated uniformly around the minor axis with a rotation rate in the range of $6^{\circ}-96^{\circ} \text{Gyr}^{-1}$. Likewise, Bailin & Steinmetz (2004) measured figure rotation in 288 of their 317 dark matter haloes, finding a tilting rate of $6.2^{\circ} \text{Gyr}^{-1}$ with a log-normal distribution having $\sigma = 0.58^{\circ} \text{Gyr}^{-1}$. Bryan & Cress (2007) found that 63 per cent of the 115 haloes they considered exhibited significant figure rotation, with an average pattern speed of $13.8^{\circ} h \text{Gyr}^{-1}$.

The figure rotation of triaxial haloes leads to time varying torques on discs. Debattista et al. (2015) showed that a stellar disc, lacking gas, within a triaxial halo aligns its spin axis with the minor axis of the halo. Even when perturbed by a satellite, the disc settles back to this alignment. Thus a tilting halo will drag a disc along with it. Yurin & Springel (2015) inserted live stellar discs into eight, MW-sized, high-resolution dark matter haloes from the Aquarius simulation. They found typical tilting rates of $5^{\circ}-6^{\circ} \text{Gyr}^{-1}$, comparable with halo tilting rates. While no direct evidence of tilting haloes exists, tidal torques exerted on a stellar disc by a rotating dark matter halo have been explored as a possible cause for warps (Dubinski & Kuijken 1995; Dubinski & Chakrabarty 2009) and as a driving mechanism for spiral structure in dark matter-dominated galaxies (Bureau et al. 1999).

Galaxies such as the MW are generally thought to be surrounded by hot gas coronae, with masses greater than the stellar disc itself (e.g. Spitzer 1956; White & Rees 1978; Savage & de Boer 1979; White & Frenk 1991; Dahlem 1997; Wang et al. 2001; Fukugita & Peebles 2006). The quiescent cooling of this hot gas then sustains star formation over a long time (Fall & Efstathiou 1980; Brook et al. 2004; Kereš et al. 2005; Robertson et al. 2006; Brooks et al. 2009). However, the angular momentum of coronae is usually misaligned with that of their embedded stellar disc (van den Bosch et al. 2002; Roškar et al. 2010). This contributes misaligned angular momentum to the disc, causing its orientation to change. Debattista et al. (2015) showed that under these circumstances, the orientation of the disc spin is determined by a balance between the torques from the triaxial dark matter halo and the net inflow of angular momentum via cooling gas. As a result, star forming galaxies are generally misaligned with the main planes of their dark matter haloes (Sales & Lambas 2004; Brainerd 2005; Agustsson & Brainerd 2006; Yang et al. 2006; Azzaro et al. 2007; Faltenbacher et al. 2007; Wang et al. 2008, 2010; Nierenberg et al. 2011; Li et al. 2013). Debattista et al. (2013) argued for just such an orientation in the MW, by noting that the best-fitting models for the Sagittarius Stream (Law, Majewski & Johnston 2009; Law & Majewski 2010; Deg & Widrow 2013) require the disc spin to be along the halo's intermediate axis, an orientation they showed is extremely unstable. Debattista et al. (2013), therefore, argued that the modelling assumption of the disc residing in one of the symmetry planes must be violated. While this is indirect evidence, stacking of external galaxies has shown that the distribution of satellites around blue galaxies tends to be isotropic,

contrary to what is seen around red galaxies (Sales & Lambas 2004; Brainerd 2005; Yang et al. 2006; Wang et al. 2008; Nierenberg et al. 2011; Dong et al. 2014; Wang et al. 2014).

In summary in the MW, the disc may be tilting for a variety of reasons. As a first step towards understanding the tilting of the MW, in this paper, we measure the tilting rates of MW-like galaxies in a Λ CDM cosmological simulation. We compare the tilting rates of these discs to the observational limit of *Gaia* to establish whether tilting of this nature would be detectable. In Section 2, we describe the cosmological simulation. Then in Section 3, we describe the samples of galaxies selected on the basis of virial mass, merger history and total satellite mass. In Section 4, we describe the methods we use to calculate the tilting rates. Section 5 presents the results and provides a comparison with the observational limit of *Gaia* for a variety of different local configurations and environments. We present our conclusions in Section 6, showing that even galaxies in quiet systems tilt at a rate that would be detectable by *Gaia*.

2 NUMERICAL SIMULATION

The simulation we use here was performed with *GASOLINE*, a multi-stepping, parallel, tree code with smoothed particle hydrodynamics (SPH) (Wadsley, Stadel & Quinn 2004). The version of *GASOLINE* used for this work includes radiative and Compton cooling for a primordial mixture of hydrogen and helium. The star formation algorithm is based on a Jeans instability criterion (Katz 1992), but simplified so that gas particles satisfying constant density and temperature thresholds in convergent flows spawn star particles at a rate proportional to the local dynamical time (see Stinson et al. 2006). The star formation efficiency was set to 0.05 based on simulations of the MW that satisfied the Schmidt–Kennicutt Law (Schmidt 1959; Kennicutt 1998), and we adopt a star formation threshold of 0.1 particles per cubic centimetre. The code also includes supernova feedback using the blast-wave formalism as described in Stinson et al. (2006), and a UV background following Haardt & Madau (1996); see Governato et al. (2007) for a more detailed description.

We used as a starting simulation one of the cosmological cubes described in Macciò, Dutton & van den Bosch (2008), namely our box has a size of 180Mpc and contained 300^3 dark matter particles. This box was created using WMAP5 (Komatsu et al. 2009) initial conditions with $(h, \Omega_M, \Omega_L, \Omega_b, \sigma_8) = (0.72, 0.258, 0.742, 0.0438, 0.796)$ and was run with the code *PKDGRAV* as detailed in Macciò et al. (2008).

From this simulation, we selected at $z = 0$ a volume of about $(25 \text{Mpc})^3$ with the requirement of not containing any haloes with a virial mass above $5 \times 10^{12} M_{\odot}$. For this purpose, we use the halo catalogue from Macciò et al. (2008), which was generated using a Spherical Overdensity halo finder algorithm. The choice of this particular mass threshold is motivated by our interest in studying the properties of galaxies with a total mass equal or lower than the MW.

We then traced back to the initial conditions the Lagrangian region defined by this redshift-zero volume, making sure to obtain a continuous region (i.e. no holes) at the initial redshift ($z = 99$). Finally, we used the standard zoom-in technique to enhance the resolution of the dark matter particles in the selected region by a factor of 10^3 , and adding baryons (gas particles) with the same high resolution. As a final result, this high resolution region contains more than 10^8 particles, and reaches a mass resolution of 6.6×10^6 and $1.1 \times 10^6 M_{\odot}$ for dark matter and gas, respectively, with a gravitational softening length of 1.24 kpc for dark matter and 0.5 kpc for gas.

We then used the `GASOLINE` code described above to evolve these new high resolution initial conditions from $z = 99$ to 0 taking into account gas cooling, star formation and feedback in a self-consistent way. To generate the catalogue of virially bound haloes, we use the grid based code `AMIGA Halo Finder` (Knollmann & Knebe 2009) on the simulation outputs.

3 THE SAMPLES

We identify 182 haloes spanning the mass range $9 \times 10^{10} - 4.4 \times 10^{12} M_{\odot}$. Of the 41 saved time steps during the time interval $z = 0.3$ to 0, we use a subset of ten time steps with an average separation of ~ 0.37 Gyr to determine the stellar mass fractional growth rate, and to track the merger history of each galaxy. We calculate the tilting rate once for each galaxy, by measuring the angular momentum within 5 per cent of the virial radius at $z = 0.3$ and 0.

Subsample A contains haloes within a specified mass range comparable to the MW. The motivation for this mass cut is two-fold. First, we are interested in galaxies with similar halo mass as the MW. Secondly, we wish to choose galaxies where the mass of the dark matter halo and the stellar mass are in good agreement with abundance matching results. We impose an upper limit of $M_{200} \leq 1.2 \times 10^{12} M_{\odot}$ in order to constrain the sample to a mass range that is comparable with the virial mass of the MW (Klypin, Zhao & Somerville 2002). We also find that above this limit the full sample is dominated by ellipticals that, due to their evolutionary history, generally have lower specific angular momentum. Fig. 1 compares the halo mass–stellar mass relation of the full sample with the relation derived by the abundance matching method of Kravtsov et al. (2014). This figure shows that galaxies residing within haloes of mass $M_{200} \geq 9 \times 10^{11} M_{\odot}$ in the simulation match this relationship well. Lower mass haloes, however, have an excess stellar mass. Therefore, we use this mass as a lower limit for subsample A. Implementing the mass range $1.2 \times 10^{12} \geq M_{200} \geq 9 \times 10^{11} M_{\odot}$ leaves 19 galaxies in subsample A.

Subsample B has the same mass constraint with two added limits: one on the change in stellar mass to remove galaxies that have

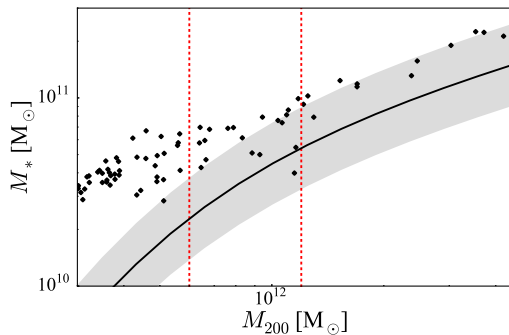


Figure 1. Stellar mass versus halo mass at redshift $z = 0$ for the most massive galaxies in the initial sample (black points). We measure the stellar mass within 5 per cent of the virial radius (r_{200}), where the mean interior density is 200 times the critical density. For comparison, the black line shows the M_* – M_{200} relation of Kravtsov, Vikhlinin & Meshcheryakov (2014) derived using halo abundance matching. The grey shaded region shows the scatter in this relation. The red dashed lines illustrate the bounds that subsample A lies within.

Galaxy tilting in the era of Gaia 4097

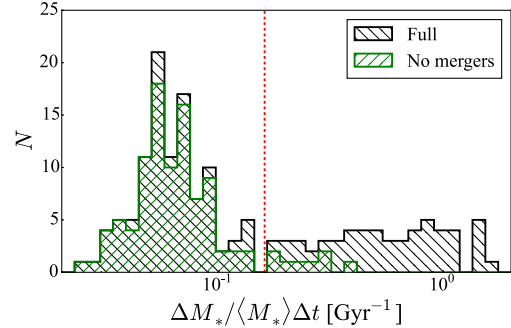


Figure 2. Distribution of the maximum rate of change in stellar mass normalized by average stellar mass between t_i and t_{i+1} within 5 per cent of the virial radius. The black histogram shows the rates for the full sample of 182 haloes. The green histogram shows the distribution of rates for galaxies that did not undergo any mergers between $z = 0.3$ and 0. The red dashed line indicates the upper limit we impose on subsample B.

undergone mergers above a certain mass ratio, and the second on the ratio of galaxy mass to total satellite mass. First, we observe the evolution of the galaxies by visual inspection to construct a catalogue of galaxies that have not undergone mergers between $z = 0.3$ and 0. By comparing this catalogue to the full sample, we can constrain the rate of change in stellar mass such that above this limit the sample is dominated by galaxies that have undergone mergers. Fig. 2 shows the distribution of fractional growth rates for galaxies that do not undergo mergers and the full sample. From Fig. 2, we set an upper limit on the maximum stellar mass fractional growth rate of 0.16 Gyr^{-1} within 5 per cent of the virial radius, under which galaxies have not undergone significant minor or major mergers. We construct subsample B from subsample A with the added constraint that $\Delta M_*/(\langle M_* \rangle \Delta t)$ must fall below this value. Two galaxies that fell below this limit were observed undergoing a minor merger, however, the maximum stellar mass accreted was roughly one per cent that of the central galaxy so they are included in subsample B. Lastly, we stipulate that the total satellite stellar mass must be less than 40 per cent that of the central galaxy at every time step. To measure the total satellite mass, we subtract the total stellar mass within $0.1r_{200}$, where r_{200} is the virial radius, from the total stellar mass inside r_{200} . This leaves us with just seven galaxies in subsample B.

4 ANALYSIS

To derive accurate tilting rates, we first find the kinematic centres of the galaxies. We adopt the position of the lowest potential dark matter particle as our kinematic centre. We verify that this method is reliable by computing the kinematic centre using an iterative shrinking sphere method. Starting with a sphere of 200 kpc, we iterate centring on the centre of mass and halving the radius each step to a final value of ~ 10 pc. Using the lowest potential dark matter particle, we are able to obtain kinematic centres for our entire sample of 182 galaxies.

We then measure the angular momentum of the galaxy by summing the angular momentum of each star particle within $R < 0.05r_{200}$. This radius is selected to include the disc of the galaxy, but exclude any warps. Briggs (1990) found that warps become detectable within the Holmberg radius (R_{Ho}). For a typical

virial radius of ~ 200 kpc, we would expect a Holmberg radius of ~ 15 kpc, 5 kpc greater than the radius we would consider for $0.05r_{200} \sim 10$ kpc. We also select this radius to avoid selecting just the bulges of our galaxies, which tend to have lower specific angular momentum.

In order to determine the uncertainty in the tilting rates, we measure the difference in the direction of the angular momentum vector at different radii. We measure the angular momentum at seven linearly spaced radii spanning $0.01 < R/r_{200} < 0.04$. We then use the average angular discrepancy between the vectors as the error (σ) on the measurement of the angular momentum vector, and hence on the tilting rate. For each of these errors, we assign a weight w such that $w = 1/\sigma^2$, which will be used in the calculation of the mean and standard deviation of each subsample.

5 RESULTS

5.1 Tilting rates

First we consider subsample A, i.e. galaxies with virial mass comparable to the MW's, within the range $9 \times 10^{11} \leq M_{200} \leq 1.2 \times 10^{12} M_{\odot}$. We measure the tilting rate once, between the two time steps $z = 0.3$ and 0. This subsample tilts with a mean rate of $7.6^{\circ} \text{ Gyr}^{-1}$, and a standard deviation of $4.5^{\circ} \text{ Gyr}^{-1}$, well above the average error for this subsample of just $0.05^{\circ} \text{ Gyr}^{-1}$. All 19 of the galaxies in this subsample exhibit significant tilting above *Gaia*'s detection limit of $0.28^{\circ} \text{ Gyr}^{-1}$ (Perryman et al. 2014).

Next we consider subsample B, i.e. the galaxies with similar mass to the MW, that have low fractional stellar mass change from $z = 0.3$ to 0, and have a maximum total satellite mass of 40 per cent that of the central galaxy. Fig. 3 shows tilting rates for sample B versus the ratio of stellar mass to satellite stellar mass. Each data point in this figure corresponds to a tilting rate of a single galaxy, with the mass ratio measured at $z = 0$. The green squares show only the five galaxies that were not observed to undergo any mergers since $z = 0.3$, while the black squares were the two galaxies that did undergo a minor merger within the same time.

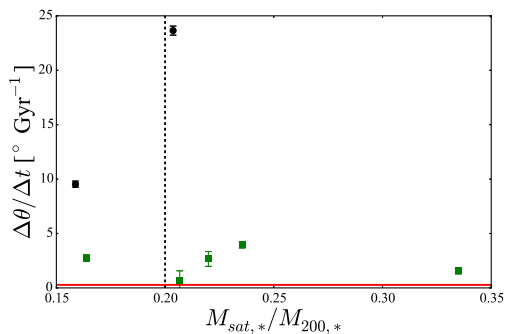


Figure 3. Tilting rate versus the present day fraction of satellite to galaxy stellar mass ($M_{\text{sat},*}/M_{200,*}$) for subsample B, i.e. galaxies that have mass comparable to the MW and have low fraction stellar mass change between $z = 0.3$ and 0. The (green) squares represent the galaxies that were observed to not have undergone any mergers since $z = 0.3$, the (black) circles show the galaxies that undergo a minor merger. The black dashed line shows recent estimates of the mass ratio of the LMC relative to the MW (Kallivayalil et al. 2013; Gómez et al. 2015; Peñarrubia et al. 2016). The red horizontal line is *Gaia*'s predicted detection limit (Perryman et al. 2014).

The tilting rates of this subsample have an average of $6.3^{\circ} \text{ Gyr}^{-1}$, with a standard deviation of $6.5^{\circ} \text{ Gyr}^{-1}$, well above the average uncertainty of $0.13^{\circ} \text{ Gyr}^{-1}$. This subsample also tilts with a rate well above *Gaia*'s detection limit.

5.2 Environmental dependence

To determine if there is any dependence between the tilting rates of galaxies and their local environment, we compare the tilting rates of the galaxies with their normalized local density. We calculate the density within various radii centred on each galaxy, and then normalize by the critical density at $z = 0$. Fig. 4 shows the distribution of densities for spheres with radii 3, 4, 5 and 6 Mpc. We find that for large radii (5 and 6 Mpc) that there is a strong correlation for subsample A with p values of 0.8 for both, although, for smaller radii (3 and 4 Mpc), the correlation weakens, with p values of 0.2 and 0.6, respectively. When we consider subsample B, the correlations are enhanced, with p values of 0.7, 0.95, 0.97 and 0.96 for radii 3, 4, 5 and 6 Mpc, respectively.

The MW has a close massive neighbour M31 within 1 Mpc. We compare the tilting rates with the distance D to the nearest massive ($M_* > 9 \times 10^{11} M_{\odot}$) galaxy in subsample A. Fig. 5 shows the tilting rate versus D ; galaxies in subsample A span a range of D , including some with very close neighbours and some very isolated. We see no relation between D and the tilting rate. Considering galaxies in subsample B, we do find a weak anti-correlation. One of our galaxies does appear to be tilting extremely fast without a close neighbour.

5.3 Dependence on gas

The angular momenta of the hot gas corona surrounding a galaxy and of the disc are not generally aligned. As the gas corona continually feeds cool gas to the disc, this misalignment causes gas being accreted to change the angular momentum of the disc. To investigate this effect on the tilting rate, we define the hot gas corona in two different ways. In the first, we choose all gas with a temperature $T > 5 \times 10^4$ K, and in the second, we choose all gas between two spherical shells of radii $0.2r_{200}$ and r_{200} . The angular momentum calculated from each definition is in good agreement, with $p = 0.99$. We compare the tilting rates of the hot gas corona to the tilting rate of the disc for both of these methods. Fig. 6 shows that for both methods of defining the corona, there is no correlation between the angular momentum tilting rate of the corona and disc for MW mass galaxies. Even when we consider subsample B, we find no correlation for both methods.

Next we compare the tilting rates of the disc to the angular misalignment between the disc and the hot gas corona for both methods of defining the hot gas corona. Fig. 7 shows the relation between the tilting rates of discs and the angular misalignment of the hot gas corona and disc angular momentum. We find a weak correlation with p values of 0.4 and 0.5 for both methods, respectively, for subsample A. However, for subsample B, the correlation strengthens considerably for both methods with p values of 0.86 and 0.87.

The large-scale structure (LSS) may influence the flow of gas into the halo and subsequently the misalignment between the stellar and coronal angular momentum. When we compare the misalignment of the hot gas corona from the stellar disc with the normalized local density, we find similar correlations as those we found in Fig. 4. Therefore it is not possible to determine from this simulation if the effect of the environment directly governs the tilting of the galaxy or if the LSS affects the tilting via its effect on the coronal

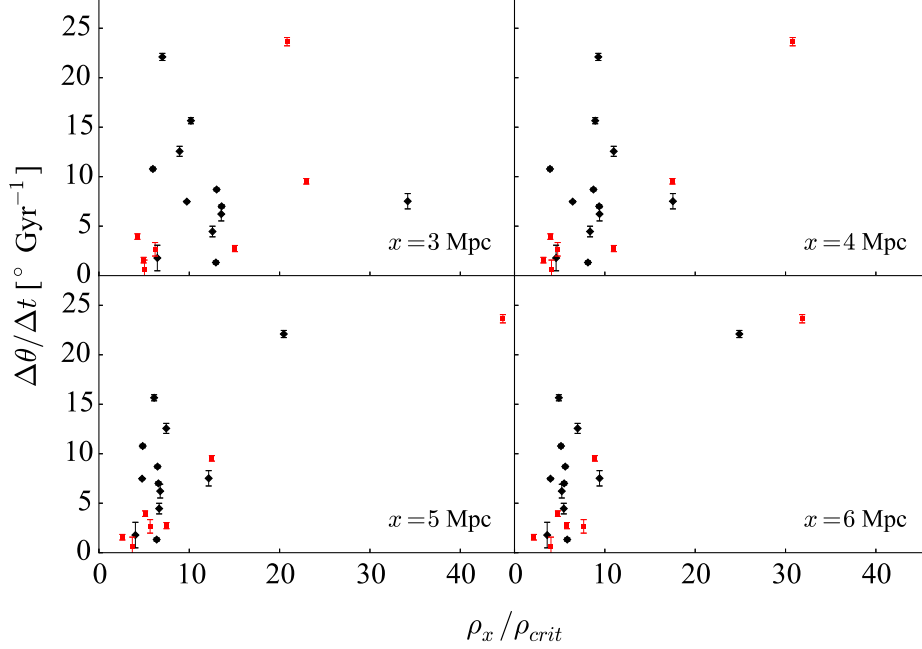


Figure 4. Tilting rate versus the local density within a sphere of radius x at redshift $z = 0$. In all panels, the (black) diamonds represent galaxies in subsample A with masses comparable to the MW and the (red) squares show galaxies in subsample B with comparable mass and undergoing no interactions since $z = 0.3$. We measure correlation coefficients for each panel $x = 3, 4, 5$ and 6 Mpc of $p = 0.2, 0.6, 0.8$ and 0.8 , respectively, for all points, while for subsample B, we find p values of $0.7, 0.95, 0.98$ and 0.97 , respectively.

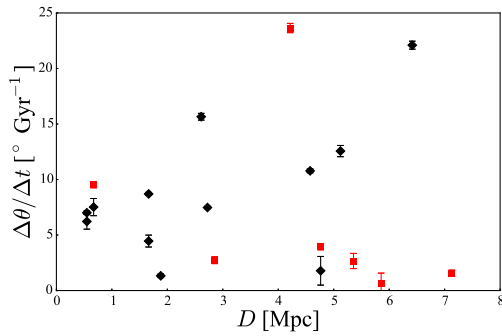


Figure 5. Tilting rate versus distance D to nearest galaxy with comparable mass to the MW measured at $z = 0$. The (black) diamonds represent subsample A and the (red) squares show subsample B. We find a correlation coefficient of $p = -0.05$ for subsample A and $p = -0.3$ for subsample B.

angular momentum, as seems likely. Debattista et al. (2015) found that galaxies lacking gas generally aligned with the minor axis of their halo. However, when gas is allowed to cool on to the disc, the orientation can be more arbitrary. For both of our subsamples, we find that galaxies with higher star formation generally tilt with higher rates. These results favour the gas driven tilting scenario.

When we compare the angular momentum misalignment between the disc and the gas corona with the local density, we find similar correlations as those in Fig. 4. Thus the mechanism by which the

LSS affects the disc's tilting rate is unclear. The LSS may torque the disc directly, or it may influence the flow of gas into the halo, driving the misalignment between the stellar and coronal angular momentum, which in turn drives the tilting (e.g. Debattista et al. 2015). One possible clue comes from comparing the tilting and the star formation rate. For both of our subsamples, we find that galaxies with a higher star formation rate generally tilt faster, suggesting that it is the delivery of misaligned angular momentum through gas that dominates the tilting.

6 DISCUSSION AND CONCLUSIONS

When we consider galaxies with halo masses comparable to the MW (subsample A), we find significant tilting with an error weighted mean rate of $7.6^\circ \text{Gyr}^{-1}$ and a standard deviation of $4.5^\circ \text{Gyr}^{-1}$. The entire subsample displays significant tilting with rates higher than the detection limit of *Gaia*. We further restrict to a sample with low relative stellar accretion and a maximum stellar mass fraction in satellites of 40 per cent (subsample B), finding a lower mean tilting rate of $6.2^\circ \text{Gyr}^{-1}$, with a range from 0.65 to $24.6^\circ \text{Gyr}^{-1}$.

A variety of processes may drive the change in angular momentum that we have measured. Interactions with other galaxies are the most violent processes changing the angular momentum of discs drastically over a short period. However, we have found that even when we exclude strong interactions, we still measure significant tilting above the detection limit of *Gaia*. Therefore, we must turn to secular processes such as halo torques and the accretion of

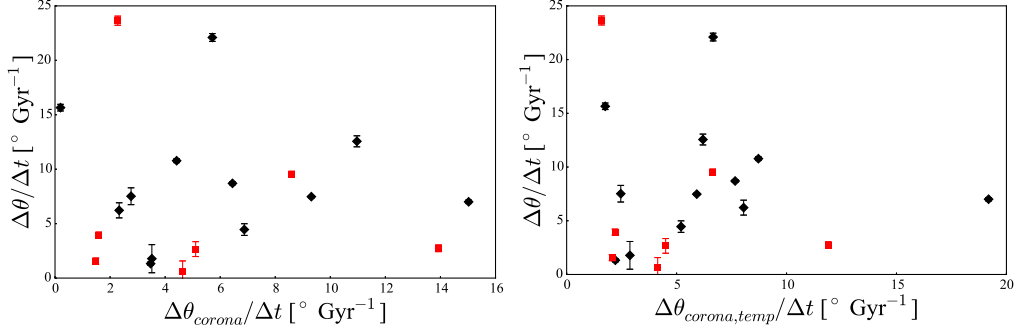


Figure 6. Left-hand panel: The tilting rate of the stellar disc versus the tilting rate of the corona, defined as all gas between radii $0.2r_{200}$ and r_{200} . We find no correlation for subsample A (black diamonds) with a coefficient of $p = -0.08$. For subsample B (red squares), we find no correlation with $p = -0.18$. Right-hand panel: The tilting rate of the stellar disc versus the tilting rate of the corona, defined as all gas with a temperature $T > 5 \times 10^4$ K. We find no significant correlation for subsample A (black diamonds), with $p = -0.035$. Similarly for subsample B (red squares), we find no correlation, with $p = -0.27$.

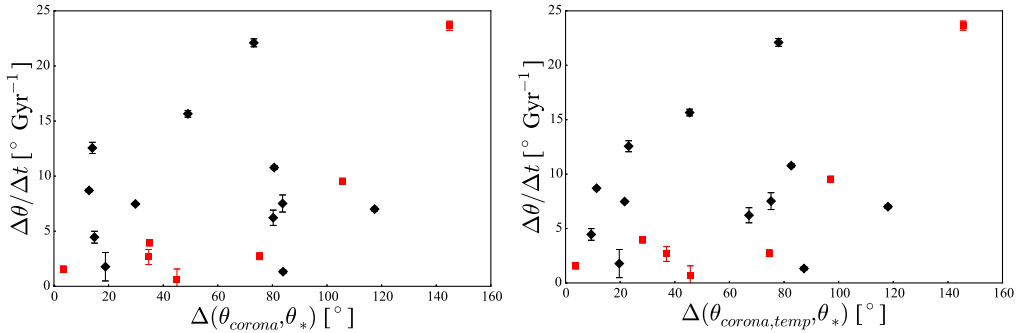


Figure 7. Left-hand panel: The tilting rate of the stellar disc versus the angular difference in angular momentum orientation between the stellar disc and the hot gas corona, defined as all gas between radii $0.2r_{200}$ and r_{200} . We find a weak correlation for subsample A (black diamonds), with $p = 0.4$, and a strong correlation for subsample B (red squares), with $p = 0.86$. Right-hand panel: The tilting rate of the stellar disc versus the difference in orientation between the stellar disc and the hot gas corona, defined as all gas with temperature $T > 5 \times 10^4$ K. We find a weak correlation for subsample A (black diamonds) with $p = 0.5$, and a strong correlation for subsample B (red squares) with $p = 0.87$.

misaligned cold gas on to the disc to explain the entire phenomena of disc tilting.

We investigated the effect of the local environment on the tilting rate of the disc. Comparing the local density against the tilting rate, we find that the tilting rate does not correlate with the normalized local density within 3 Mpc for subsample A. However, for subsample B, we do find a correlation. When we consider larger radii, we find a correlation between the tilting rate and the local environment for both subsamples. Galaxies in denser regions generally tilt at higher rates than galaxies in lower density regions, irrespective of the galaxies stellar mass accretion.

The MW has a very close, similar mass, neighbour M31. In order to compare to the MW's configuration, we measured the distance to the nearest massive galaxy and determined the correlation with the tilting rates. We find almost no correlation for subsample A; however, for subsample B, we do find very weak anti-correlation. This suggests that the local configuration is unlikely to be a large contributing factor when the disc is accreting significant mass. Our sample contains galaxies in similar configurations to the MW with companion galaxies within a few hundred kpc; these galaxies exhibit tilting rates similar to more isolated galaxies.

To determine the effect of misaligned gas accreting from the hot gas corona, we measured both the tilting rate of the hot gas corona and the angular misalignment between the stars and the corona. We find no correlation between the tilting rates of the two different components for either subsample. We also compared the tilting rate of the disc to the angular momentum misalignment between the two components: For subsample A, there is a weak correlation, which becomes stronger for subsample B. We also find a correlation between the misalignment of the disc and coronal angular momentum and the LSS. Thus, the LSS may directly affect the tilting rate via torques, or indirectly by influencing the flow of gas into the halo. For both subsamples, galaxies with higher star formation tilt faster, perhaps indicating that the role of the LSS is in driving the misaligned gas. We conclude that the angular momentum misalignment between the corona and disc is an important, possibly dominant, driver of disc tilting.

In this paper, we have measured the tilting rates for a wide variety of galaxies of similar mass to the MW, in various configurations, some similar to the local configuration of the MW. Every configuration yielded a tilting rate above the *Gaia* limit and should be detectable. Confirmation of a tilting disc would have

important consequences for understanding the evolution of the MW. For example, the tilt of the disc will make the potential seen by the Sagittarius Stream time varying. Conversely failure to detect tilting may suggest the MW is in an unexpectedly quiet configuration.

ACKNOWLEDGEMENTS

SWFE would like to thank Dominic Bowman for useful conversations. VPD is supported by the Science and Technology Funding Council Consolidated grant #ST/M000877/1. VPD acknowledges the support of the Pauli Center for Theoretical Studies, which is supported by the Swiss National Science Foundation (SNF), the University of Zürich, and ETH Zürich. Simulations were performed at the Rechen Zentrum of the Max Planck Society in Garching (RZG) on the THEO and HYDRA machines.

REFERENCES

- Agustsson I., Brainerd T. G., 2006, *ApJ*, 650, 550
 Allgood B., Flores R. A., Primack J. R., Kravtsov A. V., Wechsler R. H., Faltenbacher A., Bullock J. S., 2006, *MNRAS*, 367, 1781
 Alves D. R., Nelson C. A., 2000, *ApJ*, 542, 789
 Azzaro M., Patiri S. G., Prada F., Zentner A. R., 2007, *MNRAS*, 376, L43
 Bailin J., Steinmetz M., 2004, *ApJ*, 616, 27
 Bailin J., Steinmetz M., 2005, *ApJ*, 627, 647
 Bardeen J. M., Bond J. R., Kaiser N., Szalay A. S., 1986, *ApJ*, 304, 15
 Barnes J., Efstathiou G., 1987, *ApJ*, 319, 575
 Bett P. E., Frenk C. S., 2012, *MNRAS*, 420, 3324
 Bett P. E., Frenk C. S., 2016, *MNRAS*, 461, 1338
 Brainerd T. G., 2005, *ApJ*, 628, L101
 Briggs F. H., 1990, *ApJ*, 352, 15
 Brook C. B., Kawata D., Gibson B. K., Freeman K. C., 2004, *ApJ*, 612, 894
 Brooks A. M., Governato F., Quinn T., Brook C. B., Wadsley J., 2009, *ApJ*, 694, 396
 Bryan S. E., Cress C. M., 2007, *MNRAS*, 380, 657
 Bureau M., Freeman K. C., Pfizner D. W., Meurer G. R., 1999, *AJ*, 118, 2158
 Dahlem M., 1997, *PASP*, 109, 1298
 Debattista V. P., Roškar R., Valluri M., Quinn T., Moore B., Wadsley J., 2013, *MNRAS*, 434, 2971
 Debattista V. P., van den Bosch F. C., Roškar R., Quinn T., Moore B., Cole D. R., 2015, *MNRAS*, 452, 4094
 Deg N., Widrow L., 2013, *MNRAS*, 428, 912
 Dong X. C., Lin W. P., Kang X., Ocean Wang Y., Dutton A. A., Macciò A. V., 2014, *ApJ*, 791, L33
 Dubinski J., 1992, *ApJ*, 401, 441
 Dubinski J., Carlberg R. G., 1991, *ApJ*, 378, 496
 Dubinski J., Chakrabarty D., 2009, *ApJ*, 703, 2068
 Dubinski J., Kuijken K., 1995, *ApJ*, 442, 492
 Fall S. M., Efstathiou G., 1980, *MNRAS*, 193, 189
 Faltenbacher A., Li C., Mao S., van den Bosch F. C., Yang X., Jing Y. P., Pasquali A., Mo H. J., 2007, *ApJ*, 662, L71
 Frenk C. S., White S. D. M., Davis M., Efstathiou G., 1988, *ApJ*, 327, 507
 Fukugita M., Peebles P. J. E., 2006, *ApJ*, 639, 590
 Gómez F. A., Besla G., Carpintero D. D., Villalobos Á., O’Shea B. W., Bell E. F., 2015, *ApJ*, 802, 128
 Governato F., Willman B., Mayer L., Brooks A., Stinson G., Valenzuela O., Wadsley J., Quinn T., 2007, *MNRAS*, 374, 1479
 Haardt F., Madau P., 1996, *ApJ*, 461, 20
 Huang S., Carlberg R. G., 1997, *ApJ*, 480, 503
 Jing Y. P., Suto Y., 2002, *ApJ*, 574, 538
 Kallivayalil N., van der Marel R. P., Besla G., Anderson J., Alcock C., 2013, *ApJ*, 764, 161
 Katz N., 1992, *ApJ*, 391, 502
 Kennicutt R. C., Jr, 1998, *ApJ*, 498, 541
 Kereš D., Katz N., Weinberg D. H., Davé R., 2005, *MNRAS*, 363, 2
 Klypin A., Zhao H., Somerville R. S., 2002, *ApJ*, 573, 597
 Knollmann S. R., Knebe A., 2009, *ApJS*, 182, 608
 Komatsu E. et al., 2009, *ApJS*, 180, 330
 Kravtsov A., Vikhlinin A., Meshcheryakov A., 2014, preprint (arXiv:preprint)
 Law D. R., Majewski S. R., 2010, *ApJ*, 714, 229
 Law D. R., Majewski S. R., Johnston K. V., 2009, *ApJ*, 703, L67
 Li Z., Wang Y., Yang X., Chen X., Xie L., Wang X., 2013, *ApJ*, 768, 20
 Lindegren L. et al., 2008, in Jin W. J., Platais I., Perryman M. A. C., eds, *IAU Symp. 248, The Gaia Mission: Science, Organization and Present Status*. Kluwer, Dordrecht, p. 217
 Macciò A. V., Dutton A. A., van den Bosch F. C., 2008, *MNRAS*, 391, 1940
 Moore B., Kazantzidis S., Diemand J., Stadel J., 2004, *MNRAS*, 354, 522
 Nierenberg A. M., Unger M. W., Treu T., Marshall P. J., Fassnacht C. D., 2011, *ApJ*, 731, 44
 Peñarrubia J., Gómez F. A., Besla G., Erkal D., Ma Y.-Z., 2016, *MNRAS*, 456, L54
 Perryman M. A. C. et al., 2001, *A&A*, 369, 339
 Perryman M., Spergel D. N., Lindegren L., 2014, *ApJ*, 789, 166
 Read J. I., Lake G., Agertz O., Debattista V. P., 2008, *MNRAS*, 389, 1041
 Robertson B., Bullock J. S., Cox T. J., Di Matteo T., Hernquist L., Springel V., Yoshida N., 2006, *ApJ*, 645, 986
 Roškar R., Debattista V. P., Brooks A. M., Quinn T. R., Brook C. B., Governato F., Dalcanton J. J., Wadsley J., 2010, *MNRAS*, 408, 783
 Sales L., Lambas D. G., 2004, *MNRAS*, 348, 1236
 Savage B. D., de Boer K. S., 1979, *ApJ*, 230, L77
 Schmidt M., 1959, *ApJ*, 129, 243
 Spitzer L. Jr, 1956, *ApJ*, 124, 20
 Stinson G., Seth A., Katz N., Wadsley J., Governato F., Quinn T., 2006, *MNRAS*, 373, 1074
 van den Bosch F. C., Abel T., Croft R. A. C., Hernquist L., White S. D. M., 2002, *ApJ*, 576, 21
 van der Marel R. P., Alves D. R., Hardy E., Suntzeff N. B., 2002, *AJ*, 124, 2639
 Wadsley J. W., Stadel J., Quinn T., 2004, *New A*, 9, 137
 Wang Q. D., Immler S., Walterbos R., Lauroesch J. T., Breitschwerdt D., 2001, *ApJ*, 555, L99
 Wang Y., Yang X., Mo H. J., Li C., van den Bosch F. C., Fan Z., Chen X., 2008, *MNRAS*, 385, 1511
 Wang Y., Park C., Hwang H. S., Chen X., 2010, *ApJ*, 718, 762
 Wang Y. O., Lin W. P., Kang X., Dutton A., Yu Y., Macciò A. V., 2014, *ApJ*, 786, 8
 White S. D. M., Frenk C. S., 1991, *ApJ*, 379, 52
 White S. D. M., Rees M. J., 1978, *MNRAS*, 183, 341
 Yang X., van den Bosch F. C., Mo H. J., Mao S., Kang X., Weinmann S. M., Guo Y., Jing Y. P., 2006, *MNRAS*, 369, 1293
 Yurin D., Springel V., 2015, *MNRAS*, 452, 2367

This paper has been typeset from a \LaTeX file prepared by the author.